Flow physics and control of trapped vortex cell flows

POLITECNICO DI TORINO

SCUOLA DI DOTTORATO

Dottorato in Fluidodinamica – XXV ciclo

Tesi di Dottorato

Flow physics and control of trapped vortex cell flows

Davide Lasagna

Tutore
prof. Gaetano Iuso

Coordinatore del corso di dottorato
prof. Gaetano Iuso

Febbraio 2013

There are more things in heaven and earth,
Horatio, than are dreamt of in your philosophy.

Contents

Motivations and objectives 12

1 Review of the literature 14
- 1.1 Flow in a trapped vortex cell . . . 14
- 1.2 Flows in canonical rectangular cavities . . . 19
  - 1.2.1 Unsteady phenomena . . . 19
  - 1.2.2 Three dimensional properties . . . 21
  - 1.2.3 Recirculating flow . . . 22

2 Design of the experiment 23
- 2.1 Design rationale . . . 23
- 2.2 The wind tunnel . . . 24
  - 2.2.1 Modifications to the wind tunnel test section . . . 24
- 2.3 The probe traverse system . . . 26
- 2.4 The boundary layer suction system . . . 26
- 2.5 The cavity model . . . 27
- 2.6 The cavity suction system . . . 28
- 2.7 The synthetic jet system . . . 29
- 2.8 Measurements techniques . . . 30
  - 2.8.1 Data acquisition and signal generation hardware . . . 34

3 Unactuated flow in the cell 36
- 3.1 Preliminary considerations . . . 36
- 3.2 Results for CASE1 . . . 41
  - 3.2.1 Upstream conditions . . . 41
  - 3.2.2 Shear layer evolution . . . 42
  - 3.2.3 Spectral and correlation analyses . . . 46
  - 3.2.4 Upstream/downstream boundary layer comparison . . . 53
  - 3.2.5 Flow visualisations . . . 57
  - 3.2.6 Three dimensional properties of the flow . . . 60
- 3.3 Results for CASE2 . . . 63

3.3.1 Shear layer evolution . . . 64
3.3.2 Upstream/downstream boundary layer comparison . . . 66
3.3.3 Spectral analysis . . . 69
3.3.4 Flow visualisations . . . 74
3.3.5 Three dimensional structure of the flow . . . 76
3.4 Remarks and discussion . . . 78

4 Control of the TVC flow by suction 80
4.1 Preliminary remarks . . . 80
4.2 Control for CASE1 . . . 81
4.2.1 Flow visualisations . . . 90
4.2.2 Spectral analysis . . . 91
4.2.3 Three dimensional organisation of the cell flow . . . 95
4.3 Control for CASE2 . . . 99
4.3.1 Three dimensional structure of the flow . . . 104
4.4 Effectiveness of the control . . . 107
4.5 Control of the flow by suction in region B . . . 109
4.5.1 CASE1 . . . 109
4.5.2 CASE2 . . . 114
4.5.3 Discussion about the location of suction . . . 117
4.6 Remarks and conclusions . . . 117

5 Open-loop control of the TVC flow with a synthetic jet actuator 120
5.1 Premise . . . 120
5.1.1 Design of the synthetic jet device and motivations . . . 120
5.1.2 Objectives . . . 121
5.2 Characterisation of the synthetic jet actuator . . . 121
5.3 Results . . . 124
5.3.1 Results for CASE1 . . . 125
5.3.2 Control for CASE2 . . . 131
5.3.3 A further investigation at lower speed, CASEx . . . 136
5.4 Effects of the control on the downstream boundary layer momentum thickness . . . 137
5.5 Dynamic response of the flow for CASE1 . . . 139
5.6 Remarks and conclusions . . . 142

6 Optimisation of open-loop control signal using Evolutionary Strategies. 143
6.1 Signal parameterisation . . . 144
6.2 The Evolution Strategy (ES) algorithm . . . 145
6.2.1 Algorithm control . . . 146

6.3 Results and discussion . . . 147
6.3.1 Sinusoidal open-loop forcing . . . 147
6.3.2 Optimal open-loop forcing . . . 147
6.4 Remarks and conclusions . . . 152

7 Evolutionary design of closed-loop control systems 154
7.1 Physical system and block diagram . . . 156
7.2 Controller structure . . . 158
7.3 Controller design by evolutionary computing . . . 161
7.3.1 Algorithm design . . . 161
7.4 Practical implementation of the controller . . . 162
7.5 Results . . . 164
7.6 Remarks . . . 167

Conclusions 169

A Theoretical foundations of the Multi-Time-Delay Linear Stochastic Estimation technique. 173
A.1 Multi-time-delay Linear Stochastic Estimation approach . . . 173
A.1.1 Single-point, multi-time-delay linear Stochastic Estimation . . . 175
A.1.2 Multi-point multi-time-delay Stochastic Estimation . . . 176

List of Figures

1.1 Schematic concept of an airfoil with TVC control. 14
1.2 Drawing of the airfoil with the trapped vortex cell tested by Lasagna et al. [2011] 16
1.3 Lift coefficient curves for the four configurations tested in Lasagna et al. [2011]. 17
1.4 Drag coefficient curves for the four configurations tested in Lasagna et al. [2011]. 17
1.5 Schematic showing the mechanism determining self-sustained oscillation of the shear layer in a rectangular cavity flow. Taken from Cattafesta et al. [2008]. 20

2.1 Sketch of the simplified configuration chosen for the experimental investigation. 23
2.2 Front and rear views of the "Fucsia" wind tunnel used for the investigation. 24
2.3 Pictures of the convergent ramp, supports and flat panels. 25
2.4 On the left: CAD model of the wind tunnel test section, with details of the top panel supported by two spanwise rails. On the right: picture of the top panel, showing also the probe traverse system. 26
2.5 Sketch of the cavity geometry and of the reference system, (a), and CAD drawing of the cavity model, (b). 28
2.6 Detail of the porous surface on the downstream cavity edge, in region B. 29
2.7 Sketch of the side view of the cavity with the synthetic jet actuator. . 30
2.8 Detail of the hot wire probe holder. Flow is from left to right. 31
2.9 Sketch of the side view of the cavity model at the span of the central row of microphones, (a); top view (b). 31
2.10 Top view of the central row of condenser microphones. 32
2.11 Acquisition modules. From left to right: three 24-bit modules for the condenser microphones signals, the relay module for motion control and the 16-bit resolution module for hot-wire signal. 35

3.1 Upstream velocity/frequency spectrogram for the pressure fluctuation from microphone $m7$. 37
3.2 Upstream velocity/frequency spectrogram for the velocity fluctuation in the shear layer at $x/L = 0.58$, $y/\delta_0 = 0.22$. 39
3.3 Upstream boundary layer profiles at $x = -10$ mm. (a) - mean velocity profile $\overline{u}/u_e$, experimental data and a Blasius solution fit are depicted; (b) - profile of u'_{rms}/u_e. 42
3.4 Selected mean velocity profiles $\overline{u}$ along the shear layer. About one each three profiles is shown, for clarity. The downstream edge of the cavity model is also visible. Flow is from left to right. Horizontal and vertical axes are in real scale. 43
3.5 Selected profiles of u'_{rms}/u_e along the shear layer. About one each three profiles is shown, for clarity. The red curve is the streamwise evolution of $\max(u'_{rms}/u_e)$. Horizontal and vertical axes, (the left one), are in real scale. 43
3.6 Streamwise evolution of broadband, circle, and narrow-band power spectral densities, at $f = f_{wt}$, triangles, and $f = 2f_{wt}$, squares. 45
3.7 Streamwise evolution of the non-dimensional vorticity thickness $\delta_\omega/\delta_{\omega_0}$. 46
3.8 Power spectral density of the normalised velocity fluctuations $u^* = u/u_e$, at three reference points: (a) - $x/L = 0$, $y/\delta_0 - 3.4$; (b) - $x/L = 0.58$, $y/\delta_0 = 0.45$; (c) - $x/L = 1.0$, $y/\delta_0 = -0.45$. See figure 2.9 to locate the measurement points. 47
3.9 colour map of the power spectral density of the normalised velocity fluctuations $u^* = u/u_e$, at the frequency of the first mode $f_{wt} = 150Hz$. The value is obtained by integration of the spectral density in a band large 1 Hz around f_{wt}. 48
3.10 Power spectral density of the normalised pressure fluctuations $p^* = 2p/(\rho u_e^2)$, for microphone $m7$, (a), microphone $m8$, (b) and microphone $m3$, (c). Please refer to figure 2.9 for the exact positions of the microphones. 49
3.11 Cross-correlation coefficient functions $\rho_{up_j}(\tau)$. The velocity time series is measured at the reference point, $x/L = 0.58$, $y/\delta_0 = 0.45$. Microphone $m7$, (a), microphone $m8$, (b) and microphone $m3$, (c). Please refer to figure 2.9 for the exact positions of the microphones. . 50
3.12 colour map of the maximum absolute value of the cross-correlation coefficient functions ρ_{up_7}, across the entire shear layer. 51
3.13 Squared coherence functions $\gamma^2_{up_j}$. The velocity time series is measured at the reference point, $x/L = 0.58$, $y/\delta_0 = 0.45$. Microphone $m7$, (a), microphone $m8$, (b) and microphone $m3$, (c). Please refer to figure 2.9 for the exact positions of the microphones. 52

3.14 The colour maps show the spatial distribution of the reconstructed fluctuating velocity component in the shear layer in four selected time instants. The time delay between successive snapshots of the sequence is $45\Delta t$, where $\Delta t = 1/8000$ s is the sampling interval. The grey colour shading represents the modulus of the velocity fluctuation. Eight iso-lines have been drawn for values of $|\hat{u}'/u_e|$ equal to ± 0.11, ± 0.08, ± 0.05, ± 0.02; dashed contours indicate a negative value. . . . 54
3.15 Conceptual sketch explaining the moving wall effect. 55
3.16 Comparison of the upstream $x/L = -0.14$, and downstream, $x/L = 2.05$, boundary layer mean velocity profiles, (a), and of the profiles of the root-mean-square value of the velocity fluctuation, (b). 57
3.17 Snapshot sequence for CASE1 in the mid-span, sorted left to right, top to bottom. 59
3.18 Mean value, top, and root-mean-square value, bottom, of the velocity measured at $x/L = 0.59$, $y/\delta_0 = -1.69$, in the cavity region. 60
3.19 Spectra of the velocity fluctuations at $z/b = -0.04$ and $z/b = -0.26$ of the velocity fluctuation measured at $x/L = 0.59$, $y/\delta_0 = -1.69$, in the cavity region. 61
3.20 Mean, top, and root-mean-square value, bottom of the velocity fluctuation measured at $x/L = 1.32$, $y/\delta_0 = 0.45$, in the turbulent boundary layer downstream of the cavity. 62
3.21 Profiles of $\overline{u}/u_e$, (a), and of u'_{rms}/u_e, (b), for the upstream boundary layer at $x = -10$ mm for CASE2. 63
3.22 Profiles of $\overline{u}/u_e$ at several spatial locations along the shear layer. One each three velocity profiles is shown for clarity. The downstream cavity shoulder is also visible on the right. 64
3.23 Profiles of u'_{rms}/u_e at several spatial locations along the shear layer. One each three velocity profiles is shown for clarity. The downstream cavity shoulder is also visible on the right. 65
3.24 Evolution of the shear layer vorticity thickness along the streamwise direction. 67
3.25 Comparison of the upstream $x/L = -0.14$, and downstream, $x/L = 2.05$, boundary layer mean velocity profiles, (a), and of the profiles of the root-mean-square value of the velocity fluctuation, (b) 67
3.26 Power spectral density of the normalised velocity fluctuations $u^* = u/u_e$ at three control points. 69
3.27 Example of velocity time history at control point B, located inside the cavity at $x/L = 0.58$, $y/\delta_0 = -0.68$. 70
3.28 Pressure fluctuation spectra for three representative microphones. The grey curve is the velocity spectrum at $x/L = 0.58$, $y/\delta_0 = -1.1$, reported for comparison over an fictitious vertical scale. 71

3.29 Profiles of $\max|\rho_{up_i}(\tau)|$ for microphones $m7$ located under the cusp, $m8$ located in the impingement region, and $m3$, far downstream of the cavity. 72
3.30 Cross-correlation coefficient function $\rho_{up}(\tau)$, where u is the velocity signal inside the cavity region, at $y/\delta_0 = -1.1$, and p is that from microphone $m8$, part (a), or microphone $m7$, part (b). 73
3.31 Squared coherence function $\gamma^2_{up}(f)$, where u is the velocity signal inside the cavity region, at $x/L = 0.58$, $y/\delta_0 = -1.1$, and p is the pressure measured by microphone $m8$, part (a), or by microphone $m7$, part (b). 74
3.32 Snapshot sequence for CASE2, sorted left to right, top to bottom. Time interval between successive frames is 3/125 s. One of each three snapshots in shown, to complete almost a full revolution of the vortex core. 75
3.33 Spanwise profiles in the cavity region at $x/L = 0.58$, $y/\delta_0 = -1.36$. Mean velocity, (a), and root-mean-square value of the velocity fluctuations, (b). 77
3.34 Power spectral densities of the velocity fluctuations in the mid-span, $z/b = 0.0$ lighter line, and at $z/b = 0.43$, darker line, where u'_{rms}/u_e is minimum. 77

4.1 Sketch of the cavity geometry showing the two regions where suction was separately applied. 81
4.2 Effects of the suction rate on the mean velocity at a control point downstream of the cavity, at $x/L = 2.05$, $y/\delta_0 = 0.23$. 82
4.3 Effects of the suction rate on the profiles of mean velocity and of the root-mean-square value of the velocity fluctuations, at $x/L = 2.05$. The upstream case and the no-control case are also reported. 83
4.4 Selected mean velocity profiles $\overline{u}(y)/u_e$ along the shear layer. Approximately one each four profiles is shown, for clarity. The downstream edge of the cavity is also visible. Flow is from left to right. 84
4.5 Fraction of the height of the upstream boundary layer associated to a given suction parameter S. 86
4.6 Sketch of the proposed boundary layer ingestion model. 86
4.7 Selected profiles of u'_{rms}/u_e along the shear layer. Approximately one each four profiles is shown, for clarity. The downstream edge of the cavity is also visible. Flow is from left to right. The small vertical segments indicate the value of $u'_{rms}/u_e = 0.1$. The vertical dashed line indicates the location where the profile is taken, and the value of $u'_{rms}/u_e = 0$ 87
4.8 Effects of the suction rate on the velocity profiles at $x/L = 0.58$. . . . 89

4.9 Effects of the suction rate on the mean velocity at a control point inside the cavity region, at $x/L = 0.58$, $y/\delta_0 = -2.27$. 89
4.10 Snapshot of flow visualisation for CASE1 with suction, $y_q/\delta_0 \approx 1.85$. 91
4.11 Power spectral density of the normalised velocity fluctuations $u^* = u/u_e$ at $x/L = 0.58$, and at a value y/δ_0 corresponding to the peak of the profiles of u'_{rms}/u_e as of figure 4.8, for different values of the suction parameter. Curve (a), $S = 0$; (b), $S = 0.009$; (c), $S = 0.021$; (d), $S = 0.032$; (e), $S = 0.065$; (f), $S = 0.097$. 92
4.12 Power spectral density distribution of the velocity fluctuations at $x/L = 0.58$, across the entire shear layer, for $S = 0.097$. 93
4.13 Detail of the power spectral density of the normalised velocity fluctuations $u^* = u/u_e$ at $x/L = 0.58$ and $y/\delta_0 = -2$, for different values of the suction parameter. Curve (a), $S = 0$; (b), $S = 0.009$; (c), $S = 0.021$; (d), $S = 0.032$; (e), $S = 0.065$; (f), $S = 0.097$. 94
4.14 Distribution of the power spectral density of the velocity fluctuations across the boundary layer at $x/L = 2.05$, for $S = 0.037$. 94
4.15 Effects of the suction rate on the spanwise profile of the mean velocity at a control point in the cavity, at $x/L = 0.58$, $y/\delta_0 = -2.27$. 96
4.16 Effects of the suction rate on the spanwise profile of the root-mean-square value of the velocity fluctuations at a control point in the cavity, at $x/L = 0.58$, $y/\delta_0 = -2.27$. 97
4.17 Effects of the suction rate on the spectral distribution of the velocity fluctuations at a control point in the cavity, at $x/L = 0.58$, $y/\delta_0 = -2.27$. Figure (a), $S = 0$; (b), $S = 0.009$; (c), $S = 0.032$; (d), $S = 0.065$; (e), $S = 0.097$. 98
4.18 Effects of the suction rate on the mean velocity at a control downstream of the cavity, at $x/L = 2.05$, $y/\delta_0 = 0.045$. 99
4.19 Effects of the suction rate on the profiles of $\overline{u}/u_e$ and u'_{rms}/u_e at the downstream position $x/L = 2.05$. Profiles for the upstream reference boundary layer are also reported. 100
4.20 Fraction of the height of the upstream boundary layer associated to a given suction parameter S. 101
4.21 Effects of the suction rate on the profiles of $\overline{u}/u_e$ and u'_{rms}/u_e in the shear layer region, at $x/L = 0.58$. 102
4.22 Selected mean velocity profiles along the shear layer for $S = 0.054$. For each profile two vertical dashed lines indicate marks for $u = 0$ and $u = u_e$. The first mark also indicates the x/L position where the mean velocity profiles was measured. 103

4.23 Selected profiles of u'_{rms}/u_e along the shear layer for $S = 0.054$. For each profile, the vertical dashed line indicates the x/L position where the profile was measured and the value $u'_{rms}/u_e = 0$. The smaller red segment indicates a mark for $u'_{rms}/u_e = 0.1$, and its vertical position follows the peak of u'_{rms}/u_e, whose y/δ_0 position is indicated by a red dot. 104

4.24 Spanwise profiles of the mean velocity at $x/L = 0.58$, $y/\delta_0 = -0.45$, for several values of the suction parameter S, indicated in the figure. The vertical red lines indicate the position of the ribs of the cavity model, at which suction is interrupted for a width of $0.023b$. 105

4.25 Spanwise profiles of u'_{rms}/u_e at $x/L = 0.58$, $y/\delta_0 = -0.45$, for several values of the suction parameter S, (scale on the right), superimposed to colour maps of the distributions of the energy of the velocity fluctuations across the span. Figure (a): $S = 0$, (b): $S = 0.008$, (c): $S = 0.024$, (d): $S = 0.039$, (e): $S = 0.055$. 106

4.26 Effects of the suction rate on the reduction of the momentum thickness of the boundary layer at $x/L = 2.05$. The suction rate has been rescaled using the parameter y_q/δ_0. 108

4.27 Comparison of the profiles of $\overline{u}/u_e$, left, and of u'_{rms}/u_e, right, between the suction regions A and B, for two conditions of suction, at $x/L = 2.05$. 109

4.28 Comparison of the profiles of $\overline{u}/u_e$, left, and of u'_{rms}/u_e, right, between the suction regions A and B, for two conditions of suction, at $x/L = 0.58$. 111

4.29 Snapshot sequence of the flow visualisation for CASE1 in the midspan, sorted left to right, top to bottom. $S = 0.1$. Time delay between two subsequent snapshot is $3/400$ s. 113

4.30 Comparison of the profiles of $\overline{u}/u_e$, left, and of u'_{rms}/u_e, right, between the suction regions A and B, for two conditions of suction, at $x/L = 2.05$. 114

4.31 Comparison of the profiles of $\overline{u}/u_e$, left, and of u'_{rms}/u_e, right, between the suction regions A and B, for two conditions of suction, at $x/L = 0.58$. 116

5.1 Color map of the mean jet velocity u_j, as a function of the forcing frequency f_j and the forcing voltage amplitude A_j, figure (a). Behaviour of u_j as a function of f_j, for three selected voltage amplitudes, figure (b). 123

5.2 Color map of the mean velocity in $x/L = 1.91$, $y/\delta_0 = 0.3$, as a function of synthetic jet control parameters. 125

5.3 Profiles of the mean velocity, (a), and of the root-mean-square value of the velocity fluctuations (b), at $x/L = 1.91$, for different forcing amplitudes, at $f_j = 75$. The corresponding profiles for the upstream laminar boundary layer are also shown for comparison. 126
5.4 Color map of the mean velocity inside the cavity, under the cusp at $x/L = 0$, $y = -2.27$, as a function of synthetic jet control parameters. 127
5.5 Profiles of the normalised mean velocity, (a), and of the normalised root-mean-square value of the velocity fluctuations (b), at $x/L = 0.05$, for different forcing amplitudes, at $f_j = 75$ Hz. The no-control condition is also shown for reference. 128
5.6 Mean velocity profiles across the shear layer in control conditions in CASE1 with $f_j = 75$ Hz and $R = 1.29$. 129
5.7 Profiles of the normalised root-mean-square value of the velocity fluctuations u'_{rms}/u_e across the shear layer in control conditions in CASE1 with $f_j = 75$ Hz and $R = 1.29$. 130
5.8 Color map of the mean velocity inside the cavity, under the cusp at $x/L = 0$, $y = -10$ mm, as a function of synthetic jet control parameters. 131
5.9 Profiles of the mean velocity, (a), and of the root-mean-square value of the velocity fluctuations (b), at $x/L = 0.58$, for different forcing amplitudes, at $f_j = 75$ Hz. 132
5.10 Color map of the mean velocity downstream of the cell at $x/L = 1.91$, $y/\delta_0 = 0.09$, as a function of synthetic jet control parameters. . 133
5.11 Profiles of the mean velocity, (a), and of the root-mean-square value of the velocity fluctuations (b), at $x/L = 1.91$, for different forcing amplitudes at $f_j = 75$ Hz. The upstream profiles are also reported for comparison. 134
5.12 The colour maps show the power spectral densities of the velocity fluctuations across the boundary layer downstream of the cell at $x/L = 2.05$, for three forcing conditions at $f_j = 75$ Hz and in no-control conditions. 135
5.13 Profiles of the mean velocity, (a), and of the root-mean-square value of the velocity fluctuations (b), at $x/L = 1.91$, for different forcing conditions at $u_e = 5$ m/s. The upstream profiles are also reported for comparison. $f_j = 75$ Hz. 137
5.14 Upstream/downstream boundary layer momentum thickness ratio as a function of the jet velocity ratio, for all the investigated cases. . . . 138
5.15 Forcing amplitude-frequency spectrograms of the normalised velocity fluctuations in $x/L = 0.58$, $y/\delta_0 = 0$, for several values of the forcing frequency. 141

6.1 Discrimination and re-sampling of the control signal, (a), and vector representation of a candidate solution, (b). 145
6.2 Mean velocity percent increment at point P as a function of the forcing frequency of a pure sinusoidal control signal. The sine amplitude is 1 Volt. 147
6.3 Objective function evolution history. 148
6.4 Optimized control signal. 149
6.5 Velocity time history measured at the slot exit for the optimized signal, (a), and for the sinusoidal signal at $f_j = 72$ Hz, (b). 150
6.6 Profile of the mean streamwise velocity $\overline{u}/u_e$, (a), and of the root-mean-square value of the velocity fluctuations u'_{rms}/u_e, (b), at location $x/L = 2.05$, downstream of the cavity. 151

7.1 Schematic of the closed-loop control system. 156
7.2 Example of controller's poles and zeros on the complex z plane. Only the positive imaginary half-plane is shown, since it is specular to the negative half-plane, as the controller coefficients must be real. 159
7.3 Amplitude response, upper, and phase response, lower, of the controller of figure 7.2 160
7.4 Sketch of the genome of a single individual controller. The controller is defined by its zeros and by the gain. 162
7.5 Labview FPGA code implementing the closed-loop control logic . . . 163
7.6 Behaviour of an example controller in the initial generations. Time history of the hot wire filtered voltage signal, (a), and time history of the control signal, (b). Closed-loop control is switched on at $t = 1$ s. . 165
7.7 Behaviour of an example controller in "lock-in" conditions. Time history of the hot wire filtered voltage signal, (a), and time history of the control signal, (b). Closed-loop control is switched on at $t = 1$ s. . 166
7.8 Behaviour of an example controller after the optimisation process has come to the end. Time history of the hot wire filtered voltage signal, (a), and time history of the control signal, (b). Closed-loop control is switched on at $t = 1$ s. 167

List of Tables

3.1 Summary of the main parameters of the cases tested. The pedix $_0$ denotes quantities at the upstream reference station, at $x/L = -0.14$, i.e. $x = -10$ mm. 41

Motivations and objectives

The main objective of this work is to investigate on the physics and on the control of the flow in a Trapped Vortex Cell, often referred to as TVC in the following. A TVC is a cavity with a particular geometry, which is optimised to trap a vortical structure. This configuration has recently gained interest has a device to control the flow past thick airfoils, but fundamental research is still required to make this technique effective.

Specifically, a first goal of this work is to investigate on the fundamental physics of this flow, by studying the basic elements and the dominant phenomena. In fact, this flow field is the result of the complex interaction of several flows, such as the upstream boundary layer, the shear layer detaching from the cavity leading edge, the vortex core, and the boundary layer developing downstream. A further issue of interest addressed in this work is that related to the role of unsteadiness of the cell flow, and in particular of the shear layer, whose self-sustained oscillations are a common feature of open-cavity flows.

The understanding of the driving physical mechanisms of the base flow is required to successfully proceed in developing a control strategy aiming at the control of the flow, because it is necessary to manipulate this flow in order to make the TVC an effective control device. Therefore, a second goal is to study and compare two different control techniques targeting the cavity flow. The first of the two is steady suction of the flow in the cell and has been already applied in past researches, but some additional insight into its effects on the base flow is required. The second proposed control technique is open-loop control with a synthetic jet actuator, a more efficient device whose unsteady action can couple to or drive the relevant mechanisms of the flow. Furthermore, open-loop control studies with a synthetic jet are propaedeutic for closed-loop control of the flow, briefly investigated in the last part of research.

This thesis is divided as follows. Chapter 1 presents a review of the literature regarding aspects relevant to this research. Chapter 2 presents the experimental setup designed to address the above issues. Chapter 3 presents and discusses the results of the investigation on the basic uncontrolled flow, for two significant conditions. Chapter 4 and 5 discuss the result of control of the TVC flow using the two different

techniques. Chapter 4 discusses the effect of control by flow suction, while chapter 5 deals with the flow controlled by a synthetic jet actuator, and highlights the differences with the first control technique. In chapter 6 an optimisation procedure is carried out to search for the control signal which optimally controls the cavity flow. A preliminary discussion of closed-loop control studies is given in chapter 7. Finally, conclusions of this work are detailed.

Chapter 1

Review of the literature

1.1 Flow in a trapped vortex cell

A Trapped Vortex Cell is a particular cavity whose shape is designed as to trap a vortex. Such a configuration has been proposed, Chernyshenko [2009], as a device to control the flow past an airfoil, in order to enhance its aerodynamic performances. The basic idea of this control technique is to place a TVC on the upper surface of an airfoil, in a region close to the separation of the boundary layer, as depicted in figure 1.1. Then a suitable interaction of the incoming boundary layer with the cavity flow can result in a more energetic boundary layer downstream of the cell, with respect to the solid wall case, i.e. no cavity, which is less prone to separation, resulting in a lower drag and higher lift.

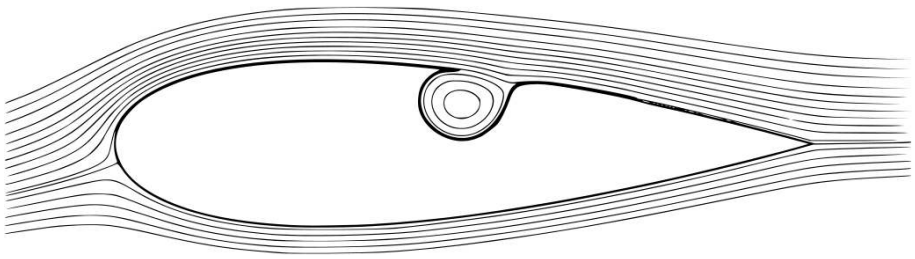

Figure 1.1. Schematic concept of an airfoil with TVC control.

The idea of trapping a vortex is not new as it was first mentioned by Ringleb [1961]. Following this work, several applications of the trapped vortex concept for flow control have been studied. Adkins [1975] demonstrated experimentally that the pressure recovery in a short diffuser could be strongly enhanced by a stabilised trapped vortex. There are also two known examples of flight testing, namely the Kasper wing, (see Kasper [1974]) and the EKIP aircraft, (see Savitsky et al. [1995]).

More recently, several investigations, theoretical, numerical and experimental, have been carried out in the framework of the EU project VortexCell2050, which had the objective of advancing the state-of-the-art of the technology of control by trapped vortex cells. Particular emphasis was given to study the characteristics of the vortex flow. In fact, one issue regarding this control technique concerns the inherent instability of the trapped vortex as a two dimensional flow. Theoretical work on trapped vortices, Chernyshenko et al. [2003], Zannetti [2006], Bunyakin et al. [1998], has shown that a trapped vortex is usually unstable.

A three dimensional instability of the flow was also identified in both experimental and numerical investigations. For example Savelsberg and Castro [2008] studied experimentally the flow inside a large aspect ratio cylindrical cell. In this case, the flow in the cavity, driven by the shear layer forming in the opening, showed a nearly solid body rotation, with low turbulence level in the vortex core. These authors noticed a significant distortion into an "S" shape of the mean velocity profile, which the authors attributed to three dimensional effects. In fact, they observed a spanwise modulation of the entire cells flow, which they suggested to be due to a natural three-dimensional instability. Further work by the same authors, Tutty et al. [2012], confirmed their hypothesis.

This spanwise modulation was also observed in a large eddy simulation performed by Hokpunna and Manhart [2007]. The authors argued that the three-dimensionality of the flow is due to an inviscid instability of the vortex core, and also showed the appearance of a marked spanwise modulation of the Reynolds stresses along the cavity span. However, no specific indication of the effects of such three dimensional instability on the effectiveness of the TVC a a control technique was given by the above authors.

Nevertheless, the problem of stability of the trapped vortex flow directly leads to the problem of its control. A first solution is passive control of the flow which can be realised by careful design of the cavity geometry. For example, Chernyshenko et al. [2008] set up an evolutionary algorithm to search in the space of cavity geometries for that which reduces internal secondary separation of the cell's flow, which is an undesirable feature of this flow. Active control of the cavity flow has been also investigated. De Gregorio and Fraioli [2008] have investigated experimentally, by means of PIV measurements, the effectiveness of a cavity located on an airfoil. The upstream interior part of the cavity was porous, in order to allow suction of the flow. Unfortunately, their setup did not allow to measure lift and drag of the controlled airfoil, since the airfoil was embedded on the bottom surface of the wind tunnel. Nevertheless, the effectiveness of the control was assessed by considering the size of the region of separated flow downstream of the cavity. The authors observed that, in passive conditions, i.e. no suction, the sole presence of the cavity yielded performances poorer than that of a clean airfoil, with a large separation region starting from the cavity cusp. By gradually increasing the suction, they

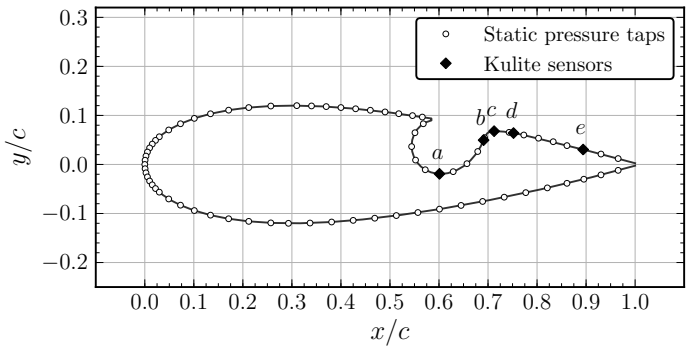

Figure 1.2. Drawing of the airfoil with the trapped vortex cell tested by Lasagna et al. [2011]

observed the formation of a coherent vortex in the cavity, accompanied by partial flow reattachment and by a decrease of the separation region downstream of the cell itself.

A further investigation of the TVC technique is the wind tunnel testing of a thick airfoil equipped with a TVC control device, performed by Lasagna et al. [2011]. This work is briefly discussed here, since it is the most relevant work for this project.

The airfoil chosen was a thick NACA0024 profile. Several configuration were tested and compared: the baseline NACA0024 profile, (B), the same profile but with a classical boundary layer suction system, (BS), and a NACA0024 profile equipped with a TVC, as in figure, 1.2. The latter configuration featured a porous cavity surface, in order to apply suction in the cavity region, similarly to what performed by De Gregorio and Fraioli [2008], resulting in the configurations TVC, no suction, and TVCS, with suction. Aerodynamic coefficients were measured by integration of the static pressure distribution, for the lift, and by momentum balance, for the drag. Tests were mainly performed at a chord-based Reynolds number of 10^6.

The lift coefficient results of the four configurations tested are reported in figure 1.3. The results indicates that the TVC configuration with no suction, i.e. passive control, yields virtually no improvements, since the lift coefficient is essentially the same of the B configuration, if not worse. However, when suction is applied to the trapped vortex cell the lift increases, by a small amount at small-to-medium incidences, and by a larger, but not exceptional, amount at high incidences. In any case, in terms of lift, the performance of the TVCS configuration were *never* superior to that of the classical boundary layer suction system, BS, neither at low nor at high incidences. The explanation provided by Lasagna et al. [2011] for the larger lift observed at high incidences for the TVCS, and BS, configurations is the delay of flow separation on the upper surface of the airfoil, mainly due to the suction applied in this region, in spite of the way this suction was applied, i.e. at the wall of the clean airfoil, or in the cavity region.

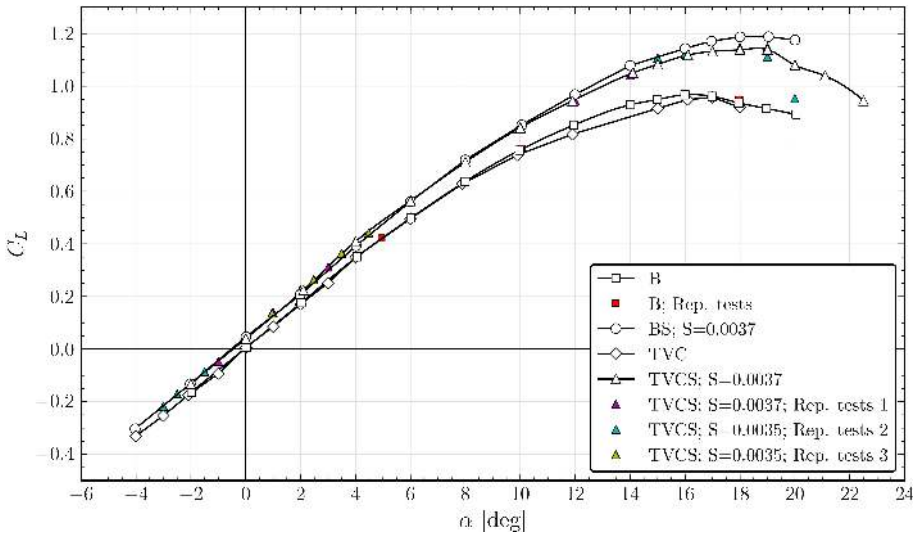

Figure 1.3. Lift coefficient curves for the four configurations tested in Lasagna et al. [2011].

Much more revealing were the drag coefficients curves, reported in figure 1.4. The results indicated that the TVC is not effective as a passive control device, since

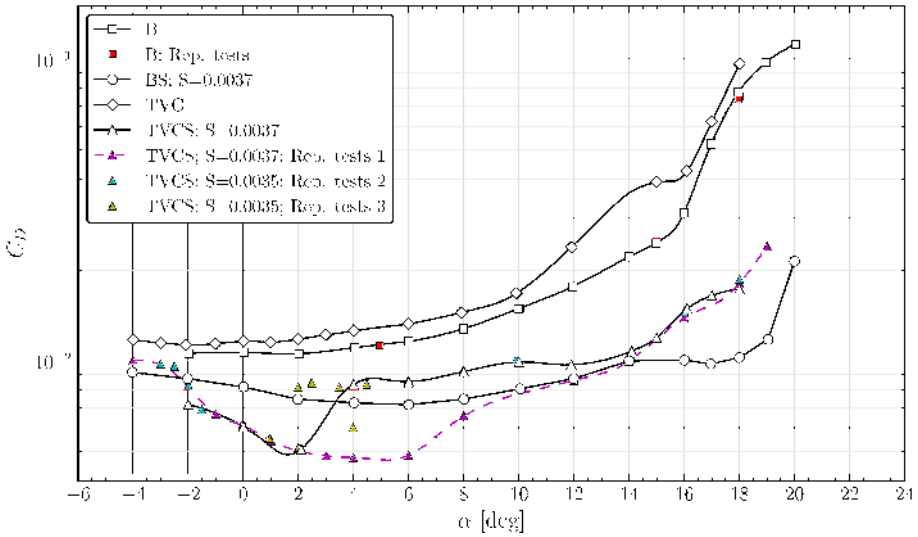

Figure 1.4. Drag coefficient curves for the four configurations tested in Lasagna et al. [2011].

the drag of the TVC configuration, open diamonds, always resulted in a drag larger than that of the baseline configuration, open squares, from small to large incidences.

In stark contrast, the drag curve of the TVCS configuration was significantly below that of the baseline configuration, for all the incidences. However, complex

behaviour was observed for this configuration. In fact, results of several tests performed on this configuration, in slightly different experimental conditions, gave rise to a bifurcative behaviour, with two branches separating at $\alpha = 2°$, merging again at around $\alpha \approx 14°$. These two branches were called low-drag and high-drag branches, for obvious reasons. A similar behaviour was observed at $\alpha = -2°$, where the drag curve of the TVCS configuration showed a sudden decrease in C_D, from a high-drag to a low-drag mode. The observed drag reduction with respect to the baseline case is significant and it was larger than 50% at $\alpha = 6°$, although a strong amount of suction was required to achieve this result, with a strongly unfavourable energy balance.

However, the most important results of this research was that, despite this complex behaviour, in a narrow range of incidence, mostly at small angles of attack, $-2° < \alpha < 10°$, the TVCS system resulted in a drag coefficient significantly lower than that of the BS configuration, for the same amount of suction.

Spectral analyses of the pressure fluctuation signals, measured by Kulite pressure transducers mounted in the region of the cell, see figure 1.2, indicated that the two drag modes were characterised by two very different flow regimes. It was postulated that in the low-drag mode the cavity was filled with a very stable and coherent vortical structure, with the shear layer displaying a characteristic Kelvin-Helmoltz instability, clearly evidenced in the power spectral density plots as a sequence of sharp peaks, at frequencies well matching results on rectangular cavity flows, i.e. at a Strouhal number based on the cavity length of the order of the unity. By contrast, in the high-drag mode, the spectra of the pressure signals displayed a very large energy peak at a very low frequency, at a Strouhal number about 0.065. This peak was associated to the presence of a "wake mode", that is a large scale, low frequency flow regime reported in the literature of rectangular cavity flows. These results clearly pointed out the relevance of unsteady phenomena for this control technique of which they strongly influence the effectiveness.

To explain such a large reduction in drag and the better performances with respect to the BS configuration, the "moving-wall" effect introduced by Donelli et al. [2009] was proposed. This mechanism suggests that the "moving surface" generated by the vortex flow, replacing the solid wall of the baseline airfoil, results in a wall flow downstream of the cell more energetic and thus less prone to separation, than the baseline case. Lasagna et al. [2011] added that, for small incidences, where the flow is fully attached and pressure drag is limited, the more energetic boundary layer would be characterized by a lower momentum thickness up to the trailing edge, resulting in a narrower wake, that is in a lower drag. It must be noted that in the experiments of Lasagna et al. [2011], this mechanism has only been postulated and no direct evidence was actually observed, due to limited measurements. Furthermore, very few results are available in the literature that provide specific evidence of this mechanism.

Control of the flow over a thick airfoil with a cavity was also investigated by Olsman and Colonius [2011]. These authors investigated by direct numerical simulation and by flow visualisations in a water tunnel the passive control on a low-Reynolds-number flow, at $Re_c = 2 \cdot 10^4$, where c is the airfoil's chord. These authors evidenced a very complex interaction between the structures generated by the cavity shear layer, subject to a Kelvin-Helmoltz instability, and the separated flow downstream of the cavity, which eventually resulted in an increase of the lift-to-drag ratio of the airfoil. The control mechanism found by the authors is fundamentally different to that proposed by Donelli et al. [2009], even though its effects may become less pronounced at higher Reynolds number conditions.

1.2 Flows in canonical rectangular cavities

We present here a short review of the literature regarding the main issues of the physics and the control of flow in rectangular cavities. It is argued that despite the different geometry, they share some many common issues and phenomena with trapped vortex cells. Furthermore, such configurations have been extensively studied in the past decades since they have important practical applications in aerospace and industry, but also because they are an important and challenging canonical flow to design control strategies, Rowley and Williams [2006]. Because of this large body of research, it may be easier to interpret the physics of the flow in a trapped vortex cell, as well as designing effective control strategies. Furthermore, few research studies have focused on using cavities as control devices for fluid flows, and, thus, this work adds insight into this topic.

1.2.1 Unsteady phenomena

The most significant dynamical feature of cavity flows, and studied in depth, is that they often develop strong oscillations of velocity field, strongly coupled with intense fluctuations of the acoustic field. The accepted mechanism explaining such phenomenon is represented in figure 1.5 and is known at least from the pioneering work of Rossiter [1964]. The upstream boundary layer, with a given thickness δ and momentum thickness θ, detaches at the leading edge of the cavity and evolves downstream spanning the entire length L of the cavity. The shear layer eventually impinges on the downstream edge of the cavity where strong acoustic waves are scattered and travel upstream. When an acoustic wave arrives at the cavity leading edge, it develops into a flow perturbation depending on the receptivity of the separating boundary layer layer. Such initial perturbations are amplified by the instability of the shear layer, strongly determined by its mean velocity profile, and eventually saturate developing coherent spanwise rollers of vorticity, which, at the

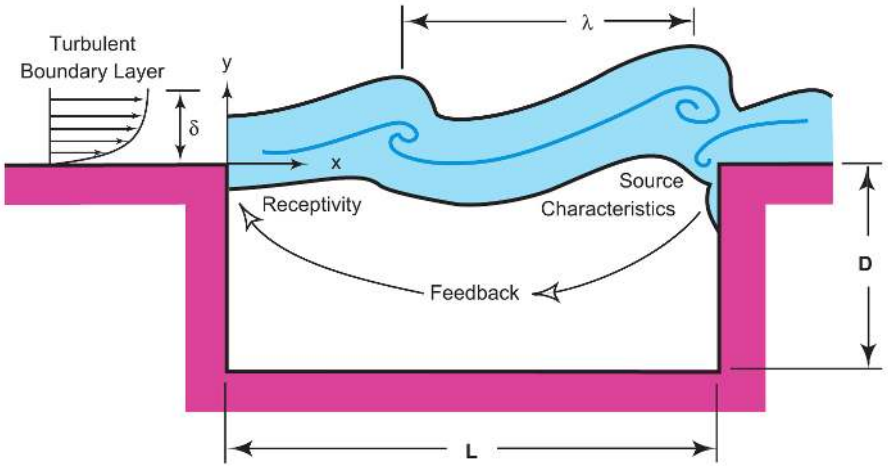

Figure 1.5. Schematic showing the mechanism determining self-sustained oscillation of the shear layer in a rectangular cavity flow. Taken from Cattafesta et al. [2008].

impingement produce strong acoustic wake, resulting in a feedback process. This mechanism results in very well defined spectral peaks at distinct frequencies and produce strong resonant oscillation, also known as cavity or Rossiter tones.

For compressible flows, the frequencies of the resonant tones can be predicted with good accuracy with Rossiter equation:

$$f_n = \frac{u_e}{L}\frac{n-\alpha}{M+1/k} \tag{1.1}$$

where f_n is the frequency of the n-th mode, α is a parameter which takes into account the phase lag between the impingement of a coherent structure and the production of an acoustic wave, k defines the ratio of the phase velocity of the convective disturbances in the shear layer to the external velocity, while M is the freestream Mach number.

The intense acoustic field resulting from this mechanism produce strong unsteady loads which may lead to structural damages and, therefore, the study of its physics has a profound impact in many applications, such as landing gear and weapon bays, Bruggeman et al. [1991], sunroofs and windows in automobiles, Mongeau et al. [1997], as well as in many other industrial applications.

A further unsteady phenomenon which may characterise a cavity flow is the wake mode oscillation, observed experimentally by Gharib and Roshko [1987] and in numerical simulations by Rowley et al. [2001] and Suponistsky et al. [2005]. This mechanism is dominated by a low frequency large scale vortex shedding, similar to the shedding of vortices in the wake of bluff bodies. Such a regime is associated to an increase of the cavity drag, with large amplitude fluctuations at a Strouhal

number of the order of 0.07. As pointed out by Rowley et al. [2001], this mechanism is not due to acoustics, but it is the result of an absolute global instability of the cavity flow.

1.2.2 Three dimensional properties

Although the geometry of a rectangular cavity is simple, the flow topology is highly complex and, as several workers have reported, it is essentially three-dimensional. Maull and East [1963] first documented the strong three dimensional nature of this flow with oil visualisations showing the occurrence of a cell-like structure of the flow. They reported that this flow organisation was found only when the cavity span was set to certain values: the steadiest and most regular conditions were found when the cavity span was an integral number of cell spans. They also noted a strong influence of this particular flow topology on the spanwise pressure distribution in the cavity. In fact, a periodic modulation of the pressure was present, with a period roughly equal to twice the cavity length.

The occurrence of such spanwise modulation in the flow characteristics at high Reynolds numbers was also confirmed in recent LES simulations performed by Larchevêque et al. [2007]. They have also found these modulations to be caused by the presence of a cell-like organisation of the flow. They report of a bifurcative behaviour of the flow, with two possible asymmetrical flow solutions, being mirror images of each other and which could be selected by imposing a different asymmetric in-flow condition. They also report of a transient, less stable symmetrical configuration, which would occasionally break-down into one of the two non symmetrical configurations. Three-dimensional characteristics have been also found if the shear layer region, as reported by Rockwell and Knisely [1980]. Direct observation of the flow revealed a coupling between the roll-up of the primary spanwise vortices in the mixing layer with the growth of secondary streamwise vortices, which led to a severe distortion of the primary vortices.

The above studies found three dimensional characteristics which have a length scale of the same size of the cavity dimension. However, other studies have demonstrated the presence of small scale coherent three dimensional structures such as Taylor-Gortler like vortices, as found by Faure et al. [2009]. These authors have demonstrated that the occurrence of such structures is strongly tied to a centrifugal instability due to the curvature of the flow in the recirculation region, which trigger the formation of such structures. Similar conclusions were drawn by Migeon [2002], which examined the details of the flow start up in a square lid driven cavity experiment, observing the presence of such vortices.

1.2.3 Recirculating flow

A further important element is the recirculating flow inside the cavity. The structure of this flow is strongly dependent on the geometrical characteristics of the cavity, and mainly by the ratio L/D, where L is the cavity length and D is the cavity depth, see for example Faure et al. [2006]. The typical structure is composed of a main recirculating flow. If the ratio L/D is high enough, the interaction of the main vortex with the fluid upstream of it may result in the formation of a secondary counter-rotating vortex. Typically, corner vortices may also develop.

It has been shown that there is a clear interaction between the recirculating cavity flow and the shear layer evolution. In fact, Lin and Rockwell [2001] suggest that the large-scale flow structures in the recirculating zone may affect the disturbance growth in the shear layer and consequently the oscillating nature of the overall flow.

Kuo and Huang [2001] studied the effects on the oscillations of the cavity shear layer by introducing flow path modifier and by modifying the slope of the bottom surface of the cavity itself. The authors observed, by both flow visualisations and LDV measurements, that the upstream part of the recirculating flow have an important effect on the instability characteristics of the shear layer.

Chapter 2

Design of the experiment

This chapter presents the experimental setup designed and realised for the investigation. It discusses the basic rationale behind the chosen configuration and describes all the components. The hardware required for the two control techniques is also presented, leaving a thorough discussion to their respective chapters. Instrumentation, other hardware and measurement techniques are also documented.

2.1 Design rationale

The configuration chosen for the experimental investigation is a TVC embedded onto the bottom flat surface of the wind tunnel test section, as sketched in figure 2.1.

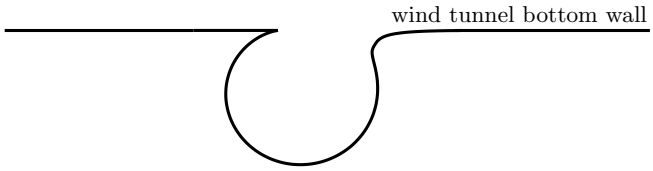

Figure 2.1. Sketch of the simplified configuration chosen for the experimental investigation.

This configuration differs from that of the TVC equipped airfoil mainly by the fact that there is no external pressure gradient imposed on the cell. The chosen configuration is simpler since it purposely eliminates some of the phenomena present on the airfoil, such as flow separation or wake dynamics, and the possible couplings between the cavity flow, the wake and the separated region. It is argued that separation of these effect, tough a strong simplifying assumption, is paramount to ease the effort of understanding basic mechanisms.

This simplified configuration is chosen since the main objective of the research project is focused towards the understanding of the physics of the TVC flow itself. In this regards, the aerodynamic performance of a TVC controlled airfoil were not in the scope of this particular project, but connections between the two configurations will be often made. In fact, it is argued that the performances of the cell in controlling the flow over the complete airfoil are strongly connected to how the cell itself modifies the boundary layer flowing past it, for example by increasing the mean velocities in the near-wall flow downstream of it. Such effects can be easily studied on the simplified configuration and may shed some light over the control of the flow on the complete airfoil.

Nevertheless, the extent by which the full airfoil configuration differs from the chosen simplified configuration and how the basic mechanisms discussed in this work are affected must certainly be the object of future research.

2.2 The wind tunnel

The open-circuit blower wind tunnel "Fucsia", shown in figure 2.2, was chosen for the experiments. It is a small facility, adapt for fundamental research studies. The test section of the wind tunnel is long more then 4 meters and, in the region chosen for the investigation, it has a width and a height of 750 and 550 mm, respectively. The maximum speed is of the order of 14 m/s.

Figure 2.2. Front and rear views of the “Fucsia” wind tunnel used for the investigation.

2.2.1 Modifications to the wind tunnel test section

A large amount of design and work has been dedicated to modify the test section region. A first task has been to raise the bottom wall of the test section by about 200

mm, in order mainly to leave space for the cavity model and for instrumentation. This task was accomplished by designing a support system, adaptable in height, covered with flat panels spanning the full width and length of the test section area. The reduction of the test section area also resulted in a increase of the maximum velocity. Furthermore, a ramp was positioned in the first region of the test section to smoothly recover the difference in height between the two sections. This region of the test section has been checked by smoke flow visualisations to not produce inconvenient separated regions, which would introduce spurious fluctuations into the boundary layer flow. The left picture in figure 2.3 show a detail of the convergent ramp and the adjustable support system. The picture on the right shows instead the flat panels recreating the bottom wall of the test section.

Figure 2.3. Pictures of the convergent ramp, supports and flat panels.

A second important task has been to modify the test section in order to allow both optical and manual access to the investigation area. To this end, the two lateral walls of the test section have been replaced by transparent Plexiglas panels. One of them was also designed to be easily removable to provide operation access to the investigation area.

Particular attention has been paid to the design of the top wall. The requirements for this element were: it should provide full optical access from above, (mainly to a laser sheet for flow visualisations) and it should give a mean to hold hot wire probes and to move them in the three directions. In order to satisfy these requirements the top wall was manufactured with a large Plexiglas panel, with a long longitudinal slot in its centerline to allow the insertion and the motion of a probe holder into the flow or of a laser sheet. The panel was supported on the two longitudinal ends by two spanwise rail guides, providing an adjustable displacement of the panel slot along the spanwise direction. The left picture in figure 2.4 shows a CAD model of the top panel.

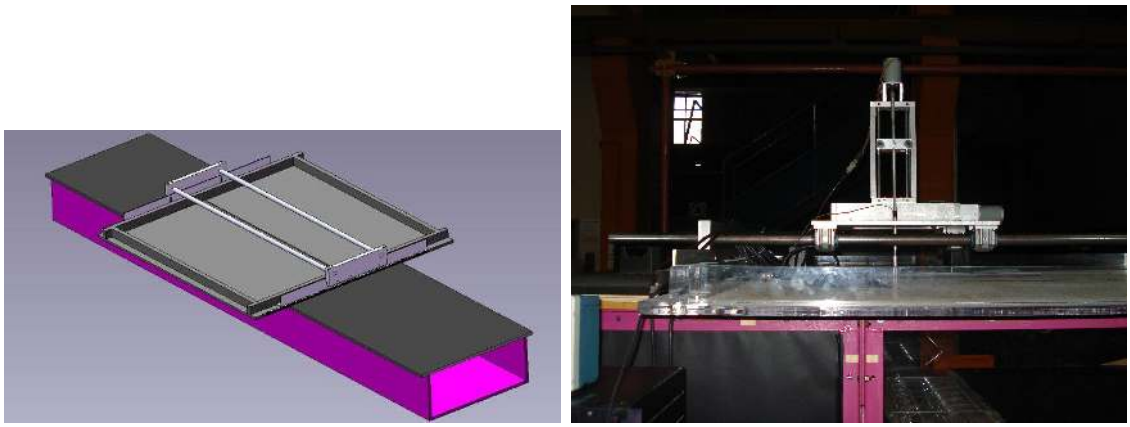

Figure 2.4. On the left: CAD model of the wind tunnel test section, with details of the top panel supported by two spanwise rails. On the right: picture of the top panel, showing also the probe traverse system.

2.3 The probe traverse system

One of the requirements of the experimental setup was to achieve a full automatisation of the probe motion, such as to minimise run times. To this end, a two-axes traverse system equipped with stepper motors was positioned above the top panel, outside of the test section, on two longitudinal rails. The right picture in figure 2.4 shows a picture of the traverse system in place. This configuration allowed fine control of the streamwise and vertical position of the probe, while control in the spanwise was achieved by manual displacement of the entire top panel along the two spanwise rails. Furthermore, fast but uncontrolled motion along the streamwise direction was obtained by sliding the entire positioning system along the two longitudinal rails. The stepper motors were driven by their power supply units, usually controlled by a Labview system. This allowed, for example, to semi-automatise the entire motion-acquisition process, saving significant time.

2.4 The boundary layer suction system

It is known that the flow regime in a cavity is markedly affected by the properties of the upstream boundary layer, and mainly by the ratio of the cavity length to momentum thickness L/θ, see e.g. Rockwell and Knisely [1980]. For this reason, a boundary layer suction system was designed to be located about 400 mm upstream of the cavity leading edge, in order to control the characteristics of the boundary layer detaching at the cavity cusp.

The system is composed of a 120 mm long flat perforated plate spanning the

entire width of the test section, which replaces the corresponding region of the test section bottom wall. The plate covers a drawer embedded in the bottom wall and connected to a suction system, composed by a commercial blower for air conditioning. Inside the drawer, dividing vanes ensure a good uniformity of the boundary layer properties across the span. This was checked by preliminary boundary layer measurements at the cavity leading edge. The flow rate of the blower was measured by measuring the difference between the pressure in the suction ducts and the ambient pressure, which was previously correlated against the flow rate by measuring the exit velocity on a fine grid over the exit section of the blower.

The suction system was tested at different wind tunnel speeds and suction rates and for each test condition a boundary layer profile was measured, in the mid-span section and at 10 mm upstream of the cavity cusp. As an example, at a flow speed equal to 6 m/s, at which a significant part of the tests has been conducted, the boundary layer momentum thickness could be varied within 0.6 and 3 mm.

Preliminary investigations were dedicated to asses the uniformity of the incoming flow and to tune the experimental apparatus, in particular the boundary layer suction system and small details in the junctions between the elements of the bottom surface.

2.5 The cavity model

The geometry chosen for the experiments, shown in figure 2.5-(a), is identical to that of the numerical simulation of Hokpunna and Manhart [2007]. In the figure, the reference system adopted is also shown, together with the symbols of the main parameters of this geometry.

The cavity opening length L is the projection along the x axis of the cavity opening, D is a characteristic diameter of the cell, taken as the largest distance between the upstream and downstream faces of the cell. δ_0 and θ_0 are the 99% boundary layer thickness and momentum thickness of the reference upstream boundary layer, measured at $x/L = -0.14$, i.e. $x = -10$ mm, in the mid-span section. The letters A and B denotes the two regions were suction was applied to control the cavity flow, as will be discussed later.

The choice of the cavity sizes, mainly the opening length L and its span b, not indicated in the figure, was driven by several requirements and constraints. One of the most important requirement was the achievable range of values for fundamental parameters of the flow, such as the cavity Reynolds number Re_L or the ratio opening length to momentum thickness L/θ. The manufacturing process, availability of materials, the size of various probes were also important aspects of the design. In the final configuration, the cavity had a nominal opening length equal to $L = 68$ mm and a span b of 420 mm, so that the aspect ratio was about 6.6. The internal

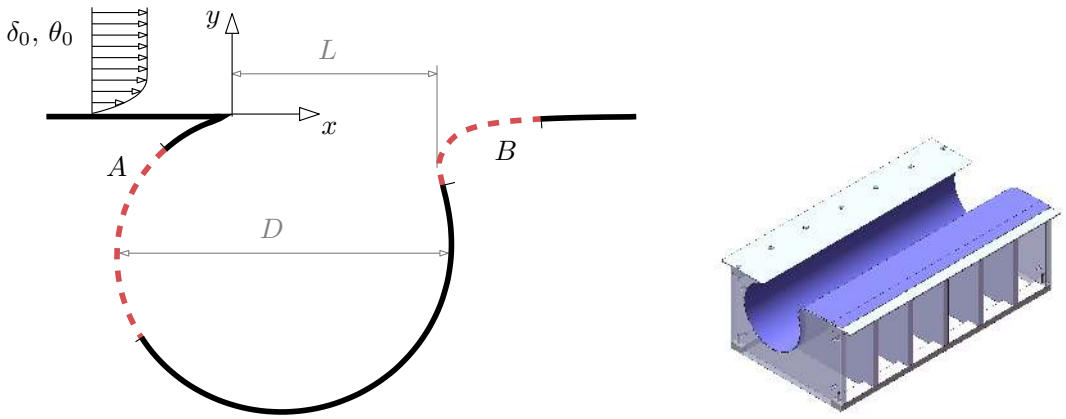

(a) (b)

Figure 2.5. Sketch of the cavity geometry and of the reference system, (a), and CAD drawing of the cavity model, (b).

diameter of the cavity D was equal to 114 mm. The cavity spanned 56% of the test section width, leaving a free space of about 160 mm between the cavity ends and the vertical test section walls. This prevented interactions between the corner flows developing at the angles of the test section with the cavity flow.

The cavity model was built as a ribbed structure with Plexiglas material, as shown in figure 2.5-(b), with transverse rods to keep the model in place. This solid structure was then covered with a transparent 0.5 mm poly-carbonate film, which further improved the stiffness of the model. The thickness of the film was chosen to be as large as the manufacturing process allowed, in order to prevent fluid-structure coupling induced by the fluid oscillations that were expected. Appropriate care was taken to ensure that the poly-carbonate film remained attached to the ribs, to maintain the geometry.

2.6 The cavity suction system

One of the active control techniques which have been investigated is that of suction of the cavity flow. As represented in figure 2.5-(a) two regions were chosen to apply suction, and the motivations are briefly discussed here. The first, denoted by letter A, was motivated by the idea of manipulating the structure of the flow inside the cell. Furthermore, this same region was investigated by other authors, e.g. Lasagna et al. [2011] and De Gregorio and Fraioli [2008]. On the other hand, suction in the second region, denoted by B, was chosen with the idea of manipulating the flow near the impingement region, which, in no control conditions, is a region of strong

unsteadiness. An in depth discussion of the motivations behind these choices is given in chapter 4, devoted to the discussion of the control with suction.

The solution adopted to perform suction of the flow has been to make the polycarbonate film porous, by drilling many small holes in the chosen suction area. Holes of 1.5 mm where drilled on a square pattern with edge equal to 5 mm, thus making an equivalent porosity equal to 12.5%. Figure 2.6 shows a picture of the porous wall on the downstream edge of the cavity, in region B.

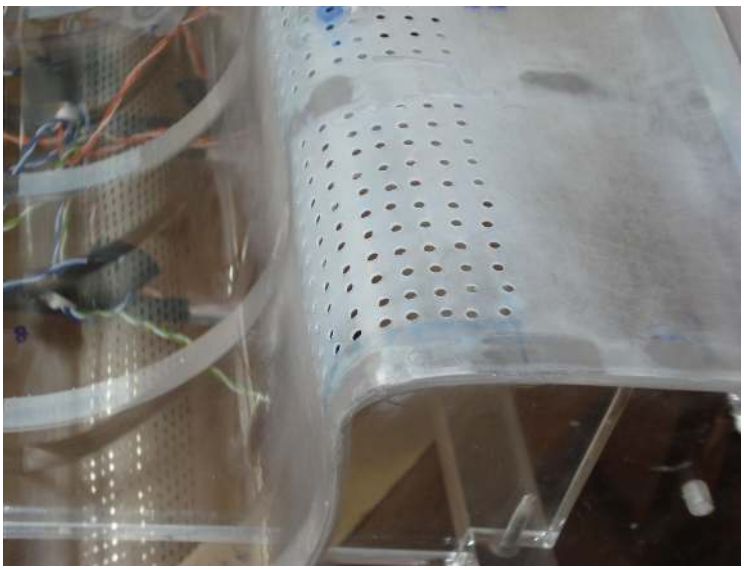

Figure 2.6. Detail of the porous surface on the downstream cavity edge, in region B.

Please note that the two regions have been manufactured on the same polycarbonate sheet, but tests were conducted separately, by covering one of the two regions with a thin, less than 0.1 mm, adhesive film.

The entire Plexiglas cavity model was then embedded into a watertight drawer, connected to a suction pump located outside the wind tunnel. A flow meter and a regulating valve, connected into the pneumatic line, provided means to measure and vary the suction rate, respectively.

2.7 The synthetic jet system

The second control technique investigated is based on a synthetic jet actuator. A drawing of the actuator system configuration is shown in figure 2.7.

The injection location is located on the downstream side of the cavity and it is directed tangentially into the cavity. The idea behind this particular positioning is to inject momentum into the cavity, such as to favour the formation of an intense

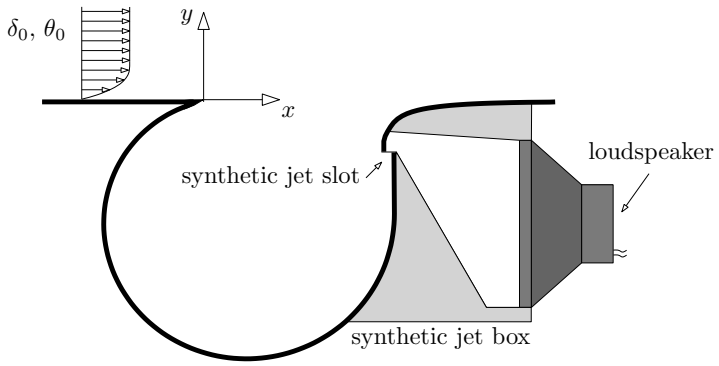

Figure 2.7. Sketch of the side view of the cavity with the synthetic jet actuator.

vortical structure. The injection slot was actually divided along the span into six 60 mm slots separated by 10 mm due to the presence of the cavity ribs. The six slots were fed by watertight plenum chambers connected in couples to the actuators. These consists of three 4 Ω 150 Watt loudspeakers, driven by a Coraline power amplifier, each driving two slots.

Control of the loudspeaker input signal was performed via a NI9263 Analog Output module, controlled by an appropriate Labview program, implementing a signal generator. Such a flexible arrangement provided a significant step in task automatisation and provided a strict control on the input signal waveform.

2.8 Measurements techniques

To investigate the cavity flow two measurement techniques were used, namely hot-wire anemometry for the velocity in the flow field and condenser microphones to measure pressure fluctuations at the wall.

Hot-wire anemometry Extensive velocity measurements were performed using constant temperature hot wire anemometry. An A.A. LabSystems AN1003 anemometer with a built-in signal conditioning unit was used to measure the velocity component normal to sensor. A single-wire probe, (length 0.9 mm and diameter 5 μ mm). The probe was frequently calibrated in situ, in the middle of the vein and at a sufficient distance upstream of the cavity to render negligible its influence.

The probe holder was tilted by about 40 degrees with respect to the freestream direction, as shown in figure 2.8, in order to minimise its protrusion into the shear layer and into the cavity flow.

Figure 2.8. Detail of the hot wire probe holder. Flow is from left to right.

Pressure fluctuation measurements Pressure fluctuation measurements were performed using high-sensitivity electret condenser microphones, of a similar type as those used by other authors, e.g. Zhang and Naguib [2011], Garcia-Sagrado and Hynes [2011]. Twelve microphones were positioned allover the cavity model, and their location is shown in figure 2.9. Figure (a) shows a side view of the cavity

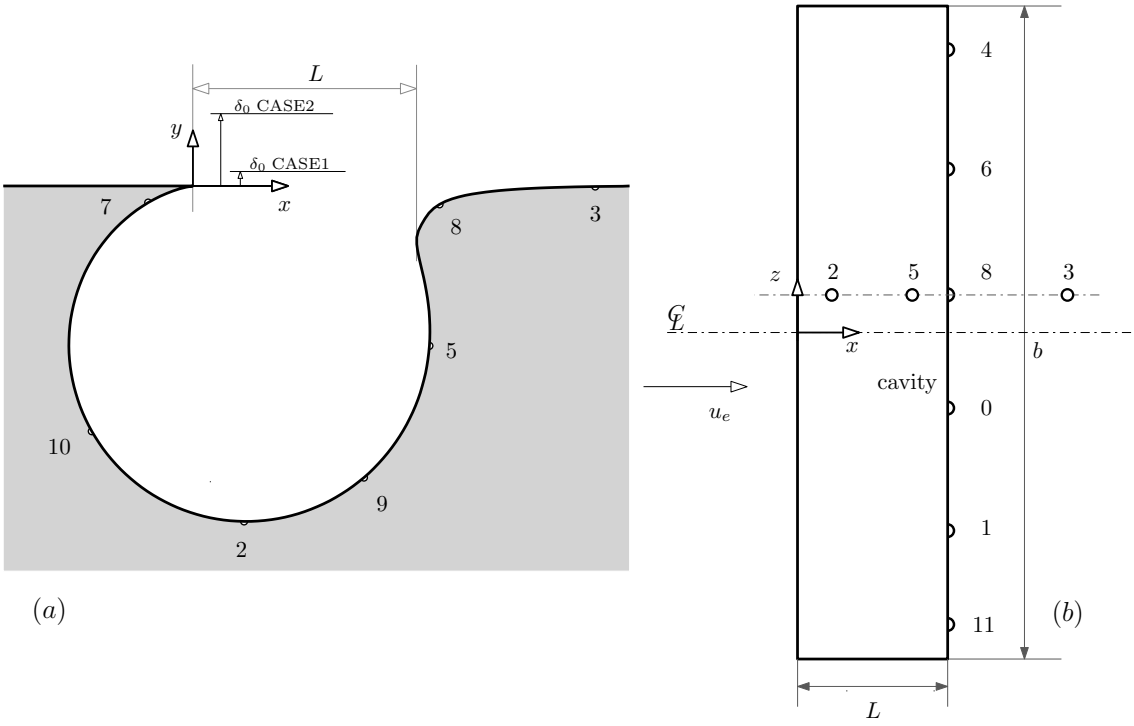

Figure 2.9. Sketch of the side view of the cavity model at the span of the central row of microphones, (a); top view (b).

model, in a section about 15 mm away from the centerline of the cavity span, due to the presence of a rib in the mid-span section. The figure also show the relative thickness of the boundary layer for the two conditions extensively investigated in this work, CASE1 and CASE2, discussed later. This figure serves as a reference for the discussion of the results presented later, since the measurement location will be often given in non dimensional units, x/L and y/δ_0. Figure (b) shows a top view of the cavity model, showing the position of the microphones located along the span, on the downstream edge of the cavity. These microphones were spaced along the span by 65 mm, and their signals were used mainly to assess the 2D properties of the shear layer flow.

The microphones, with a diameter and height of 9.7 and 6 mm, respectively, were powered by a dedicated power supply unit through custom-made RC circuits. These microphones, which only measure the fluctuating component, were positioned under the poly-carbonate film of the cavity, and aligned with a 2 mm hole. The large diameter of the hole was chosen as a compromise between the need to maximise the signal to noise ratio and minimisation of spatial filtering effects. Figure 2.10 shows a picture taken from the top of the central row of microphones. The microphone holes, the silicone mountings and the wires are also visible.

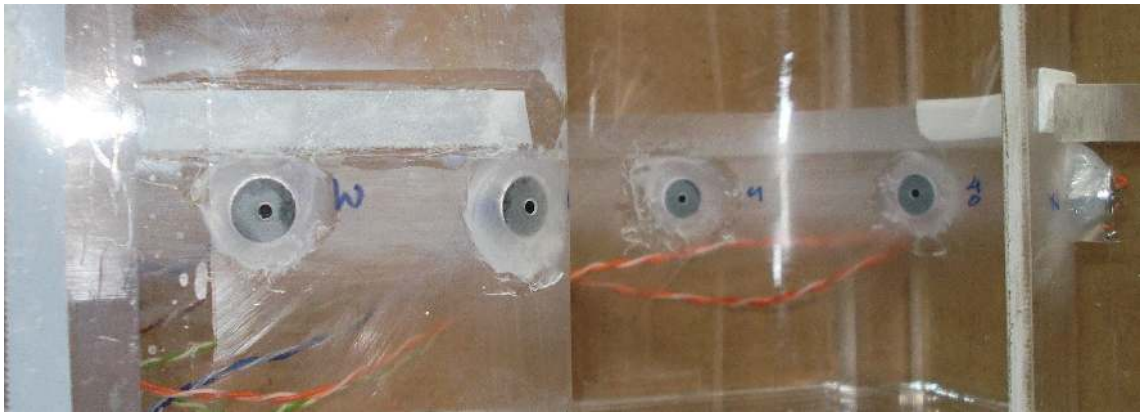

Figure 2.10. Top view of the central row of condenser microphones.

Seven microphones were located in a section of the cavity 15 mm away from the mid-span, as shown in figure 2.9. Five other microphones were located transversely along the downstream shoulder of the cavity in the same position of microphone $m8$ with a spacing of 60 mm.

The dynamic properties of the microphones were estimated by an ad-hoc calibration similar to that performed by Zhang and Naguib [2011] and Garcia-Sagrado and Hynes [2011]. The objective of the calibration was to find the microphone transfer function $H(f)$. These dynamic properties are summarised in terms of gain in mV/Pa and phase delay, as a function of the frequency. The calibration setup consisted in a

flat plate located at a distance of 50 cm in front of a high power loudspeaker, which produced a fluctuating pressure field on the plate. The electret microphones were positioned on this plate with the same arrangement of the measurements described above. A reference high-precision microphone was flush-mounted in the centre of the plate. This was a high quality 1/4" Brüel&Kjær (type 4939) condenser microphone. This microphone has pre-amplification, flat frequency response in the range 10-10000 Hz and selectable gain by means of a dedicated power-supply/signal conditioning unit.

The microphones calibration was performed according to system identification procedures, described in detail by Ljung [1998]. A zero-mean Gaussian noise, pass-band filtered between 2 and 2500 Hz, was fed to the loudspeaker through an amplifier. Because the loudspeaker signal values was sampled from a Gaussian distribution, large values exceeding the input capability of the loudspeaker could occur. For this reason the signal was clipped between $\pm e_{th}$, a chosen threshold voltage. However, since clipping the signal in the time domain affects the signal spectrum in the frequency domain, the clipping and band-pass filtering were repeatedly applied to the signal, until it reached satisfactory time and frequency domain characteristics.

Simultaneous measurements from the electret and the B&K microphone were sampled at a frequency of 10 kHz and for 120 s. The length of the time histories was such as to provide satisfactory convergence of the spectral characteristics of the signals. Transfer function estimates, evaluated according to Bendat and Piersol [1986], were then obtained as:

$$H(f) = \frac{\Phi_{Bm}(f)}{\Phi_{BB}(f)} \tag{2.1}$$

where $\Phi_{Bm}(f)$ is the cross-spectral density between the voltage signal of the electret microphone and the pressure signal of the B&K microphone, while $\Phi_{BB}(f)$ is the power-spectral density of the B&K microphone signal. All the spectral densities were obtained via the Welch algorithm, to improve the quality of the spectral density estimate.

Amplitude and phase response plots were analysed in detail for each microphone under test. As expected, the microphones significantly attenuated low-range frequency components below 10 Hz. The gain of each microphone was found to be sufficiently constant in the band 20-1000 Hz, in which most of the shear layer dynamics were expected, and was practically constant in successive calibration experiments. The phase shift introduced by the microphone was found to be negligible, of the order of 50 μs in the frequency range of interest. For this reason, it was not taken into account in the subsequent analyses. Furthermore, resonance effects due to the arrangement were not observed. Finally, in order to test the linearity properties of the microphones, different calibration experiments with different amplitude of the

loudspeaker driving signal were performed. Linear behaviour was observed for a range of pressure amplitudes much larger than those expected in the cavity flow.

Smoke flow visualisations Smoke flow visualisations were performed to qualitatively investigate the structure of the cell flow, where hot wire measurements were too intrusive. The visualisations were performed in the mid-span section on the $x-y$ plane, which was illuminated by a laser sheet produced by a cylindrical lens located outside, on the top of the test section, and passing through the same longitudinal slot which was used for the hot wire probe holder. The thickness of the laser sheet was less than 1 mm. An high-speed camera, (Dantec Dynamics 80C37 Nanosense MKIII, 1280×1024), was located on the side of the test section, where optical access to the investigated region was granted by a Plexiglas window. Seeding of the flow was performed by injecting large amount of smoke inside the cavity region, but high-frame-rate acquisition of the flow field was started after a transient, to let the cavity flow reach an appropriate concentration of seeding. Post-processing of the images, i.e. mean subtraction and grey balance, was then performed to increase the quality of the visualisations.

2.8.1 Data acquisition and signal generation hardware

Signals from the hot-wire probe and from the condenser microphones were acquired using high-resolution digital acquisition modules, mounted on a National Instruments CompactDAQ 9172 Chassis. The hot-wire signal was sampled with a NI9215 module, with four 16-bit resolution channels, allowing simultaneous sampling. The hot-wire signal was adequately pre-conditioned before sampling, by adjusting gain and offset of the anemometer amplifier in order to span the entire range of the module, ±10 Volt.

The condenser microphones signals were sampled using 24-bit resolution modules. The higher resolution was required because of the relatively low output of the microphones which were not equipped with a signal conditioning unit, but were sampled "as is". The modules used were the NI9239, four channels, 24-bit resolution, simultaneous sampling modules. These were mounted on the NI9172 chassis together with the NI9215 module for sampling the hot-wire signal. All the acquisition modules have an internal anti-aliasing filter set at $0.46 f_s$, where f_s is the sampling frequency. Furthermore, all the signals were simultaneously sampled, to allow cross-correlation, cross-spectra and stochastic estimation analyses.

The power units of the stepper motors, used to control the motion of the hot wire probe, were controlled by a NI9481 relay module. By opening and closing programmatically, via Labview, the four relay channels on the module, the power units received commands to move the probe up/down, and upstream/downstream, that is over the two axes x and y. This system allowed the automatisation of the

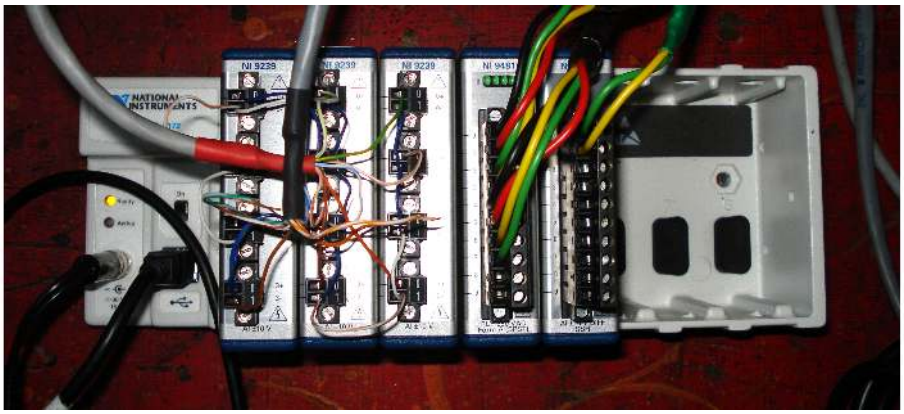

Figure 2.11. Acquisition modules. From left to right: three 24-bit modules for the condenser microphones signals, the relay module for motion control and the 16-bit resolution module for hot-wire signal.

motion and acquisition of the hot wire probe, with significant time saving. The complete set of acquisition and control modules is shown in figure 2.11.

Chapter 3

Unactuated flow in the cell

This chapter presents the experimental findings regarding the uncontrolled flow in the trapped vortex cell. The chapter starts by presenting preliminary results performed at several freestream velocities, covering a broad range of inflow conditions, both in terms of Reynolds number and of boundary layer characteristics. Then the focus is shifted on two specific flow conditions, chosen to be fully investigated since they were the most representative.

The specific objective of this chapter is to present the basic flow physics of the TVC flow highlighting the most important elements of the flow and its mechanisms. In fact, a strong understanding of the flow in uncontrolled condition is necessary to proceed with control of the flow, discussed in the subsequent chapters.

3.1 Preliminary considerations

Preliminary investigations over a wide range of flow conditions were performed in order to assess the general characteristics and to study the general phenomenology of the cavity flow.

As an example of these studies, time histories of velocity and pressure fluctuation were measured in the shear layer region and at the wall, respectively, for several upstream velocities u_e from about 2 to 14 m/s, spanning a range of Reynolds number based on the cavity opening length from 9000 to 68000. The boundary layer suction pump was always set at the maximum level, such as to obtain the thinnest boundary layer. Then for each condition, the power spectral density of the velocity and pressure signals were computed. Here, and like in the rest of this work, spectral densities have been computed using the Welch algorithm by averaging spectra from several blocks of data, in order to improve the accuracy of the spectral estimate. Typically, a Hanning window has also been applied to the blocks, in order to reduce side lobe leakage effects, see Bendat and Piersol [1986].

Figure 3.1 shows the result of this investigation in the form of an upstream velocity/frequency spectrogram. The colour map indicate the base ten logarithm of the power spectral density of the normalised pressure fluctuations measured by microphone $m7$, located under the cusp of the cavity. The normalisation of the pressure fluctuation is performed by dividing by $1/2\rho u_e^2$, where ρ is ambient air density.

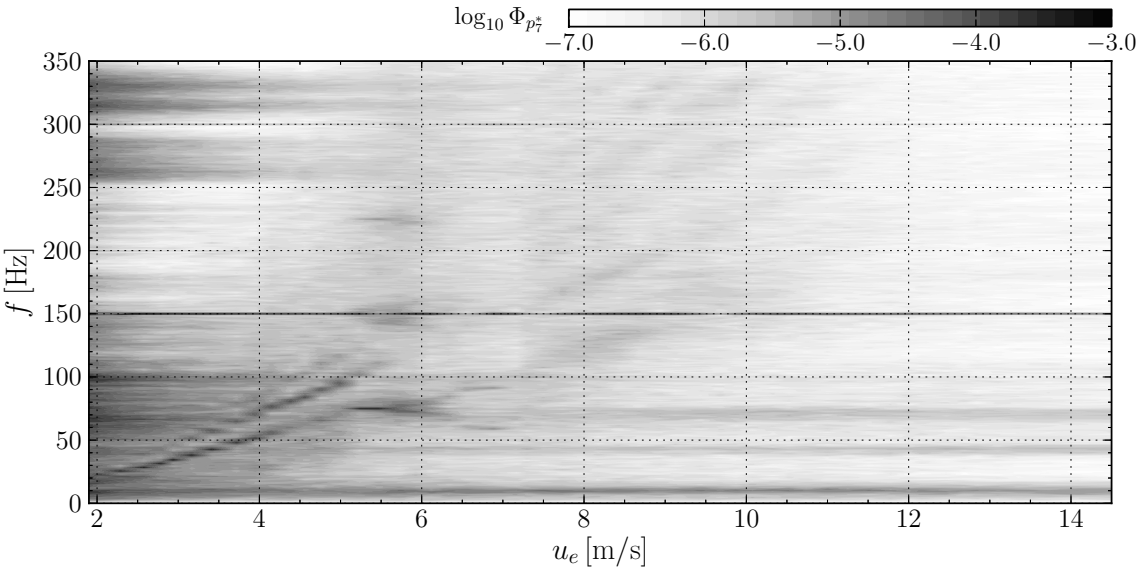

Figure 3.1. Upstream velocity/frequency spectrogram for the pressure fluctuation from microphone $m7$.

The plot shows, in the range $2 < u_e < 5$ m/s and for frequencies between 25 and 100 Hz, three narrow energy concentration bands. These are the strong signatures of the second, third and fourth natural instability modes of the shear layer, which is a proof of the strong aero-acoustic coupling of the TVC flow. These frequencies are well predicted by the Rossiter equation:

$$f_n = \frac{u_e}{L}\frac{n-\alpha}{M+1/k} \tag{3.1}$$

where f_n is the frequency of the n-th mode, α is a parameter which takes into account the phase lag between the impingement of a coherent structure and the production of an acoustic wave, k defines the ratio of the phase velocity of the convective disturbances in the shear layer to the external velocity, while M is the freestream Mach number. Good correlation between the experimental results and the Rossiter equation are found by setting the phase lag α equal to zero, as it is commonly observed in low Mach number flows, (Cattafesta et al. [9]), and an

average value of k approximately equal to 0.5. Interestingly, the signature of the first shear layer mode cannot be directly observed in the pressure signal.

The signature of the natural instability modes can barely be detected for velocities larger than 7 m/s, for which the incoming boundary layer is fully turbulent. Furthermore, the slope of the bands appears to increase as the external velocity increases, which means that k slightly increases with the external velocity. This is probably due to the variation of the boundary layer properties as the wind tunnel speed is increased.

The horizontal bands, except for that at 150 Hz, are due to background noise from the wind tunnel and from the pump of the upstream boundary layer suction system. On the other hand, the strong energy peak at 150 Hz, visible at all frequencies, is due to an acoustic resonance of the wind tunnel facility. This frequency has been identified to be due to a wind tunnel acoustic resonance, (see AGARD-AR-336 [1998]), which originates in the settling chamber of the wind tunnel. The presence of this resonance was previously found in pressure fluctuation measurements in the test section without the cavity installed. In terms of dynamics of the shear layer, the wind tunnel resonance acts as a source of narrow-band periodic disturbance, which enter directly into the delicate acoustic feedback process of the shear layer.

The presence of the signature of acoustic modes is crucial, since it indicates that large flow oscillations are expected. As will be shown later, this strong unsteadiness of the shear layer flow is certainly detrimental to the performances of the TVC as a control device since the instability of the shear layer will provide a mean to extract energy from the external fresh flow in the form of coherent spanwise rollers of vorticity, whose energy will be ultimately dissipated downstream.

The signature of the natural instability modes is visible also in the spectrogram of the normalised velocity fluctuations $u^* = u/u_e$, reported in figure 3.2. The velocity is measured at $x/L = 0.58$, $y/\delta_0 = 0.22$, in a characteristic region of the shear layer characterized by large amplitude velocity fluctuations. The signatures of the second, third and fourth modes are again clearly detected by the spectral analysis. However, for upstream velocities larger then 9 m/s there is no further evidence of coherent oscillations of the shear layer flow. In fact, for velocities larger than 8 m/s the upstream boundary layer becomes turbulent and relatively thick, despite the strong boundary layer suction operated upstream. At these velocities the spectrum is characteristic of a turbulent flow, and no significant peaks are detected, a symptom of the absence of self-sustained oscillations of the shear layer at these freestream velocities.

Nevertheless, for velocities larger than 12 m/s, a small peak is observed at low frequencies, e.g. 5−10 Hz, with a characteristic frequency slightly increasing with the speed. A will be shown later, this peak is associated to a low-frequency oscillatory motion of the entire cavity flow.

For what concerns the spectrogram of the velocity fluctuations, the energy at

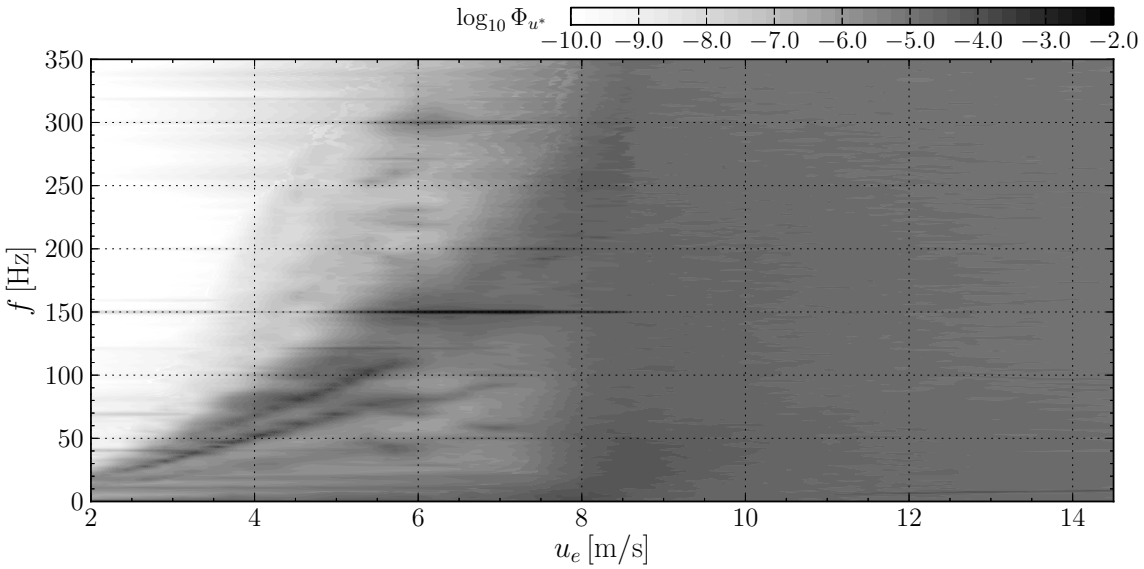

Figure 3.2. Upstream velocity/frequency spectrogram for the velocity fluctuation in the shear layer at $x/L = 0.58$, $y/\delta_0 = 0.22$.

f_{wt} is not significant for the shear layer dynamics at low velocities, i.e. $u_e < 5$ m/s, and most of the fluctuation occurs at the natural frequencies. At these velocities, the frequency of the acoustic forcing is too far from the natural frequency and fluctuations at f_{wt} are not amplified by the shear layer. However, when the upstream velocity increases past this value, together with the frequencies of the natural instability modes, the energy at f_{wt} starts to strongly increase by several orders of magnitude, and the energy of the velocity fluctuations at the natural instability modes substantially decreases. The shear layer is thus locked at to acoustic forcing since the wind tunnel resonance frequency is close to its natural instability frequencies. In this conditions, a peak also appears at 300 Hz, i.e. at the first harmonic of the wind tunnel resonance frequency, as well several other peaks for the higher harmonics, not visible in the figure.

Indeed, fluctuations at the shear layer resonance frequency reach a maximum amplitude for $u_e = 6.8$ m/s, exactly at the velocity where $f_{n=3} = 3f_{wt}$, i.e. when the resonance frequency matches that of the third natural instability mode. This behaviour is characteristic of a lock-in phenomenon, whereby the shear layer dynamics are "captured" by the external forcing. It is frequently encountered in experimental investigations, e.g. Chatellier et al. [2004], where acoustic modes of the facility couple to some relevant dynamics of the flow.

From a practical flow control viewpoint, the lock-in phenomenon of a TVC shear layer may be of paramount concern in the sense that fluid-structure interactions may arise between the TVC flow and the structure hosting the cell. These aspects

were object of substantial research and a thorough discussion can be found in by Olsman and Colonius [2011]. The lock-in phenomenon will also be discussed in detail in chapter 5 dedicated to the study of oscillatory control of the cavity flow with a synthetic jet. In that case, both the frequency and the amplitude of the source of forcing will be varied and the full non-linear response of the shear layer will be characterized.

More insight into the response of the shear layer to the wind tunnel resonance forcing can be obtained by observation of the spectrogram of the pressure fluctuations, in figure 3.1. The first point to notice is that the intensity of the pressure fluctuations associated with the wind tunnel forcing are, for $u_e < 4.5$ m/s, by far larger than that associated to the natural instability modes. This indicates that the resonance forcing is very strong. However, as it has been demonstrated in figure 3.2, the shear layer develops coherent oscillations at its natural instability frequencies. This basically occurs because the difference between the forcing and the natural frequency is large and the shear layer dynamics cannot be driven so far away from its natural conditions.

However, as the upstream velocity increases to 5 m/s the shear layer couples with the forcing and most of the oscillations occurs at the forcing frequency. A complex interaction between the wind tunnel acoustic resonance and the natural instability modes can be observed in this case. At velocities where the frequencies of natural instability modes of the shear layer are close to f_{wt}, the shear layer locks in to the forcing frequency. This condition is evidenced as a strong increase of the wall-pressure fluctuations energy at the resonance frequency. This phenomenon is evident at speeds equal to 5.6, 6.5 and 8.4, where lock-in between the fourth, third and second natural shear layer mode occurs, respectively. Lock-in conditions also occur at non-integer frequencies of the wind tunnel resonance mode. At $u_e = 5$ m/s, the second shear layer mode locks in to the first sub-harmonic of the wind tunnel acoustic resonance for $f = f_{wt}/2 = 75$ Hz. At slightly higher velocities, two energy bands bifurcate symmetrically with respect to this frequency. A similar interaction, but with lesser intensity, develops at this same velocity for a frequency equal to $f = 3/2 f_{wt}$.

Nevertheless, as the upstream boundary layer becomes turbulent, the intensity of the coherent shear layer oscillation is reduced, as it was evidenced in figure 3.2, for velocities larger than 9 m/s. However, the acoustic forcing of the wind tunnel is still very strong and it is the dominant feature of the spectrum of the pressure signal for the microphone under consideration.

After these preliminary investigations, two conditions were chosen to be further investigated in detail. The first condition, referred to as CASE1 corresponds to an upstream velocity of 6 m/s, at the maximum value of suction of the upstream boundary layer suction system. This condition is chosen since the upstream boundary layer profile is still laminar and the shear layer flow displays strong forced oscillations.

The second condition, CASE2, is that corresponding to an upstream velocity of 12.40 m/s, where the incoming boundary layer is turbulent and thicker with respect to the cavity length L. In such a condition, the shear layer, fully turbulent, does not develop self-sustained oscillations, despite the strong forcing of the wind tunnel acoustic resonance which can substantially be neglected in this case. The relevant parameters pertaining to the two conditions discussed in this work are reported for reference in table 3.1. In the table δ_0 is the 99% thickness of the upstream boundary layer, δ_0^* its the displacement thickness, θ_0 its momentum thickness and H_0 its shape factor.

Case	u_e	Re_L	δ_0 [mm]	δ_0/D	θ_0 [mm]	Re_θ	L/θ_0	δ_0^* [mm]	H_0
CASE1	6.0	27000	4.4	25.9	0.60	240	113	1.32	2.20
CASE2	12.4	56000	22.0	5.2	2.00	9000	34	2.96	1.48

Table 3.1. Summary of the main parameters of the cases tested. The pedix $_0$ denotes quantities at the upstream reference station, at $x/L = -0.14$, i.e. $x = -10$ mm.

3.2 Results for CASE1

3.2.1 Upstream conditions

In CASE1 the free-stream velocity u_e is equal to 6.00 m/s, at which the Reynolds number based on the cavity length $L = 68$ mm is equal to $Re_L = LU_e/\nu \approx 2.7 \cdot 10^4$. The level of suction operated on the perforated plate upstream of the cavity is sufficient to produce a laminar boundary layer at the cavity leading edge. In fact, the mean velocity profile, measured at the reference upstream location $x = -10$ mm, $x/L = -0.14$, and in the mid-span section, reported in figure 3.3-(a), shows a fair agreement with a least-squares fit of the Blasius laminar solution, although some deviations can be detected especially at the boundary layer edge. The mean velocity profile has a shape factor $H_0 = \delta_0^*/\theta_0 = 2.19$, where $\delta_0^* = 1.32$ mm, (displacement thickness), and $\theta_0 = 0.60$ mm (momentum thickness). With such a boundary layer, the ratio L/θ_0 is equal to 120. This is a fairly high value, and shear layer oscillation occurs, as demonstrated in the previous section. The momentum-thickness based Reynolds number Re_{θ_0} is equal to 240. An estimated value of the skin friction coefficient, based on the fitted Blasius solution, is $C_f = 3.4 \cdot 10^{-7}$. The 99% boundary thickness δ_0 is taken to be equal to 4.4 mm.

Figure 3.3-(b) shows the profile of root-mean-square value of the velocity fluctuations u'_{rms}/u_e, measured at the same location as the mean velocity profile. The

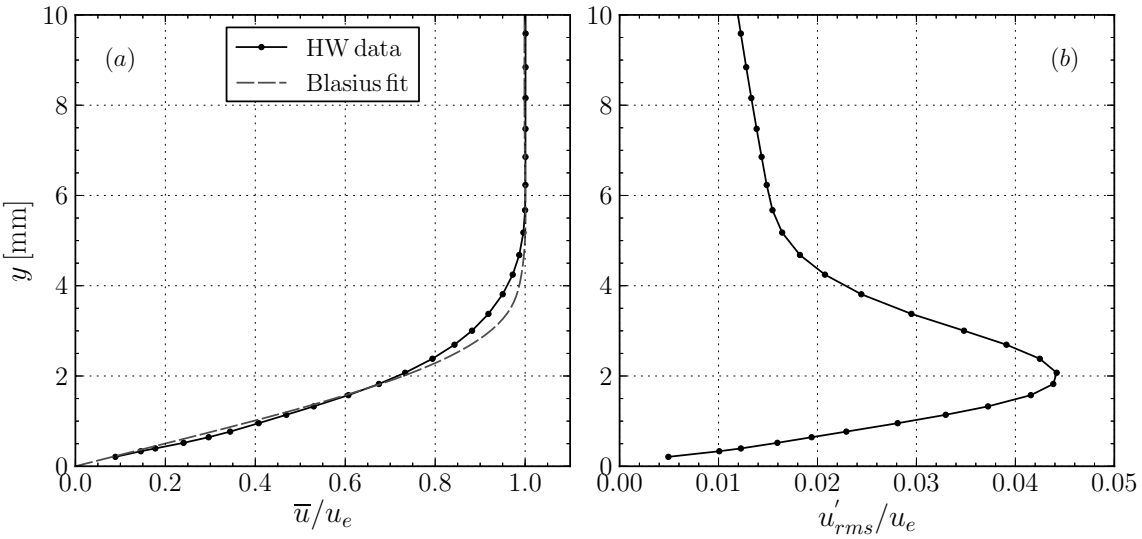

Figure 3.3. Upstream boundary layer profiles at $x = -10$ mm. (a) - mean velocity profile $\overline{u}/u_e$, experimental data and a Blasius solution fit are depicted; (b) - profile of u'_{rms}/u_e.

profile indicates the presence of weak velocity fluctuations in the boundary layer region, below $y = 5$ mm. These fluctuations have been associated with low amplitude modulations of the laminar boundary layer, due to initiation of transition just before the cavity.

3.2.2 Shear layer evolution

Figure 3.4 depicts the streamwise evolution of selected vertical profiles of the mean streamwise velocity. For each profile, two dashed lines represent marks for $u = 0$ and $u = u_e$. Flow is from left to right. Furthermore, the mark for $u = 0$ indicates the position where the velocity profiles was measured.

The velocity profile at $x/L = 0$ quickly changes from the boundary layer profile of figure 3.3 to a shear layer profile. Inside the cavity, the flow is much slower than the external flow and the velocity measured inside the cavity at $x/L = 0$ is quite low, of the order of $0.05u_e$, although a slight increase is observed along x. This low value are clear evidence of poor recirculation of the cavity flow.

The profiles clearly evidence the thickening of the shear layer as it develops downstream. In particular the spreading of the shear layer occurs towards the interior of the cavity, such that the topmost layers of fluid inside the cavity are entrained and accelerated by the viscous stresses, due to the $\partial u/\partial y$ component across the shear layer. However, the associated momentum transfer towards the cavity flow is quite weak and thus the rotational speed of the recirculating flow is

low. The mean velocity profiles also indicate that, as the shear layer flow passes

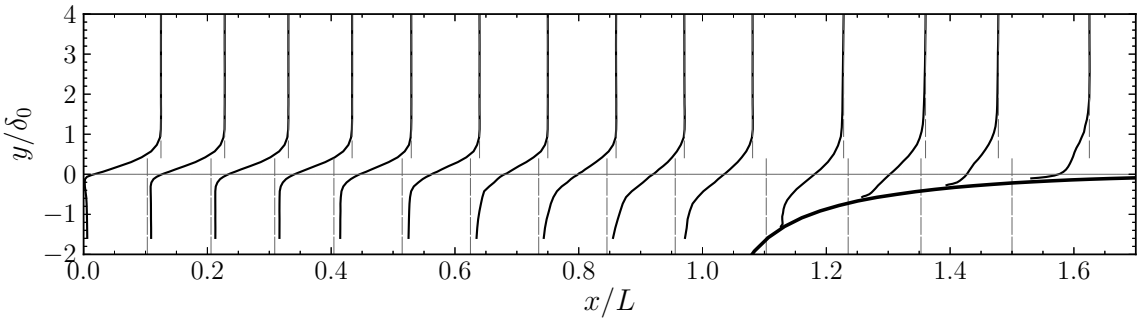

Figure 3.4. Selected mean velocity profiles $\overline{u}$ along the shear layer. About one each three profiles is shown, for clarity. The downstream edge of the cavity model is also visible. Flow is from left to right. Horizontal and vertical axes are in real scale.

by the impingement region, it lifts up over the downstream cavity edge, and the thickness of the resulting flow developing from this region is significantly larger then δ_0. In fact, this thickness is comparable to that of the shear layer at the impingement.

In figure 3.5, selected vertical profiles of the root-mean-square value of the velocity fluctuations along the streamwise coordinate are reported. The vertical scale associated to the y/δ_0 value is on the left. The horizontal and vertical axes are in scale. The same plot reports in red the evolution of the maximum value of u'_{rms}/u_e along the shear layer, with its associated vertical scale on the right-hand side. The

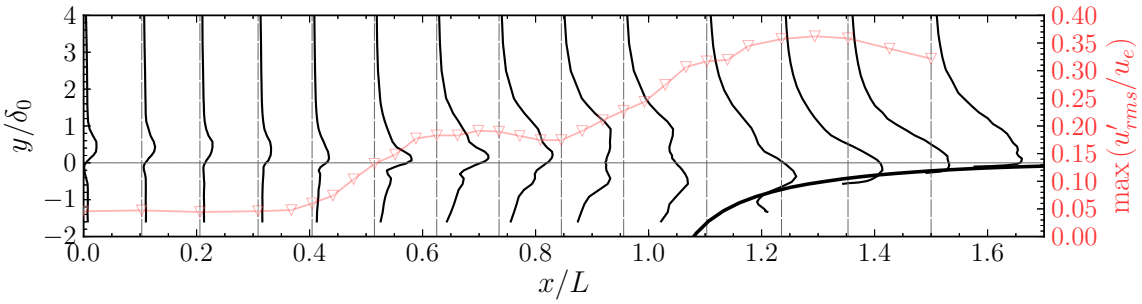

Figure 3.5. Selected profiles of u'_{rms}/u_e along the shear layer. About one each three profiles is shown, for clarity. The red curve is the streamwise evolution of $\max(u'_{rms}/u_e)$. Horizontal and vertical axes, (the left one), are in real scale.

figure indicates that the intensity of the fluctuations remains practically the same for the first third of the shear layer, up to about $x/L \approx 0.35$. In this region, the value of u'_{rms}/u_e is the same of the value in the upstream boundary layer. Furthermore, in this first region, the profile do not change significantly, even though a slight modification of the mean velocity profile was observed in figure 3.4.

However, as the shear layer reaches $x/L \approx 0.35$ a marked increase of the velocity fluctuations can be observed up to $x/L \approx 0.6$, where the fluctuations saturate at a value of $0.18u_e$. This increase in the peak value is also associated to a remarkable increase of the vertical region interested by the fluctuations. This means that the spatially averaged value of u'_{rms}/u_e along y increases much more then the curve of $\max(u'_{rms}/u_e)$. A second peak appears on the profile in this region, at around $y/\delta_0 = -0.45$. This second peak, below $y/\delta_0 = 0$, is common for cavity flows, e.g. Basley et al. [2010].

The plateau region of constant $\max(u'_{rms}/u_e)$ lasts up to $x/L \approx 0.85$, where a second marked increase of the fluctuation intensity is observed. It is argued that this second increase is due to the break up into small scale structures of the coherent rollers of vorticity developing in the shear layer, as they approach the impingement region. Evidence for this hypothesis will be given by flow visualisations reported in section 3.2.4. The increase continues past the end of the cavity, up to $x/L \approx 1.3$, where the large fluctuations are associated to the turbulent wall flow.

It is also noteworthy that the strong increase of the boundary layer thickness observed in figure 3.4 is associated to the strong increase of the velocity fluctuations observed for example in the last profile of figure 3.5. This indicates that the evolution of the shear layer and the properties of the boundary layer developing downstream of the cavity are tightly connected.

The overall behaviour is a strong increase of the velocity fluctuations all along the shear layer, resulting in a highly turbulent flow reattaching on the downstream edge and developing downstream from there. Therefore, the interaction between the incoming boundary layer and the cavity flow is strongly dissipative in nature, essentially due to the instability of the shear layer. This phenomenon completely hinders the development of a thinner laminar boundary layer downstream of the cavity and thus makes it difficult to achieve drag reduction on a TVC controlled airfoil.

The red curve of figure 3.5 demonstrates the increase of the integral fluctuation intensity, i.e. across the entire spectrum. This value comprises broadband components and it is not really significant regarding the growth of the amplitude at the shear layer resonance frequency. To this end, figure 3.6 shows the streamwise evolution of the narrow-band energy in a frequency band wide 1 Hz around the wind tunnel resonance frequency $f_{wt} = 150$ Hz and around its first harmonic, as well as the broadband integral value. For each streamwise location, the data refer to the y point across the shear layer where the largest integral fluctuation energy is observed. The figure indicates that the growth of the fluctuation amplitude at both the first and the second mode is essentially exponential, since the experimental data show a good fit with a line representing an exponential on this semi-logarithmic plot. This exponential amplification of the fluctuations occurs up to about $x/L \approx 0.55$, where they saturate to a constant value. A different amplification factor between the two

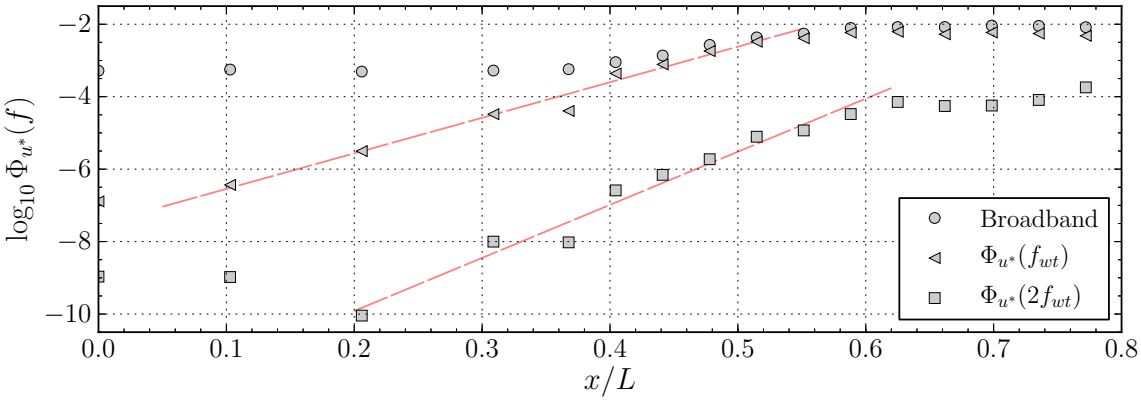

Figure 3.6. Streamwise evolution of broadband, circle, and narrow-band power spectral densities, at $f = f_{wt}$, triangles, and $f = 2f_{wt}$, squares.

modes is observed, and the amplification factor for mode two, is about 50% larger then for mode one.

It is also observed that in the plateau region, $0.55 < x/L < 0.8$, most of the fluctuations are due to the first oscillation mode, which is thus the most energetic phenomenon driving the shear layer flow. On the other hand, the energy at the first harmonic is at least two orders of magnitude lower, allover the shear layer.

The shear layer development is a key element of the aero-acoustic resonance process, constantly driving the velocity fluctuations across the entire shear layer flow. Its growth along the streamwise coordinate is strictly connected to the amplitude of the oscillations: larger oscillations imply larger dissipation and larger spreading. A clear numeric measure of such a spreading is the streamwise derivative of the vorticity thickness δ_ω, defined as:

$$\delta_\omega = \frac{\Delta u}{\max \partial\overline{u}/\partial y} \tag{3.2}$$

where Δu is the velocity difference between the outer and internal flows. This quantity is often used, e.g. Rowley et al. [2001], to characterise the shear layer thickness in cavity flows. It is a local measure of the maximum shear in the flow and of the thickness of the vorticity layer.

The evolution of the vorticity thickness δ_ω is shown in figure 3.7. These results were obtained by computing the derivative of the mean velocity profile $\partial\overline{u}/\partial y$ by analytic differentiation of a smoothing spline interpolant to reduce oscillations due to the finite difference operator on the experimental data. The plot terminates at $x/L = 0.9$, since there is no physical meaning of the results downstream of this region.

Most of the results on cavity flows indicate a linear growth of the vorticity thickness even though there is some scatter of the growth rate among the different

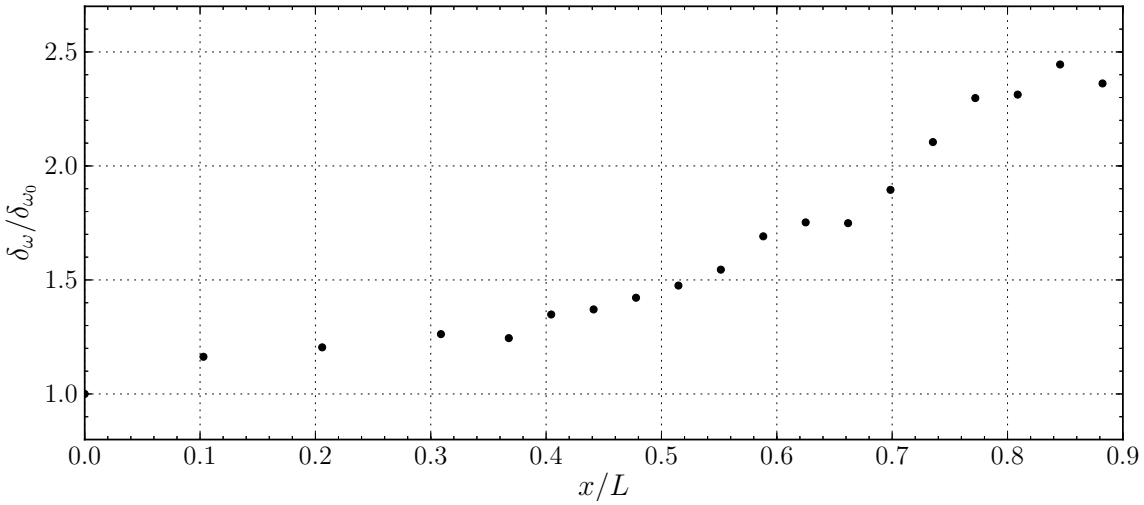

Figure 3.7. Streamwise evolution of the non-dimensional vorticity thickness $\delta_\omega/\delta_{\omega_0}$.

authors. Furthermore, the growth rate also depends on the ratio L/θ as reported by Sarohia [1975]. In our results of figure 3.3 it is observed that the vorticity thickness grows consistently up to $x/L \approx 0.85$, in the location of the downstream shoulder of the cavity. The thickness displays a slow growth up to $x/c \approx 0.5$ with a growth rate $\mathrm{d}\delta_\omega/\mathrm{d}x$ approximately equal to 0.04. This slope then increases significantly and reaches a maximum growth rate equal to about 0.15 at around $x/c \approx 0.7$. Such a marked increase of the vorticity thickness is connected to the drastic increase of the velocity fluctuations from $x/L \approx 0.5$, as shown in figure 3.5, which enhances the spreading rate of the shear layer.

3.2.3 Spectral and correlation analyses

Extensive temporal analyses have been conducted for CASE1, to shed light on the relevant temporal dynamics of the flow. Figure 3.8 shows the power spectral density of the normalised velocity fluctuations $u^* = u/u_e$ at three significant points. Figure (a) refers to $x/L = 0$, $y/\delta_0 = -3.4$, inside the cavity flow, at the beginning of the shear layer; figure (b) refers to $x/L = 0.58$, $y/\delta_0 = 0.45$, in the most unsteady region of the shear layer; figure (c) refer to $x/L = 1.0$, $y/\delta_0 = -0.45$, near the impingement region.

The most significant feature is that the three spectra are characterized by a sharp peak at the wind tunnel resonance frequency $f_{wt} = 150$ Hz. This oscillation is present in the entire flow field with an amplitude dependent on the spatial location. The spectrum of the velocity time history in the cavity region has very low energy across the entire spectrum, which is dominated mostly by low frequencies. Here, the

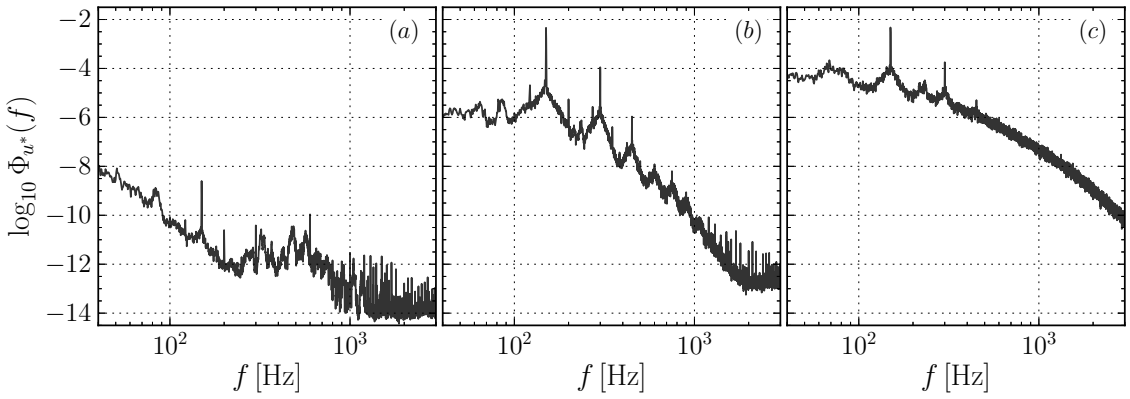

Figure 3.8. Power spectral density of the normalised velocity fluctuations $u^* = u/u_e$, at three reference points: (a) - $x/L = 0$, $y/\delta_0 - 3.4$; (b) - $x/L = 0.58$, $y/\delta_0 = 0.45$; (c) - $x/L = 1.0$, $y/\delta_0 = -0.45$. See figure 2.9 to locate the measurement points.

peak at f_{wt} is very low. On the other hand, the velocity fluctuations in the shear layer, figure 3.8-(b), are energetically dominated by the Kelvin Helmoltz instability, which drives the shear layer to fluctuate strongly at f_{wt}, showing several other peaks of decreasing intensity at its harmonics. The spectrum in figure (c), referring to the velocity fluctuations in the impingement region, is still dominated by two sharp peaks at $f = f_{wt}$ and $f = 2f_{wt}$, but presents characteristics of the spectrum of a turbulent flow, with a wide range of spatial and temporal scales. In fact, this region sees the strong break up of the coherent vorticity rollers developing in the shear layer, which results in an highly turbulent flow developing downstream.

The spectra in figure 3.8 show that the entire cavity flow is subject to a strong pulsation at f_{wt}, but the amplitude does vary in space. Figure 3.9 show the distribution across the entire shear layer of the spectral density at f_{wt}. The value is obtained by integration of the spectral density in a band large 1 Hz around f_{wt}, for each point in the shear layer where a velocity time history was measured. The entire external flow, in particular before $x/L = 0.2$, is permeated by a weak amplitude of the velocity fluctuation at the resonance frequency, which, nonetheless, is able to force the initial region of the shear layer, and to cause the development of significantly energetic fluctuations. The amplification of the shear layer velocity fluctuations in its first part is in fact clearly visible, especially in the region for $0 < y/\delta_0 < 0.5$, corresponding to the first half of the incoming boundary layer flow. The fluctuation amplitude eventually saturates at around $x/L = 0.55$. Then, a significant vertical spreading of the the region subject to strong fluctuations is observed, characterized by two lobes, one around $y/\delta_0 \approx 1$, the other around $y/\delta_0 \approx -0.5$. An interesting feature of the energy distribution of figure 3.9 is the very low level of fluctuations in a very thin region around $y/\delta_0 = 0$, which extends up to where the fluctuation

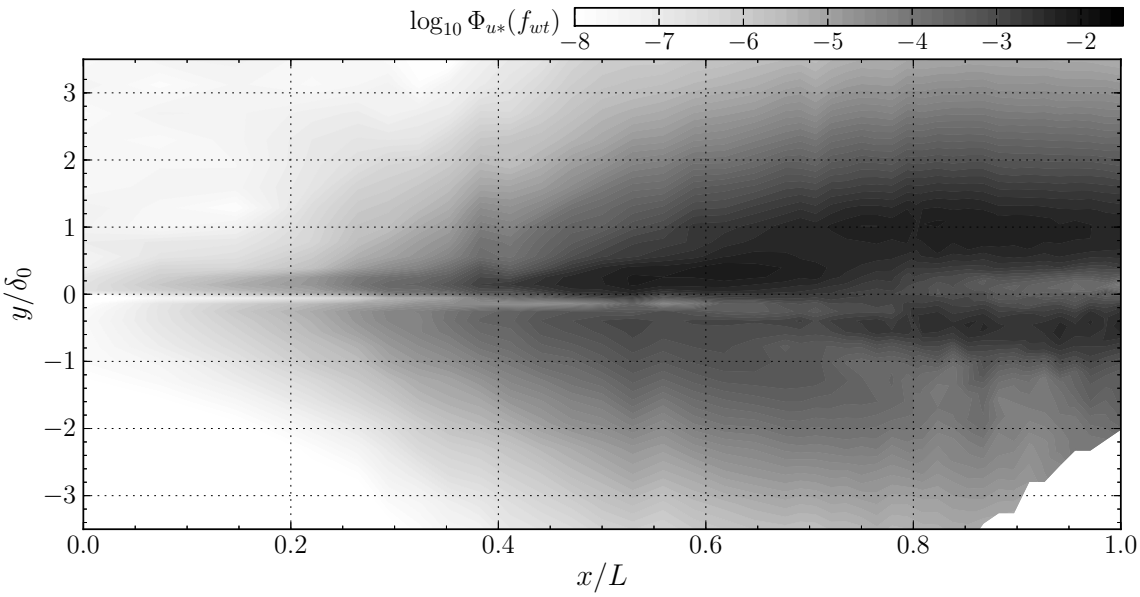

Figure 3.9. colour map of the power spectral density of the normalised velocity fluctuations $u^* = u/u_e$, at the frequency of the first mode $f_{wt} = 150Hz$. The value is obtained by integration of the spectral density in a band large 1 Hz around f_{wt}.

energy saturates, at $x/L \approx 0.55$

These results are in very good qualitative agreement with those corresponding to rectangular cavity flows. For example, Basley et al. [2010], investigated a rectangular cavity flow characterized by $Re_L = 12000$, half of that of the current experiment, with a ratio $L/\theta_0 = 77$, thus with a laminar boundary layer slightly thicker then that of CASE1. These authors reported an energy distribution at the first shear layer mode frequency which presented the same qualitative features as those in figure 3.9. Such a similarity essentially indicates that the basic mechanism at the hearth of the phenomenon is the same, and it is expected that significant insight can be gained regarding the control of the flow in CASE1 by previous research on the control of rectangular cavity flows, especially when dealing with oscillatory blowing/suction.

Some insight into the behaviour of the cavity flow can be gained by observation of the pressure fluctuations spectra, reported in figure 3.10 for three different microphones. These are microphone $m7$, located in the cavity under the cusp, figure (a), microphone $m8$, located in the impingement region, figure (b), and microphone $m3$, located outside the cavity at $x/L = 1.72$. The spectral density unit is Hz^{-1}, since the pressure signal is made non dimensional with $2\rho u_e^2$, before being Fourier transformed. The two most energetic features of the spectrum of the signal p_7^* are the two very sharp peaks at $f = f_{wt}$ and $f = 2f_{wt}$. By contrast the spectrum of p_3^* has very little energy at these two frequencies, which is essentially of the same level of the wind tunnel resonance energy. This difference clearly indicates how

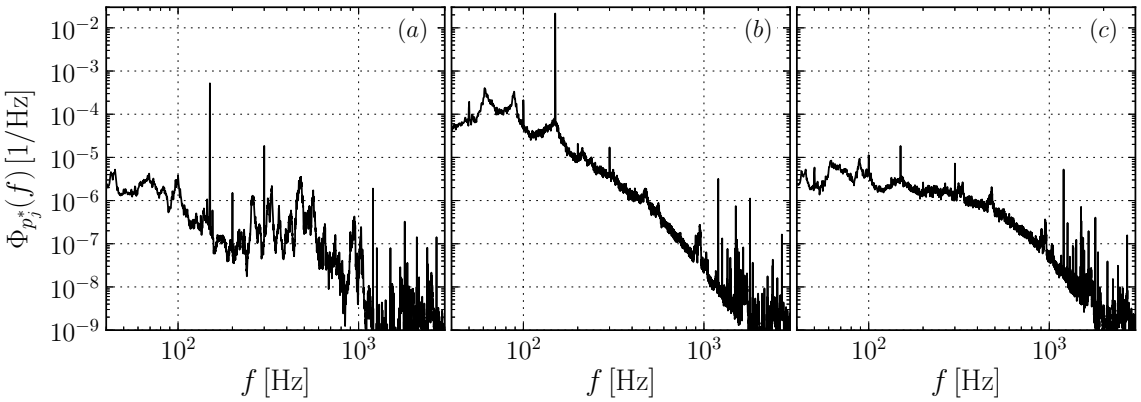

Figure 3.10. Power spectral density of the normalised pressure fluctuations $p^* = 2p/(\rho u_e^2)$, for microphone $m7$, (a), microphone $m8$, (b) and microphone $m3$, (c). Please refer to figure 2.9 for the exact positions of the microphones.

the cavity flow is subject to a strong pressure-velocity coupling, which dramatically increase the level of pressure fluctuations, periodically forcing the shear layer at is most receptive region, i.e. its initial part. This is confirmed by the very high level of energy at f_{wt} for microphone $m8$, located in the impingement region, where the coherent structures of the shear layer periodically break up at the wall, producing a very strong signature, clearly evidence by the spectrum.

Interestingly, there is no clear evidence of energy peaks at the harmonics of f_{wt} higher than the second, i.e. at $f = kf_{wt}$ for $k = 3, 4, \ldots$. This is in stark contrast with the spectrum of the velocity signal in the shear layer, see figure 3.8-(b), where harmonics up to $k = 6$ were detectable in the spectrum. One answer could be that these harmonics result in very feeble pressure fluctuations at the wall, which are thus covered by the very high level of background noise.

The different character of the flow in the three region is highlighted by considering the behaviour of the spectrum at higher frequencies. In fact, the spectrum of p_7^*, figure 3.10-(a), shows a large number of peaks in the range $200\,\text{Hz} < f < 1000\,\text{Hz}$. These have been verified to be due almost entirely to coloured noise generated by the experimental setup, such as wind tunnel noise and vibrations or noise generated by the pump of the boundary layer suction system. Nonetheless, the dynamics of the cavity flow occurring in this band are very weak, due to the low speeds of the fluid in the cavity, such that their signature is entirely covered by the above noise sources.

Microphone $m8$ shows much higher energy levels across the entire spectrum, and particularly in the band $200 < f < 1000$ Hz, as discussed in the previous paragraph. The spectrum shows the clear signature of the turbulent pressure fluctuations in thee impingement region even though the most energetic feature is still that associated to the resonance process of the shear layer. The spectrum of the signal p_8^* also

features two weak peaks at $f \approx 60$ and 90 Hz. The origin of these peaks is clear by observation of figure 3.1. They are in fact due to a lock-in phenomenon of the shear with the sub-harmonic of the wind tunnel resonance frequency $f_- = f_{wt}/2 = 75$ Hz. These two peak very also barely visible in the velocity fluctuations spectrum of figure 3.8-(b).

The pressure fluctuations from microphone $m3$, located beneath the turbulent wall-flow developing downstream of the cavity, show a spectrum which is similar in character to that of microphone $m8$, with the same energy peaks at the same frequencies. Nevertheless, the energy of the fluctuations is much lower for this microphone, especially that at f_{wt}.

As discussed above there is a strong aero-acoustic coupling in the cavity flow which both drives and is the result of a coherent oscillation of the shear layer due to the Kelvin-Helmoltz instability. Evidence of this strong coupling is given in

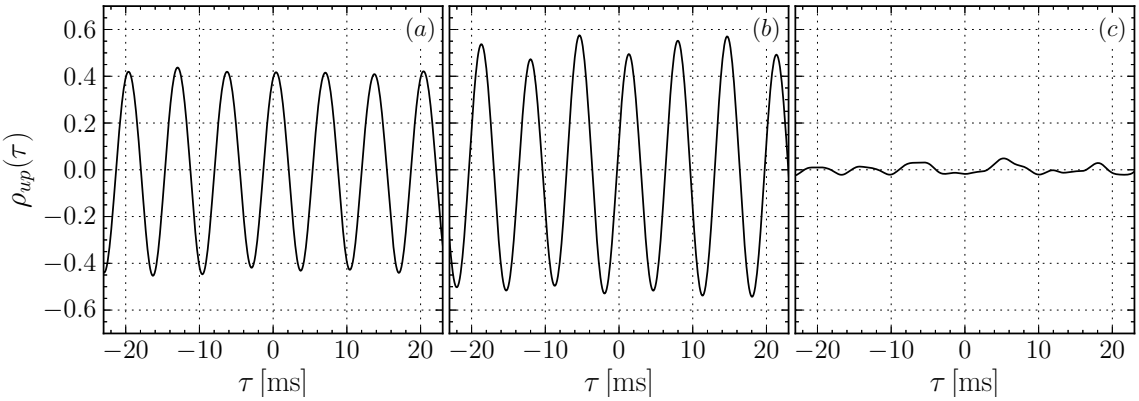

Figure 3.11. Cross-correlation coefficient functions $\rho_{up_j}(\tau)$. The velocity time series is measured at the reference point, $x/L = 0.58$, $y/\delta_0 = 0.45$. Microphone $m7$, (a), microphone $m8$, (b) and microphone $m3$, (c). Please refer to figure 2.9 for the exact positions of the microphones.

figure 3.11, which displays cross-correlation coefficient functions between the velocity fluctuations at $x/L = 0.58$, $y/\delta_0 = 0.45$, in the most unsteady region of the shear layer, and the three reference microphones, $m7$, $m8$ and $m3$, in figures (a), (b) and (c), respectively.

The cross-correlation function for the first two microphones clearly highlights a strong pressure-velocity coupling, which has a strong periodic nature, evidently due the strong oscillatory behaviour of the flow. In fact, the period of the cross-correlation function is approximately equal to the inverse of f_{wt}. The level of correlation between the fluctuations of u and p is significant and of the order of $0.4 \div 0.6$. By contrast, the cross-correlation function of the velocity fluctuations with p_3^* is much lower and no clear periodicity can be identified. This result can be explained by considering the physical distance separating the shear layer flow and microphone

$m3$, and by observation that this microphone is outside the cavity, i.e. the region where the strong aero-acoustic coupling drives the fluctuations in the flow.

The level of correlation between the pressure and the velocity fluctuations is clearly function of the point where the velocity is measured. Thus, for each point in the shear layer the cross-correlation coefficient function has been calculated, for lags up to 750 cycles of the main oscillation, and the maximum absolute value of $\rho_{u(x,y)p_j}(\tau)$ is taken as an indication of the correlation level of the pressure fluctuations measured from microphone mj with the velocity at point (x, y). Figure 3.12 shows the results of this analysis, in the form of a colour map of $max|\rho_{up_7}|$, i.e. considering microphone $m7$. The colour map shows some irregularity, mostly due

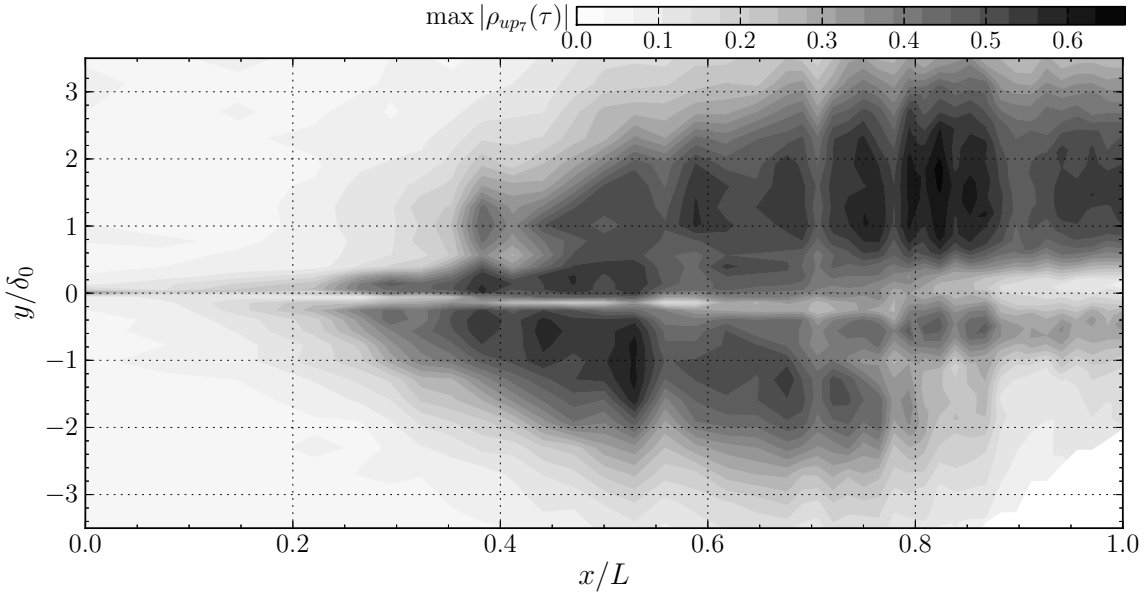

Figure 3.12. colour map of the maximum absolute value of the cross-correlation coefficient functions ρ_{up_7}, across the entire shear layer.

to the limited spatial resolution of the hot wire measurements and of the limited acquisition times. Nonetheless, the figure clearly indicates the regions where the flow field is most correlated with the pressure fluctuations at the wall. These are two horizontally elongated lobes, symmetrically located above and below $y/\delta_0 = 0$, developing from $x/L \approx 0.3$ and extending up to $x/L = 1$ and probably more downstream for the upper lobe. The correlation value in these lobes is high, of the order of 0.4-0.6. Although not shown here, the correlation map for $max|\rho_{up_8}|$ is very similar in shape to that of figure 3.12, with similar values, as expected. On the other hand, for microphone $m3$ the correlation levels are much weaker, across the entire flow field.

The spatial distribution of the correlation level is remarkably similar to the

distribution of $\Phi_{u^*}(f_{wt})$ of figure 3.9, but this result has to be expected since it is the oscillation at f_{wt} which is responsible of the correlation between the pressure and the velocity.

Evidence for this claim can be obtained by inspection of the coherence function between the pressure and the velocity fluctuations. An example of the extensive analyses which have been conducted in this direction is given in figure 3.13, which reports the squared coherence function between pressure signals from the three significant microphones and the velocity fluctuations measured at $x/L = 0.58$, $y/\delta_0 = 0.56$. It

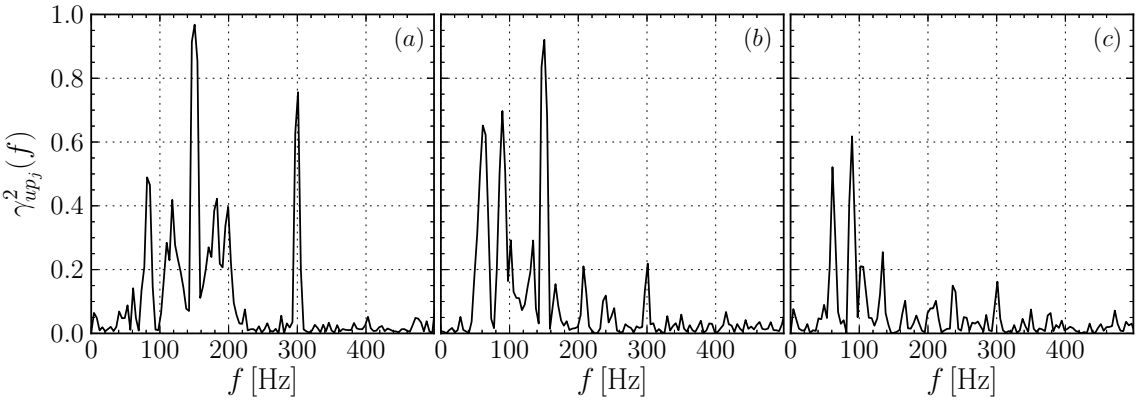

Figure 3.13. Squared coherence functions $\gamma^2_{up_j}$. The velocity time series is measured at the reference point, $x/L = 0.58$, $y/\delta_0 = 0.45$. Microphone $m7$, (a), microphone $m8$, (b) and microphone $m3$, (c). Please refer to figure 2.9 for the exact positions of the microphones.

is very clear that the aero-acoustic coupling is very narrow-band in nature, since the coherence function is statistically different from zero only at few distinct frequencies. At the fundamental frequency $f = f_{wt} = 150$ Hz, the squared coherence function can be as high as 0.95 for both microphones $m7$ and $m8$, located inside the cavity region. Regarding microphone $m3$, the coherence at f_{wt} is practically zero, as was expected by observation of the cross-correlation functions. At the fist harmonic, $f = 2f_{wt} = 300$ Hz, the coherence function is lower, of the order of 0.75 for microphone $m7$, and as low as 0.25 for microphone $m8$. Interestingly, the coherence at the higher harmonics is practically zero. This may indicate that the aero-acoustic coupling is mainly driven by the first two shear layer modes.

The squared coherence function of the three microphones is also characterized by several other peaks, especially at the two frequencies corresponding to the lock-in at the first sub-harmonic of the fundamental frequency. However, despite the relatively high levels of coherence these peak seem to have scarce dynamic relevance, as observed by the low energy of the velocity fluctuations spectrum of figure 3.8 at these frequencies.

To gain some more insight into the dynamics of the shear layer and into the pressure-velocity coupling, some results of the application of the Multi-Time-Delay Linear Stochastic Estimation, (Lasagna et al. [2013]), to the cavity shear layer are presented and discussed. Details of the technique are reported in appendix A.

The spatio-temporal dynamics of the velocity fluctuations in the shear layer have been estimated by using the pressure time-history measured by microphone $m7$, located under the cusp, see figure 2.9. For each of the points in the shear layer where a velocity time history was measured, the estimation coefficients of equation A.5 are computed. Then, using a single pressure time history, it is possible to estimate the velocity in the flow field. Figure 3.14 shows the time-resolved reconstruction of the spatial distribution of the non-dimensional velocity fluctuation in the shear layer, using the Multi-Time-Delay approach with $n = 1000$. The temporal resolution between successive snapshots is $45\Delta t$, i.e. one snapshot out of every forty-five reconstructed snapshots is shown.

It is clearly visible that the reconstructed flow field shows a distinct spatial organisation characterized by a periodic alternation of regions of positive and negative velocity fluctuation. This feature is a characteristic for a cavity flow the in shear-layer mode, Rowley et al. [2001], where the flow is subject to global instability in the form of convective Kelvin-Helmoltz waves excited by feedback from pressure waves generated near the cavity trailing edge. The vertical dimension of the region interested by the phenomenon is comparable to the size of the shear layer estimated from figure 3.5.

The convection properties of the coherent structures in the shear layer are also well resolved by the Multi-Time-Delay approach. In fact, the coherent structures convection speed ratio $\kappa = U_c/U_e$ was estimated by performing cross-correlation analyses between estimated velocity time histories in adjacent points at $y/\delta = cost$, for all the point in the shear layer. Examination of the time lag, with respect to the separation Δx between the points, led to a map of κ as a function of the spatial location. The value of κ was almost constant in all the shear layer for $x/L < 0.7$ and equal to about 0.5, decreasing to about 0.4 only after $x/L = 0.7$. These values are in agreement with the previous findings of several authors which investigated flows past rectangular cavities, e.g Chatellier et al. [2004].

3.2.4 Upstream/downstream boundary layer comparison

It has been postulated by Donelli et al. [2009] that the presence of a rotating vortical flow in the cell determines a more energetic boundary layer downstream of the cell, with respect of the solid wall case, such that it is less prone to detach from the wall and large flow separation which is responsible of large pressure drag can be avoided. Therefore, the crucial test, which is given particular focus in this work, is to assess the effectiveness of the cell in controlling the flow around an airfoil is

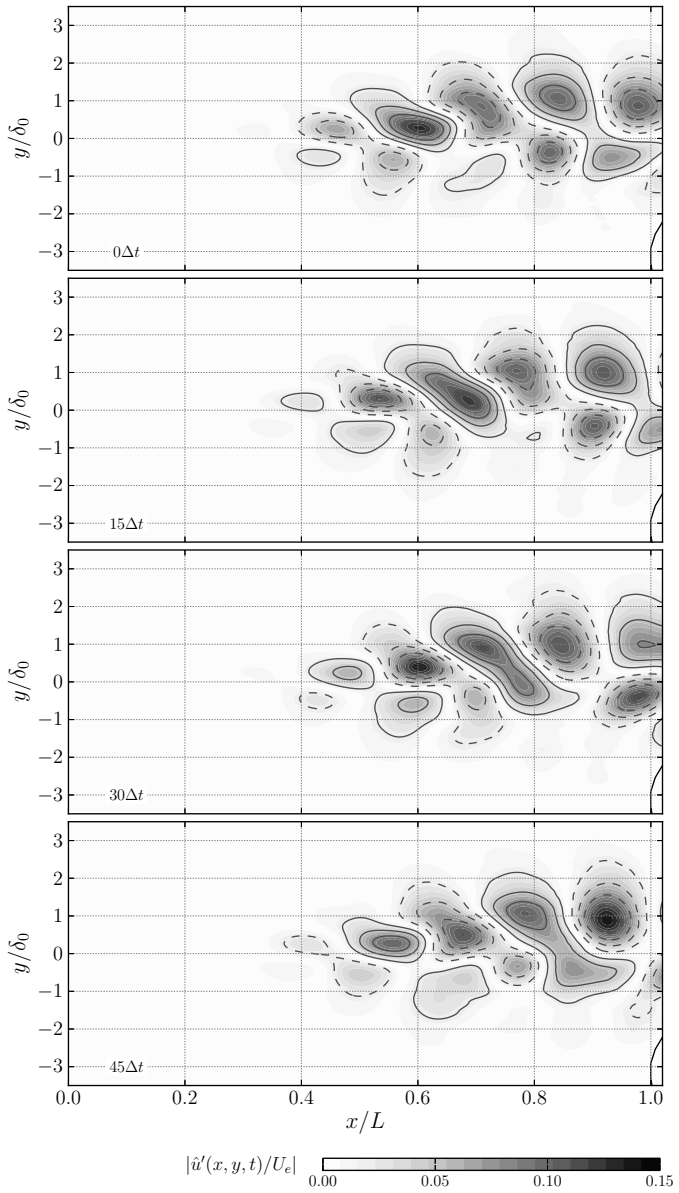

Figure 3.14. The colour maps show the spatial distribution of the reconstructed fluctuating velocity component in the shear layer in four selected time instants. The time delay between successive snapshots of the sequence is $45\Delta t$, where $\Delta t = 1/8000$ s is the sampling interval. The grey colour shading represents the modulus of the velocity fluctuation. Eight iso-lines have been drawn for values of $|\hat{u}'/u_e|$ equal to ± 0.11, ± 0.08, ± 0.05, ± 0.02; dashed contours indicate a negative value.

to compare the boundary layer mean velocity profiles upstream and downstream of the cell itself. However, before presenting the result of this investigation, a brief discussion regarding what can be reasonably achieved on a flat plate is given.

In figure 3.15 a conceptual sketch explaining the "moving wall" effect is reported. Suppose to have a flat wall, indicated by the line w, along which flows a laminar boundary layer, with the 99% thickness and the momentum thickness increasing with known laws $\delta(x)$ and $\theta(x)$. Two reference stations are selected on the flat plate, 0 and 2, where the momentum thickness will be equal to θ_0 and θ_2. Between these two stations the momentum thickness will increase as dictated by the integral boundary layer equation:

$$\theta_2 = \theta_0 + \int_{x_0}^{x_2} \frac{C_f(x)}{2} \mathrm{d}x \tag{3.3}$$

where $C_f(x) = 2\tau_w(x)/\rho u_e^2$ is the skin friction coefficient due to the wall shear stress $\tau_w(x)$. Therefore, the momentum thickness of the boundary layer increases in reason of the friction forces at the wall. The figure shows this increase in boundary layer thickness by the velocity profiles in black, representative of the solid-wall condition.

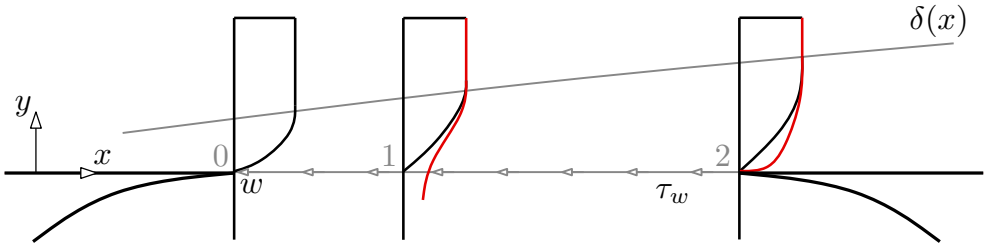

Figure 3.15. Conceptual sketch explaining the moving wall effect.

Now suppose that between stations 0 and 2 the flat wall is replaced by a trapped vortex cell. Suppose that the flow is steady and, for simplicity of the discussion, let us suppose that both the upstream and downstream edges are sharp cusps. For mass conservation reasons the two edges will be connected by a streamline, forming an interface dividing the internal and the external flows. This streamline will not be probably flat as line w, but for simplicity we assume it is. Because of the absence of the wall, there will be a viscous momentum transfer across the interface from the boundary layer flow to the internal cavity flow, which is thus put in rotation by this flux. In a steady condition, this energy flux, sustaining the rotation of the vortex flow, will balance the dissipation of energy in the cavity flow due to viscous forces.

The crucial point is that this momentum flux will be proportional to the derivative $\partial u/\partial y$ along the interface, which in the case of the trapped vortex cell will be

lower than the solid wall case, because of the rotation of the flow in the cavity. In fact, at station 1 the mean velocity profile will look like the red curve, with the bottom velocity according with the speed of the fluid in the cavity. At the downstream edge, the flow will reattach and the boundary layer will be likely fuller than the solid wall case at the same station 2, i.e. the momentum thickness will have increased less than in the solid wall case. This increase can be obtained as:

$$\theta_2^* = \theta_0 + \int_{x_0}^{x_2} \frac{C_f^*(x)}{2} \mathrm{d}x \tag{3.4}$$

where the asterisk denotes the case with TVC. In this equation C_f^* is the friction coefficient obtained from the shear stress on the dividing streamline.

For the "moving wall" effect we should have that $\theta_2^* < \theta_2$, that is the momentum thickness at station 2 with TVC will be lower than in solid wall conditions. However, the important limit to notice here is that $\theta_2^* > \theta_0$, that is there can be no reduction of the momentum thickness between the stations 0 and 2, basically because no energy is added to the flow. This has important consequences. For a laminar flow, since C_f is very low, the maximum achievable gain in terms of θ, is also very low, due to the fact that the momentum thickness does not increase very much. For a turbulent boundary layer, and if the model above still holds true, the increase of momentum thickness on the solid wall is more significant, and thus the potential reduction of θ in TVC conditions could be more large. Since in CASE1 the upstream boundary layer is laminar, the expected increase of momentum thickness is very low and practically below the accuracy of the estimation of θ by integration of the experimental data. Thus it would be practically impossible to assert that the passive TVC is effective, even though is it perfectly possible to assert that it is not.

Indeed, in figure 3.16-(a) a comparison between the upstream, $x/L = -0.14$, and downstream, $x/L = 2.05$, boundary layer mean velocity profiles is reported. As anticipated, and as can be noted from the figure, the boundary layer downstream of the cavity is fully turbulent essentially because of the intense unsteadiness introduced by the break up of the large scale motions in the shear layer. The strong turbulent fluctuations arising from this interaction, figure 3.16-(b), extend farther in the outer flow and significant values of u'_{rms}/u_e can be found up to three times the original height of the upstream boundary layer. Indeed, the strong amplification of fluctuations in the shear layer provides means to enlarge the vertical scale of the region interested by such phenomenon.

The mean velocity profile at $x/L = 2.05$ is characterized by a high momentum in the near wall region with respect to the upstream boundary layer, even though the boundary layer is much more thick and there is a consistent velocity deficit with respect to upstream from $y = 2.8$ mm upwards. The net result is that the momentum thickness varies from 0.60 mm of the upstream laminar boundary layer, to 1.4 mm for the downstream turbulent boundary layer, with a ratio $\theta/\theta_0 = 2.3$.

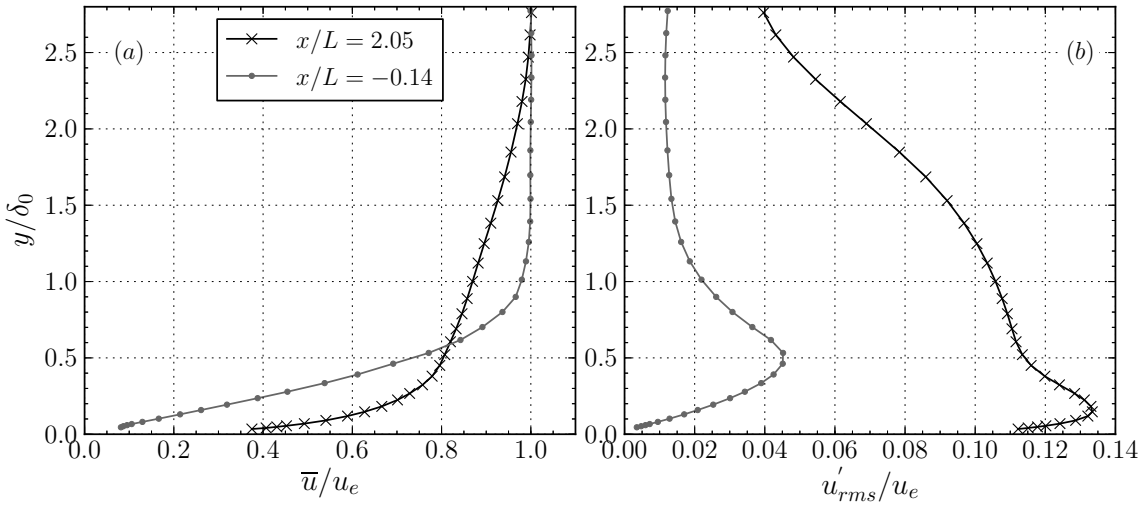

Figure 3.16. Comparison of the upstream $x/L = -0.14$, and downstream, $x/L = 2.05$, boundary layer mean velocity profiles, (a), and of the profiles of the root-mean-square value of the velocity fluctuation, (b).

These results suggests that the presence of the cavity is detrimental to the characteristics of the boundary layer, and ultimately to the drag of an airfoil equipped with one of such cavities. In fact, the drag of an airfoil can be computed by integration of the momentum deficit in the wake which, in fully attached flow conditions, is directly related to the momentum deficit of the upper and lower surfaces boundary layers at the trailing edge. Thus a strong localised increase of θ is certainly not beneficial. This is aggravated as a turbulent boundary layer, as that produces by the TVC, certainly increase its momentum thickness more quickly than a laminar boundary layer. However, it may be the case that the periodic unsteady ejection of vortical structures into the boundary layer may be beneficial to alleviate flow separation on the complete airfoil, thus increasing its performances. Such a mechanism has been observed by Olsman and Colonius [2011], although its control experiments were conducted on a low Reynolds number airfoil.

3.2.5 Flow visualisations

Flow visualisation studies were performed to complement the hot wire measurements and to help in the interpretation of the results. In addition, these investigations were significant to get a better understanding of the internal dynamics of the cavity flow, since for practical considerations most of the hot wire measurements could not target this inner region.

Figure 3.17 reports a sequence of six consecutive snapshots of smoke flow visualisation of the cavity flow in CASE1, in the mid-span vertical plane. The snapshots

were sampled at a frequency of 100 Hz, thus making the shear layer oscillations under-sampled. However, the low sampling frequency and the associated higher exposure time (9997 μs) allowed a better identification of the cavity flow structures at a sufficient speed to capture its dynamics. The upstream part of the cavity flow is not clearly visible, due to the shadow cast by the cavity cusp, since the laser source is located on the top. The images were post-processed by subtraction of the time averaged image and by black/white equalisation to better highlight the significant features of the flow. In the figure, the snapshots are separated by $\Delta t = 2/100$ s, since one each two sampled snapshots is reported to cover a wider time interval. The sequence is sorted left-right, top-bottom.

The snapshots clearly point out the presence of a recirculating vortical flow, with a centre slightly shifted downstream and towards the cavity opening. However, a large spatial range of smaller structures is embedded in the vortex flow, especially in the downstream region of the cavity.

The visualisations provide evidence of the mechanism driving the rotation of the cavity flow. A first element is the momentum transfer from the external flow through viscous stresses by the shear layer, which accelerates the uppermost layers of the cell flow. However, it is believed that this mechanisms alone cannot account for the observed total amount of rotation, since viscous transport of momentum is weak. In fact, such a mechanism alone, cannot justify the relatively large rotation of the fluid in the cavity because, for equilibrium considerations, the energy transferred by the above mechanism has to be dissipated in the cell, and mainly by the wall shear stress on the entire cavity surface.

A closer inspection to the animation of the complete sequence of snapshots is more revealing with regards to a further mechanism driving the cavity flow. In fact, an intermittent injection of fresh, high momentum fluid packets down into the cavity from the downstream edge is observed. Such phenomenon is well evident in the snapshots as a large black area, thus containing high-momentum external fluid with no tracer, which is pushed from the cavity edge inside it. Similar features have been observed for rectangular cavity flows, although the mechanism may be actually different in the present case, since the geometry of the impingement region is rounded and not sharp as it is commonly used in the literature. For example Faure et al. [2006] evidenced a periodic injection of mass into the cavity and he argued that it was connected to the shear layer oscillations resulting in a pulsed jet-like flow. Similar flow structures have been observed in visualisations of the TVC flow at smaller upstream velocities, but are reported here.

An additional note is that the sequence shown in figure 3.17 was taken in the mid-span section of the cavity. Thus when ingestion of fluid is observed in this section, for mass-conservation principles, an equivalent ejection of low momentum fluid in the external flow must happen, which is probably also a key element in the large thickening of the downstream boundary layer.

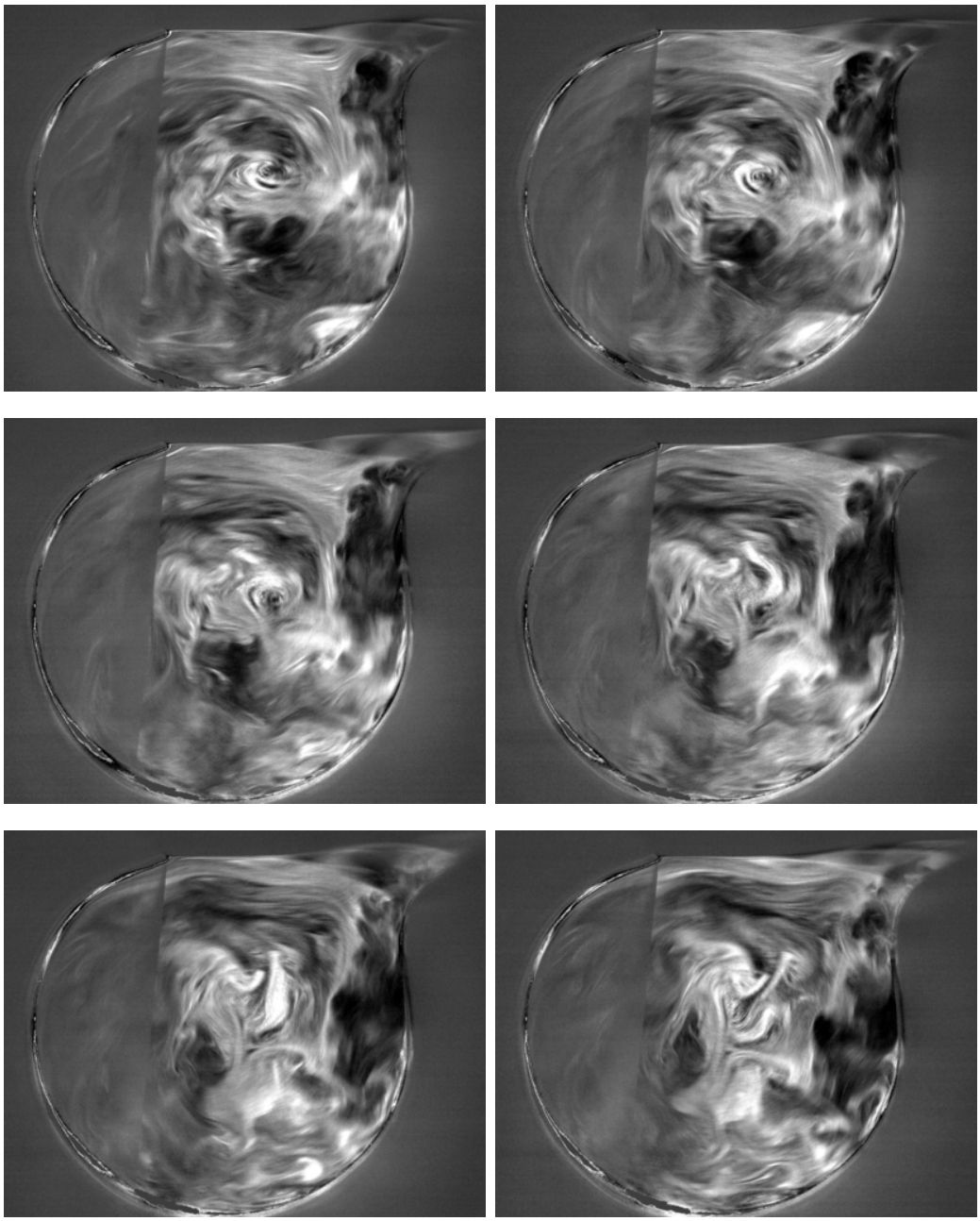

Figure 3.17. Snapshot sequence for CASE1 in the mid-span, sorted left to right, top to bottom.

This mechanism, suggested also by Hokpunna and Manhart [2007] by analysis of Large Eddy Simulations on this same configuration, although at a higher Reynolds number and with an turbulent incoming boundary layer, is responsible in the largest

measure, for the rotation of the cell flow. However, this must happen at the expenses of a large energy dissipation, since this process of energy capture from the external flow seems highly dissipative. In fact, the impingement region is subject to a strong turbulence activities, as evidenced by the profiles of u'_{rms}/u_e of figure 3.5.

3.2.6 Three dimensional properties of the flow

Three dimensional characteristics in cavity flows have been observed by several researchers in both numerical and experimental setups, e.g. Larchevêque et al. [2007], Maull and East [1963], which investigated rectangular geometries. Evidence of 3D modulations of the flow in trapped vortex cells have also been pointed out during the VortexCell2050 project, both by numerical simulations, e.g. Hokpunna and Manhart [2007], as well as in experiments, Savelsberg and Castro [2008], Tutty et al. [2012]. These authors have shown that the cell's flow displays a marked 3D behaviour, but it is not known how this 3D characteristics could affect the performances of a TVC as a control device.

In the present work, the three dimensional character of the flow has been investigated by traversing the hot wire probe along the z axis at several x, y positions. Care was taken to verify that when the probe was traversed it remained at a constant distance from the wall, in order to avoid large drifts in the measured value, due to in-plane variations of the flow.

Figure 3.18 shows profiles of $\overline{u}/u_e$ and u'_{rms}/u_e measured at $x/L = 0.59$, $y/\delta_0 = -1.69$, inside the cavity region. The most striking feature is observed in the be-

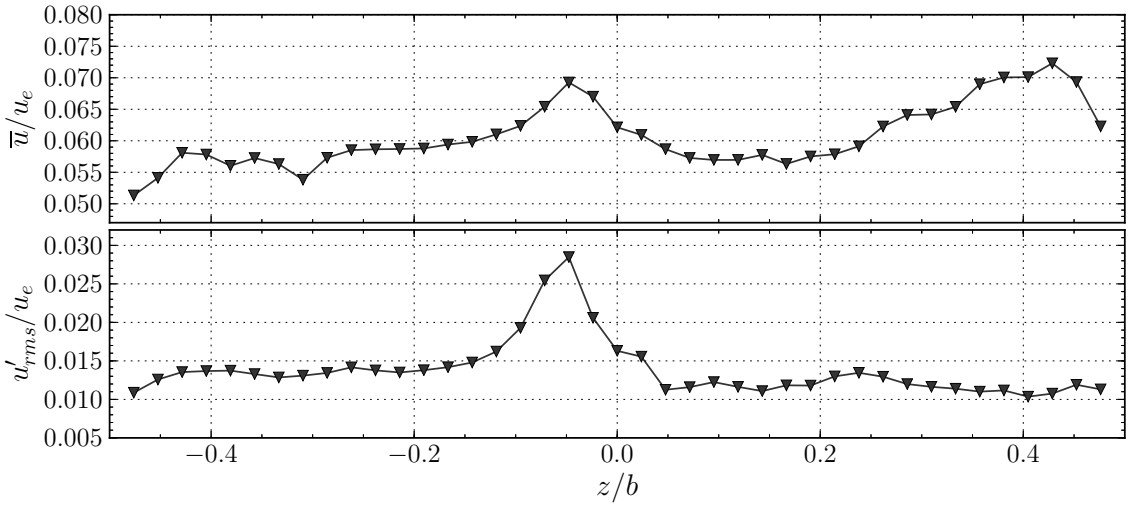

Figure 3.18. Mean value, top, and root-mean-square value, bottom, of the velocity measured at $x/L = 0.59$, $y/\delta_0 = -1.69$, in the cavity region.

haviour of the rms of the velocity fluctuations. Indeed, the graph is characterized

by a sharp peak located someway of the left of the mid-span section. The value of the rms is more than doubled with respect to the average value found along the span at that x, y position. This peak is also associated to a slight increase of the mean velocity value. The flow is thus not symmetric with respect to the mid-span and in fact a moderate drift in the mean velocity value is also observed.

To help explaining this growth, figure 3.19 shows the power spectral density of the velocity fluctuations at the point of largest rms, $z/b = -0.04$ and one point of the left, $z/b = -0.26$, characteristic of the background value. In the frequency

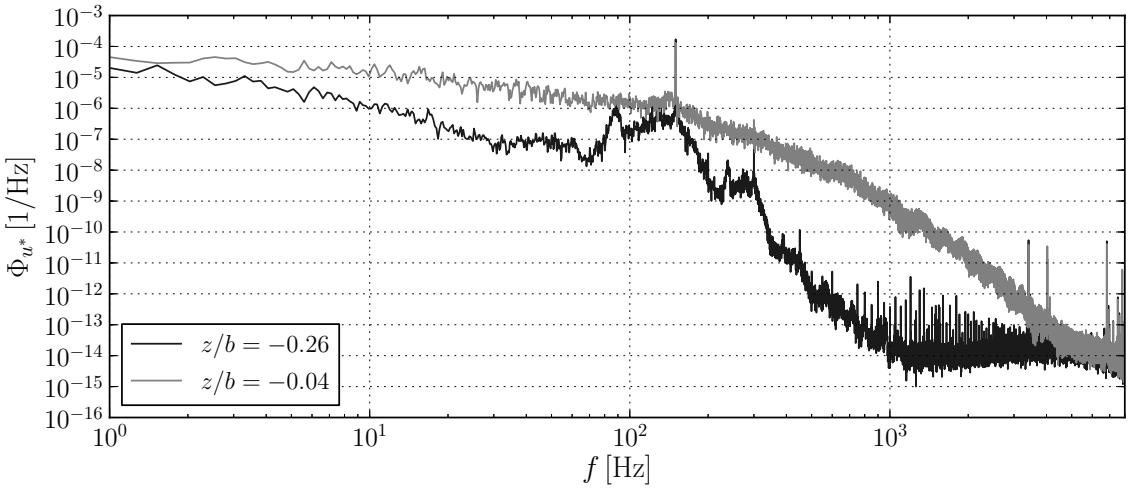

Figure 3.19. Spectra of the velocity fluctuations at $z/b = -0.04$ and $z/b = -0.26$ of the velocity fluctuation measured at $x/L = 0.59$, $y/\delta_0 = -1.69$, in the cavity region.

domain, the peak of fluctuations in the mid-span region is associated to a larger energy over a broad range of frequency up to several kHz, even though the most significant feature of the spectrum is still the fundamental resonance frequency of the shear layer, at $f = 150$ Hz. On the other hand, for the spectrum of the velocity fluctuations next to the peak, at $z/b = -0.26$, the energy is concentrated in a narrow band between about 80 and 200 Hz, where most of the large-scale dynamics of the cavity flow take place. This spectrum is indeed characterized by a sharp energy drop-off at about 300-400 Hz, plateauing after 1 kHz at the level of the background noise.

These spectra suggests a fundamental difference in the flow regime taking place in the two sections of the cavity. For $z/b = -0.04$ is characteristic of a turbulent flow, with a large range of spatial and temporal scales. On the other hand, on the end regions, the flow has much narrower dynamics. However, the nature and the origin of such sharp difference would deserve further investigation, since the difference in the mean velocity is not so large to be attributed to a different rotational speed of

the cell's flow.

A further investigation was performed to quantify the influence of such three-dimensionality of the cavity flow on the properties of the boundary layer downstream of it. Figure 3.20 shows results of this investigation at $x/L = 1.32$, $y/\delta_0 = 0.00$, further downstream the cavity, where the wall flow is turbulent. Please note that, although $y/\delta_0 = 0.00$, the hot wire probe is detached from the wall, due to the curvature of the cavity geometry. The top figure shows the profile of $\overline{u}/u_e$, while the bottom one shows the transverse profile of u'_{rms}/u_e. Downstream of the cavity, the flow has a more uniform behaviour in the spanwise direction, both in terms of mean velocity and of u'_{rms}/u_e. In fact, the variations of the mean value are bounded approximately in a range from $0.55u_e$ to $0.63u_e$, with no spanwise drifts. In addition, the values of u'_{rms}/u_e along the span do not vary significantly even if they show an moderate scatter around the average value, $u'_{rms}/u_e \approx 0.15$, mostly due to the limited sampling time, i.e. $T = 40.3$ s.

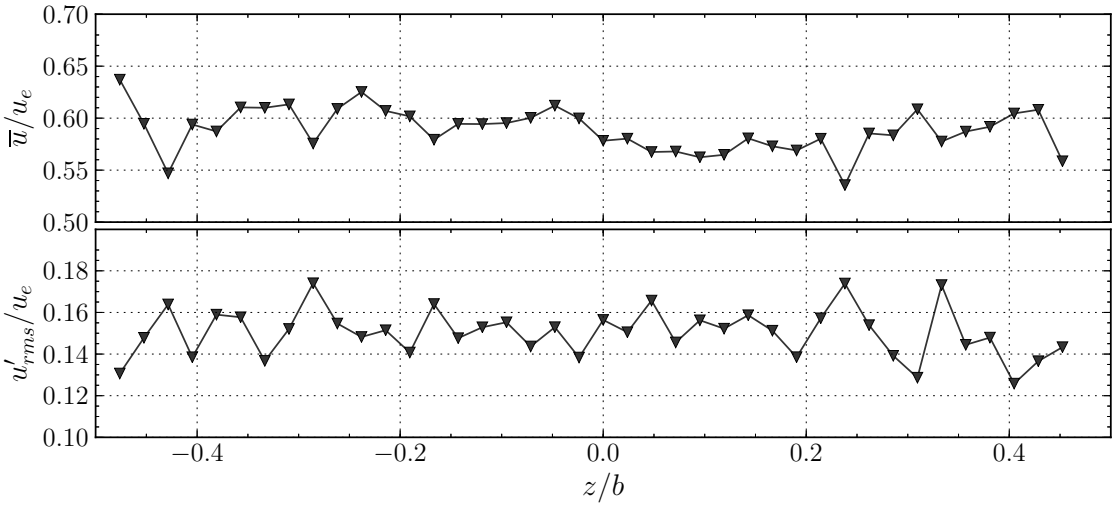

Figure 3.20. Mean, top, and root-mean-square value, bottom of the velocity fluctuation measured at $x/L = 1.32$, $y/\delta_0 = 0.45$, in the turbulent boundary layer downstream of the cavity.

More important is the fact that there is no trace of the large peak of u'_{rms}/u_e observed in the mid span section of the cavity in figure 3.18. This would suggest an important observation, i.e. that a weak interaction between the 3D modulation of the internal cavity flow with the wall-flow developing downstream of the cell. In fact, the latter flow is much more affected by the shear layer flow featuring a Kelvin-Helmoltz instability, which is a two-dimensional instability, (Brès and Colonius [2008]). From this perspective, it is not surprising to observe a good two-dimensional flow downstream of the cavity.

3.3 Results for CASE2

CASE2 is a high-Reynolds number flow condition characterized by a thick turbulent incoming boundary layer. This condition is relevant for a number of reasons. First, the shear layer developing from a thick boundary layer does not develop large coherent fluctuations, and thus a different result concerning the upstream/downstream boundary layer properties is expected, since the mechanism governing the shear layer evolution is different. This condition has also practical significance dye to the fact that the TVC technique is devised to control separation of high-Reynolds-number flows, with turbulent boundary layers. This is also supported by the fact that the "moving wall" effect may be more effective in turbulent boundary layer conditions due to the higher skin friction coefficient. Further, it serves as a comparison with the results of a LES performed by Hokpunna and Manhart [2007] on this very configuration

Upstream conditions For CASE2 the reference freestream velocity is equal to 12.4 m/s, and the Reynolds number based on the cavity opening length is thus $Re_L = 5.6 \cdot 10^4$. The Reynolds number based on the cavity diameter Re_D is instead equal to $9.40 \cdot 10^4$. The boundary layer suction system is not activated, in order to achieve the largest thickness of the incoming boundary layer. The resulting boundary layer mean velocity profile, measured at a reference location 10 mm upstream of the cavity cusp, is shown in figure 3.21-(a). On its left, figure 3.21-(b), the profile of u'_{rms}/u_e is also reported. The mean velocity boundary layer profile is estimated to have

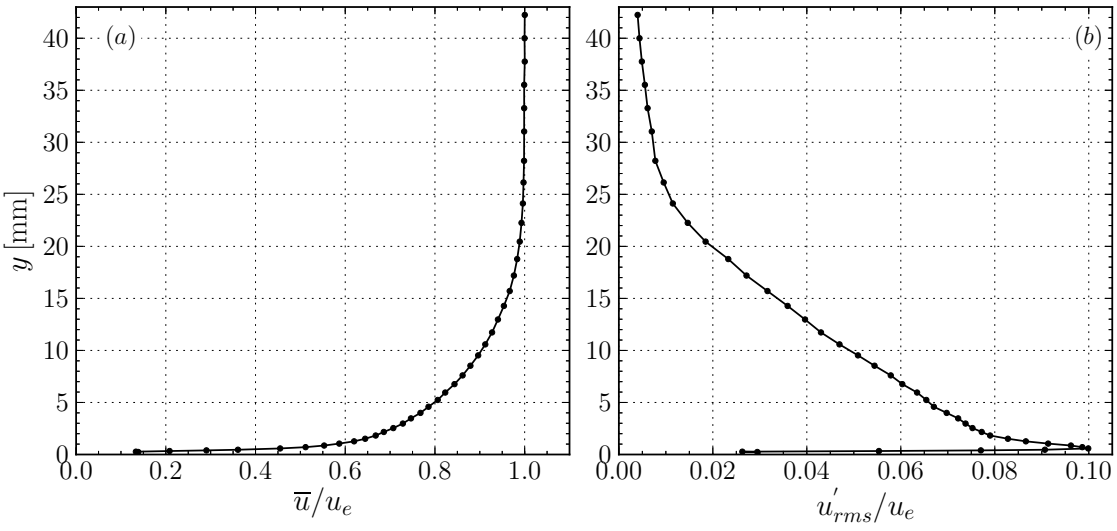

Figure 3.21. Profiles of $\overline{u}/u_e$, (a), and of u'_{rms}/u_e, (b), for the upstream boundary layer at $x = -10$ mm for CASE2.

a 99% thickness δ_0 of about 22 mm, a momentum thickness $\theta_0 = 2.0$ mm, and a displacement thickness δ_0^* equal to 2.8 mm. With these values, the ratio L/θ is equal to 34, thus below the threshold above which initiation of shear-layer self-sustained oscillations occurs, Sarohia [1975], Gharib and Roshko [1987]. The ratio δ_0/D is equal to 0.19. An estimated value of the local skin friction coefficient, using Clauser method is $C_f = 3.95 \cdot 10^{-3}$.

The values of these parameters are as close as the experimental setup allowed to those of the LES simulations performed by Hokpunna and Manhart [2007]. In their work, the cavity Reynolds number Re_D is equal to $9.6 \cdot 10^4$ and the ratio δ_0/D is equal to 0.25, thus the boundary layer in their numerical setup is slightly thicker.

3.3.1 Shear layer evolution

Figure 3.22 shows mean velocity profiles at several streamwise locations along the shear layer. For clarity one each three of the velocity profiles which have measured is reported. For each profile, two vertical dashed lines indicate marks for $u = 0$ and for $u = u_e$.

In the first mean velocity profile, at $x/L = 0$, the signature of the cavity cusp is clearly evident, dividing the outer boundary layer from the internal cavity flow. This first profile indicates that the value of the velocity associated to the outer region of the vortex flow is about 0.22 u_e and thus the flow rotates faster in CASE2 than in CASE1. Furthermore, the mean velocity profile in the cavity indicates the presence of a boundary layer flowing over the cavity surface in clockwise direction. Interestingly, the outermost layers of fluid in the cavity have a velocity close to that obtained by Hokpunna and Manhart [2007] by LES simulations in a very similar configuration, at the corresponding locations.

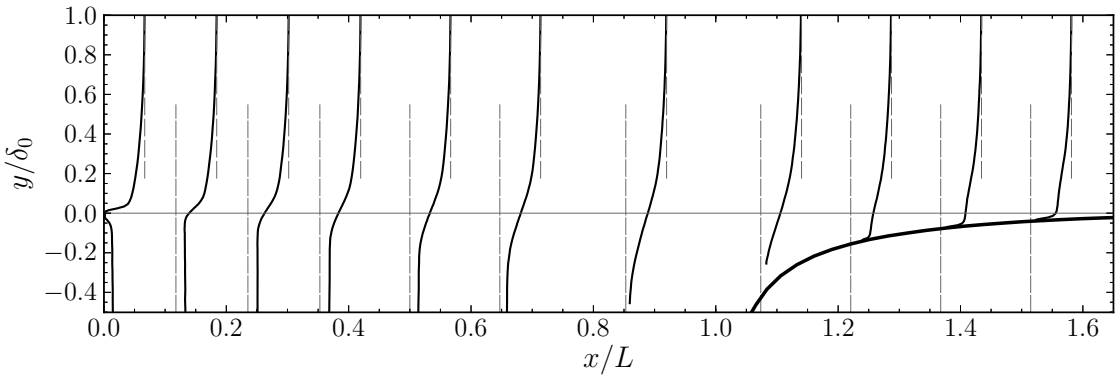

Figure 3.22. Profiles of $\overline{u}/u_e$ at several spatial locations along the shear layer. One each three velocity profiles is shown for clarity. The downstream cavity shoulder is also visible on the right.

The velocity deficit associated with the cusp is quickly eroded and the thickness of the turbulent shear layer increases quickly due to the high mixing operated by the turbulent fluctuations, spreading towards the interior of the cavity. This essentially indicates a momentum transfer from the external high momentum fluid to the cavity flow operated by the turbulent stresses $-\rho\overline{u'v'}$. This momentum transfer is larger than in the previous case, CASE1, where the momentum transfer in the shear layer was operated by the viscous stress due to the term $\mu\partial u/\partial y$. As a consequence, the vortex rotates faster, as evidenced by the higher value of the velocity in the cavity region.

When the flow reattaches, somewhere between $x/L = 1$ and 1.2, the mean velocity profile is characterized by a significant velocity deficit. This can be attributed to the highly dissipative evolution history of the shear layer, and thus the resulting wall-flow downstream of the cavity is not more energetic than the upstream one as will be shown later.

Figure 3.23 shows the profiles of the normalised root-mean-square value of the turbulent velocity fluctuations u'_{rms}/u_e, at the same streamwise location as in figure 3.22. For each profile, the dashed vertical line sets the zero value, while the small vertical segment marks the value $u'_{rms}/u_e = 0.1$. The upper part of the profile

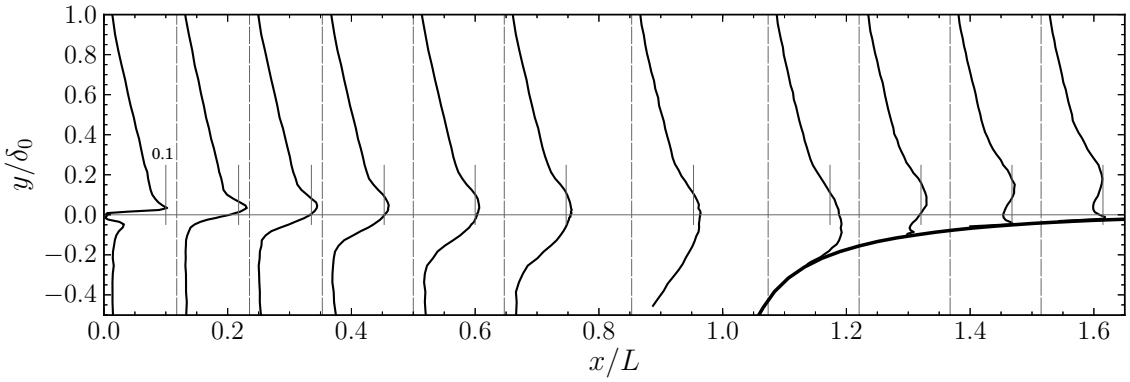

Figure 3.23. Profiles of u'_{rms}/u_e at several spatial locations along the shear layer. One each three velocity profiles is shown for clarity. The downstream cavity shoulder is also visible on the right.

measured at $x/L = 0$ is the same as that of figure 3.21-(b), with the characteristic peak of fluctuation of the buffer region of the incoming boundary layer. The lower part, $y/\delta_0 < 0$, of the same profile shows a weak peak of fluctuations and confirms the presence of a weak turbulent boundary layer flowing on the cavity surface, emerging from the cusp and merging with the outer flow. This first region of the shear layer is characterized by very intense intermittent velocity fluctuations, with a flatness of the order of 40 and a positive skewness of the order of 4. In fact, this region of the

flow is characterized by large velocity gradients with the associated large values of turbulent kinetic energy production.

The cavity flow is characterized by quite low values of turbulence activity, with values of $'_{rms}/u_e$ of the order of 0.015 in the region $-0.5 < y/\delta_0 < -0.1$, and for $x/L < 0.4$. These values are slightly lower than what observed by Hokpunna and Manhart [2007], despite the better agreement concerning the mean velocities in the same region.

As the shear layer evolves downstream the peak value of u'_{rms}/u_e remains essentially unchanged from the initial value of about $0.12u_e$, but a significant large spreading of the high fluctuation area is observed upwards, but more prominently downwards, toward the cavity interior, as also the position of the peak of u'_{rms}/u_e moves slightly in this direction. Larger intensities of fluctuations, but only larger by a 20 to 30% than that of the peak in the upstream boundary layer, are observed near the impingement region, an index of the large unsteadiness developing in the region of the flow.

As the shear layer reattaches on the cavity shoulder, the peak of high turbulent fluctuations lifts up and remains detached from the wall, at a distance of about $0.25\delta_0$. Interestingly, this area is the same associated to the velocity deficit observed in the corresponding profiles of $\overline{u}/u_e$ in figure 3.22. Furthermore, a narrow peak of u'_{rms}/u_e appears near the wall for the last three profiles, which can be associated to the buffer region of the turbulent wall-flow.

The rate of spreading of the turbulent shear layer for CASE2 is presented in figure 3.24, where the evolution of the shear layer vorticity thickness δ_ω is plotted against the streamwise coordinate x/L. The vorticity thickness increases much more quickly than in CASE1, mainly because of the very large velocity gradients that characterise the shear layer in the first region of the shear layer. The vorticity thickness increases with an initial slope $\mathrm{d}\delta_\omega/\mathrm{d}x$ of about 0.41, but the slope of the curve slightly decreases as the shear layer evolves downstream.

3.3.2 Upstream/downstream boundary layer comparison

Figure 3.25 presents a comparison of the boundary layer profiles between the reference upstream and downstream locations. Part (a) of the figure shows the mean velocity profiles, while part (b) shows the profiles of the root-mean-square value of the velocity fluctuations. This comparison in crucial since it is a direct indication of the effects of the cell on the boundary layer flow. The mean velocity profile downstream of the cell, at $x/L = 2.05$, clearly shows a velocity deficit from $y < 2$ mm up high up to the outer layers, with a major depression at around $y = 7$ mm. The velocity deficit is associated to a loss of momentum in the region of the flow separating the two x locations and can be attributed to a transfer of momentum towards the vortical flow in the cavity which then serves to sustain its the rotation

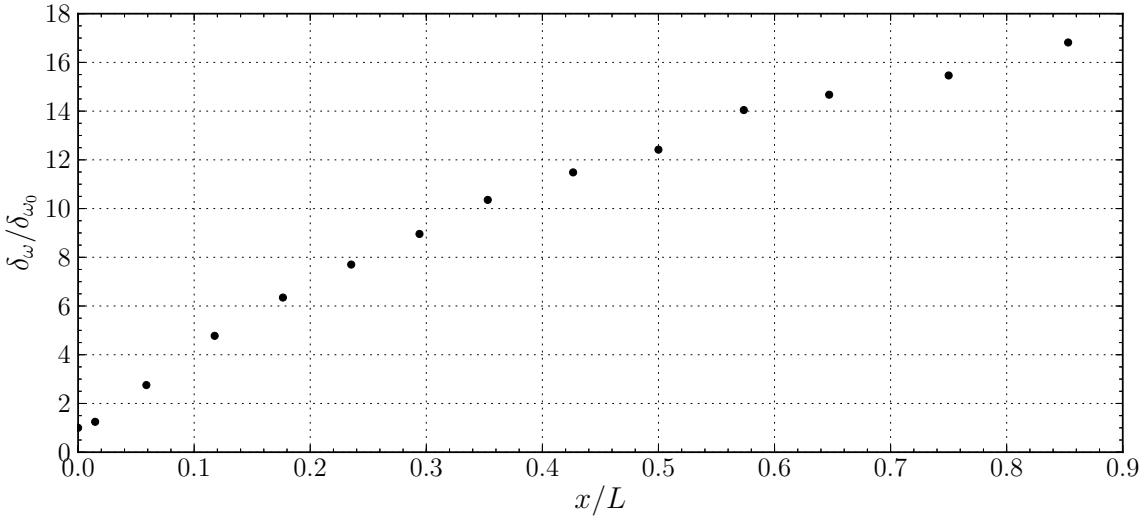

Figure 3.24. Evolution of the shear layer vorticity thickness along the streamwise direction.

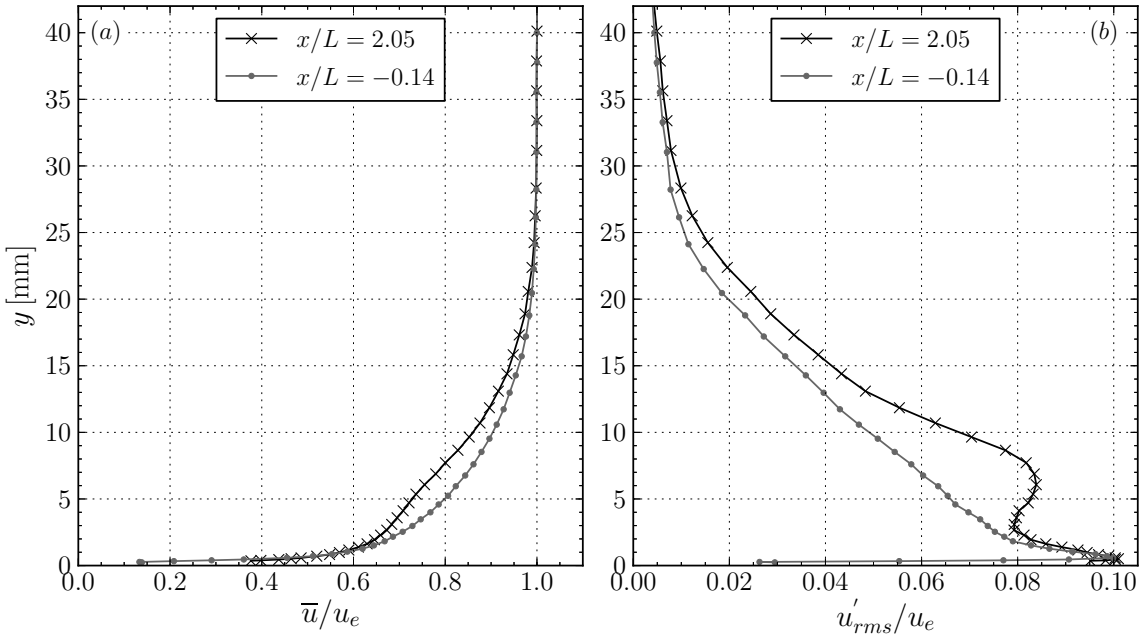

Figure 3.25. Comparison of the upstream $x/L = -0.14$, and downstream, $x/L = 2.05$, boundary layer mean velocity profiles, (a), and of the profiles of the root-mean-square value of the velocity fluctuation, (b)

against the wall shear stress along the cavity wall.

As a consequence of this loss, the momentum thickness of the boundary layer varies from 2.05 mm, upstream location, to 2.53 mm, downstream of the cavity,

accounting for an increase of about 25%. The increase is lower than what observed in CASE1, where θ increased by as much as 100%. In fact, in the previous case, the strong increase was due essentially to the laminar boundary layer becoming turbulent, as a consequence of the break up of the coherent oscillations of the shear layer. Thus, also for CASE2, the boundary layer flowing past the cavity is not energised by the presence of the cell, but it is true the opposite, i.e. it is weakened.

To be fair, the profile downstream of the cavity should not be compared to the profile upstream, but it should be compared with an hypothetical velocity profile at the same location, $x/L = 2.05$, with the cavity replaced by a flat solid plate. In this case the increase of θ can be estimated using the boundary layer integral equation. It holds that:

$$\frac{\mathrm{d}\theta}{\mathrm{d}x} = \frac{C_f}{2}. \tag{3.5}$$

With the conservative assumption that C_f is constant from $x/L = -0.14$ to $x/L = 2.05$ and it is equal to the value estimated at the first section, i.e. $C_{f_0} = 3.95 \cdot 10^{-3}$, we get that:

$$\Delta\theta = \Delta x \frac{C_{f_0}}{2} = (2.05 + 0.14)0.068 * 3.95 \cdot 10^{-3}/2 = 0.294 \text{ mm} \tag{3.6}$$

Therefore, the measured value of θ downstream of the cavity, $\theta = 2.53$ mm, should be compared with $\theta_0 + \Delta\theta = 2.34$ mm. In spite of the fact that the natural increase of θ is taken into account, the result is still unfavourable. Note that for CASE1, where C_{f_0} is very low, this additional increase is practically below the uncertainty in the evaluation of θ and has not been discussed. Crucially, these results indicate that the dissipation of energy along the walls of the cell and in the cell itself is larger than the loss of energy due to skin friction along a solid flat wall.

The comparison of the profiles of figure 3.25 provides insight into the origin of the deficit in the mean velocity profile downstream of the cavity. In fact, the velocity depression is associated to a significant large region of high turbulence levels, extending from $y = 3$ mm high up to the outer flow, peaking at around $y = 7$ mm. By observation of the profiles in figure 3.23, this region can be associated to the highly turbulent flow developing in the central part of the shear layer, which first move towards the interior of the cavity, for $x/L < 1.0$ and which is then lifted upwards after the impingement on the cavity shoulder. Although not shown here for the sake of brevity, spectral analyses indicate that the increase of u'_{rms}/u_e at a distance from the wall of about 7 mm is broadband in nature, with larger energies across the entire spectrum. More details regarding the spectral analysis of the velocity fluctuations are given in the next section.

3.3.3 Spectral analysis

Figure 3.26 shows the power spectral density of the normalised velocity fluctuations at several control points. The points chosen are: A in the middle of the shear layer region, at $x/L = 0.5$ and at a $y/\delta = 0$, point B located inside the cavity at $y/\delta = -0.68$ at the same streamwise coordinate as for point A and point C, which is located at $x/L = 2.05$ and $y = 2$ mm, very close to the wall and below the region of the velocity defect, (see figure 3.25-(b) for reference).

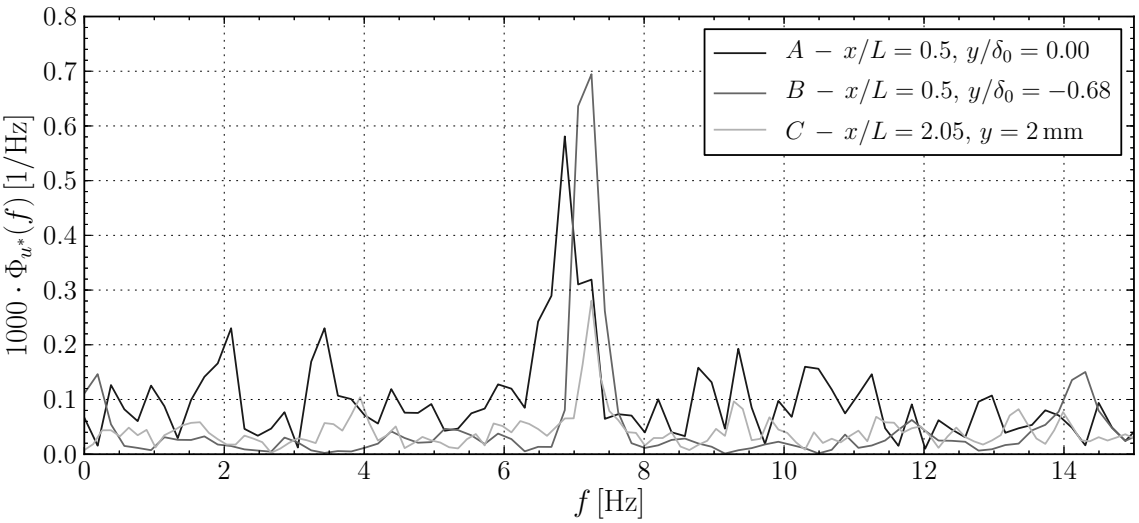

Figure 3.26. Power spectral density of the normalised velocity fluctuations $u^* = u/u_e$ at three control points.

The spectra are reported in a linear-linear scale and only the low frequency range is shown in order to better highlight its most significant feature. Even though the frequency resolution is limited, the spectrum at the three points is characterized by a clear peak at a very low frequency, of the order of 7 Hz. The peak is higher for point B, located inside the cavity, and slightly weaker for the point in the shear layer. For point C, located further downstream in the boundary layer the weak signature of the same phenomenon can still be observed.

It has to be remarked that this peak is the only significant feature of a spectrum which is otherwise characteristics of a turbulent flow. Furthermore, the turbulent shear layer is certainly not subject to self-sustained oscillations, (due to the relatively high thickness of the incoming boundary layer), which would in any case develop at much larger frequency than 7 Hz. It is thus anticipated, and it will be supported by stronger evidence in a later stage, that the observed peak is associated to a large scale unsteadiness of the recirculating cavity flow. Evidence of such low frequency motions in cavity flows, mostly for rectangular configurations, is abundant in the literature, e.g. Brès and Colonius [2008], Savelsberg and Castro [2008], and the usual

interpretation is to associate this oscillation as the result of a spanwise instability of the vortex core, Brès and Colonius [2008].

Interestingly, if this interpretation holds true, the weak peak observed for point C suggests that the vortex instability can affect the wall-bounded flow developing downstream. However, examination of the velocity spectra at a varying distance from the wall suggest that from $y = 4$ mm upwards the signature of the low-frequency modulation cannot be detected anymore, and is certainly not visible in the velocity defect region of the downstream boundary layer.

In the time domain, a typical time series of the velocity in the cavity at point B appears as in figure 3.27. The time trace is characterized by an alternating sequence of wide and narrow velocity valleys, separated by a period of about 0.13 s, approximately $(7Hz)^{-1}$, i.e. the inverse of the peak frequency. The total amplitude

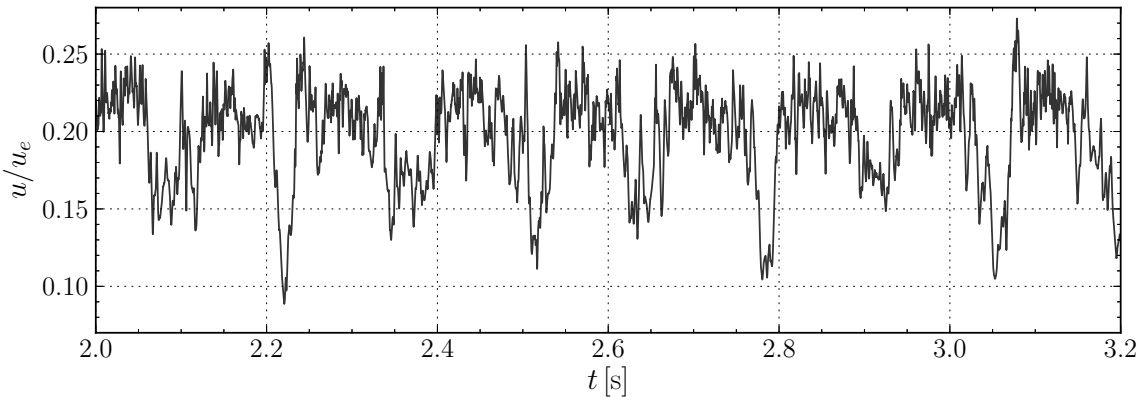

Figure 3.27. Example of velocity time history at control point B, located inside the cavity at $x/L = 0.58$, $y/\delta_0 = -0.68$.

associated to this oscillation is of the order of $(0.25 - 0.10)u_e = 0.15u_e$, which may appear weak if compared to the velocity of the outer flow. However, the mean value of the velocity inside the cavity at point B is equal to $0.19u_e$, and thus the oscillatory phenomenon is very significant for the dynamics of the inner flow.

To complement this analysis, pressure fluctuation spectra are shown in figure 3.28, for three representative microphones. These are microphone $m7$, located under the cusp, microphone $m8$, located in the impingement region, and microphone $m3$, located far downstream of the cavity, (see figure 2.9). On each subplot, the gray curve is the velocity spectrum at $x/L = 0.58$, $y/\delta_0 = -1.1$, reported for comparison over a fictitious vertical scale. We observe a significantly larger amount of integral energy for microphone $m8$, since the standard deviation of the pressure fluctuation signal is 4.05 Pa, about three time larger then for microphone $m7$, $p'_{7\,rms} = 1.45$ Pa, and microphone $m3$, $p'_{3\,rms} = 1.66$ Pa. Please note that these are conservative measures, since a large fraction of energy for the three signals is concentrated around

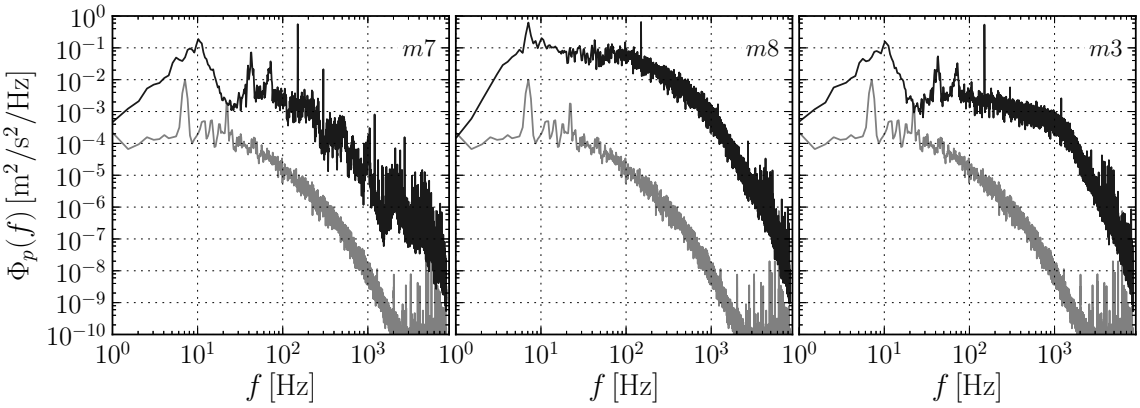

Figure 3.28. Pressure fluctuation spectra for three representative microphones. The grey curve is the velocity spectrum at $x/L = 0.58$, $y/\delta_0 = -1.1$, reported for comparison over an fictitious vertical scale.

$f_{wt} = 150$ Hz, visible in the figures as a sharp peak. What is more, the amplitude of the peak is constant for the three microphones since there is no pressure-velocity coupling enhancing the energy for the microphones inside the cavity, as it was observed in CASE1. Therefore, excluding the energy at this frequency, which is not dynamically significant for the cavity flow, the variance of the pressure fluctuations on microphone $m8$ is even higher in proportion to that of microphone $m7$.

There are two remarkable features which distinguish $m8$ from $m7$. The first is the significantly larger energy over a wide range of frequencies, from $f \approx 50$ Hz above. The reason is that $m8$ is located in a highly turbulent region, where a wide range of small scale turbulent structures from the turbulent shear layer impinge on the wall. By contrast, over this same range of frequencies, microphone $m7$ has a much reduced fluctuation energy and most of the small peaks can be attributed to background noise. The second feature is that $m8$ is characterized by a distinct peak at $f \approx 7$ Hz, which has observed before, is a feature deriving from the dynamics of the vortex flow. Interestingly, this peak is not observed for microphone $m7$, even though some energy is present at that frequency.

It must be noted that the electret microphones used in this research have significant attenuation below 10 Hz, as demonstrated by the drastic decrease of energy below this frequency in the spectra of figure 3.28. Nevertheless microphone $m8$ can still detect the signature at such low frequency.

The spectrum of the pressure signal measured by microphone $m3$ is very similar to that from microphone $m7$ at low-mid frequencies, below 150 Hz. This indicate that the peaks in this range are not due to some relevant dynamics of the flow inside the cavity. By contrast, the spectra of microphone $m3$ has a significantly different behaviour for larger frequencies, since it evidences larger energies at these frequencies, although not as high as for microphone $m8$. This part of the spectrum

is likely due to the pressure fluctuation associated with the turbulent wall flow over this sensor.

Due to the absence of a strong acoustic resonance process, the pressure-velocity coupling is weaker in CASE2. A significant example of this behaviour is given in figure 3.29. This figure shows the y profile at $x/L = 0.58$ of the peak of the correlation

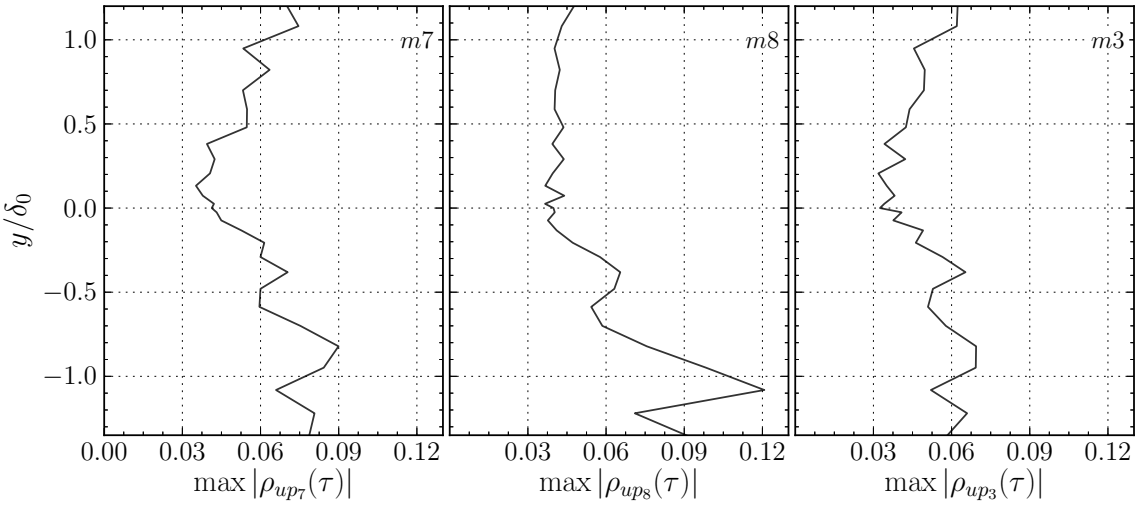

Figure 3.29. Profiles of $\max|\rho_{up_i}(\tau)|$ for microphones $m7$ located under the cusp, $m8$ located in the impingement region, and $m3$, far downstream of the cavity.

coefficient function $\rho_{up_j}(t)$, i.e. the maximum absolute value of correlation between the hot wire velocity measurement and the microphones pressure signal, for three microphones. These are microphone $m7$, located under the cusp, microphone $m8$, located in the impingement region, and microphone $m3$, far downstream the cavity. Please refer to figure 2.9 for the exact position of these microphones. These plots serve as an indication of the level of correlation in the flow between the velocity and the pressure.

For all the microphones, the correlation levels are very weak, i.e. less then 0.1, both in the shear layer region, $-0.2 < y/\delta_0 < 1$, and in the region of the cavity flow. As expected the lowest levels of correlation are observed for microphone $m3$, in reason of its large physical distance with the hot wire probe location, of the order of L, that is by far larger then the largest physical length scale of the flow. For microphone $m7$, located under the cusp, the correlation levels are quite weak, a strong confirmation that there is no self-sustained oscillation of the shear layer flow. Interestingly, the level of correlation remains weak even in the cavity flow region, $y/\delta_0 < 0.2$, despite the fact that due to the flow recirculation, both sensors are subject to the same flow.

The interesting features of the correlation analysis emerge when considering microphone $m8$. We observe the same level of correlation, i.e. $\rho_{up_8} \approx 0.04$ for most

of the height y, but a not negligible peak at around $y/\delta_0 = -1.0$ can be clearly observed, with a value slightly exceeding 0.12. At this height in the cavity flow,

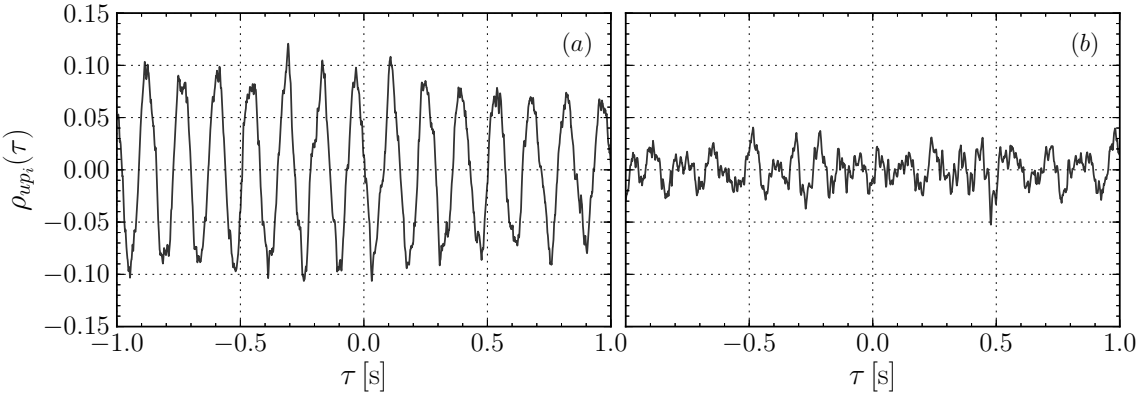

Figure 3.30. Cross-correlation coefficient function $\rho_{up}(\tau)$, where u is the velocity signal inside the cavity region, at $y/\delta_0 = -1.1$, and p is that from microphone $m8$, part (a), or microphone $m7$, part (b).

$y/\delta_0 = -1.1$, the cross-correlation coefficient function $\rho_{up_8}(\tau)$ appears as in figure 3.30-(a). The cross-correlation is clearly periodic and it retains moderately large values over quite a significantly large time scale, of the order of seconds. The periodicity is entirely due to the low-frequency motion of the vortex flow, which will be discussed in depth in the following section dedicated to flow visualisations. By contrast, for microphone $m7$, figure 3.30-(b), there is no clear periodicity as for microphone $m8$, likely because the signature of the low-frequency oscillation is too weak.

This is confirmed by coherence analysis between the velocity and the pressure signals. Figure 3.31 shows the squared coherence function $\gamma^2_{up}(f)$ for microphone $m8$, part (a), and for microphone $m7$, part (b). Despite the poor frequency resolution of the coherence function, (the Welch algorithm for the estimate of γ^2 is used by averaging the spectra from 16 blocks of 2^{14} samples), a clear strong peak is observed for microphone $m8$ at around $f = 7$ Hz, with a significant value of 0.6. On the other hand, for microphone $m7$ the squared coherence function is practically zero at low frequencies, meaning that there is no measurable correlation between the cavity flow and the pressure fluctuations measured by $m7$. The coherence spectrum is not shown for clarity for $f > 400$ Hz, but no statistically relevant peaks are observed for larger frequencies, as expected by the absence of energetic motions at these times scales.

We offer the following explanation for the stronger correlation between the cavity flow, i.e u, and the pressure fluctuations in the impingement region. We argue that the low-frequency oscillation of the cavity flow is by itself very weak and its spectral signature on the pressure fluctuations time history is very feeble, also in reason of

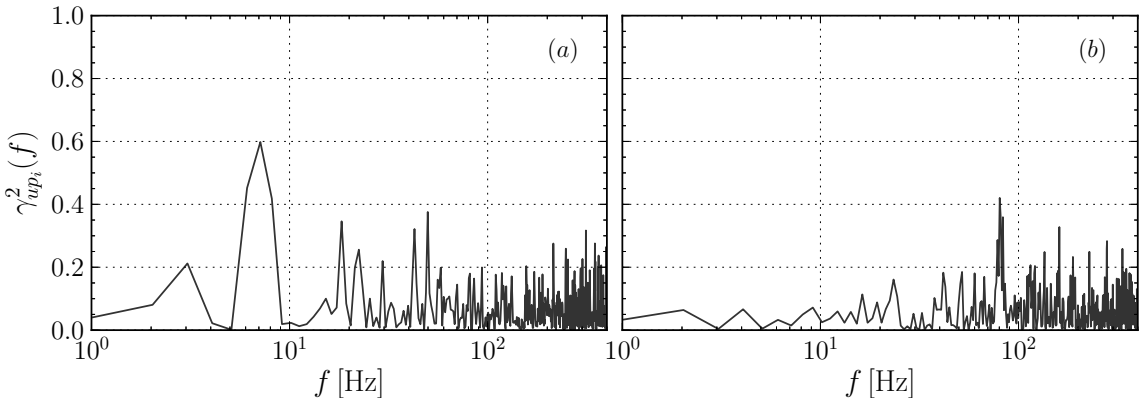

Figure 3.31. Squared coherence function $\gamma^2_{up}(f)$, where u is the velocity signal inside the cavity region, at $x/L = 0.58$, $y/\delta_0 = -1.1$, and p is the pressure measured by microphone $m8$, part (a), or by microphone $m7$, part (b).

the fact that the condenser microphones are "deaf" at such low frequency. Thus, microphone $m7$, located in a low-speed region, cannot measure such phenomenon. However, microphone $m8$ is located in the impingement region, which is subject to the perturbation induced by a much more energetic fluid, i.e. by the shear layer. It is likely that the low-frequency oscillation of the cavity flow induces a low-frequency flapping of the last part of the shear layer. In turn, this produces on the wall a consistent fluctuations of the dynamic pressure on $m8$, with the consequent larger pressure fluctuation.

3.3.4 Flow visualisations

Smoke flow visualisations were performed for CASE2 with the objective of shedding light over the low-frequency modulation observed in the hot wire and pressure fluctuation measurements. In figure 3.32 a sequence of eight snapshots of the cavity flow is shown. The snapshots were sampled at a frequency of 125 Hz, but in the figure one each three snapshots is reported, in order to capture almost one complete cycle. The images are slightly blurred due to the relatively high exposure time. However, it was not possible to decrease it further, since the images would have been too underexposed, hiding much of the features of the flow. As for CASE1, the images are post-processed by subtraction of the mean image and by black/white equalisation, to highlight the salient features.

By careful inspection of the entire animated sequence of snapshots, a counterclockwise motion of the vortex core is observed. Indeed, the vortex centre moves in a circular motion around the geometric centre of the cavity in a direction *opposite* to that of the flow. The sequence of snapshots clearly evidences this motion, as well as the total radial displacement of the vortex centre, which is estimated to be as

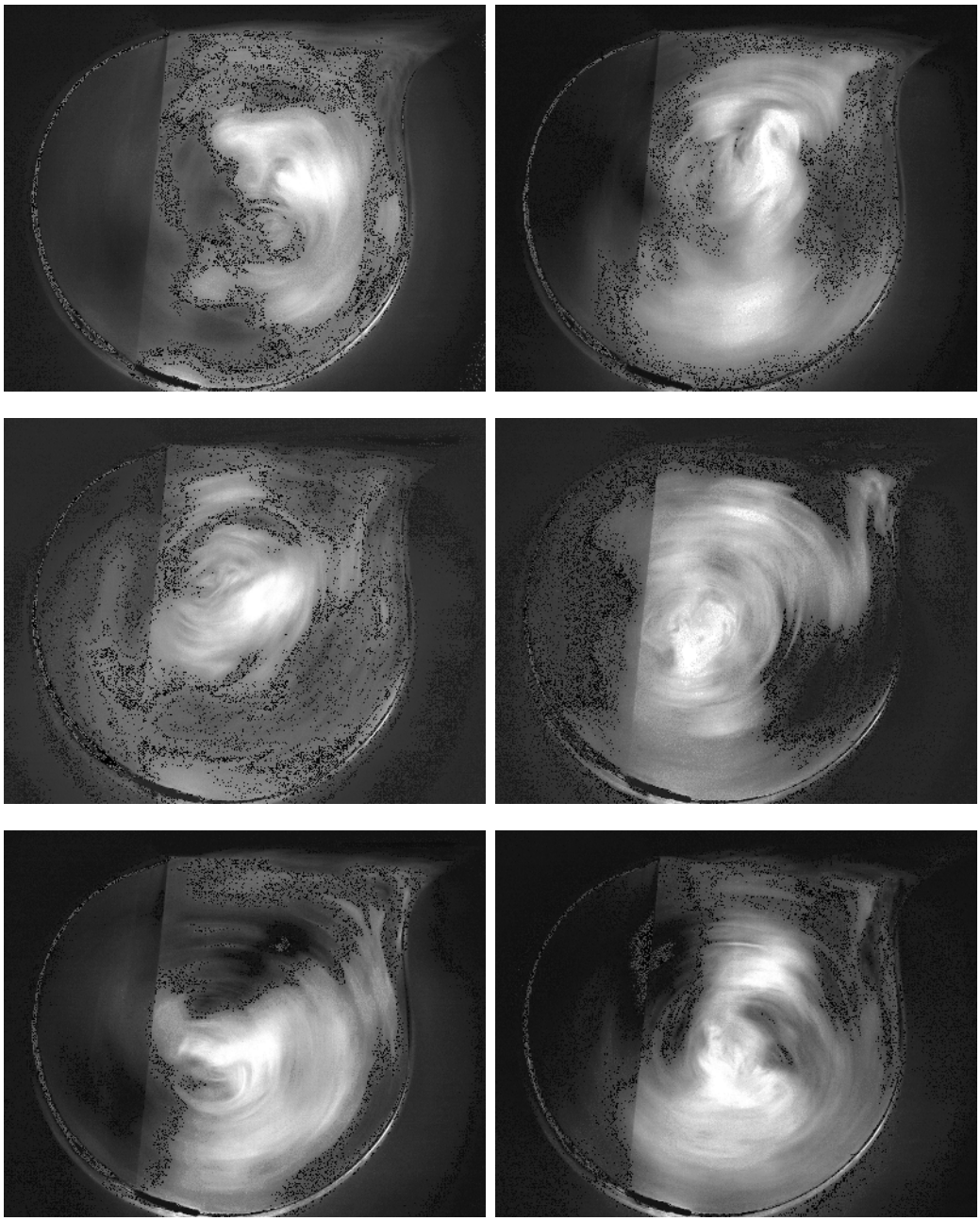

Figure 3.32. Snapshot sequence for CASE2, sorted left to right, top to bottom. Time interval between successive frames is 3/125 s. One of each three snapshots in shown, to complete almost a full revolution of the vortex core.

high as half of the cavity size D.

This large scale motion is responsible of the oscillatory features of the velocity

time trace in figure 3.27. In fact, it is likely that the valleys in the velocity time history are due to the low-speed vortex core passing over the hot wire probe. In fact, an average of about 18 frames, sampled at 125 Hz, is required to completed one oscillation cycle. However, an explanation for the presence of two "types" of valleys, one narrow and intense, the other larger but weaker, is not available at the moment, and the flow visualisation are not helpful in this regard.

Further interesting features of the flow regime in CASE2 can be identified. One of these regards the injection of fresh, high-energy fluid packets from the impingement region downwards into the cavity. A similar feature was observed for CASE1 too, and therefore it is argued to be a characteristic feature of the TVC flow, probably connected to the roundness of the downstream cavity shoulder. As these packets enter into the cavity they help driving the rotation of the vortex core, but the extent by which this phenomenon couples to or even drives the low-frequency oscillation of the vortex core is not known and deserves further explanation.

In the previous section it was conjectured that the higher level of pressure fluctuations on $m8$ at the low frequency of the vortex flow motion was due to a weak flapping of the last portion of the shear layer. Evidence of such phenomenon can indeed be observed in the animated sequence of snapshots, but it is very weak and the above argument should be further investigated.

3.3.5 Three dimensional structure of the flow

Figure 3.33 shows spanwise profiles of the mean velocity $\overline{u}/u_e$, part (a), and of the root-mean-square value of the velocity fluctuations u'_{rms}/u_e, part (b), measured in the interior of the cavity region, at $x/L = 0.58$ and $y/\delta_0 = -1.36$. The spanwise coordinate is made non-dimensional by (b), the cavity width. This depth is higher then the thickness of the turbulent shear layer and, therefore, these profile are representative of the structure of the internal cavity flow. The mean velocity profile, figure 3.33-(a), is characterized by a distinct periodic pattern which affects the whole cavity, but which is significantly enhanced at the two ends of the cavity. The total amplitude of the mean velocity oscillation is very small, of the order of $0.015u_e$. However, when compared to the spatial spanwise average it accounts for as much as 15%. The spanwise wavelength λ_p of this pattern can be estimate only roughly, but a value of $\lambda_p/b \approx 0.2$ seems reasonable. This value corresponds to a non-dimensional wavelength based on the cavity diameter equal to $\lambda_p/D = 0.75$.

By examining part (b) of the figure, the profile of $u'_{rms}(z/b)$ clearly evidences the same peculiar pattern, mostly in the two extreme thirds of the cavity span, for $z/b > 0.2$ and for $z/b < -0.2$. The pattern consist of an alternation of regions of high and low value of u'_{rms}/u_e, with a peak-to-peak variation of the order of $0.02u_e$. This pattern is broken in the central part of the cavity, where the value is essentially the same as for the peak in the lateral region.

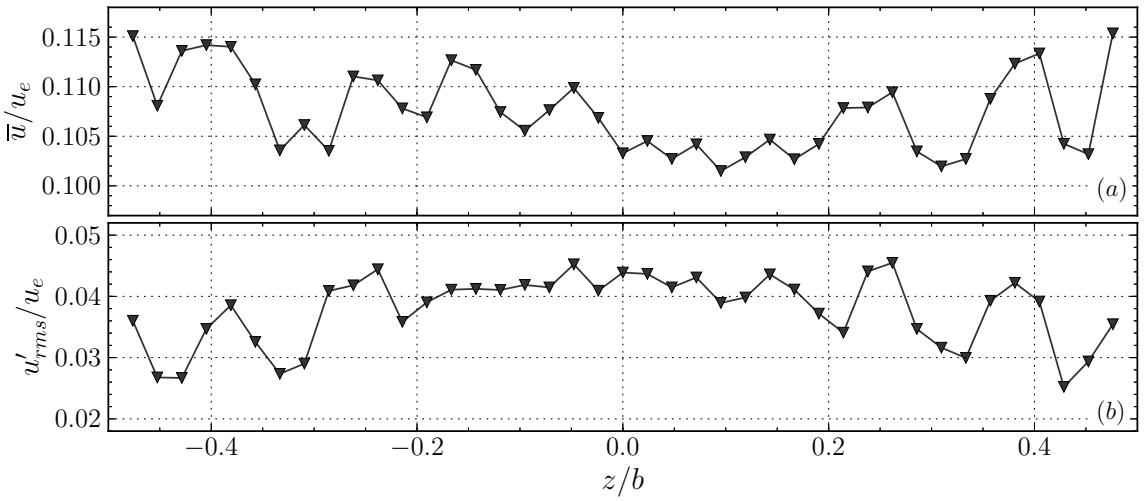

Figure 3.33. Spanwise profiles in the cavity region at $x/L = 0.58$, $y/\delta_0 = -1.36$. Mean velocity, (a), and root-mean-square value of the velocity fluctuations, (b).

Some insight into the origin of this spanwise pattern can be gained by considering the spectra of the velocity signal. These are shown in figure 3.34, for two spanwise locations, $z/b = 0.0$ and $z/b = 0.43$, the position where u'_{rms}/u_e is minimum. By

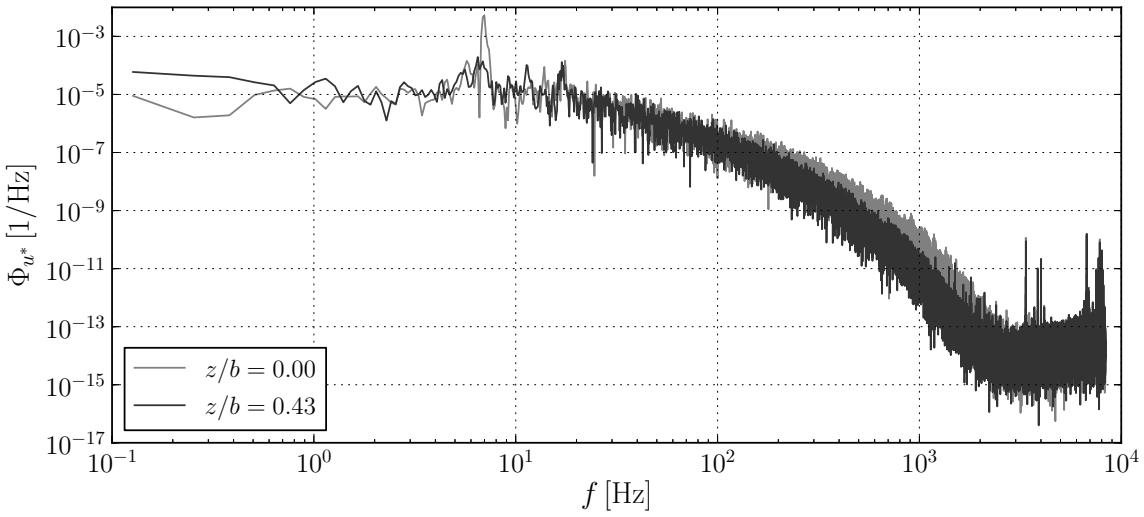

Figure 3.34. Power spectral densities of the velocity fluctuations in the mid-span, $z/b = 0.0$ lighter line, and at $z/b = 0.43$, darker line, where u'_{rms}/u_e is minimum.

observation of the two spectra, it is clear that the difference in total energy between the velocity signals at the two control locations is essentially due to the low-frequency oscillation of the vortex flow. In fact, at the lateral position the peak is at least one decade less intense then in the mid span. Further difference are observed at higher

frequencies, $100 < f < 2000$ Hz, but due to the logarithmic scale, they are less significant on the total variance of the signals. However, this last feature seems also to suggest a slightly different structure of the turbulence in the two control positions. This result seems to suggest that the spanwise modulation of u'_{rms}/u_e is associated to a modulation of the oscillatory motion of the cavity flow. Indeed, Tutty et al. [2012] observed and detailed in depth similar features.

3.4 Remarks and discussion

The main result of the investigation of the physics of the uncontrolled flow in the TVC is that in both cases investigated the presence of the cell is detrimental for the boundary layer flowing past it, which increases its momentum thickness more than it would occur without the presence of the cavity, in a solid wall case. This important result indicates that the TVC in passive conditions is not an effective control device to prevent/delay separation on a full airfoil, as has been demonstrated in other studies. The physical explanation for the ineffectiveness resides in an unfavourable evolution of the shear layer even though the mechanisms are different in the two cases.

For CASE1 the increase in momentum thickness is quite significant. In this case, the laminar boundary layer detaching from the cusp is subject to the Kelvin-Helmoltz instability. The velocity fluctuations in the upstream boundary layer, forced by the wind tunnel resonance condition, undergo a very strong amplification. The break-up of the large coherent structures in the shear layer then results in a thick turbulent boundary layer developing downstream. This behaviour stresses on the point that shear layer self-sustained oscillations, whether natural of forced, are detrimental, since they provide a powerful mechanism to extract energy from the external flow, ultimately dissipated in the turbulent boundary layer downstream. This observation indicates that probably one necessary condition for the TVC to be an effective control technique is the absence or the successful control of this phenomenon.

A very straightforward passive technique to prevent oscillations would be to design the cavity such that the ratio L/θ is small enough to prevent the formation of oscillations of the shear layer as in CASE2, where the thick incoming boundary layer does not develop self-sustained oscillations. As a result, the increase of the momentum thickness past the cavity is not as large as for CASE1, but it is nevertheless positive and larger than what would be observed in the case of solid wall, meaning that the cell is not effective, even without self-sustained oscillations. As suggested by flow visualisations, a great energy loss occurs in the region of the shear layer impingement, which is a highly turbulent area. It is argued that alternative shapes of this region should be considered, in order to obtain a more regular flow.

For example, a sharp downstream edge may eliminate completely the stagnation region, and would "separate" smoothly the internal and the external flows.

Finally, it is worth pointing out that CASE2 was characterized by a low frequency motion of the entire vortex flow in the cell, even though no clear evidence of its relevance in the effectiveness of the cell as a control device has been noted in the experiments.

Chapter 4

Control of the TVC flow by suction

4.1 Preliminary remarks

The first control technique investigated consist in suction of the flow in the cell. The motivation for using this technique is that it is a well-known classical control strategy, especially for boundary layer control, and a large body of research exists on this topic. In addition, suction of the flow was also investigated as a control strategy in wind tunnel experiments performed by Lasagna et al. [2011] on the complete TVC controlled airfoil, and by De Gregorio and Fraioli [2008] on a simplified configuration described in chapter 1. These authors showed that manipulation of the cavity flow by suction has large influence on the effectiveness of the TVC as a control device. Thus, one of the objectives of this investigation is to gain a better understanding of how suction modifies the uncontrolled flow. This additional insight is required to understand how a TVC controlled by suction can be an effective control device.

Significant efforts of this part of the research were dedicated to understand how the control influences the evolution and the behaviour of the shear layer, recognised in the previous chapter as one of the key elements of the TVC control technique in passive conditions. In fact, it is argued that a robust control of the flow must target the shear layer, to obtain an effective TVC control device. This chapter presents specific analysis and measurements of the flow in order to address this issue.

As discussed in section 2, the experimental setup allowed the application of suction in two different regions, as depicted in figure 4.1. One area, denoted by the letter A, was the upstream interior region of the cavity, the other, denoted by B, was located on the downstream edge of the cavity. This choice was motivated by the following considerations. Area A was chosen such as to control the cavity flow, which especially in CASE2, was characterized by a low-frequency oscillation

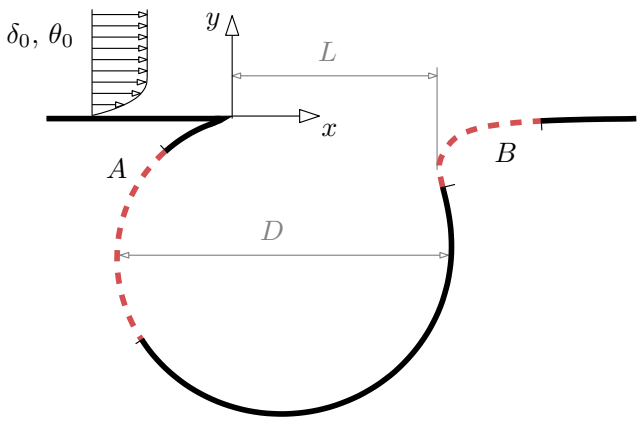

Figure 4.1. Sketch of the cavity geometry showing the two regions where suction was separately applied.

of the vortex core. The rationale is that control of this phenomenon, i.e. reduction of the associated large scale fluctuations may result in a lower dissipation of energy along the shear layer evolution. On the other hand, the choice of area B was based on the idea of controlling the flow in the impingement region, which both flow visualisations and hot-wire measurements indicated as a region of intense turbulent fluctuations. Furthermore, it is argued that suction in this region could help in reducing the erratic injection of high energy packets of fluids in the cavity, a key mechanism, driving the rotation of the cavity flow, revealed by flow visualisations on both CASE1 and CASE2. Result concerning the former condition will be presented first and in more depth, followed by a briefer discussion of the results of control by suction in region B, highlighting the main differences.

In the following sections, the intensity of the suction will be often characterized by the suction parameter S, defined as:

$$S = \frac{Q}{bLu_e} \tag{4.1}$$

where Q is the volumetric flow rate, b is the cavity span, L its opening and u_e is the external flow speed. This parameter represents the volumetric flow rate as a fraction of the volumetric flow rate associated with the plant area of the cavity and to the external flow speed.

4.2 Control for CASE1

To quickly investigate the effects of the suction rate on the flow downstream of the cavity, to assess the effectiveness of the control on the gloabl performance of the

TVC, the hot wire probe was positioned at a reference location at $x/L = 2.05$ and $y/\delta_0 = 0.22$. This distance from the wall is the point in the downstream boundary layer showing the near-wall peak of u'_{rms}/u_e. A special experimental procedure, aiming at reducing acquisition times was adopted to study the effects of varying S on the velocity in the reference point. A simultaneous acquisition of the hot-wire velocity signal and of the instantaneous flow rate, (via acquisition of the fluxmeter transducer), was performed for a sufficiently long time during which the flow rate was slowly varied from zero to its maximum value and down to zero again. Then,

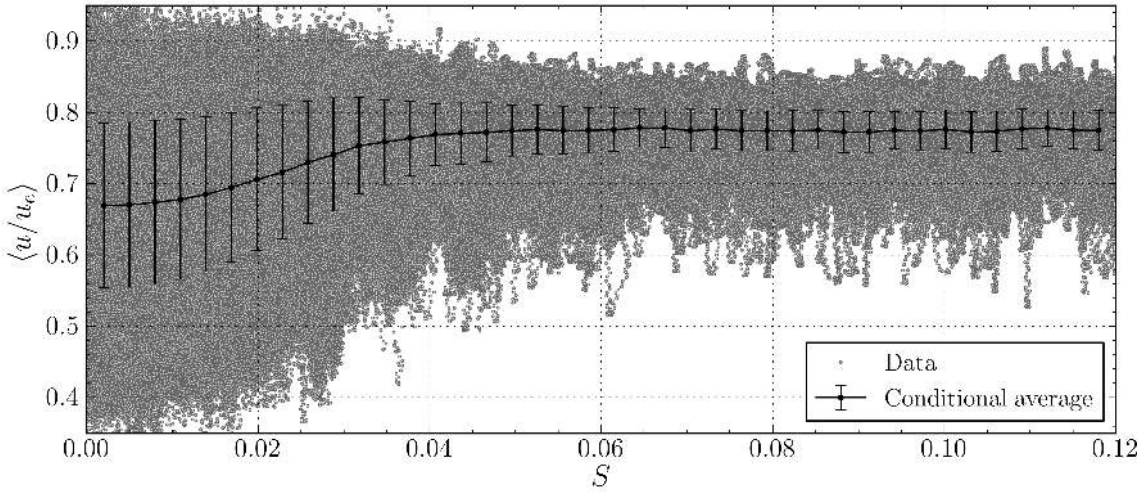

Figure 4.2. Effects of the suction rate on the mean velocity at a control point downstream of the cavity, at $x/L = 2.05$, $y/\delta_0 = 0.23$.

in order to obtain the relationship between the mean velocity in the control point and the suction rate, the conditional average of the velocity

$$\langle u/u_e \rangle = \langle u | S_e - \mathrm{d}S < S < S_e + \mathrm{d}S \rangle \tag{4.2}$$

was computed, where the condition of the average include only those sample for which the flow rate is within a small window around S_e, large $2\mathrm{d}S = 0.005$. Several conditions S_e, spanning the full range of S, were considered. The resulting data is reported in figure 4.2. The gray dots are the measured data, while the black line shows the behaviour of the conditional average. The error bars indicate the value of the conditional standard deviation, i.e. of the quantity:

$$\langle (u/u_e - \langle u/u_e \rangle)^2 \, | S_e - \mathrm{d}S < S < S_e + \mathrm{d}S \rangle \tag{4.3}$$

which is the mean value of the velocity fluctuations when $S = S_e$. No effects of hysteresis, determined by executing other tests with increasing or decreasing suction rate, were observed.

The results in figure 4.2 indicate that as the suction parameter increases, the mean velocity downstream of the cavity increase accordingly, but only up to $S \approx 0.04$, where it reaches a very flat plateau, where the velocity does not change at all, despite a very large further increase of the suction. Obviously, the increase of the suction also implies a large increase of the energy expense. Over this range of S, the velocity has increased moderately, from about $0.67u_e$ to $0.77u_e$.

Several full boundary layer velocity profiles were then measured at the same downstream reference location $x/L = 2.05$, for some significant values of the suction parameter. Some of these profiles are shown in figure 4.3. Part (a) shows profiles of the mean velocity $\overline{u}/u_e$, part (b) shows profiles of the root-mean-square value of the velocity fluctuations u'_{rms}/u_e. These profiles are reported along with the corresponding profiles of the upstream boundary layer, and of the same downstream location in no-control conditions. The red line indicates the distance from the wall of the probe for the results of figure 4.2. Please note that the curves labeled "Upstream"

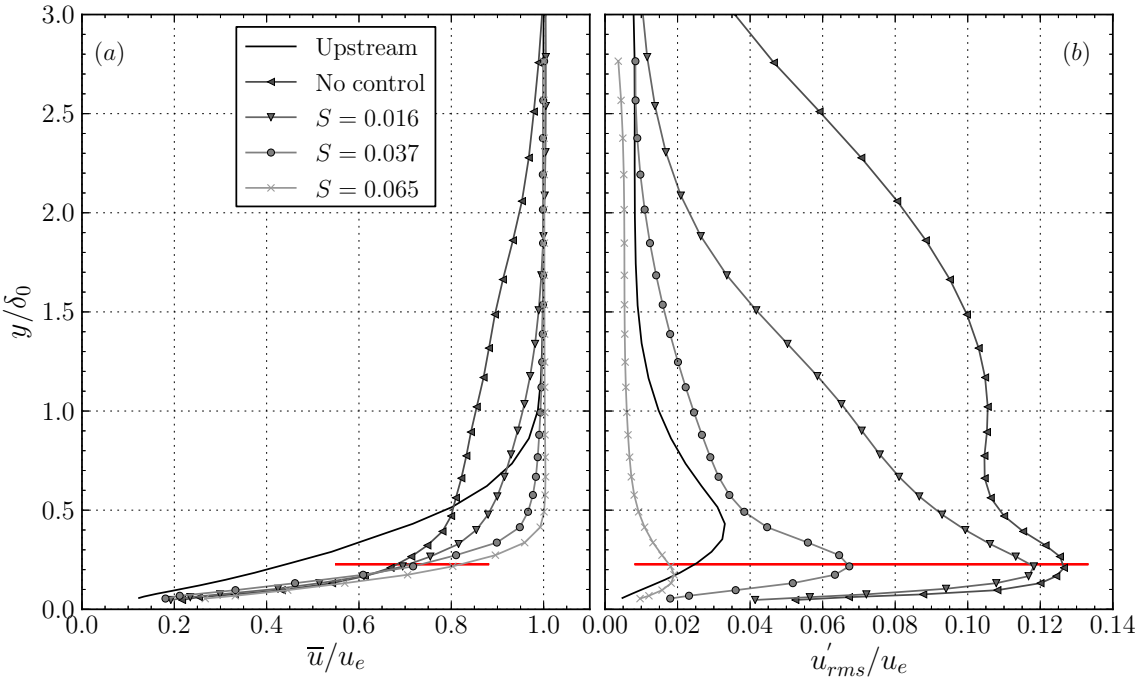

Figure 4.3. Effects of the suction rate on the profiles of mean velocity and of the root-mean-square value of the velocity fluctuations, at $x/L = 2.05$. The upstream case and the no-control case are also reported.

refers to $x/L = -0.14$. Regarding the mean velocity profiles, the effect of the suction is to strongly reduce the height of the turbulent boundary layer downstream of the cavity in no-control conditions by strongly enhancing the mean velocities resulting in a strongly energised flow. Furthermore, as the suction increases the boundary

layer developing past the cavity becomes essentially laminar, as clearly indicated by the strong reduction of the intensity of the velocity fluctuations, in figure 4.3-(b), especially for $S > S^*$. In control conditions, the boundary layer downstream of the cavity is thus more energetic than upstream, which is clearly a beneficial factor for separation control, and a clear demonstration of the effectiveness of suction. Thus, when controlled by suction the TVC can be an effective technique to prevent/delay separation on an airfoil because of the fact that a "fuller" mean velocity boundary layer profile is more resistant to separation.

It is important to point out that, although not reported in the figures for clarity, the boundary layer profiles, both for $\overline{u}/u_e$ and u'_{rms}/u_e, do not change at all when S is increased past S^*.

The profiles of u'_{rms}/u_e, in figure 4.3-(b), show a very remarkable decrease of the turbulent stresses in the boundary layer flow downstream of the cell with respect to the no-control case as the suction is increased. This decrease is observed first at large distances from the wall, and then also in the near-wall region, because the flow has become laminar. Such strong reduction in u'_{rms}/u_e suggests a profound modification of the evolution of the shear layer and a reduction of the amplification of the forced periodic disturbances in the shear layer. This will be better pointed out later. Interestingly, for $S = 0.065$ the level of fluctuations is very low, even lower than that observed in the upstream boundary layer.

To better understand the reason of such a strong action of the control, velocity profiles were measured at several x locations along the shear layer, at a value of the suction rate above S^*, i.e. for $S = 0.1$. Results of this investigation are reported in figure 4.4, which shows selected mean velocity profiles. About one each four velocity profiles is shown for clarity. For each profile, two vertical dashed lines indicates the

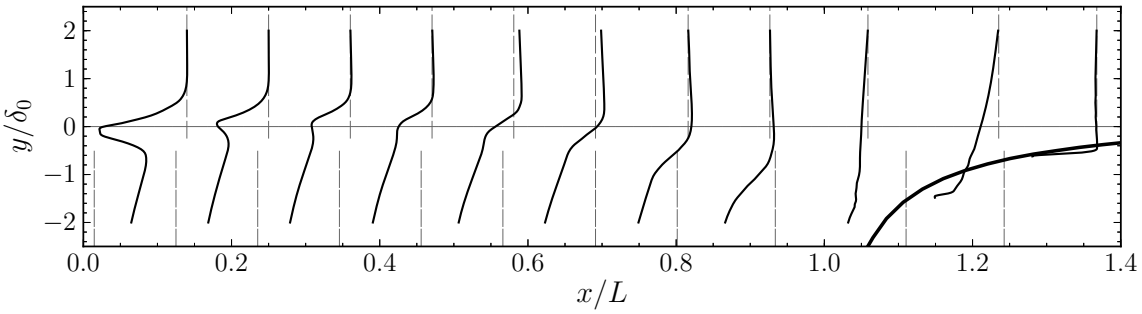

Figure 4.4. Selected mean velocity profiles $\overline{u}(y)/u_e$ along the shear layer. Approximately one each four profiles is shown, for clarity. The downstream edge of the cavity is also visible. Flow is from left to right.

value of $\overline{u}/u_e = 0$ and 1. Furthermore, the mark for $\overline{u} = 0$ indicates the location of the profile. The first mean velocity profile clearly indicates that the flow in the cavity is rotating strongly, with maximum velocities in the region of the order of

$0.5u_e$. This mean velocity profile clearly shows for $y/\delta_0 < 0$ the signature of the boundary layer flow developing along the cavity wall, after the region A of suction. An approximate thickness of this layer is $y/\delta_0 = 0.6$.

As the shear layer evolves downstream, the velocity deficit associated to the upper and lower boundary layers is eroded. A strong indication of the mechanism at play is given by observation of the last three velocity profiles before $x/L = 1.0$, i.e those at $x/L = 0.68,\ 0.80$ and at 0.94. In this region, the shear layer, indicated by the region of stronger velocity gradient, shows a marked displacement downwards into the cavity. This indicates that the entire flow is being deviated downwards by the action of the suction.

As a result, the shear layer flow does not impinges anymore on the downstream edge of the cavity but it is ingested inside the cavity. This must follow by simple mass conservation of the cavity flow. We argue that the flow rate S ingested by the porous surface inside the cell must be compensated and this mass of fluid comes from the upstream boundary layer flow. The external flow at the outer edge of the shear layer is also deviated downwards, and ultimately impinges on the cavity shoulder. At the impingement, this high momentum flow creates a thin laminar boundary layer, which then develops downstream.

To give quantitative support this claim we propose a straightforward approach to associate the suction in the cavity with the boundary layer flow. It is possible to create a boundary layer flow rate curve by integrating the mean velocity profile, i.e. by calculating

$$Q_{BL}(y)/b = \int_0^y \overline{u}(y)\mathrm{d}y \tag{4.4}$$

where $Q_{BL}(y)/b$ is the flow rate per unit span associated to the layers from 0 to y. Recalling the definition of S, equation 4.1, we can normalise the boundary layer flow rate as

$$S_{BL}(y) = \frac{1}{L}\int_0^y \overline{u}(y)/u_e\mathrm{d}y. \tag{4.5}$$

Then, neglecting effects due to the finite span of the cavity, we can write mass conservation as

$$S = S_{BL}(y_q) \tag{4.6}$$

which means that a thickness y_q of the upstream boundary layer is entering into the cavity to compensate for S.

Therefore, given the reference mean velocity profile for CASE1 it is possible to plot the curve (S, y_q), or in non-dimensional form $(S, y_q/\delta_0)$. This plot is reported in figure 4.5. The horizontal axis range corresponds to the range of S in the present experiments. The meaning of this plot is to provide the thickness y_q as a function of the cavity suction S.

The most important feature to notice in this figure is that at a suction parameter equal to about 0.045 corresponds a volumetric flow rate equal to that associated to

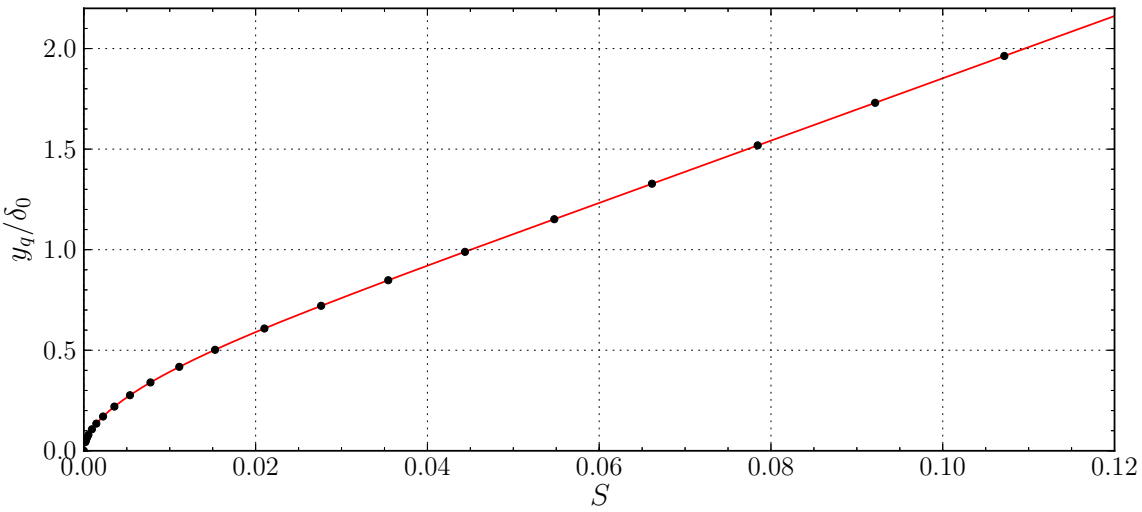

Figure 4.5. Fraction of the height of the upstream boundary layer associated to a given suction parameter S.

the upstream laminar boundary layer for CASE1, i.e. $y_q/\delta_0 = 1$. This value is strikingly similar, if not equal, to the value of S^*, highlighted in figure 4.2 as the threshold value for S above which no increase in the mean velocity in the control point downstream, of the cavity was observed.

Figure 4.6 shows a sketch which explains graphically the proposed approach. Since the thickness y_q represents the fraction of the upstream boundary layer which must be ingested for mass conservation principles, the streamline passing at $y = y_q$ is the line dividing the outer flow, which will flow downstream forming a thin boundary layer, by the internal flow, which will be ingested by the suction system.

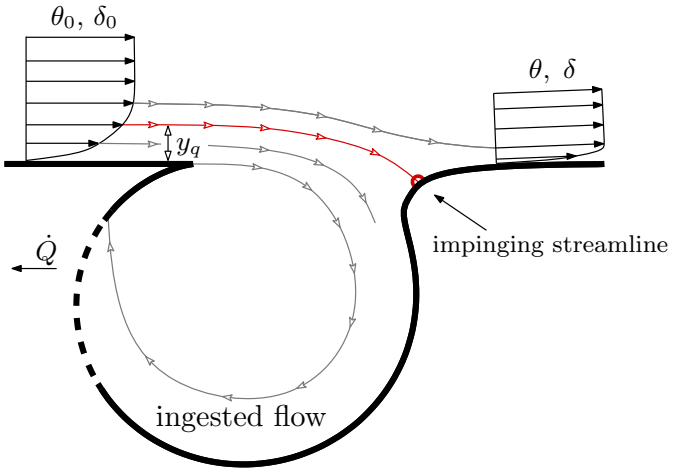

Figure 4.6. Sketch of the proposed boundary layer ingestion model.

This simple yet effective model, confirmed by flow visualisations reported in section 4.2.1, also helps explaining why there is no further gain in the mean velocity downstream the cavity for $S > S^*$. In fact, the slow momentum fluid of the shear layer has already been completely ingested, there is no point in further increasing S, since only high momentum external flow would being ingested.

A further confirmation of this mechanism is reported in figure 4.7, which shows selected vertical profiles of u'_{rms}/u_e taken along the streamwise coordinate at the same x coordinate as in figure 4.4. For each profile, a vertical dashed gray line indicate the x position at which the profile was taken while the red solid line indicates a value of $u'_{rms}/u_e = 0.1$.

The first profile, taken at $x/L = 0.015$, shows a significantly large peak below the cavity cusp, at $y/\delta_0 \approx -0.38$, with a value slightly in excess of 0.11. This peak is originated by the boundary layer developing on the cavity surface as a result of the vortical flow, strongly intensified by the suction, as visible from the corresponding mean velocity profile in figure 4.4. It must be noted that suction does not add energy into the flow but work by modifying the flow structure in order to redistribute energy across the flow field. Thus, a sound explanation for the strong increase of the velocity of the cell's vortical flow can be given, in accordance with the above proposed model of the shear layer ingestion. The layers of fluid which get ingested in the cavity, for mass conservation principles, transport into the cavity a significant amount of momentum, which is directed downwards, tangential to the cavity. This high speed fluid flows steadily along the cavity surface, in a thickness which must be proportional to y_q. It also entrains the rotation of the remaining bulk of fluid such that, as a result, the entire cavity is filled with a strongly rotating flow. This hypothesis is supported by flow visualisations performed in this configuration and shown later in this thesis.

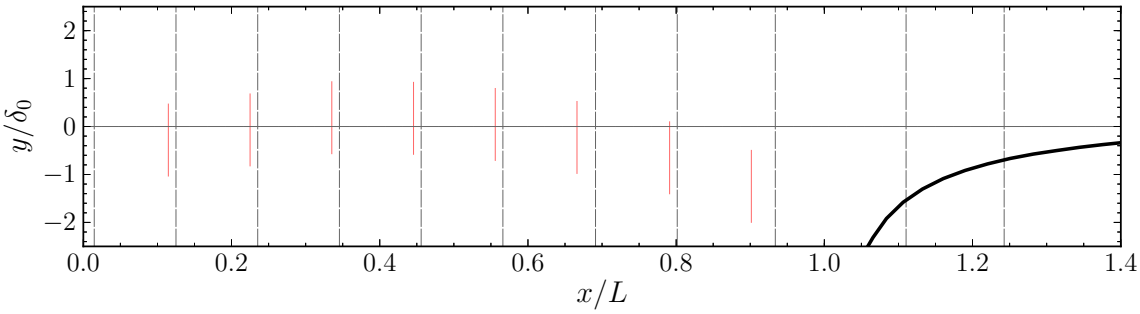

Figure 4.7. Selected profiles of u'_{rms}/u_e along the shear layer. Approximately one each four profiles is shown, for clarity. The downstream edge of the cavity is also visible. Flow is from left to right. The small vertical segments indicate the value of $u'_{rms}/u_e = 0.1$. The vertical dashed line indicates the location where the profile is taken, and the value of $u'_{rms}/u_e = 0$

As the shear layer evolves downstream, a second peak starts to appear at $y/\delta_0 \approx 0.3$, while the peak of fluctuations associated to the cavity boundary layer flow decreases considerably. The second peak forming above y/δ_0 is associated to the shear layer instability which is still being forced by the wind tunnel acoustic resonance. However, it must be noted that the amplification of this peak, and the resulting maximum value along the shear layer, is much lower when compared to that of the unforced flow, shown in figure 3.5. It is likely that modification of the base flow by the control alters the instability characteristics of the shear layer, resulting in a lower total amplification of the initial disturbances at f_{wt}. Evidence for this modification will be given later in the text, when presenting results of the spectral analysis.

In the last third of the shear layer, the peak of u'_{rms} significantly deviates downwards because it is transported by the flow turning into the cavity. Eventually, all the shear layer, i.e. the region of large u'_{rms}/u_e is ingested into the cavity. This is clearly evidenced by the profile at $x/L = 1.11$, after the impingement point, which shows a level of fluctuation intensity equal to that of the undisturbed external flow. Eventually, a small level of fluctuation intensity develops as the laminar boundary layer develops downstream, probably initiating transition at some distance downstream.

The effect of the variation of suction on the shear layer is shown in figure 4.8, which presents profiles of the mean velocity, in part (a), and of u'_{rms}/u_e, in part (b), for four values of the suction parameter S, included the no-control condition, $S = 0$. These profiles refer to the reference x position, at $x/L = 0.58$. In no-control conditions, the shear layer has an approximate thickness of about $1.6\delta_0$ and the edge velocity in the cavity is of the order of $0.1u_e$. However, as the suction increases, a downward shift of the entire profile is observed, due to the displacement of the flow induced by the suction. In addition, the edge velocity in the cavity, i.e. at $y/\delta_0 = -1$, has increased substantially, and it has reached a value of the order of $0.5u_e$. Interestingly, the velocity of the external flow has also slightly increased, showing an overshoot of about 10% of u_e. The profiles of u'_{rms}/u_e, figure 4.8-(b), also clearly evidences the downward displacement of the shear layer flow. In fact the peak moves from $y/\delta_0 = 0.3$ down to $y/\delta_0 = -0.5$. Interestingly, the peak value shows a slight reduction as the suction is increased.

A thinning of the shear layer region is also observed in figure 4.4, which for the largest value of S reported in the figure is of the order of $1.0\delta_0$. The strong reduction of the shear layer vertical scale is caused essentially by a strong reduction of the spreading, which in turns is connected to a reduction of the of the velocity fluctuations with respect to the uncontrolled case, which are ultimately responsible of the thickening of the shear layer.

The increase of the velocity in the cavity is also clearly evidenced in figure 4.9, which shows the effect of the suction rate on the mean velocity in a point in the cavity, at $x/L = 0.58$ and $y/\delta_0 = -2.27$. This figure is obtained in the same way as

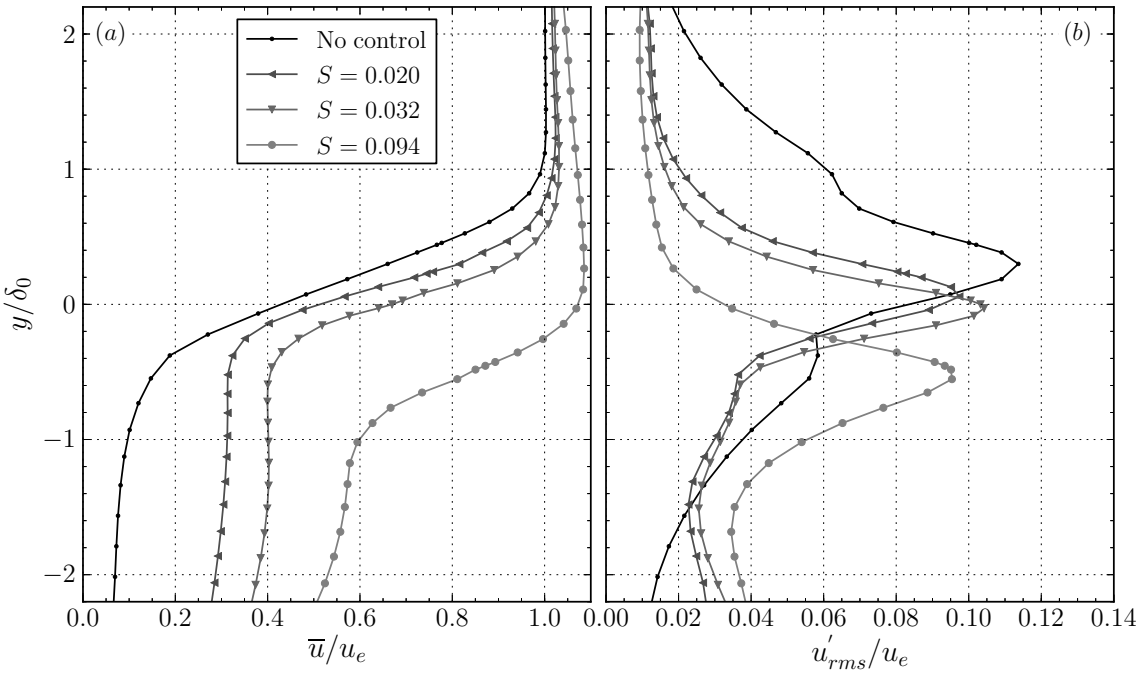

Figure 4.8. Effects of the suction rate on the velocity profiles at $x/L = 0.58$.

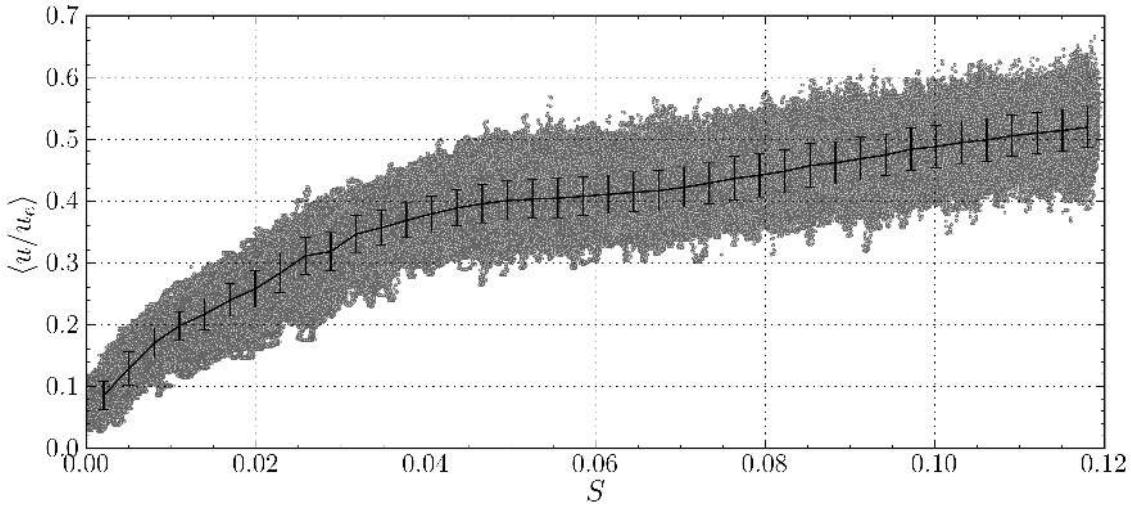

Figure 4.9. Effects of the suction rate on the mean velocity at a control point inside the cavity region, at $x/L = 0.58$, $y/\delta_0 = -2.27$.

discussed for figure 4.2. The figure indicates a strong monotonic increase of the mean velocity associated to the vortex flow, allover the range of S. However, the increase is stronger up to $S^* \approx 0.045$. Then a reduction of the slope of the curve is observed, but the curve continues to increase, despite the boundary layer downstream is not

affected anymore. This is likely associated to the fact that the increase of S is associated to an increase of the ingestion of high momentum fluid into the cavity, which further accelerates the vortex flow, even for $S > S^*$.

The difference in behaviour between the cavity flow and the downstream flow for $S > S^*$ is significant, since it seems to diminish the importance of the "wall-slip-layer" effect for the TVC with suction, introduced by Lasagna et al. [2011]. In fact, these authors, following the work of Donelli et al. [2009] argued that the presence of an non-zero tangential velocity at the cavity opening can result in an lower loss of momentum for the boundary layer that flow past it such that the wall flow that develops downstream is more energetic than in the case of solid wall. The result presented in this thesis do not provide evidence to support this claim in the case of control by suction.

4.2.1 Flow visualisations

A snapshot from smoke flow visualisations for CASE1 is reported in figure 4.10. A single snapshot is reported since the cavity flow is much steadier than in no control conditions and there is no need to show a sequence of snapshots. The suction rate is very high and such that $y_q/\delta_0 \approx 1.85$, that is more than the entire upstream boundary layer is being ingest into the cavity. The porous region of the cavity surface is also visible, on the left side of the figure. The flow visualisation supports the proposed model of figure 4.6 and clearly evidences a region of fresh and high-momentum fluid which flows along the cavity surface, from the downstream edge up to the cusp. This area is evidenced in the snapshot as a darker layer of fluid attached to the wall, since the external flow is not seeded. As this layer passes over the porous region, it becomes thinner since this fluid is being ingested by the suction system. This high-momentum flow is responsible of the entrainment of the cell flow, strongly accelerated by this high speed layer.

However, by observation of the full animated sequence, which provides indication of the flow speed, it can be clearly observed that the entire vortex core does not develop a solid body rotation. Instead, the core region rotates much slower than expected and it is surrounded by a layer of internal flow, accelerated by the ingestion of high-momentum flow at the downstream corner, which finally merge with the upstream boundary layer at the cusp.

The animated sequence also shows the strong reduction of the velocity fluctuations in the shear layer, and the shear layer instability clearly visible for the uncontrolled flow in figure 3.17, can only be barely detected in the controlled flow. It is likely that the modification of the base flow results in a lower amplification factor of the disturbances in the shear layer.

A further remark to the visualisations is that the erratic injection of external fluid into the cavity from the downstream edge is entirely eliminated by the control

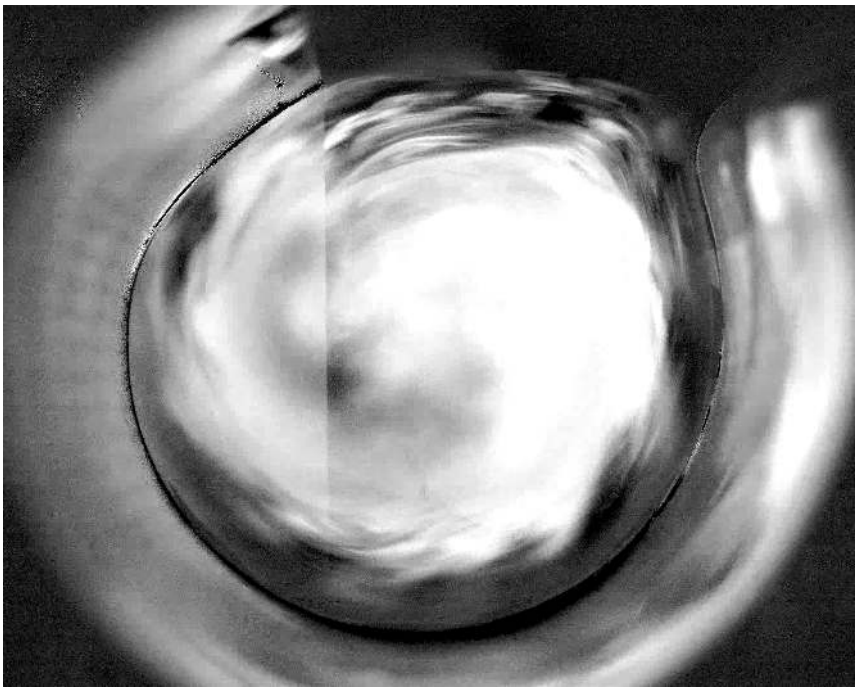

Figure 4.10. Snapshot of flow visualisation for CASE1 with suction, $y_q/\delta_0 \approx 1.85$

which strongly regularises this region of the flow field.

4.2.2 Spectral analysis

Figure 4.11 shows power spectral densities of the normalised velocity fluctuations $u^* = u/u_e$ at $x/L = 0.58$ and at a y/δ_0 corresponding to the position of the peak of u'_{rms}/u_e, as in figure 4.8. Spectra for several values of the suction parameter, indicated in the figure caption, are reported. Note that for graphical convenience, each spectrum after the first, (a), is artificially shifted upwards by three decades.

The figure clearly indicates that the spectral characteristics of the flow are strongly affected by the control. In no-control conditions, spectrum (a), the largest part of the velocity fluctuations energy is due to the the frequency of the forced Kelvin-Helmoltz instability, occurring at $f = f_{wt} = 150$ Hz. Furthermore, peaks at several higher harmonics up to 1.5 kHz, although strongly spread out, can be clearly observed.

By slightly increasing the suction up to $S = 0.009$, the spectrum is substantially modified. The higher harmonics of the resonance frequency are severely damped, and two further peaks at $f = 70$ Hz and at 140 Hz can be observed. Furthermore, a wide-band energy concentration can be observed at frequency spanning the range from 150 to 240 Hz, with at least three non-sharp peaks. Please note, that at a

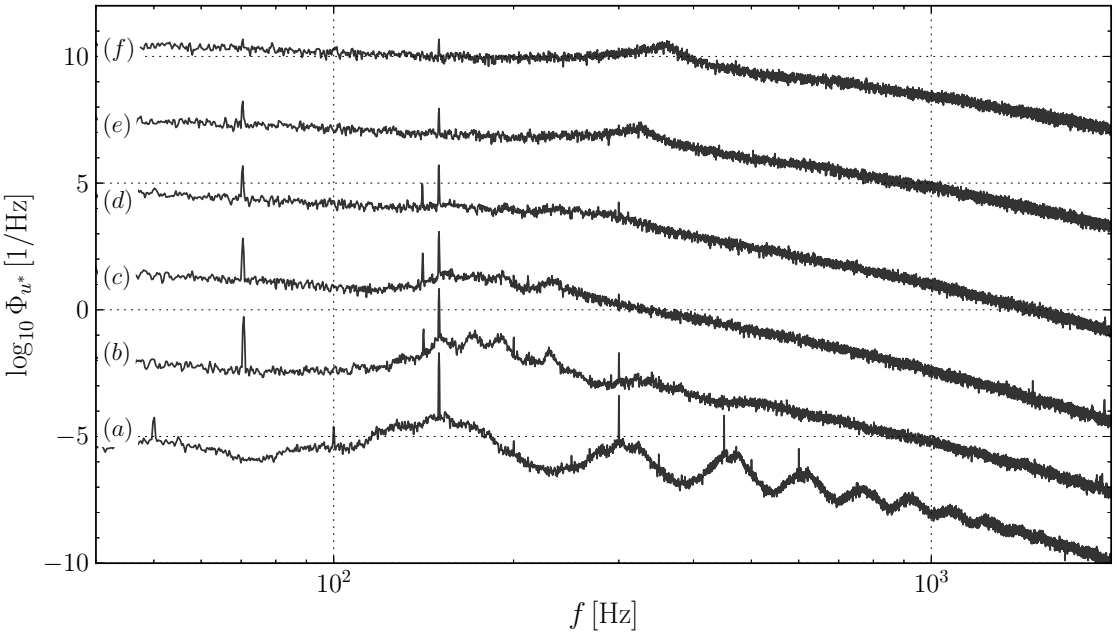

Figure 4.11. Power spectral density of the normalised velocity fluctuations $u^* = u/u_e$ at $x/L = 0.58$, and at a value y/δ_0 corresponding to the peak of the profiles of u'_{rms}/u_e as of figure 4.8, for different values of the suction parameter. Curve (a), $S = 0$; (b), $S = 0.009$; (c), $S = 0.021$; (d), $S = 0.032$; (e), $S = 0.065$; (f), $S = 0.097$.

value of $S = 0.009$ corresponds a value of y_q approximately equal to $0.4\delta_0$, see figure 4.5 for reference.

As the suction is further increased, the energy of the velocity fluctuations at the wind tunnel resonance frequency is dramatically decreased, indicating a very drastic effect of the control. The energy value has in fact decreased by a factor of at least 300. On the other hand, the energy in the spectrum has been greatly redistributed, and the spectrum shows a small peak spread around a frequency of about 350 Hz, for the largest value of S. Examination of the spectra indicates that this frequency increases with the suction rate. The origin of this energy concentration, whose frequency slightly increases as the suction rate is increased, is unknown, but is entirely a characteristic of the shear layer, and not of the cavity flow. This can be justified by observation of figure 4.12. This plot is obtained by computing the power spectral density for the velocity time history at each y/δ_0, (at $x/L = 0.58$, $S = 0.097$), and by creating a colour map showing the spectral density distribution of the velocity fluctuations across the entire shear layer. Examination of the colour map suggests that the peak is a feature of the shear layer flow and not of the cavity flow, since the energy at these frequency is substantially reduced as the probe is moved downwards past the thickness of the shear layer, i.e. below $y/\delta_0 = 2$.

A further feature of the spectral behaviour of the flow subject to the control can be observed at very low frequencies, not visible in figure 4.11, because of the poor frequency resolution of those spectra, a result of the small block size used in the Welch algorithm required to achieve an accurate estimate of the spectral density. Figure 4.13, shows the low frequency detail of the spectra of the velocity fluctuations taken, as before, at $x/L = 0.58$ but inside the cavity, at $y/\delta_0 = -2$. Here the frequency resolution of the spectra is much higher than that of the spectra of figure 4.11. The spectra indicate that for certain values of the suction parameter S, between $S = 0.021$ and $S = 0.032$, the suction seems to excite a low-frequency oscillation of the cavity flow, at a frequency around 4 Hz, increasing with the suction rate. This phenomenon eventually vanishes when the suction is further increased. One hypothesis for this behaviour is that the vortex core, whose rotation is enhanced by the control, is subject to a similar instability observed for CASE2 in the uncontrolled flow. In fact, results not shown here for the sake of brevity indicate that the amplitude of this low frequency phenomenon is also modulated in the spanwise direction, similarly to what observed in the cited case.

The signature of the low frequency oscillation of the cavity flow can be also identified in the boundary layer downstream of the cavity, to which it is strictly connected. Figure 4.14 shows the distribution of the power spectral density of the velocity fluctuations across the boundary layer at $x/L = 2.05$, for a level of suction equal to $S = 0.037$, corresponding to the mean velocity profile shown in figure 4.3, and slightly higher than the case of $S = 0.032$ in figure 4.13. This colour map has been obtained by computing the spectral density of each of the velocity time histories measured across the boundary layer. The colour map indicates a moderate level of energy at frequencies slightly exceeding 4 Hz. The spectral signature can be observed from $y/\delta_0 \approx 0.2$ up to $y/\delta_0 \approx 1.3$, thus at a distance from the wall much higher than the local boundary layer thickness, that is at least the double of this

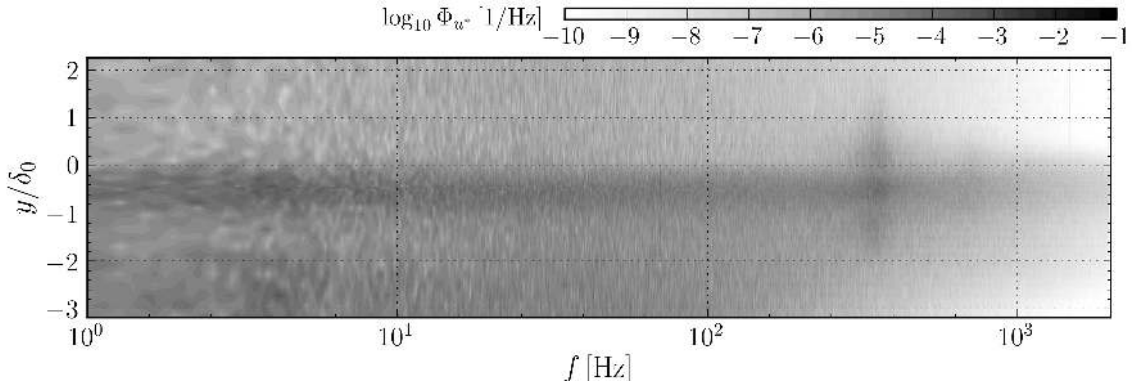

Figure 4.12. Power spectral density distribution of the velocity fluctuations at $x/L = 0.58$, across the entire shear layer, for $S = 0.097$.

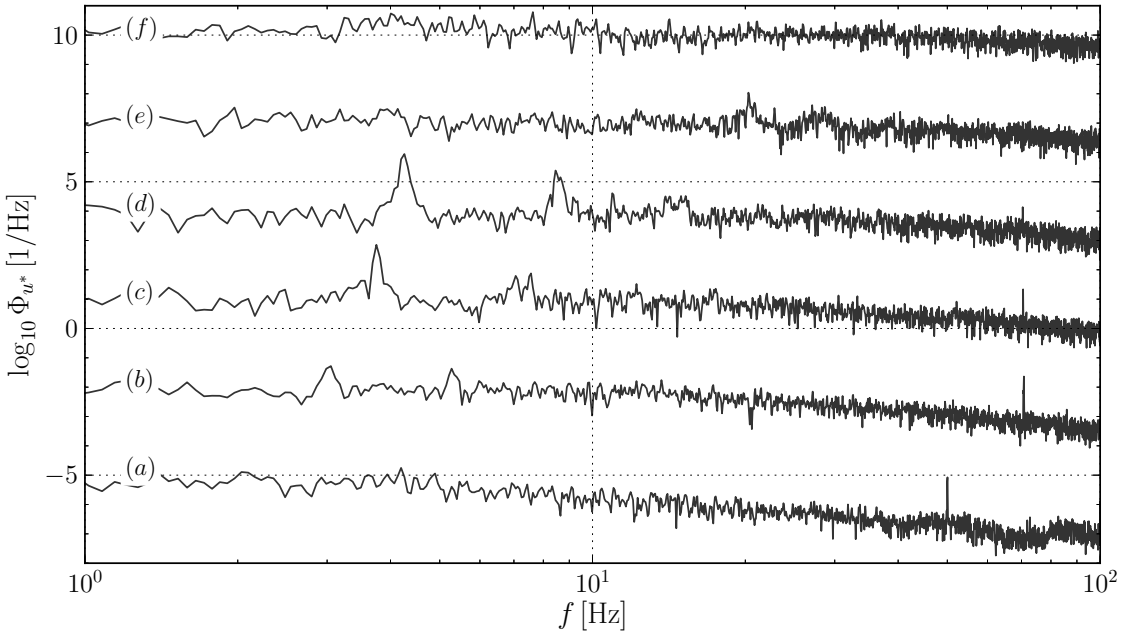

Figure 4.13. Detail of the power spectral density of the normalised velocity fluctuations $u^* = u/u_e$ at $x/L = 0.58$ and $y/\delta_0 = -2$, for different values of the suction parameter. Curve (a), $S = 0$; (b), $S = 0.009$; (c), $S = 0.021$; (d), $S = 0.032$; (e), $S = 0.065$; (f), $S = 0.097$.

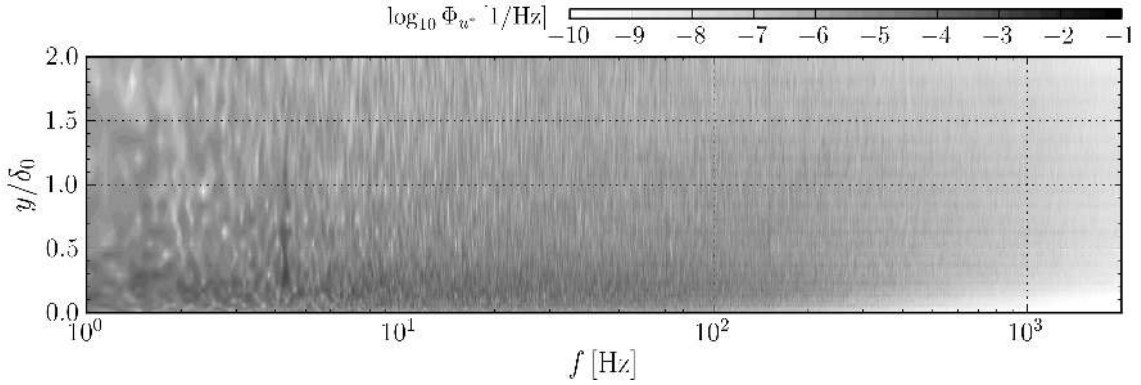

Figure 4.14. Distribution of the power spectral density of the velocity fluctuations across the boundary layer at $x/L = 2.05$, for $S = 0.037$.

thickness.

It may be argued that the low frequency oscillation of the cell flow induces a "flapping" motion of the shear layer, but it is difficult to quantify how much this low frequency oscillations conditions the effectiveness of the suction control, and as discussed previously it should be the object of further research.

It is important to notice that the variation of the spectral behaviour of the flow when control is applied, and in particular of the shear layer, is very strong. The strong amplification of disturbances in the shear layer observed in the uncontrolled case at the resonance frequency is greatly weakened, and the sharp energy peak observed in the spectrum of the velocity fluctuations in a characteristics point of the shear layer is replaced by broad-band velocity fluctuations, with a very flat peak at a frequency around 350 Hz for the largest tested value of S.

The explanation for such a drastic change is not known but an analysis of the relevant literature may provide some insight. One hypothesis is that the modification of the mean flow, as a result of the enhancement of the velocity in the cavity, modifies the instability characteristics of the shear layer. Thus, despite the strong acoustic forcing at the wind tunnel resonance frequency the shear layer does not "lock-in" to this forcing, but develops broad-band oscillations at higher frequencies. Another explanation could be that, as suggested by Sarohia and Massier [1977] which studied steady mass injection, the modification of the impingement location, induced by the downwards displacement of the shear layer, alters the acoustic feedback loop by reducing the strength of the source of pressure disturbances, as pointed out by Rockwell and Naudascher [1978]. However, this last explanation is not completely convincing since for CASE1 a strong source of disturbances is already present and it is due to the acoustic resonance of the wind tunnel facility.

4.2.3 Three dimensional organisation of the cell flow

One of the reason for applying suction of the flow in the cavity region was to manipulate the cavity flow in order to obtain a stable and steady vortex core. To understand how suction affects this issue spanwise profiles of the mean velocity and of the root-mean-square value of the velocity fluctuations were measured in the cavity region, in a control point at $x/L = 0.58$, $y/\delta_0 = -2.27$, significantly below the shear layer thickness, (see figure 4.8).

The profiles of the mean velocity are reported in figure 4.15, for several values of the suction parameter S. In the figure, the red vertical lines indicate the z/b positions of the ribs of the cavity model, which interrupted the continuity of the suction by about 12 mm, i.e. $0.03b$. In no control conditions, $S = 0$, the mean velocity along the span at the control point is of the order of $0.08u_e$ and the profile indicates a very weak modulation along the span, with slightly larger values at $\pm 0.4b$. Note that this profile is qualitatively similar to what reported in figure 3.18-(a), even though those data refers to a point in the flow slightly more outwards, at $y/\delta_0 = -1.69$. Those data also indicate a slightly lower spatially averaged value, and a possible reason for this behaviour, and of other subtle differences between these two conditions, is that the porous surface can slightly affect the delicate flow in the cavity if no suction is present. This can be justified with the argument that a slight

pressure differential across the cavity span, due to a three-dimensional organisation of the cavity flow, may lead to natural transpiration of fluid through the porous surface, associated to a cross-flow in the plenum chamber behind it. As the suction

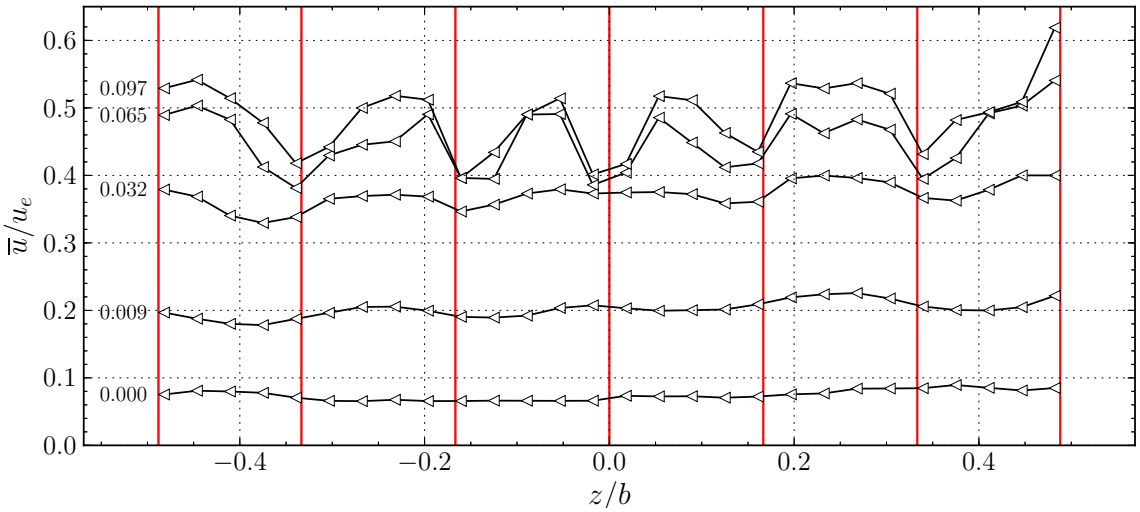

Figure 4.15. Effects of the suction rate on the spanwise profile of the mean velocity at a control point in the cavity, at $x/L = 0.58$, $y/\delta_0 = -2.27$.

is increased, the mean velocity of the cavity flow at the control point increases as well, as it does the amplitude of the modulation of the mean velocity along the span. At the lowest value of the suction, $S = 0.009$, the control seems to excite a symmetric periodic modulation of the mean velocity, with three region of larger velocity at $z/b = 0$ and $z/b = \pm 0.25$. However, it is difficult to understand if this pattern is due to a inherent behaviour of the flow or if it is due to how suction is applied, i.e. through six separate regions. In fact, as the suction is further increased a very regular pattern emerges, clearly matching the position of the ribs of the cavity models. At these locations, the mean velocity can be as much as 20% lower then what observed between two ribs.

For what concerns the profiles of u'_{rms}/u_e, figure 4.16, reports the profiles of this quantity for the same values of suction as reported in figure 4.15. Note that, for clarity, the curves for the last two values of suction have been drawn using a different line style, to evidence the different behaviour.

In no control conditions, $S = 0$, the profile of u'_{rms}/u_e indicates an average value of about $0.012u_e$ not very different from the value observed in figure 3.18-(b), which was in nominally the same conditions, with the difference that in this case part of the cavity surface is porous. In fact, the large peak of fluctuations observed near the mid-span of the figure in not observed anymore. As suggested before, the reason could be that a very weak flow though the porous surface induced by weak pressure

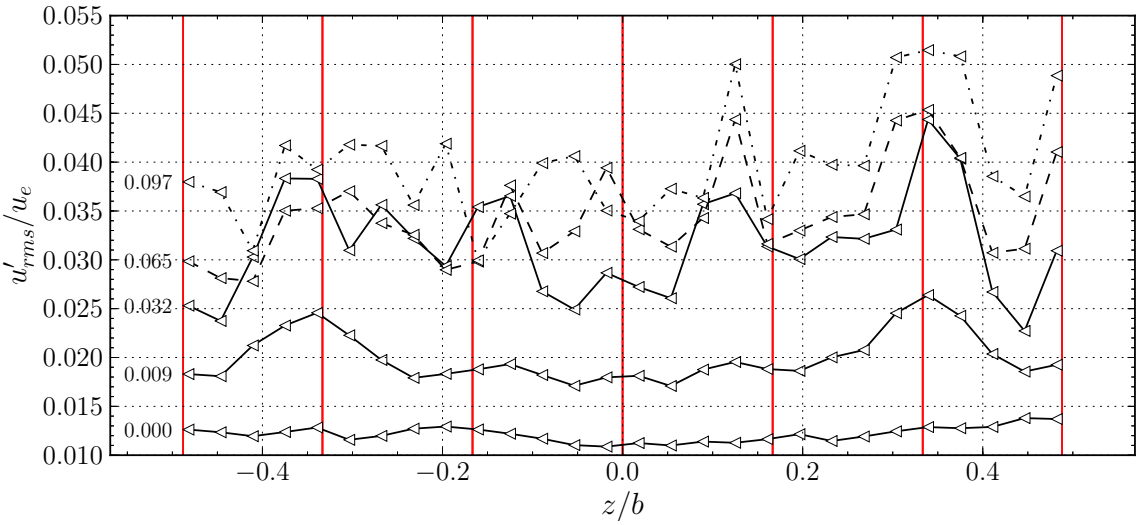

Figure 4.16. Effects of the suction rate on the spanwise profile of the root-mean-square value of the velocity fluctuations at a control point in the cavity, at $x/L = 0.58$, $y/\delta_0 = -2.27$.

differences across the surface itself, may break to delicate three dimensional flow of the cavity resulting in a different behaviour.

As the suction parameter is increased to $S = 0.009$, the average value of u'_{rms}/u_e increases, as a result of the larger mean velocities encountered in this conditions, which favour larger velocity fluctuations. Most importantly, a characteristic pattern emerges, showing two peaks symmetrically distributed around the mid-plane at ± 0.35. This pattern seems broken as the suction is increased further and the profiles for the three larger suction parameters show several small peaks with a wavelength too small to be captured clearly by the rough sampling distance of the measurements. The origin of these peaks as well as the two symmetrical peak of the case $S = 0.009$, can be identified by spectral analysis of the velocity time histories measured along the span.

Results of these analyses are reported in figure 4.17. The figure shows, for each value of S, the distribution of the spectral density of the velocity fluctuations along the span, at the same control point as in figure 4.16. In no control conditions, figure 4.17-(a), the spectra of the velocity fluctuations do not show a significant variability along the span, and are mainly characterized by random low frequency fluctuations and by a small, sharp peak at $f = f_{wt} = 150$ Hz. As the suction is slightly increases, larger energy is observed at a very low frequency of about 3 Hz, at the same z/b location of the two peak of u'_{rms}/u_e as in figure 4.16, for the same suction value of $S = 0.009$. For $S = 0.032$, the frequency of this oscillation has risen to about 4.1 Hz, and a spanwise modulation of this energy concentration is observed, matching fairly accurately the peaks of the corresponding profile of u'_{rms}/u_e. At the two larger

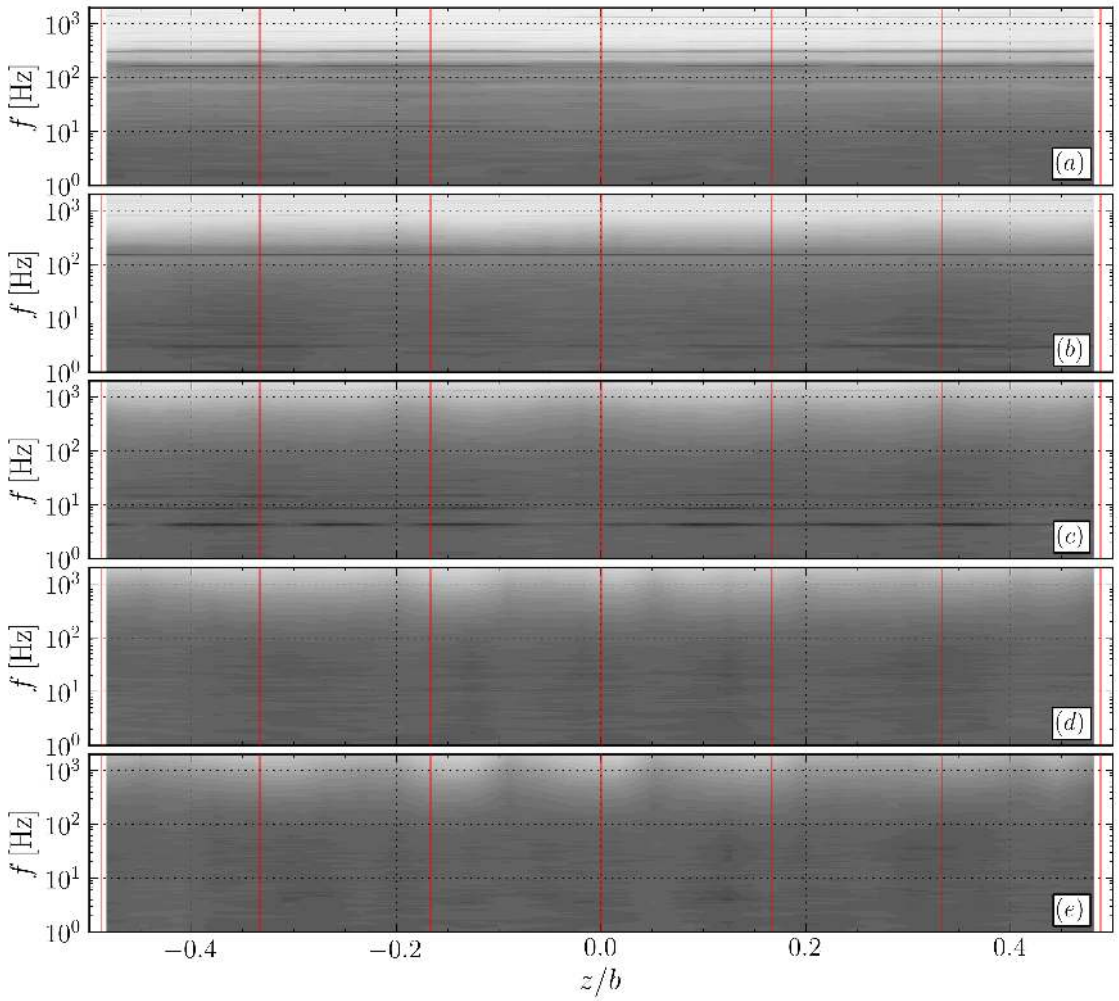

Figure 4.17. Effects of the suction rate on the spectral distribution of the velocity fluctuations at a control point in the cavity, at $x/L = 0.58$, $y/\delta_0 = -2.27$. Figure (a), $S = 0$; (b), $S = 0.009$; (c), $S = 0.032$; (d), $S = 0.065$; (e), $S = 0.097$.

suction rates, this low frequency oscillation is damped and the spanwise modulation of u'_{rms}/u_e seems to be distributed across a wider range of frequencies.

As explained previously, it is likely that this low frequency oscillation is of the same nature of a similar behaviour observed for CASE2 in no control conditions. Here, enhancement of the vortex velocities by the high energy fluid ingested in the cavity as a result of the suction trigger the same instability as in that case. However, when suction is further applied, this behaviour seems to disappear, even though the vortex core rotation is further enhanced. The reason is unknown, but one explanation could be that the strong periodicity imposed on the flow by how the suction is applied, i.e. through six porous regions, does not match the natural

periodicity of the vortex core instability, which therefore does not develop.

4.3 Control for CASE2

In CASE2, since the external velocity is about the double that in CASE1, a reduction of the effectiveness of the suction is expected. In fact, the flow rate associated to the upstream boundary layer is much higher than in CASE1 because the velocity is larger and because a turbulent boundary layer transports more flow for a given thickness than a laminar boundary layer.

Figure 4.18 shows the effect of the suction parameter S on the mean velocity downstream of the cavity, at $x/L = 2.05$ and $y/\delta_0 = 0.045$, i.e. very near the wall. The figure was obtained as discussed previously for figure 4.2, and no signs of hysteresis were observed in this case too. The figure indicates that the mean velocity

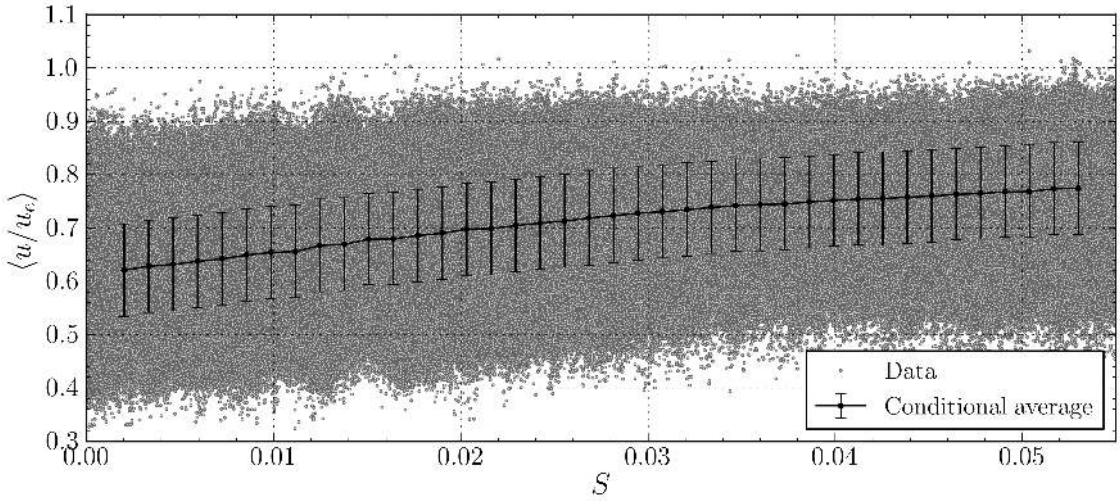

Figure 4.18. Effects of the suction rate on the mean velocity at a control downstream of the cavity, at $x/L = 2.05$, $y/\delta_0 = 0.045$.

in the near-wall region downstream of cavity increases as the control parameter is increased. The increase is moderate and the mean velocity rises from $0.62u_e$ to less than $0.8u_e$. Interestingly, the intensity of the fluctuations is not affected by the forcing. Differently from figure 4.2, there is no plateau region but the mean velocity increases continuously at S is increased. Note that for CASE2 S ranges from 0 to 0.06, while it reached 0.12 for CASE1.

Full velocity profiles were then measured downstream of the cavity at the same x location as in figure 4.18, and some of them are reported in figure 4.19. As usual, part (a) of the figure shows the mean velocity profiles, while part (b) shows the profiles of u'_{rms}/u_e. The corresponding upstream reference profiles at $x/L = -0.14$

are also reported. The horizontal red line indicates the distance from the wall at

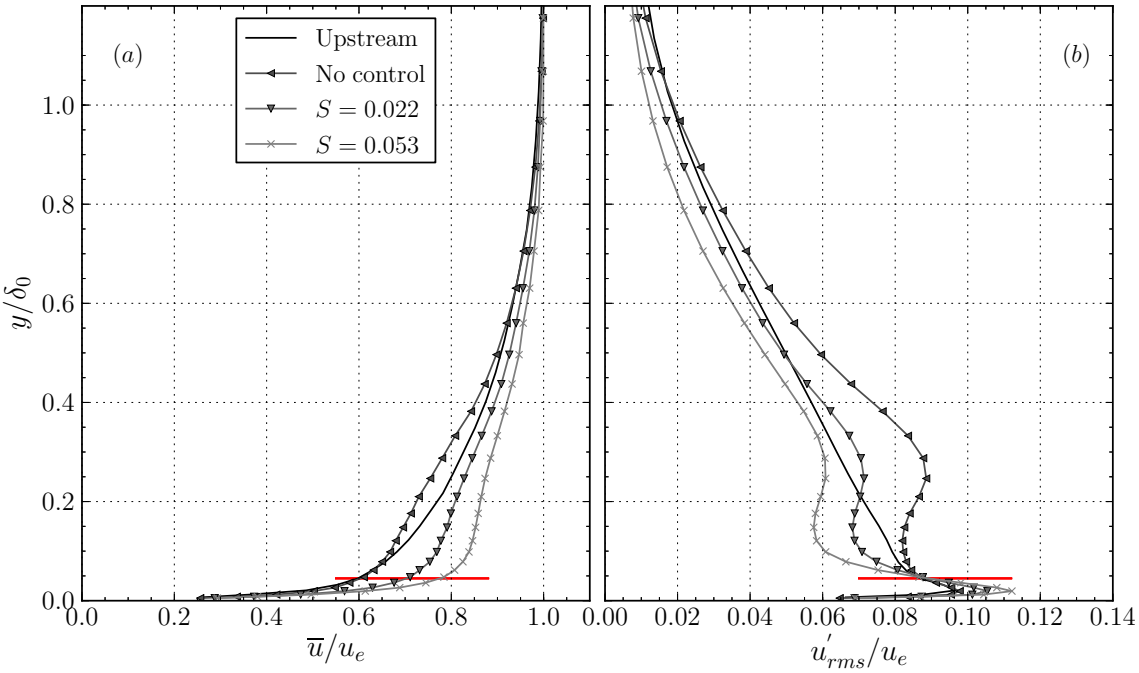

Figure 4.19. Effects of the suction rate on the profiles of $\overline{u}/u_e$ and u'_{rms}/u_e at the downstream position $x/L = 2.05$. Profiles for the upstream reference boundary layer are also reported.

which the tests of figure 4.18 were conducted.

The mean velocity profile is not profoundly affected by the suction as it was for CASE1, but a significant increase of the velocity allover its thickness can be clearly identified, with respect to the no-control profile, and for large enough values of suction also with respect to the upstream profile. The net increase of the velocity is larger in the near-wall region, below $y/\delta_0 = 0.1$, and then gradually decreases as larger distances from the wall are considered.

Despite the change in mean velocity, the shape of the profile is essentially unaffected, since the velocity deficit around $y/\delta_0 \approx 0.2$ characterising the no-control configuration is still observed in the controlled flow. An explanation for this behaviour can be given by observing the profiles of the root-mean-square value of the velocity fluctuations, in figure 4.18-(b). Here, the second peak at a distance from the wall corresponding to the velocity deficit is still observed, although its amplitude is reduced by about 25%, with respect to the uncontrolled configuration. We remember here that this peak correspond to the flow with strong fluctuations in the shear layer, which is lifted up up to this distance from the wall after impinging on the downstream cavity edge. The reduction of the amplitude of this peak suggests

that the shear layer evolution is substantially modified by the control, but that the suction is not high enough to completely eliminate it, by ingesting this flow.

On the other hand, the near-wall peak of u'_{rms}/u_e increases considerably as the control is increased. Although not clearly visible from the figure, the peak increase from 0.097, for the uncontrolled flow, to 0.112, for $S = 0.053$, possibly due to the larger near-wall velocities at this x location of the controlled flow.

For CASE2 the action of the suction is weaker, mostly because the freestream velocity is doubled. In terms of y_q, the thickness of the upstream boundary layer associated to the suction in the cavity as discussed at page 85, its behaviour is shown in figure 4.20. The figure reports the value of y_q/δ_0 as a function of S. The horizontal scaling is such that the entire range of tested S is shown. In contrast to what observed for CASE1 in figure 4.5, the thicknesses associated to a given value of suction are now much smaller, at for the maximum achievable value of S, y_q is about one quarter of δ_0.

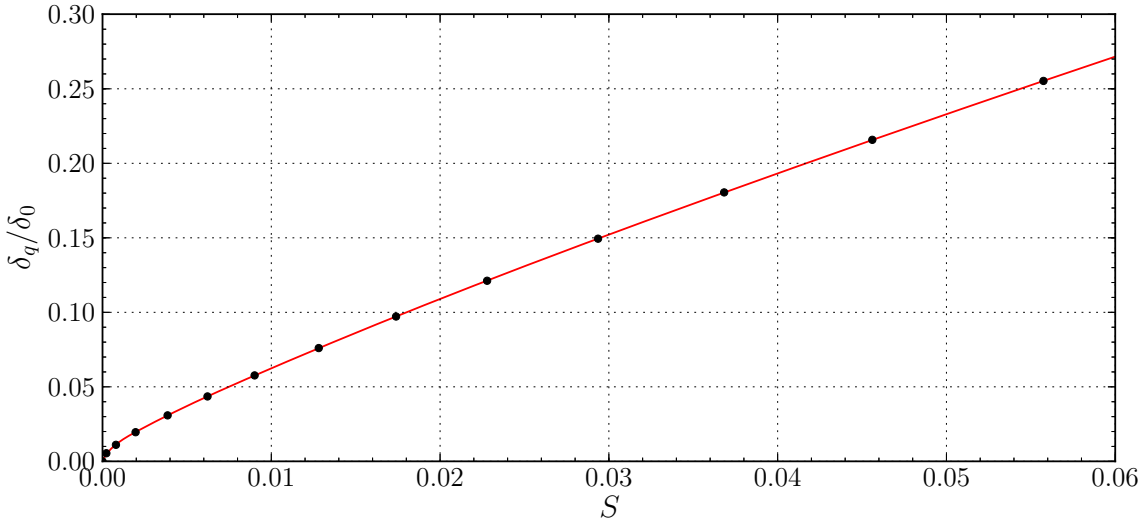

Figure 4.20. Fraction of the height of the upstream boundary layer associated to a given suction parameter S.

To obtain more insight into how the downstream mean velocity profile can become more energetic, the shear layer flow was investigated by measuring velocity profiles across its thickness at the reference location $x/L = 0.58$, for several values of the suction parameter S. Results of this investigation are reported in figure 4.21, which shows both the profiles of $\overline{u}/u_e$, in part (a), and of u'_{rms}/u_e, in part (b).

As the suction parameter is increased, the mean velocity increases all along the thickness of the shear layer, especially in the cavity region, for $y/\delta_0 < 0$. In fact, the largest velocity increase is observed at around $y/\delta_0 \approx -0.1$. The mean velocity in the cavity increases for the same reason as in CASE1, that is because of the

momentum ingested into the cavity. This addition of momentum sustains the faster rotation of the vortex flow. The velocity in the shear layer also increases at positive y. The likely reason is that the downward displacement of the whole shear layer results in an apparent increase of speed, since a layer of fluid at, say, $y/\delta_0 = 0.5$ is replaced by an equivalent layer of fluid from $y/\delta_0 = 0.5 + \Delta$.

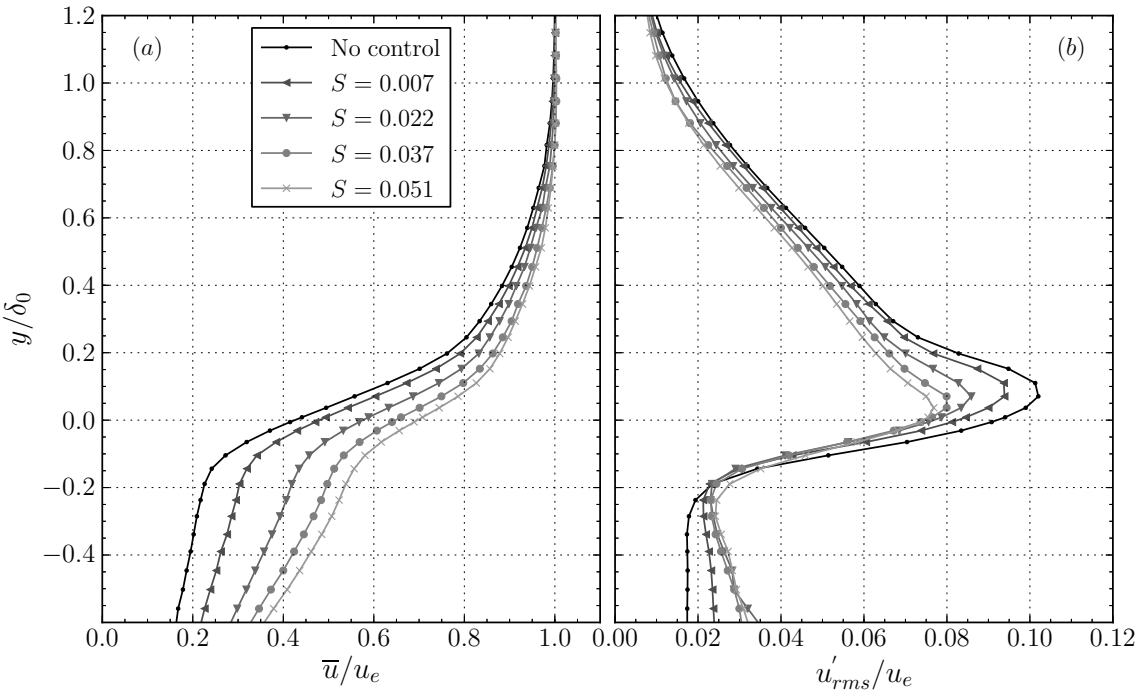

Figure 4.21. Effects of the suction rate on the profiles of $\overline{u}/u_e$ and u'_{rms}/u_e in the shear layer region, at $x/L = 0.58$.

As a result of the control the velocity profile is less steep. Thus, the lower gradient $\partial\overline{u}/\partial y$ must results in a lower turbulent kinetic energy production in the shear layer region. This is confirmed by the profiles of u'_{rms}/u_e, reported in figure 4.21-(b), which indicate a 20% decrease of the peak for $S = 0.051$, with respect to the uncontrolled condition.

The downward displacement of the shear layer is also clearly visible, although less intense than in CASE1 in figure 4.7. In fact the peak of u'_{rms}/u_e is displaced by about $0.1\delta_0$. Actually, the whole profile seems displaced downward, which seems a sound explanation for the reduction of u'_{rms}/u_e in the region $0.3 < y/\delta_0 < 1$.

The evolution of the shear layer is severely influenced by the control. Figure 4.22 shows selected mean velocity profiles along the shear layer, measured in a case where $S = 0.054$. For each velocity profile, two vertical dashed lines indicate marks for $u = 0$ and $u = u_e$, as usual. The first mark also indicates the x/L position where the mean velocity profiles was measured. As discussed above, the

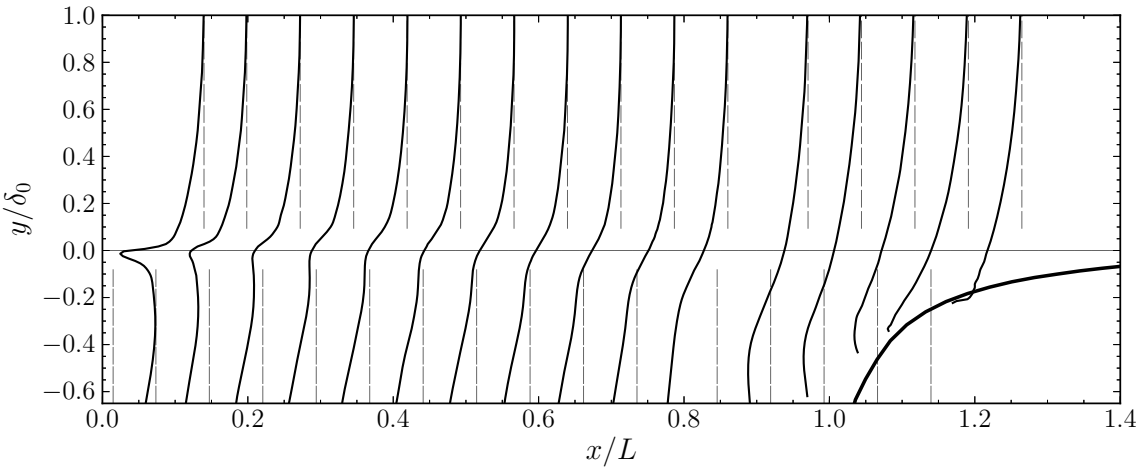

Figure 4.22. Selected mean velocity profiles along the shear layer for $S = 0.054$. For each profile two vertical dashed lines indicate marks for $u = 0$ and $u = u_e$. The first mark also indicates the x/L position where the mean velocity profiles was measured.

velocities in the cavity are significantly increased by the control which means that the velocity deficit at $y/\delta_0 = 0$ in the first profile reported is quickly filled by momentum transport operated by the strong velocity fluctuations observed in this region, before $x/L = 0.4$. The downward deflection of the shear layer is weaker in the first half of the cavity and a significant displacement of the mean velocity profile can only be noticed in the last third of the cavity opening. Nevertheless, the vertical displacement of the shear layer is small compared to δ_0. In fact, for $S = 0.054$, y_q is about one fourth of δ_0, and a larger displacement cannot be expected.

The corresponding profile of u'_{rms}/u_e are reported in figure 4.23. For each profile, the vertical dashed line indicate the x/L position where the profile was measured and the value $u'_{rms}/u_e = 0$. The smaller red segment indicates a mark for $u'_{rms}/u_e = 0.1$, and its vertical position follows the peak of u'_{rms}/u_e, whose y/δ_0 position is indicated by a red dot.

The first profile, at $x/L = 0.015$ shows two peaks around $y/\delta_0 = 0$. The upper one corresponds to the near wall peak of velocity fluctuations of the upstream boundary layer, while the bottom one is that originated by the wall flow developing over the cavity surface. Note that, because of the presence of the suction on the upstream region of the cavity, see figure 4.6, this fluid is not the same external fluid ingested into the cavity flowing along the entire cavity surface. Instead, this is the fluid of the outer layers of vortex core, strongly energised by the fast flow along the cavity surface.

At a distance downstream about $0.2L$, the two peaks have quickly merged together, due to the strong mixing of fluid in this thin region. The peak value has

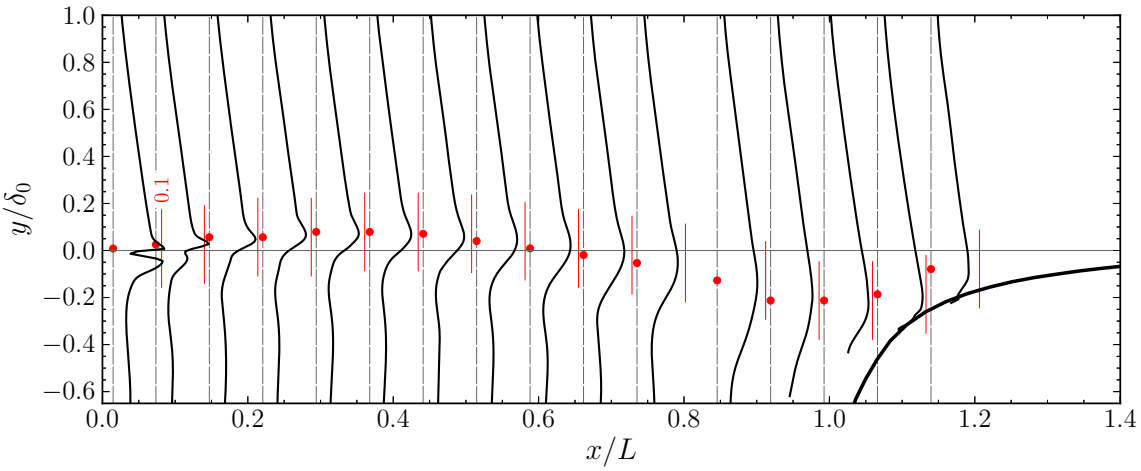

Figure 4.23. Selected profiles of u'_{rms}/u_e along the shear layer for $S = 0.054$. For each profile, the vertical dashed line indicates the x/L position where the profile was measured and the value $u'_{rms}/u_e = 0$. The smaller red segment indicates a mark for $u'_{rms}/u_e = 0.1$, and its vertical position follows the peak of u'_{rms}/u_e, whose y/δ_0 position is indicated by a red dot.

not increased, though, but it has slightly moved upwards, as it is then observed up to $x/L = 0.4$, where the peak of u'_{rms}/u_e starts to move downwards, continuously up to $x/L \approx 1$, where the shear layer lifts up, following the wall of the downstream edge.

Along the shear layer, the maximum value of u'_{rms}/u_e does not change much and remains around an average value of 0.85. This was also a feature of the uncontrolled flow, see figure 3.5, where the normalised root-mean-square value of the velocity fluctuations remained around a value of about 0.12. The region of large fluctuations in the shear layer enlarges slowly along x/L, and roughly at the same rate of the uncontrolled flow.

4.3.1 Three dimensional structure of the flow

In CASE2 the cavity flow displays, in no control conditions, a marked three dimensional structure evidenced as a regular periodic pattern, modulating both the mean velocity and the root-mean-square value of the velocity fluctuations along the span, as discussed for figure 3.33. Spectral analysis of that dataset indicated the the transverse modulation of u'_{rms}, was to be attributed essentially to a modulation of the low frequency oscillation of the vortex core. A very weak signature of this phenomenon was observed in the boundary layer developing downstream of the cavity, and it may thus be argued that this phenomenon is not so preponderant for the characteristics of this wall-flow. Nevertheless, control of this phenomenon by suction may provide

some insight into its effects.

Figure 4.24 shows spanwise profiles of the mean velocity measured at $x/L = 0.58$, $y/\delta_0 = -0.45$, for several values of the suction parameter S, indicated in the same figure. As also done before, the vertical red lines indicate the position of the ribs of the cavity model. We first observed that, in no control conditions, the

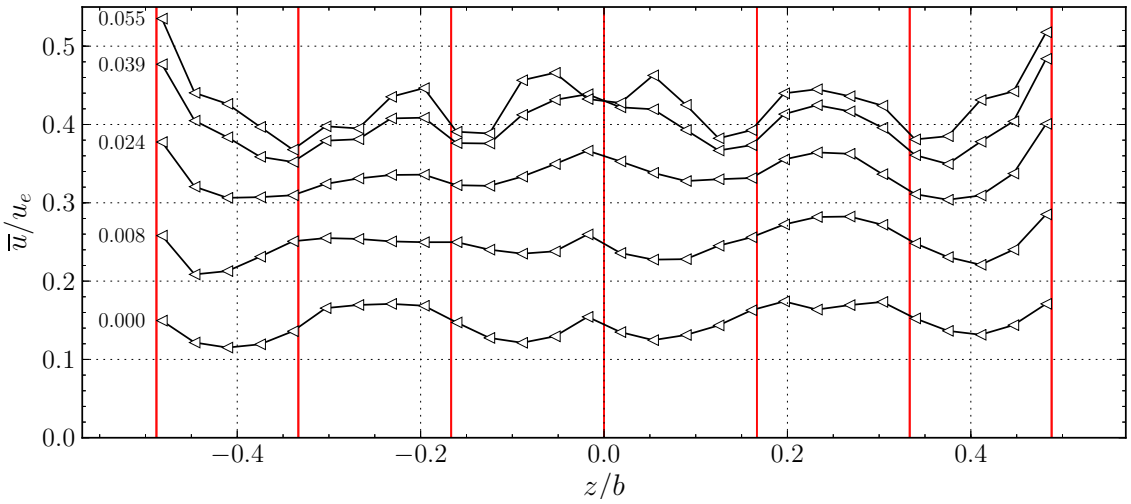

Figure 4.24. Spanwise profiles of the mean velocity at $x/L = 0.58$, $y/\delta_0 = -0.45$, for several values of the suction parameter S, indicated in the figure. The vertical red lines indicate the position of the ribs of the cavity model, at which suction is interrupted for a width of $0.023b$.

three dimensional structure of the flow in the cavity is significantly different to that observed in figure 3.33, even though those measurements were taken slightly more inside the cavity at $y/\delta_0 = -1.36$. We point out again that the main difference between the case $S = 0$ and the no control case discussed in the previous chapter is the presence of the porous region on the upstream part of the cell, which may trigger a different three dimensional structure of the flow field. In fact, the mean velocity profile shows a clear symmetric pattern, with two peaks symmetrically located around $z/b \pm 0.25$. The wavelength of this pattern seems larger than what observed in the no control case and can be estimated roughly to be of the order of $\lambda_p/b = 0.25$. In addition, the variation of mean velocity is larger in this case, of the order of $0.06u_e$ against a much lower value of 0.015 as observed in figure 3.33.

This particular structure seems to robust to the control since it maintains its coherence as the suction parameter is increased, up to about $S = 0.039$. At the largest tested value, $S = 0.055$, the pattern observed at a lower S is distorted, essentially by the presence of the ribs of the cavity model, over which there is no suction of flow. The width of the ribs is a fraction equal to 0.023 of the cavity span,

but the interruption of control over this region introduces a marked distortion into the structure of the cavity flow in this region.

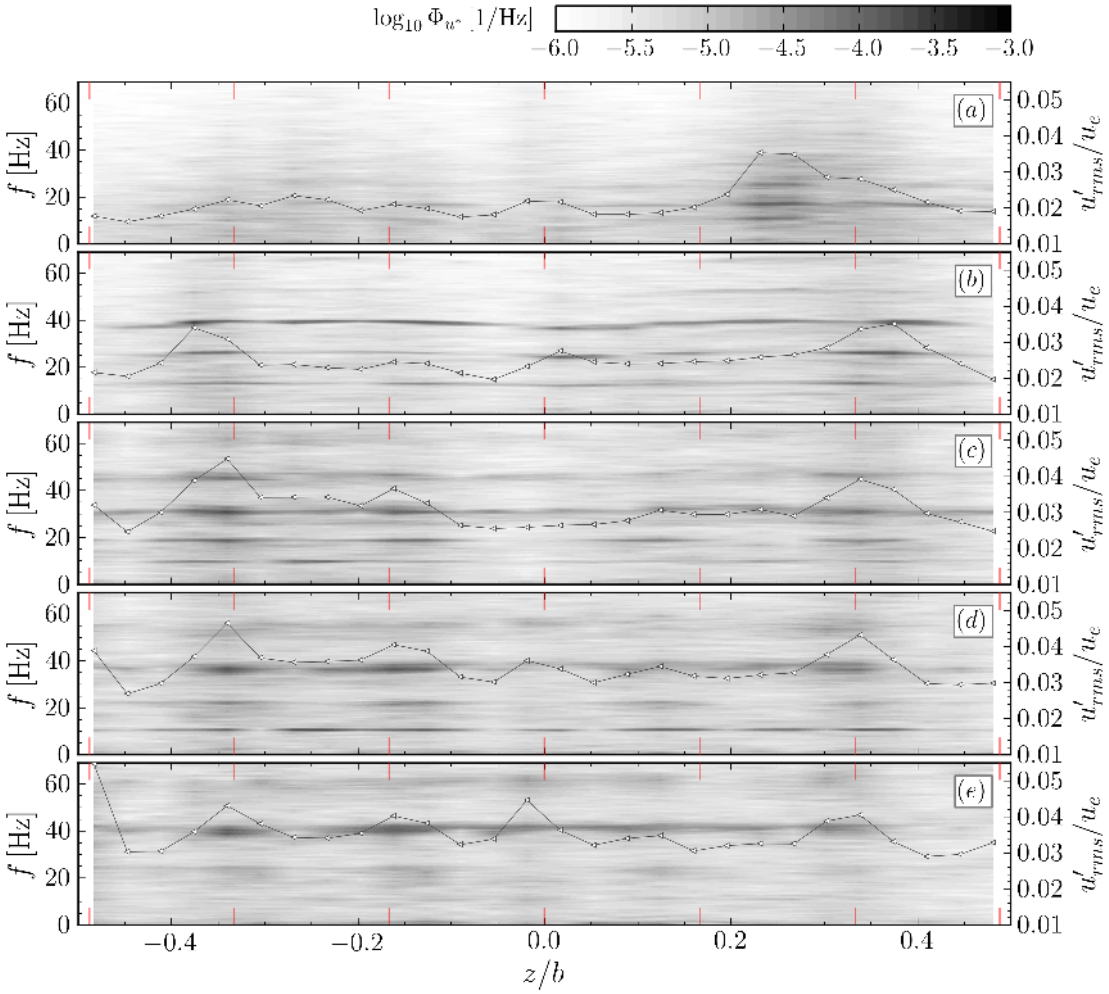

Figure 4.25. Spanwise profiles of u'_{rms}/u_e at $x/L = 0.58$, $y/\delta_0 = -0.45$, for several values of the suction parameter S, (scale on the right), superimposed to colour maps of the distributions of the energy of the velocity fluctuations across the span. Figure (a): $S = 0$, (b): $S = 0.008$, (c): $S = 0.024$, (d): $S = 0.039$, (e): $S = 0.055$.

For what regards the velocity fluctuations in the cavity region, figure 4.25 show a combined view of the profiles of u'_{rms}/u_e, with the scale on the right of the figure, and colour maps of the power spectral density distribution of the normalised velocity fluctuations with the frequency scale on the left, measured along the span at the same control point as in figure 4.24.

The profiles of the root-mean-square value of the velocity fluctuations are characterized by a quasi-symmetric pattern, except for the no control case, where there

is only one large peak of u'_{rms}/u_e located at $z/b \approx 0.25$. However, in most of the cases the peaks of the profiles coincide with the locations of the ribs of the cavity model, especially at higher values of S, which indicate a strong effect of the way suction is applied to the flow.

For what concerns the colour maps, it is not an easy task to identify a pattern describing the distribution of energy at the various frequencies and the effects of the suction, but the figure indicates that most of the fluctuation energy is found at low frequencies, and, more precisely, at multiples of a frequency around 10 Hz, not much influenced from the value of S. Even in no control case, the frequency of this low frequency motion is not exactly the same as observed in the previous chapter, where a slightly lower frequency was encountered.

In any case, the profiles of figure 4.24, and the spectral analysis of the velocity fluctuations in the cavity region, suggest that control of the flow by suction, as investigated in the experiments on configuration A is not able to dampen the three dimensional structure of the cavity flow and in particular the low frequency oscillation of the vortex core, which is strongly tied to the three dimensional modulation. It is not possible to assess from the available data if the three-dimensional characteristics of the flow in controlled conditions are due to or are enhanced by how suction is applied in the cavity, but the comparison of the mean velocity profiles before and after the cavity seems to indicate the important conclusion that the behaviour of the vortex core is not very important for the effectiveness of the TVC technique, especially when control by suction is applied to the flow.

4.4 Effectiveness of the control

The parameter which has been used to assess the effectiveness of the TVC is the ratio between the momentum thicknesses of the downstream to upstream boundary layers, θ/θ_0. This parameter is relevant since it may be used to estimate the effectiveness of the control on a complete airfoil. In fact, if $\theta/\theta_0 < 1$ the boundary layer flowing on the airfoil past the cell would be strongly energised preventing or delaying separation of the flow.

Figure 4.26 shows the behaviour of this important parameter with respect to the value of the suction, here represented by the relevant parameter y_q/δ_0 as discussed at page 85.

The figure reports data for both CASE1 and CASE2. For CASE1, the data start at 2.0 in no-control conditions, since the boundary layer becomes turbulent and strongly increase in thickness past the cavity. We observed a clear reduction of θ/θ_0 as y_q/δ_0 is increased, with a fair linearity. Then, when the suction parameter y_q/δ_0 reaches approximately a value of 1, θ/θ_0 settles on an asymptotical value at around 0.35. This curve is a clear demonstration that y_q/δ_0 is the relevant parameter

determining the effectiveness of the control by suction and confirms the proposed model of figure 3.15. The horizontal asymptote also indicates that it is not helpful to increase the suction rate beyond $y_q/\delta_0 = 1$ because no decrease of momentum thickness can be achieved, whereas the energy expenditure will increase, likely with the cube of S.

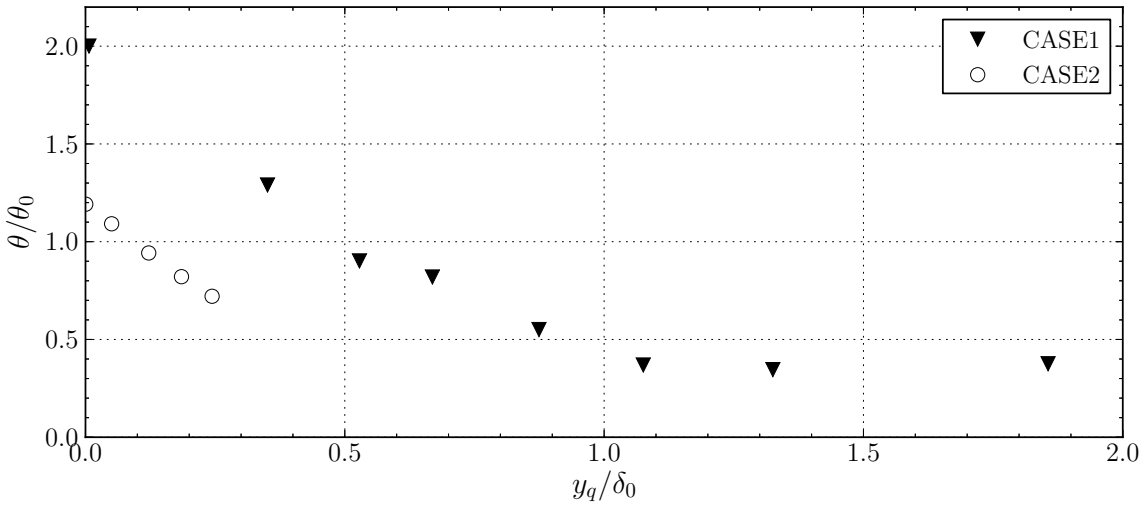

Figure 4.26. Effects of the suction rate on the reduction of the momentum thickness of the boundary layer at $x/L = 2.05$. The suction rate has been rescaled using the parameter y_q/δ_0.

For what concerns CASE2, data is limited by the very large thickness of the incoming boundary layer, which coupled to the limitation of the suction system did not allow the testing of the control for values of y_q/δ_0 larger than 0.25. Nevertheless, some considerations can be given based on by the available data only. The data starts from a value of θ/θ_0 slightly superior to one, since the effect of the cavity in no-control conditions is not as disruptive for the incoming flow as in CASE1, even though it is higher than one, meaning that there is an inherent dissipation in the presence of the TVC. Note that if no cavity was present, but a straight flat plate, the ratio θ/θ_0 would have been about 1.15, (computed with the integral boundary layer equation), in reason of the increase of θ due to the high wall shear stress of a turbulent boundary layer. Please note that for CASE1 the increase is virtually zero, because of the very low skin-friction coefficient.

As y_q/δ_0 starts to increase, the momentum thickness of the downstream boundary layer decreases as well, with a slope surprisingly similar to that of CASE1. This result was certainly not expected because of the large difference in the shape of a turbulent and of a laminar boundary layer. This means that in order to decrease θ below the upstream value, a very little amount of suction is required, of the order of $y_q/\delta_0 \approx 0.1$. By doing so, the near-wall layers of fluid in the boundary layer, i.e.

the slowest, are ingested.

Despite the limited data it is argued that the asymptotical region will be reached even for the turbulent case for $y_q/\delta_0 = 1$. Indeed, for values of y_q/δ_0 between 0.25 and 1 the curve of θ/θ_0 is expected to decrease continuously, but with a lower slope than that for $y_q/\delta_0 < 0.25$. Instead, the asymptotical value is expected to be lower than that for CASE1, essentially due to the higher Reynolds number, which will cause a thinner laminar boundary layer developing at the cavity shoulder.

4.5 Control of the flow by suction in region B

This section presents some relevant results regarding application of suction in region B, i.e. on the downstream edge of the cavity, as depicted in figure 4.1-(a). The discussion is more limited and only highlights the most significant differences between the two conditions of suction.

4.5.1 CASE1

Figure 4.27 shows a comparison between the two regions A and B, in terms of profiles of the mean velocity, figures on the left, and profiles of the root-mean-square value of the velocity fluctuations, figures on the right. The two top figures refer to no-control conditions, where $S = 0$, while the two bottom figures refer to a condition of higher suction, $S = 0.1$.

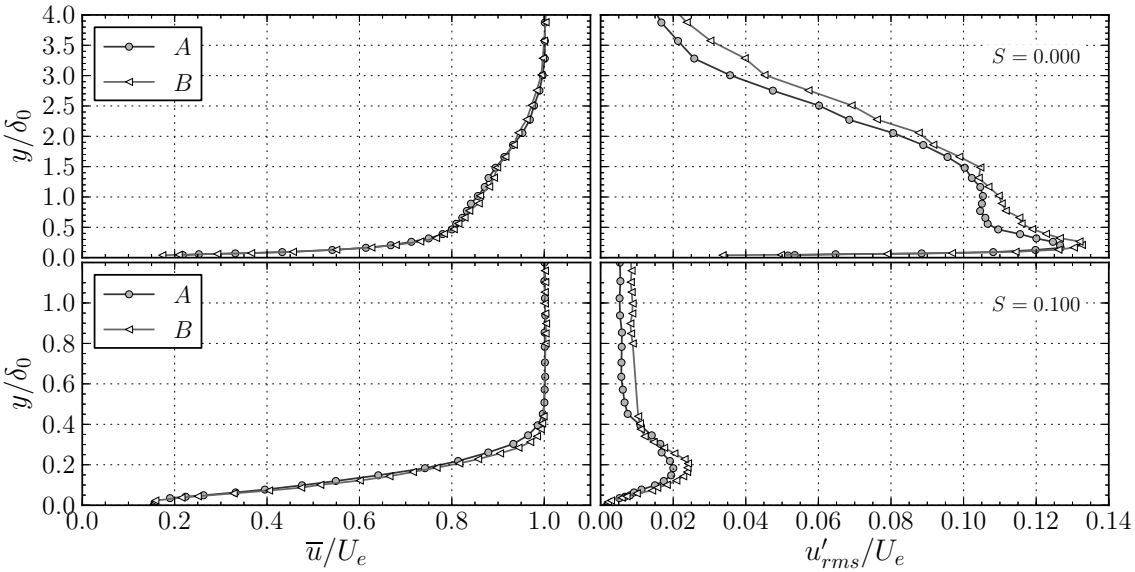

Figure 4.27. Comparison of the profiles of $\overline{u}/u_e$, left, and of u'_{rms}/u_e, right, between the suction regions A and B, for two conditions of suction, at $x/L = 2.05$.

As expected, in the no-control case the two control conditions result in a very similar structure of the near-wall flow downstream of the cell. In fact, the two mean velocity profiles have the same thickness and agree well between each other.

The no-control condition shows a weak difference in the intensity of the velocity fluctuations, top-right, since slightly larger values are observed for case B, across the entire boundary layer. Nevertheless, the structure of the profile of u'_{rms}/u_e is analogous. This slight difference is to be attributed to a different evolution of the shear layer and also probably to an interaction of the impinging flow with the porous surface on the downstream edge for region B.

When control is switched on, and for large values of the suction parameter S, as discussed in depth previously the boundary layer downstream of the cell becomes thinner, with a thickness of about 40% of that of the upstream boundary layer. This mechanism occurs for both control conditions A and B, and the resulting boundary layers have very similar thicknesses. However, close examination of the mean velocity profiles at $S = 0.1$, and at other values of S not shown in the figure, indicates that the effects of application of suction in region B seems to be slightly more effective. It is important to stress that it is not possible to understand if such a result is due to the fact that the suction region B is nearer to the measurement location $x/L = 2.05$, or if this location is more effective.

Interestingly, the reduction of the boundary layer thickness happens for two separate mechanisms for region B. One way is that part of the slower layers of fluid of the upstream flow are ingested in the cell, as discussed extensively in the previous pages, through the small portion of porous region below the downstream corner. This is the same mechanism fully at play for case A. However, since part of the porous surface also covers the region downstream of the impingement location, suction of the near-wall flow occurs similarly to classical boundary layer suction. This may also help explaining why the boundary layer thickness is slightly smaller for case B, since this flow has been subject to strong suction a short distance upstream.

For what concerns the profiles of u'_{rms}/u_e, the reduction of the intensity of the fluctuations, with respect to the no-control case, is drastic for both cases, but suction in region A seems to dampen slightly more the amplitude of the fluctuations. The very slight difference that can be noticed in the profiles of u'_{rms}/u_e is likely due to small perturbations introduced into the laminar flow by the holes of the porous region. These have a diameter of 1.5 mm which is fairly large compared to the thickness of the boundary layer forming there, which is certainly smaller than the thickness at $x/L = 2.05$, which is about 1.7 mm.

Further insight into the effects of the location of suction on the flow are given in figure 4.28, which refers to the shear layer, at $x/L = 0.58$. As before, the left figures show profiles of the mean velocity, while the figure on the right report profiles of u'_{rms}/u_e. The two top figures refer to the no-control case, $S = 0$, while the figures at the bottom refer to a condition where $S = 0.064$, slightly lower than that of the

corresponding figures in figure 4.27. For what concerns the no-control condition, top

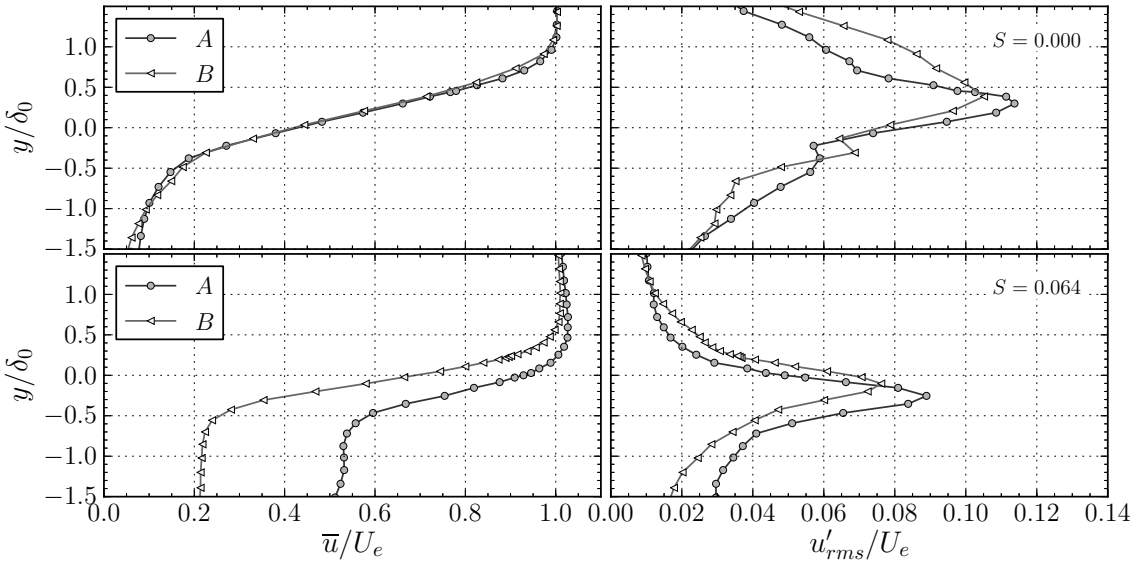

Figure 4.28. Comparison of the profiles of $\overline{u}/u_e$, left, and of u'_{rms}/u_e, right, between the suction regions A and B, for two conditions of suction, at $x/L = 0.58$.

figures, application of suction in the two regions leads to a slight difference in the mean velocity profile, even tough they should be nominally the same. For region A the velocities in the top layers of fluid in the cell, at $y/\delta_0 = -1.5$, are slightly higher, indicating a slightly faster flow in the cell. Larger differences can be noticed in the profiles of u'_{rms}/u_e, top right. In fact, the peak value is slightly smaller for case B but the region interested by intense fluctuations is larger. As stated previously, these differences might essentially be due to the presence of the porous wall, which modifies the delicate structure of the cavity flow by allowing transpiration of fluid across its surface.

The effects of control are shown in the two bottom figures of figure 4.28. There is a sharp difference between the two suction cases, especially in terms of the mean velocity profile, in spite of the quite similar structure of the flow downstream of the cell, as observed in the corresponding figure in figure 4.27. In fact, suction in region A results in much higher velocities along the entire shear layer and more significantly beneath it, in the top-most layers of the cell flow. In this latter region, the mean velocity is more than the double than that observed for case B, and it is of the order of $0.5u_e$

A likely explanation for such behaviour can be given considering the model introduced and discussed in the previous sections. It can be argued that for a given value of suction, there is more high momentum fluid entering the cavity for suction in region A than for region B. This happens because the porous surface for the

latter case is covering only partially the interior cavity wall and extends slightly further the downstream cavity corner. This means than less high momentum fluid is being ingested in the cell, resulting in a lower entrainment of the cavity flow and in lower velocities. Furthermore, the downward deflection mechanisms, discussed extensively in the previous sections, can be introduced to explain the larger velocities in the shear layer, i.e. for $-0.5 < y/\delta_0 < 0.5$. In fact, the larger amount of fluid which must enter in the cavity for mass conservation reasons will result in a higher downward displacement of the flow, which appears as a virtual increase of velocity in the shear layer. However, the larger velocities in the cell may also contribute to such an increase, especially in the lower layers of the shear layer, due a lower loss of momentum for these layers.

These results seem to indicate a very weak relationship between the intensity of the trapped vortex and the mean velocities in the near wall flow downstream of the cell.

The effects of the suction location on the profiles of u'_{rms}/u_e are reported in the bottom-right figure in figure 4.28. In both cases the peak value of u'_{rms}/u_e is reduced by the control with respect to the no-control case. This indicates also a lower spreading of the shear layer as it evolves downstream. The major difference between the two cases is that application of suction in region B seems to result in a lower peak value of the velocity fluctuations root-mean square value. Furthermore, the peak position for region B is located slightly upper than that of the other case, because of the lower downward displacement of the shear layer. As discussed above, the difference is of the order of $0.15\delta_0$. Interestingly, higher fluctuation intensity are observed in the cavity region, $y/\delta_0 < -0.75$, for case A, likely due to the larger mean velocities in this region.

Flow visualisations

Extensive flow visualisation studies, targeting the cavity flow, were performed also for this second condition of suction, and for several values of the suction parameter S. However, for the sake of brevity, only results for the largest tested value of S are reported here, i.e. $S = 0.1$. Figure 4.29 displays a short sequence of six consecutive snapshots illustrating the time evolution of the structure of the cavity flow. One each three snapshots is reported to better highlight the motion of the coherent structure in the flow, so that the time separation between two images is 3/400 s, since the frame rate was set at 400 Hz. Part of the porous region along the downstream corner of the cell is also visible, even though not so clearly.

The full animated sequence clearly highlights the vortical motion of the cavity flow, which transports a number of smaller scales structures. For case B, a similar mechanism to that introduced for condition A, to explain the enhanced rotation of the vortex flow when the control is switched on, can be introduced. However,

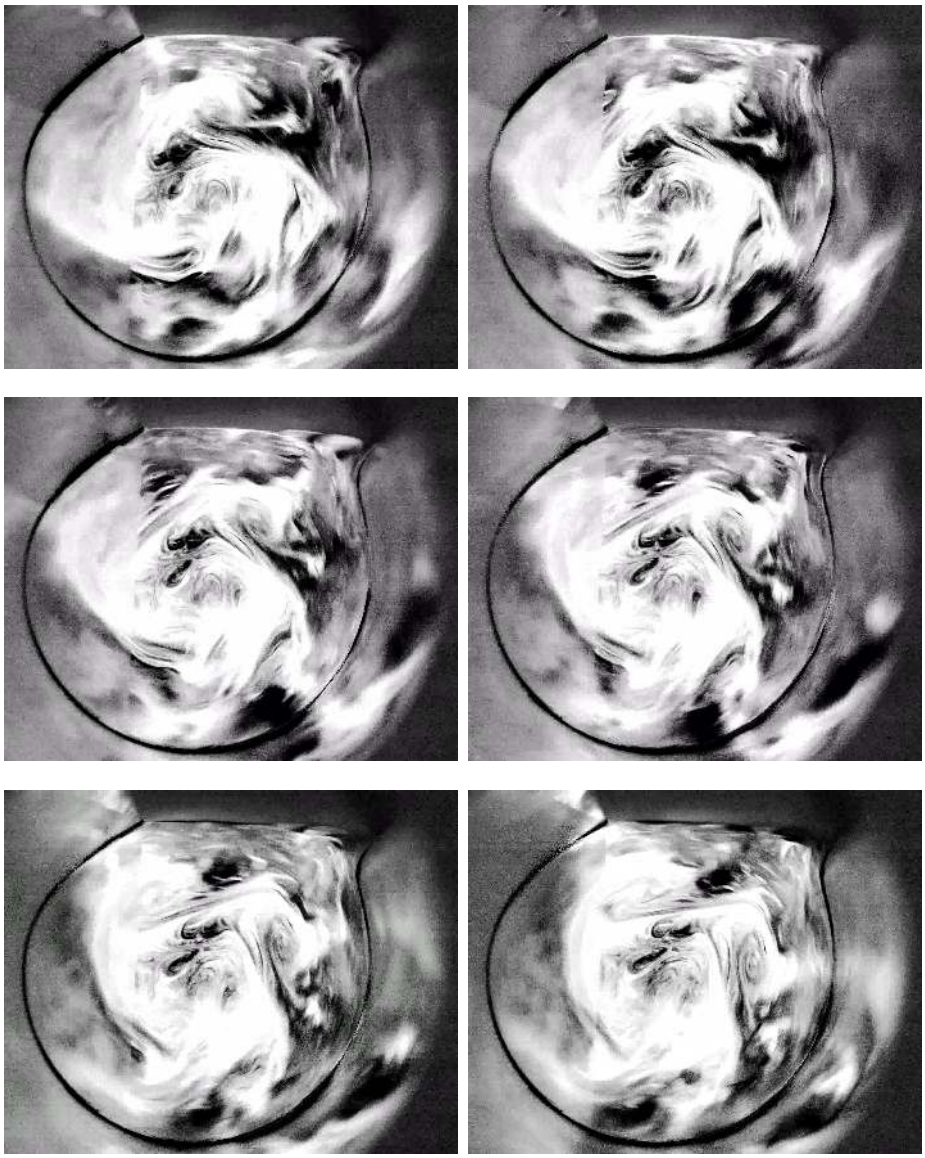

Figure 4.29. Snapshot sequence of the flow visualisation for CASE1 in the mid-span, sorted left to right, top to bottom. $S = 0.1$. Time delay between two subsequent snapshot is 3/400 s.

suction is region A, that is on the upstream side, implies that the flow entering into the cavity must flow along the entire wall. Thus, the internal vortical flow is entrained much more by this high speed fluid, resulting in larger velocities in the cavity. For case B this mechanisms is not complete, since high momentum fluid entering the cavity is quickly ingested at the downstream edge, and it cannot help

intensifying the vortical structure.

The cavity flow is bounded by a thin shear layer which, as in case A, displays much weaker coherent fluctuations than in no-control conditions, as visible in the visualisations in the last third of the shear layer. The small energetic structures generated by the Kelvin-Helmoltz instability are ingested by the suction at the impingement, which strongly reduces the unsteadiness of the flow in this region. However, it must be noted that application of suction in region A also resulted in a lower turbulence activity in this region, as a result of the strong downward deviation of the flow in this region.

4.5.2 CASE2

Figure 4.30 shows, for CASE2, a comparison between the two regions of suction in terms of profiles of the mean velocity, left figures, and of the root-mean-square value of the velocity fluctuations, right figures, in no-control conditions, top, and with control, bottom. In no-control conditions, the differences observed are to be

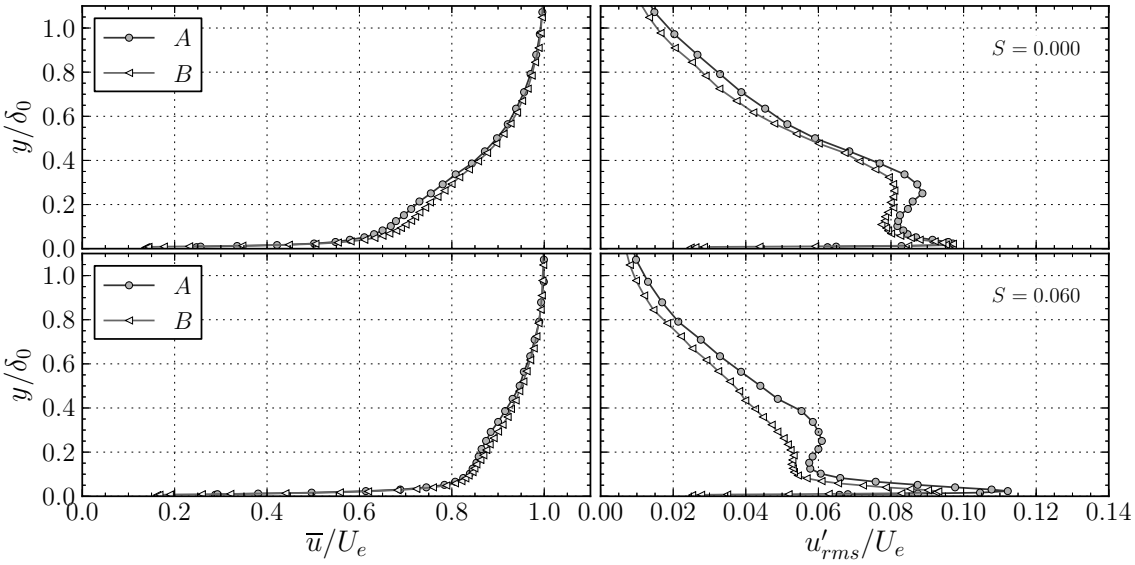

Figure 4.30. Comparison of the profiles of $\overline{u}/u_e$, left, and of u'_{rms}/u_e, right, between the suction regions A and B, for two conditions of suction, at $x/L = 2.05$.

attributed to a different interaction between the porous wall and the cavity flow, as explained previously, which also results in a different flow regime in the cell. For CASE2 this difference is such that the near-wall flow downstream of the cell is slightly faster for case B especially for distances $0.1 < y/\delta_0 < 0.4$. This is the region of velocity defect discussed for figure 4.19, which has been associated to that part

of the shear layer flow with the largest velocity fluctuations, and which after the impingement on the downstream corner lifts up from the wall up to this distance.

Slight differences between the two suction cases can also be noticed in the profiles of u'_{rms}/u_e. In fact, except for the near-wall region, $y/\delta_0 < 0.05$, the profile for region B indicates a slightly lower intensity of u'_{rms}/u_e consistently across the entire boundary layer. More importantly, the difference between the cases A and B is more pronounced at $y/\delta_0 \approx 0.3$, i.e. the second peak associated to the velocity deficit in the mean velocity profile. Such a difference is to be attributed to a diverse evolution of the shear layer in reasons of a different behaviour of the cavity flow.

When control is switched on, bottom figures in figure 4.30, the mean velocity profiles for both the cases indicate a strong enhancement of the velocities of the wall flow downstream of the cell, with respect to the unactuated case. Furthermore, there is really no such a remarkable effect of the region were suction is applied as it was also pointed out for CASE1, even though the velocity profile for case B is slightly fuller, especially around $y/\delta_0 = 0.3$.

Nevertheless, a significant difference is observed in terms of u'_{rms}/u_e, bottom right figure of figure 4.30. It can be noticed that application of suction in region B strongly reduces the intensity of the near-wall peak of the turbulent velocity fluctuations with respect to region A, which instead results in an increase of this quantity with respect to the unactuated case. Furthermore, both conditions results in a noticeable reduction of the turbulent velocity fluctuations across the entire boundary layer and especially in the velocity defect region. Here the values of u'_{rms}/u_e are about 30% lower than those observed for the unactuated flow. Furthermore, suction in case B seems to have a greater effect on the structure of the turbulence since the velocity fluctuations are more damped.

Interestingly, the y/δ_0 position of the peak in the velocity defect moves towards the wall when suction is applied in region B. A likely explanation for this result is that the wall flow after the impingement is being deviated towards the wall by the strong suction applied over this region. Such a mechanism may also explain the lower near-wall peak observed for the same case, since the buffer region of the turbulent wall flow after the impingement is ingested.

The last result concerning the comparison between the suction regions is reported in figure 4.31, which shows profiles of the mean velocity, on the left-hand-side, and of u'_{rms}/u_e, right-hand-side, for a no-control case, top, and in control conditions, bottom. Concerning the mean velocity profiles in no-control conditions, we observe a weak difference in the structure of the shear layer between the suction cases in the region $-0.7 < y/\delta_0 < -0.2$, i.e. in the topmost layers of fluid of the cavity, just beneath the shear layer. In fact, slightly larger velocities are observed for case A, with and edge velocity of the order of $0.22u_e$ against a value of $0.15u_e$ for case B. This difference, indicative of a different evolution of the SL may be held responsible of the diverse structure of the wall flow downstream of the cell.

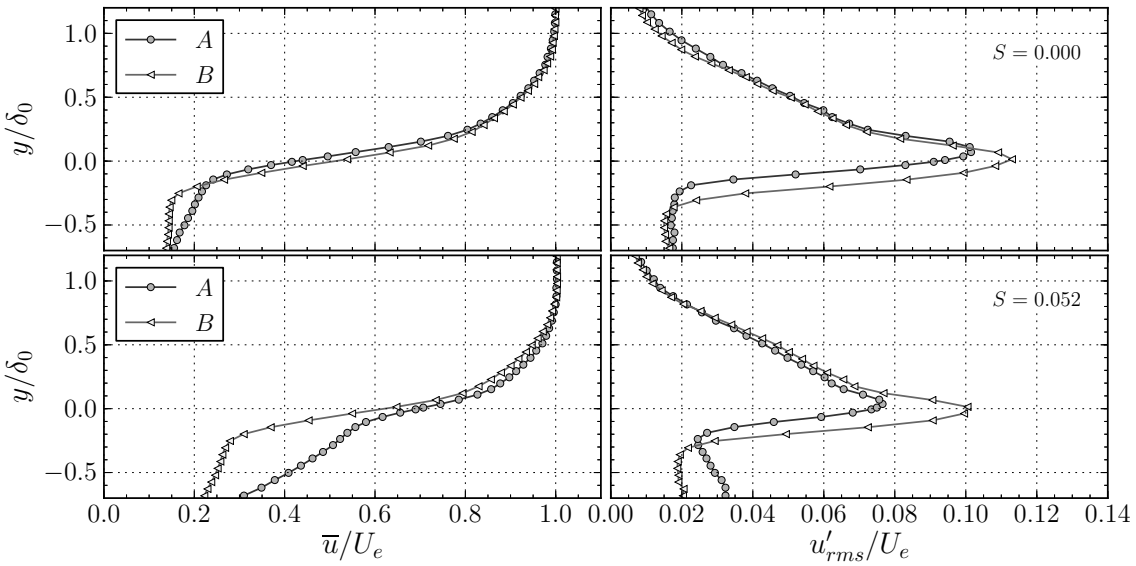

Figure 4.31. Comparison of the profiles of $\overline{u}/u_e$, left, and of u'_{rms}/u_e, right, between the suction regions A and B, for two conditions of suction, at $x/L = 0.58$.

This difference is also associated to a modification of the turbulence structure of the shear layer. In fact, the profile of u'_{rms}/u_e for case B, top-right figure, indicates a more intense peak, about 15% than for case A. In addition, the vertical size of the region of large turbulent fluctuation is higher for case B, even tough the values of u'_{rms}/u_e are very similar in the cavity region.

When control is switched on, at $S = 0.052$, the mean velocity profile for case A indicates much higher velocities across the entire vertical scale shown in the figure. In particular, the velocities are much larger than for case B in the region $-0.7 < y/\delta_0 < -0.1$. These layers of fluid are those which are accelerated by the fluid ingested into the cavity by the suction, as explained at page 90, when discussing flow visualisations for case A. The lower mean velocities for case B are certainly due to the fact that the mass of high momentum fluid ingested in the cavity is lower for this case for a given value of S since part of the porous region is located out of the cell and does not contribute to this mechanism, as explained while discussing the flow visualisations in section 4.5.1. As a result of this faster flow in the region just beneath the shear layer, the mean velocities in the shear layer itself are enhanced, likely because of the lower dissipation encountered by the turbulent flow coming from upstream, with respect to case B and the no-control case.

The structure of the turbulence in the shear layer is also significantly modified by the control, and more importantly when suction is applied in region A. In fact, a marked reduction of the peak of u'_{rms}/u_e of about 25% is observed for this condition, even tough a reduction of the peak amplitude is observed also for case B. As also

pointed out previously, this strong reduction may be connected to the the lower velocity gradients, essentially the term $\partial\overline{u}/\partial y$, of the mean flow, with the associated production of turbulent kinetic energy.

Such low values of u'_{rms}/u_e in the shear layer for case A, with respect to case B, seem to been in contrast with the lower values of this quantity in the turbulent wall flow downstream of the cell as discussed for figure 4.30. In fact, while discussing those results a lower fluctuations amplitude was noticed across the entire height of the downstream boundary layer, both in the near-wall region of the buffer layer and in the second peak at $y/\delta_0 \approx 0.3$, associated to the turbulent flow of the shear layer. This result is certainly due to the influence of wall suction downstream of the cell, since the porous region extends slightly further than the rounded corner. In fact, it is well known, Antonia et al. [1995], that control of turbulent boundary layers with suction can dramatically decrease the intensity of turbulence.

4.5.3 Discussion about the location of suction

The results presented in section 4.5 have demonstrated that there is a strong effect of the position of suction on the structure of the internal cell flow. Application of suction is region A results in larger mean velocities, for both CASE1 and CASE2, due to the enhanced ingestion mechanism. However, it appears very important to stress that, when control is on, this change is not reflected in the structure of the flow downstream of the cell, which is not severely changed by changing the location of the porous region, especially in term of the mean velocity profile. This seems to indicate that the important parameter is the *value* of the suction and not its location.

4.6 Remarks and conclusions

This chapter has presented the results of an investigation whose objective was to help understanding how suction modifies the base flow of a trapped vortex cell and how it can make a TVC an effective control device. Suction in two different regions has been investigated and more emphasis has been given to application suction inside the cell, region A, on the upstream surface.

It has been shown that suction in the cavity region, in region A, must be associated to the ingestion of part of, or all, the shear layer. The result is that high momentum fluid impinges on the downstream edge of the cavity, and forms a boundary layer thinner than that if the cavity was not present and even thinner than the upstream one, if the suction is high enough. For CASE1, and when the suction is very strong, i.e. for $y_q > \delta_0$, a laminar boundary layer develops from the downstream edge of the cavity. For CASE2, the suction is not strong enough to ingest

completely the boundary layer, but there is, nevertheless, a reduction of the momentum thickness of the downstream boundary layer. Furthermore, despite suction being an active technique, no energy is added *into* the flow, but rather it operates by redistributing the energy across the flow field.

A second effect of the suction in region A is that the ingestion of high momentum fluid into the cavity produces an increase of the mean velocities in the cell, resulting in a strongly energised vortex flow. However, the results suggest that the enhancement of the mean velocities in the wall flow past the vortex cell are not causally connected to the more intense rotation of the vortex flow, but are due exclusively to the ingestion mechanism. However, modification of the mean flow, and in particular of the shear layer mean velocity profile, strongly reduces the receptivity of the shear layer to the acoustic perturbation at the wind tunnel resonance frequency. As a consequence, the velocity fluctuations at this frequency are thus strongly damped even though some energy concentration appears at larger frequencies, at a Strouhal number of the order of 3-4, and increasing with the suction rate, i.e. with the mean velocities in the cavity.

When suction is applied in region B, the intensity of the vortex flow in the cell is not enhanced as for case A, in both CASE1 and CASE2. This occurs because a lower amount of high momentum fluid is entering the cavity, and that mass does not travel along the entire cavity wall, driving the rotation of the rest of the fluid. However, the near wall flow downstream of the cell appear very similar to that of case A, (only very slightly faster), when suction is applied in region B. Incidentally, it is not understood if this is a consequence of the fact that the location of suction is nearer to the measurement point or if that location is more favourable *per se*.

The results obtained in control conditions suggests that, on a TVC controlled airfoil, the additional momentum in the boundary layer downstream of the cell may help delaying or eliminating flow separation, such that the pressure drag on that airfoil can be substantially reduced. Furthermore, at low incidences, when the flow is fully attached and drag is mainly due to skin friction, the reduction of the momentum thickness results is a reduction of the width of the airfoil's wake, which is proportional to the thicknesses of the boundary layers on the upper and lower surfaces. Such reasoning may help explaining the good performance of the airfoil in TVCS configuration of the experiments of Lasagna et al. [2011].

An experimental comparison with a classical boundary layer suction has not been performed, but some conclusions can be drawn, to explain the difference in the drag coefficient between the BS and the TVCS configurations of the experiments of Lasagna et al. [2011]. It is postulated that, in control conditions, the presence of the cavity, which creates a impingement point for the flow on the downstream edge, may produce a more favourable development of the boundary layer developing from this point with respect to suction on a flat solid wall case, also in consideration of the strong acceleration of the flow due to negative pressure gradient after the stagnation

region on the TVC. This indication is not completely convincing, especially since this region of the flow is severely affected by the control in case B, and the structure of the flow downstream of the cell is very similar to that of case A. Nevertheless, more research should be carried out in order to fully understand the picture. In fact, the strong difference in drag coefficient of the two configurations of the experiments of Lasagna et al. [2011], seems to indicate that there may be alternative and more efficient strategies to apply suction on an airfoil surface for boundary layer control.

As a final note, it must be observed that suction of the flow is a very expensive control strategy and very likely not worth the cost and complexity. In the experiments, a very large energy was spent to provide suction of the flow in the cell and the net balance was surely strongly negative. This is one of the motivations to study more efficient active control techniques, such as synthetic jet control, as discussed in the next chapter.

Chapter 5

Open-loop control of the TVC flow with a synthetic jet actuator

In this chapter we discuss an alternative active control technique which has been investigated to control the cavity flow, such as to obtain a more energetic flow downstream of it. This technique is based on a well known type of actuator, i.e. a synthetic jet, (Glezer and Amitay [2002]). Synthetic jets have emerged as a promising flow control technique since they are able to introduce a significant amount of momentum into the flow field without requiring an external source of fluid. Seifert et al. [1993] have demonstrated that oscillatory forcing can be more effective than a steady control action, with the addition of lower power requirements. Furthermore, the intrinsic periodicity of the control can be leveraged, because the time or spatial scales of the unsteady forcing can couple to or break relevant physical mechanisms of the uncontrolled flow, (Mittal et al. [2005], Glezer and Amitay [2002]).

In fact, this second control technique has a strongly unsteady actuation, as opposed to the control strategy discussed in the previous chapter, i.e. suction, which does not have this property. Significant effects of the control unsteadiness on the cavity flow are expected in particular on the shear layer.

5.1 Premise

5.1.1 Design of the synthetic jet device and motivations

The synthetic jet system is thoroughly described in section 2.7, and, therefore, this section is devoted to present the motivations behind the choice of this actuator and of it position in the cavity geometry.

The synthetic jet slot was positioned just below the impingement region for mainly two reasons. The first was to help regularising the erratic injection of packets

of high-momentum external flow into the cavity, which was recognised as one of the driving factor of the rotation of the cell's flow in no-control conditions. The second, and more important, was based on the alleged mechanisms that the jet could inject momentum downwards into the cavity and tangentially to its surface, with the aim of driving a stronger vortical flow.

These two points are clearly in opposition with the mechanism at play in suction control. In fact, as it has been discussed in the previous chapter, the control mechanism for suction control is to remove the slower layers of fluid flowing past the cavity, such as to obtain a fresh and thinner boundary layer developing from the cavity shoulder. By contrast, synthetic jet control operates such as to increase the rotation of the vortical flow, which in turn can energise the shear layer flow flowing past the cavity, resulting in a more energetic flow downstream of it.

In this respect, it is argued that the chosen position may maximize the proposed control mechanisms. Other locations of the synthetic jet slot have been investigated in the literature of control of cavity flows, for example just under the cavity leading edge, Efe et al. [2005]. However, control of the flow from this position has a different objective since it is best suited to control and reduce the amplitude of the cavity tones, rather than to enhance the velocities in the near-wall flow downstream of the cavity itself, as it is in the present case.

5.1.2 Objectives

This part of the research was conducted in order to answer some specific questions. The first was to verify the proposed control mechanism for synthetic jet based control and its effectiveness with respect to the effects of the control parameters. A further important aspect was to study the response of the flow, in particular of the shear layer, to periodic forcing. In fact, a strong and complex coupling of the shear layer with the actuation signal was expected, as shown for example by the recent work of Sipp [2012].

These questions have to be fully answered in order to fully understand the basic dynamics of the cell's flow subject to periodic forcing. In fact, this understanding is required in order to proceed in implementing a closed-loop control strategy of the cavity flow, which is briefly discussed in the last chapter of this thesis.

5.2 Characterisation of the synthetic jet actuator

The first step of this research has been to characterise the output of the synthetic jet device, as a function of the frequency f_j and the amplitude in voltage A_j of the sinusoidal control signal $e(t) = A_j \sin(2\pi f_j t)$. These experiments were necessary, since it is usual for synthetic jet systems to have a strongly varying response, (i.e.

the mean output velocity u_j), as a function of the control signal frequency, mainly due to the geometry of the system, which may result in resonance, and to the dynamical response of the actuator, (i.e. of the loudspeaker in the present case).

To this end an hot wire probe was positioned in the slot region, at a spanwise location corresponding to the middle of one of the six spanwise division of the cavity model, (see figure 2.5 for details). Due to the strong curvature of the flow in the last part of the synthetic jet cavity before the exit at the slot, the maximum mean velocity was not observed in the exact geometric centre of the slot itself. Instead, the probe has been moved slightly such as to find this extremum position, where a more realistic characterisation of the jet output could be performed.

Tests were also conducted to assess the uniformity of the forcing along the spanwise direction, both along each of the six slots and between the slot themselves. These tests resulted in good properties of the actuator assembly, with no major difference between the six slots. Obviously, the output was zero at z positions corresponding to the location of the ribs of the cavity model.

The actuator characterisation consisted in acquiring a velocity time history for each of the 5500 couples (f_j, A_j), where f_j varied from 5 to 500 Hz, in steps of 1 Hz, and where A_j varied from 0.1 V to 1.1 V, in steps of 0.1 V. In order to provide sufficient convergence of the mean value and in order to shorten the total run times, the velocity signal was acquired for 100 periods of oscillations, thus the total acquisition time decreased as f_j increased, at a varying sampling frequency not less then $100 f_j$, to achieve good resolution of the velocity signal.

For each couple (f_j, A_j), the representative mean jet velocity, defined as:

$$u_j = \frac{1}{T} \int_0^{T_j/2} U_j(t) dt \tag{5.1}$$

was computed by taking the half the average of the measured velocity. This approximate method was necessary because of the practical difficulty to integrate the velocity signal only during the blowing phases, but was accurate enough since the velocity signal during the blowing and suction phases of the synthetic jet were reasonably similar. Please note that the velocity signal measured by the hot wire is always positive, since the probe does not distinguish the direction of the flow but senses only its absolute value.

The results of this investigation are presented in figure 5.1-(a), which shows a colour map of the mean jet velocity u_j, as a function of the forcing frequency f_j and the forcing voltage amplitude A_j. Four selected iso-lines are reported on the same figure, for clarity. In addition, part (b) of the same figure reports the behaviour of u_j as a function of f_j, for three selected voltage amplitudes.

It can be observed that the output of the synthetic jet system has a complex response to the periodic driving signal. For a given amplitude, the synthetic jet has a significantly larger output at frequencies around 75 Hz and 330 Hz, a symptom

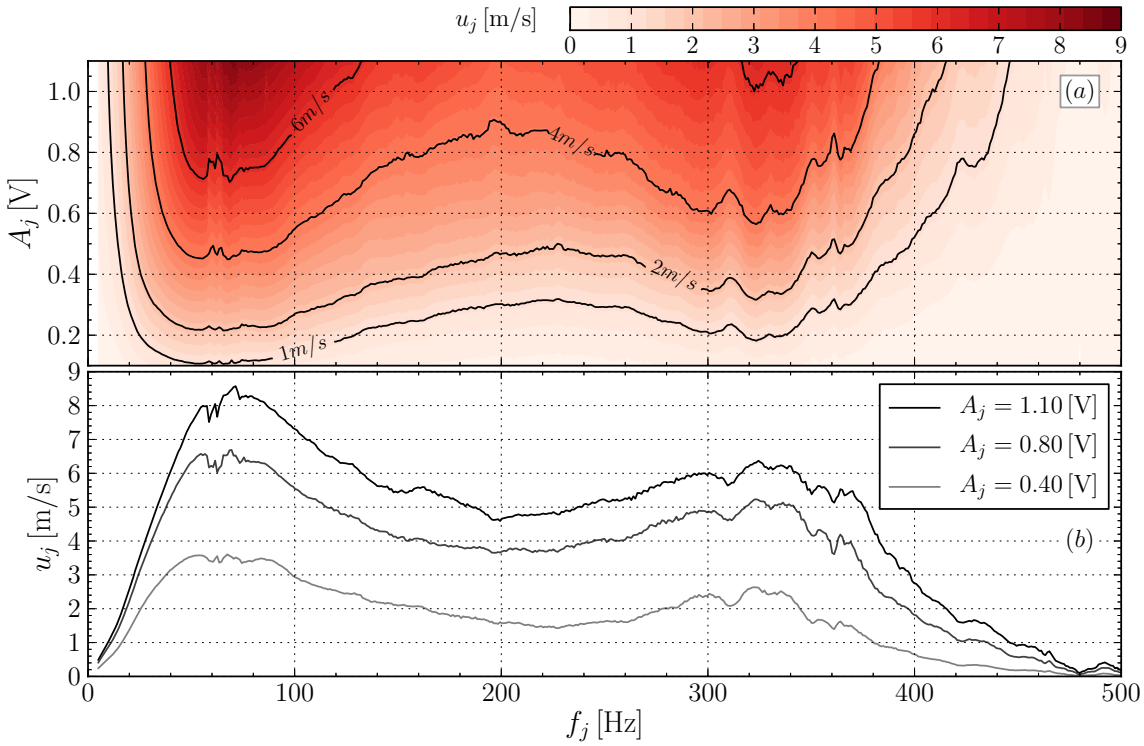

Figure 5.1. Color map of the mean jet velocity u_j, as a function of the forcing frequency f_j and the forcing voltage amplitude A_j, figure (a). Behaviour of u_j as a function of f_j, for three selected voltage amplitudes, figure (b).

of the presence of resonance frequencies of the entire assembly. On the other hand the output of the synthetic jet drastically decreases for frequencies larger than 380 Hz. The maximum output velocity is reached for $f_j \approx 75$ Hz and at the maximum amplitude, with a value slightly in excess of 8 m/s. The behaviour of the synthetic jet system is not perfectly linear, since typically doubling the voltage amplitude does not double the output velocity, but a slightly lower value is obtained. Furthermore, the small scale details of the colour map of figure 5.1, especially those near the resonance frequencies, are repeatable and are probably due to complex acoustical behaviour of the whole synthetic jet system.

Map Inversion Since the relevant fluid dynamical parameters are u_j and f_j, the voltage amplitude is just a control parameter, regarding the details of the actuator. Thus, the inverse map $A_j = g(f_j, u_j)$ needs to be estimated from the experimental data, such that given some target value for the control parameters u_j and f_j, it is possible to find the exact voltage amplitude which produce the required output velocity at the required frequency. To this end, the experimental data of the triplets (A_j, f_j, u_j) is interpolated using a cubic bivariate spline interpolation technique, such

as to yield an approximation of the function g.

The accuracy of this approach has been verified in a later step, where the measured u_j was compared with the expected one computed from the mapping, for a given couple (f_j, A_j). The accuracy of the method was such the output velocity u_j could be set with an accuracy of 0.3 m/s within the desired value, across the entire tested range of f_j and A_j.

Forcing parameters The relevant dimensional control parameters are f_j, the time scale of the actuation, and u_j which is proportional to the amplitude of the velocity perturbation introduced into the flow. Non-dimensional equivalents for this parameters can also be chosen. A convenient reduction for f_j is to normalise it with L/u_e, the time it takes for an external fluid particle to flow past the cavity opening L. We thus obtain:

$$F = \frac{fL}{u_e} \tag{5.2}$$

However, no extensive use of this parameter is made in the following and the dimensional frequency is used instead, since, as discussed in the following, the effects of the control are clearly dominated by the performances of the synthetic jet system, rather than by a specific coupling with the flow.

For the mean jet velocity u_j, one convenient normalisation is to divide it by the external flow velocity u_e, such as to obtain the jet velocity ratio:

$$R = \frac{u_j}{u_e} \tag{5.3}$$

5.3 Results

The fundamental objective of the control should be to energize the wall-flow downstream of the cavity, i.e. to generate a boundary layer fuller then the upstream one. As discussed above a relevant parameter to assess this effectiveness is the ratio θ/θ_0, but such parameter requires to measure a full boundary layer profile for each control configuration, that is for the large amount of couples (f_j, u_j) to be tested. In order to proceed more quickly, the effectiveness of each forcing configuration is estimated by measuring the mean velocity at a single point in the downstream boundary layer and comparing it to the reference value, i.e. that of the uncontrolled flow.

This preliminary step provides good indications of the most effective regions of the parameters space, and it allows to gain insight into the effects of the control parameters.

5.3.1 Results for CASE1

The results of this preliminary investigation are reported in figure 5.2. The colour map represents the value of the mean velocity downstream of the cavity at $x/L = 1.91$, at a distance from the wall equal to $0.3\delta_0$, as a function of the forcing frequency f_j and of the jet velocity ratio R. The 600 couples (f_j, u_j) are obtained from 20 frequencies ranging from 20 to 400 Hz and from 30 voltage amplitudes A_j, logarithmically spaced from 3 mV to 1.12 V. The logarithmic spacing, starting from very low voltage amplitudes, was necessary to assess the response of the shear layer flow to very small perturbations, as will be detailed later. For each couple, the hot wire velocity signal was sampled for 15 seconds, in order to achieve good convergence of the mean velocity value. The map in figure 5.2 is not defined for all values of f_j, R

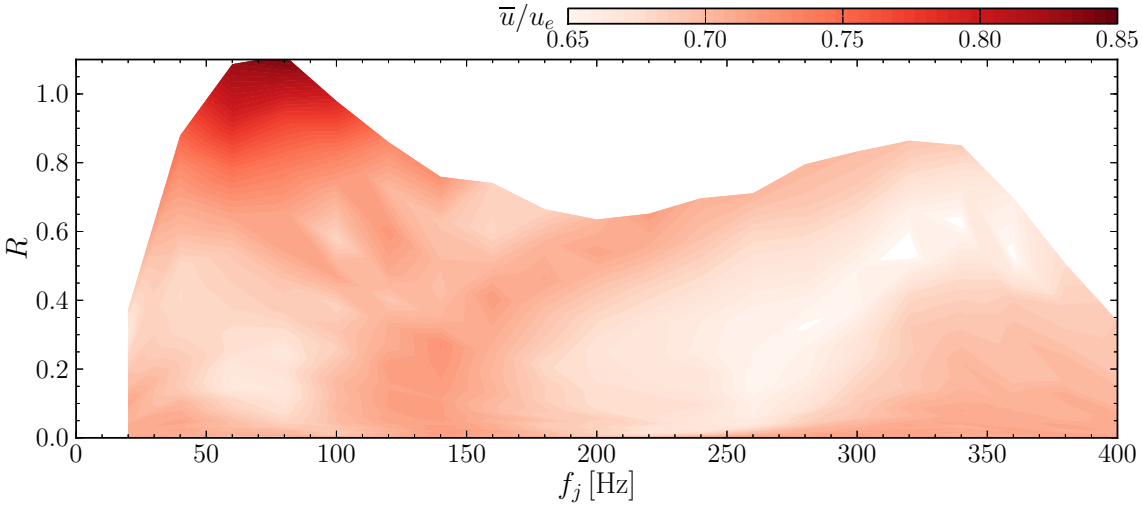

Figure 5.2. Color map of the mean velocity in $x/L = 1.91$, $y/\delta_0 = 0.3$, as a function of synthetic jet control parameters.

due to limitations of the experimental setup, since for example it is not possible to achieve $R = 1$ at a frequency $f_j = 200$ Hz, without having very large voltage amplitudes, which would damage the amplifier/loudspeaker system. In fact, the voltage amplitude is limited to 1.1 V.

The colour map clearly indicates as the most effective forcing frequency a value around $f_j \approx 75$ Hz and the higher the amplitude, the higher the effectiveness of the control. Under the most effective forcing conditions the mean velocity downstream of the cavity increases to $0.85u_e$, that is by about 20%, with respect to the uncontrolled configuration.

This first result seems to indicate a very crude control mechanism, suggesting that the larger the momentum introduced into the cavity flow, the larger is the velocity in the downstream boundary layer. However, the value of $\overline{u}/u_e$ for $f_j = 300$

and $R = 0.8$ is lower than that at $f_j = 75$ Hz at the same velocity ratio, so an effect of the frequency, even though weak, is present. As will be clearer in a later stage, this may be connected to how the flow responds to the unsteady forcing.

Several boundary layer profiles were then measured at the most effective frequency $f_j = 75$ Hz, for several jet velocity ratios R. Some of these profiles are reported in figure 5.3, which shows on the left the mean velocity profiles, and on the right the profiles of the root-mean-square value of the velocity fluctuations. The upstream, (at $x/L = -0.14$), laminar boundary layer is also reported, for comparison.

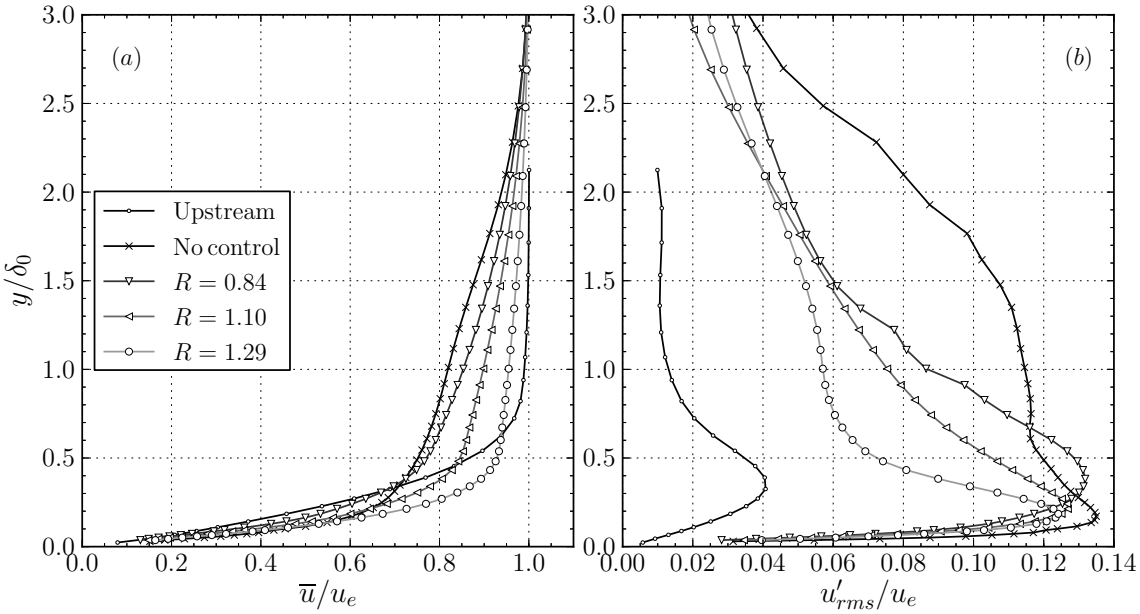

Figure 5.3. Profiles of the mean velocity, (a), and of the root-mean-square value of the velocity fluctuations (b), at $x/L = 1.91$, for different forcing amplitudes, at $f_j = 75$. The corresponding profiles for the upstream laminar boundary layer are also shown for comparison.

As discussed in section 3.2, in the uncontrolled case the downstream boundary layer is fully turbulent due to the instability of the shear layer which develops large coherent structures breaking up in the impingement region. In fact, the profile of u'_{rms}/u_e for the no-control case in figure 5.3, shows very large fluctuations amplitudes, up to a significant distance from the wall. Indeed, the boundary layer is much thicker and a large momentum deficit with respect to the thin upstream boundary layer is observed.

Surprisingly, as the jet velocity ratio increases, from 0 to about 0.8, the mean velocity profiles, (not shown in the figures for clarity), do not change substantially, even though a slightly lower velocity deficit starts to be observable for the profile for $R = 0.84$.

However, as the velocity ratio is further increased above 0.9, a drastic and rapid increase of the mean velocity in the boundary layer is observed, much larger then what observed for $0 < R < 0.8$ for a given variation of R. There is also a corresponding reduction of the amplitude of the velocity fluctuations on the outer layers of the downstream boundary layer, i.e. for $y/\delta_0 > 0.5$.

The resulting boundary layer flow developing from the cavity shoulder is not laminar, as it was for the case of control by suction, since very intense fluctuations can still be observed in the near wall region, with a peak value essentially equal to that of the uncontrolled flow.

To better understand the control mechanism the same analysis has been performed by placing the hot wire probe inside the cavity, under the cusp, at $x/L = 0.0$ and $y/\delta_0 = -2.27$. This position is representative of the behaviour of the cavity flow and of the associated velocities. Figure 5.4 shows a colour map of the mean velocity in this control point under the cusp, as a function of the forcing parameters f_j and R. The effect of the forcing is clear: the larger the velocity ratio the larger is

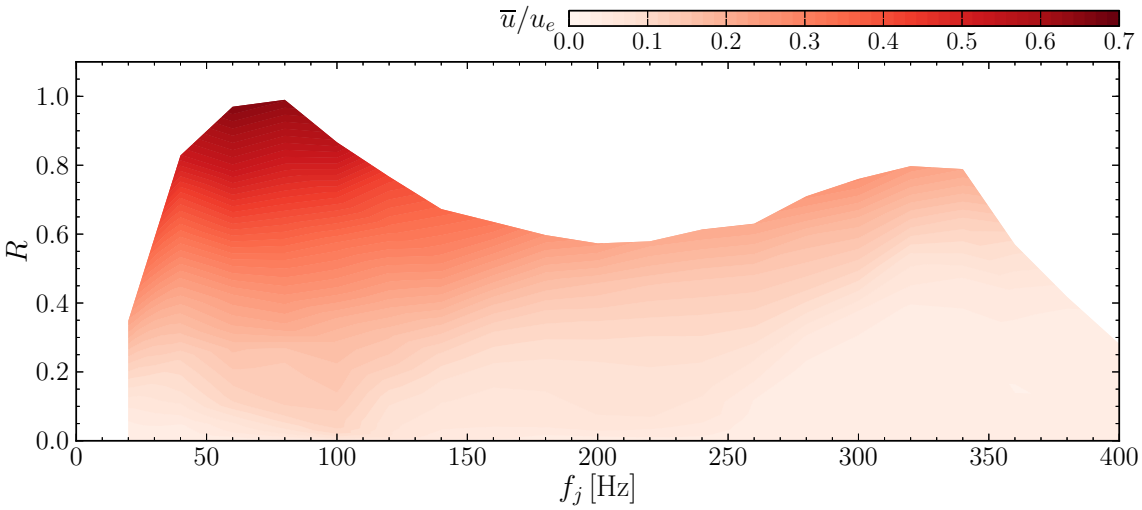

Figure 5.4. Color map of the mean velocity inside the cavity, under the cusp at $x/L = 0$, $y = -2.27$, as a function of synthetic jet control parameters.

the mean velocity at the control point, with a much weaker effect of the frequency. A very large variation of $\overline{u}/u_e$ is observed. In fact, the mean velocity increases from an almost zero value of the uncontrolled flow, with $\overline{u}/u_e$ about 0.05, up to about $0.7u_e$ again for frequencies around $70 \div 80$ Hz, where the largest velocity ratio can be achieved from the synthetic jet system, due to a favourable resonance condition in the synthetic jet box. Thus, the injection of momentum in the cavity strongly favours the formation of a very intense vortical structure.

As it was discussed above, for a given velocity ratio the effect of the forcing seems weaker at larger frequencies. This seems to suggest that a very peculiar dynamical

behaviour of the cavity flow, which seems to capture more easily the momentum from the synthetic jet at low frequencies.

The effect of the control is finally clear when observing the mean velocity profile across the shear layer just after the cusp, at $x/L = 0.05$, shown in figure 5.5-(a), as a function of the forcing amplitude R, at $f_j = 75$ Hz. Figure 5.5-(b) shows the corresponding profiles of u'_{rms}/u_e. The mean velocity profiles clearly indicate

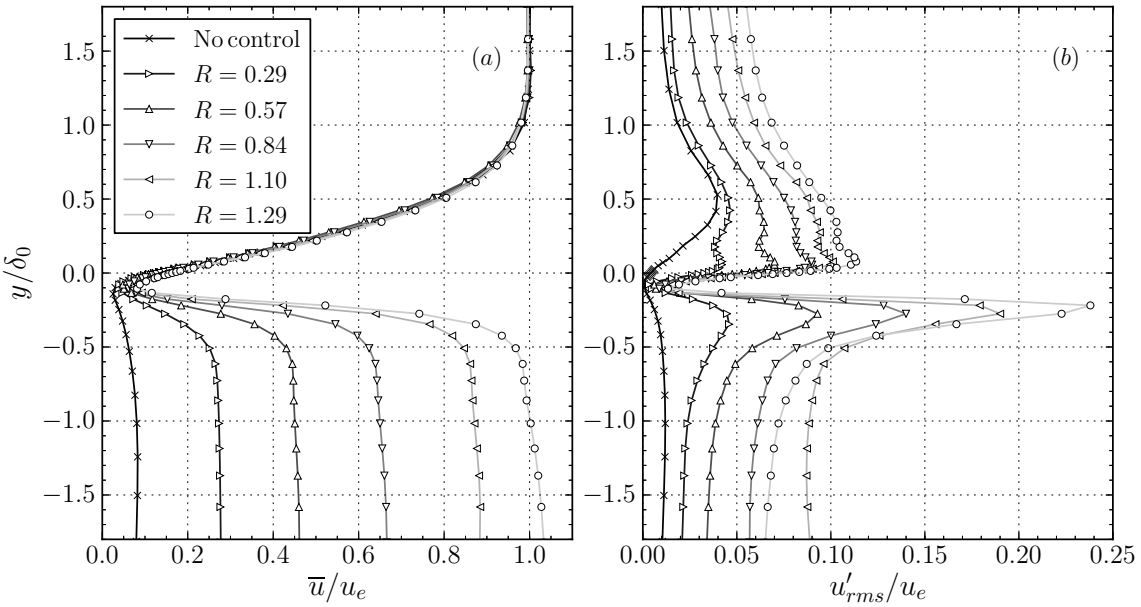

Figure 5.5. Profiles of the normalised mean velocity, (a), and of the normalised root-mean-square value of the velocity fluctuations (b), at $x/L = 0.05$, for different forcing amplitudes, at $f_j = 75$ Hz. The no-control condition is also shown for reference.

the enhancement of the rotational speed of the vortical flow in the cavity as the jet velocity ratio increases. Values as high as u_e at $y/\delta_0 = -1$ are achieved for the largest value of R. The mean velocity profile then goes to zero as the cusp is approached, indicating the presence of a boundary layer developing over the cavity surface. This boundary layer is quite thin, of the order of 2 mm, i.e. about 1/60 of the cavity height.

This internal boundary layer is a highly turbulent flow as suggested by the very large values of u'_{rms}/u_e that are observed in the near wall region under the cusp, for $y/\delta_0 \approx -0.25$, in figure 5.5-(b). However, in this region the signature of the forcing is very clear in the spectrum of the velocity fluctuations and it accounts for almost 50% of the total energy of the fluctuations at the maximum value of R.

In figure 5.5-(b) it is also visible that there is a change in the structure of flow for $y/\delta_0 > 0$ corresponding to the upstream boundary layer, which has just detached

from the cusp. As the forcing amplitude increases a marked increase of the fluctuations intensity is noticeable across the entire height for $y/\delta_0 > 0$. One contribution to this increase is due to the velocity fluctuations associated to the intense acoustic field generated by the loudspeaker. A second contribution is clearly visible in the near wall region, below $y/\delta_0 = 0.3$, as the profile of u'_{rms} clearly shows a peak in this region. This contribution may probably due to initiation of transition of the upstream boundary layer due to the intense perturbations produced by the loudspeaker, or because this region of fluid is excited by the nearby strongly fluctuating flow just below the cusp, flowing along the wall from the synthetic jet slot.

In figure 5.6 profiles of the mean velocity $\overline{u}(y)/u_e$ across the entire shear layer. For each profile the two dashed vertical lines indicates indicates marks for $u = 0$, (the x/L location of the profile), and for $u = u_e$, as usual. The profiles refer to a condition of forcing at $f_j = 75$ Hz and for a large velocity ratio $R = 1.29$. As

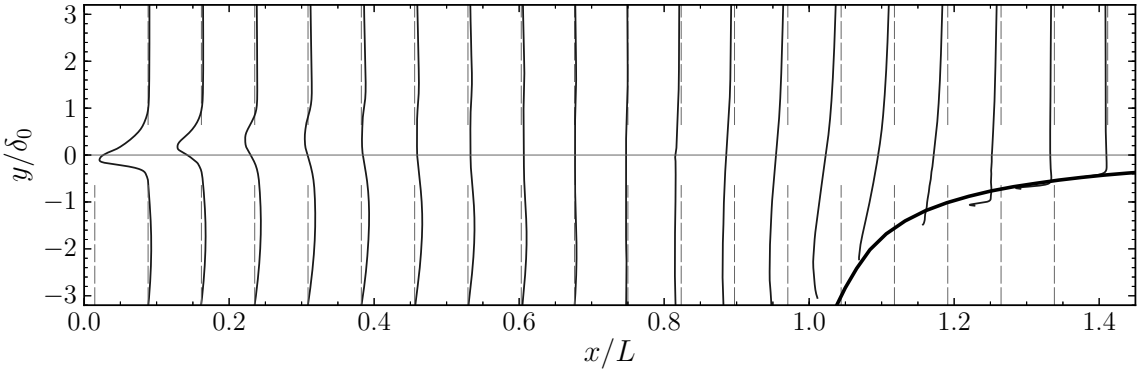

Figure 5.6. Mean velocity profiles across the shear layer in control conditions in CASE1 with $f_j = 75$ Hz and $R = 1.29$.

discussed in figure 5.5, the mean velocities in the cavity are strongly increased by the control. In the cavity region, $y/\delta_0 < 1$, and along the entire cavity opening, velocities larger than 15% more than the outer flow velocity can be clearly observed, especially for $x/L \approx 0.5$. Then, the mean velocities in the cavity region starts to decrease in the last third of the opening, since the flow is being slowed by the adverse pressure gradient generated by the presence of the impingement region on the downstream edge of the cavity. This slow down of the flow is also observable in the outer flow, with a minimum velocity at around $x/L \approx 1$.

The strong velocities in the cavity imply that the velocity deficit associated to the upstream boundary layer is quickly recovered in the first third of the shear layer. This "wake" is eroded by the momentum transfer operated by the strong turbulent velocity fluctuations observed in this region, as it was discussed in figure 5.5-(b). It is noteworthy that, since the velocity deficit is quickly recovered, there is probably no gain in having such a long cavity and probably a cavity of a size equal to one third

of that used in the present experiments would have shown adequate and equivalent performances. From this observation it follows that the size of the cavity should probably be scaled with the size of the boundary layer thickness, which would also help optimising the power consumption of the system.

The strong velocities in the cavity region for this large velocity ratio mean that there is no more a true shear layer, intended as a region of large velocity gradients. Therefore, this flow has a completely different response to the forcing.

The modification of the mean flow by the control also results in a strong modification of the second order statistics. Figure 5.7 shows profiles of the normalised root-mean-square value of the velocity fluctuations along the shear layer, for the same forcing conditions as in figure 5.6. As discussed for figure 5.5, the profile of

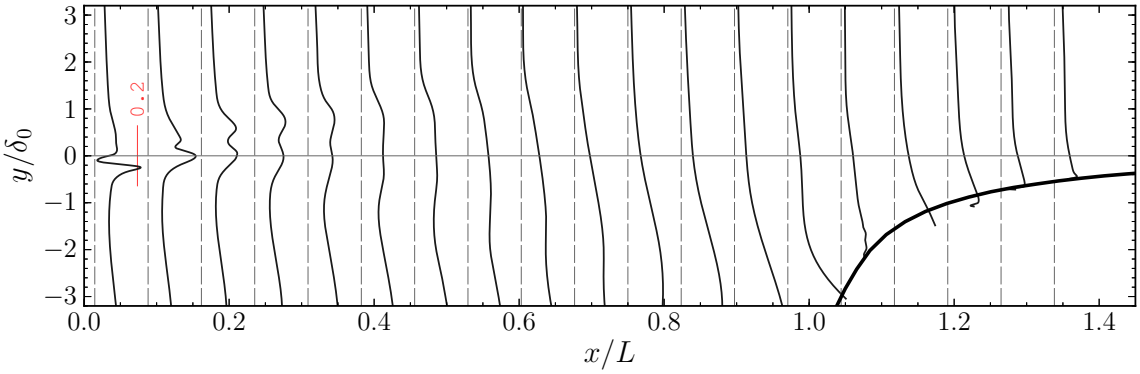

Figure 5.7. Profiles of the normalised root-mean-square value of the velocity fluctuations u'_{rms}/u_e across the shear layer in control conditions in CASE1 with $f_j = 75$ Hz and $R = 1.29$.

u'_{rms}/u_e just after the cusp shows a very large peak at $y/\delta_0 \approx -0.25$, originated by the highly turbulent boundary layer flowing along the cavity wall, from the slot to the cavity cusp, clockwise. These large velocity fluctuations are responsible for the quick recovery of the velocity deficit of the upstream mean velocity profile, as discussed in figure 5.7. At slightly larger streamwise coordinates the peak of u'_{rms}/u_e moves slightly upwards, then it follows a region, which enlarges downstream, where this peak spreads along the vertical coordinate.

Finally, larger velocity fluctuations are observed near the impingement region, around $x/L = 1.0$. Spectral analysis of the velocity fluctuations in this region demonstrates that a very large contribution to the total variance is due to the actuation, which, thus, strongly influence this region of the flow. The velocity profiles in figure 5.7 clearly indicate that the evolution of the shear layer is dramatically modified by the control as can be noticed by comparison with the corresponding profiles of the uncontrolled flow, figure 3.4.

5.3.2 Control for CASE2

Similar experiments have been conducted also for CASE2. In this case, since the external speed is more than doubled, the maximum value of R achieved is about the half of that of CASE1. Figure 5.8 shows a colour map of the mean velocity in a control point inside the cavity, $x/L = 0$, $y/\delta_0 = -0.45$, as a function of the control parameters f_j and R. To build this map, a velocity time history of 8 seconds was acquired for each of the 900 f_j, u_j couples forming from 60 frequencies from 10 to 500 Hz and 15 voltage amplitudes from 0.05 V to 1.1 V. Please note that the dimensional position y of the probe is exactly the same as in the previous case, but due to the variation of δ_0, the normalised position is different. The figure is quite

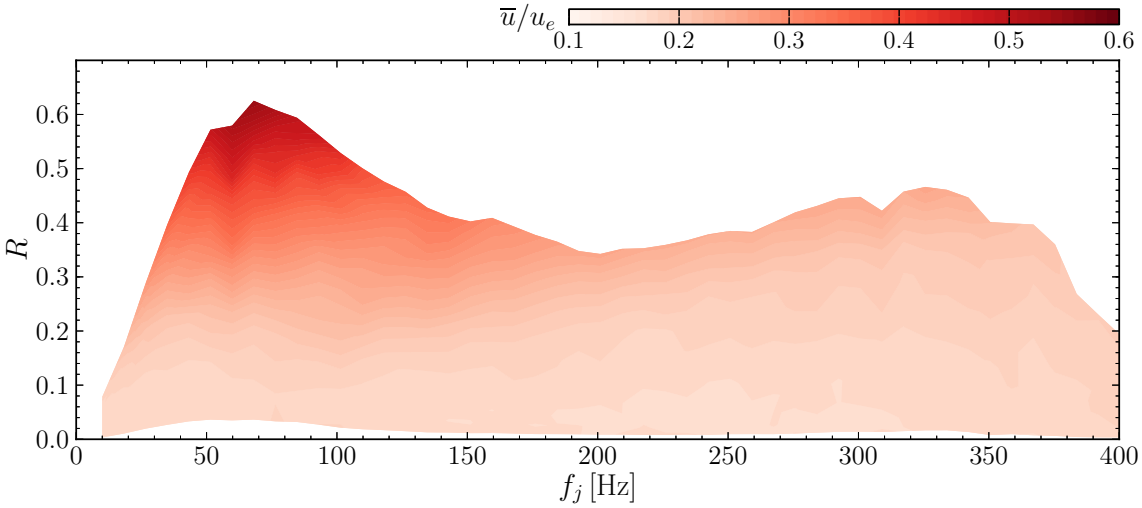

Figure 5.8. Color map of the mean velocity inside the cavity, under the cusp at $x/L = 0$, $y = -10$ mm, as a function of synthetic jet control parameters.

similar to that obtained for CASE1, figure 5.4. The largest velocities in the cavity are once again obtained for frequencies around 75 Hz. This seems to support the idea that the enhancement of the velocities in the cell were not due to coupling of the actuation with some relevant dynamics of the vortex flow, but were instead due to the fact that the output of the synthetic jet was largest at this frequency. Furthermore, the velocity in the cell increases with the jet velocity ratio, from about $\overline{u}/u_e \approx 0.1$ up to about 0.6. Finally, as for CASE1, the effect of the frequency is quite weak even though, for a given R, the increase of the frequency yields a slight decrease of the mean velocity at the control point inside the cavity.

This results seems to indicate that the control mechanism for CASE2 is identical as for CASE1. More precisely, the relevant control parameter is the jet velocity ratio, which is proportional to the momentum injected into the cavity, resulting in a more intense vortical structure.

The mean velocity increase under the cusp is a indication of a faster flow allover the cavity opening. Figure 5.9 shows profiles of $\overline{u}/u_e$, part (a), and of u'_{rms}/u_e, part (b), taken across the shear layer at $x/L = 0.58$, in the middle of the shear layer streamwise evolution, for different forcing amplitude and f_j. The effect of the

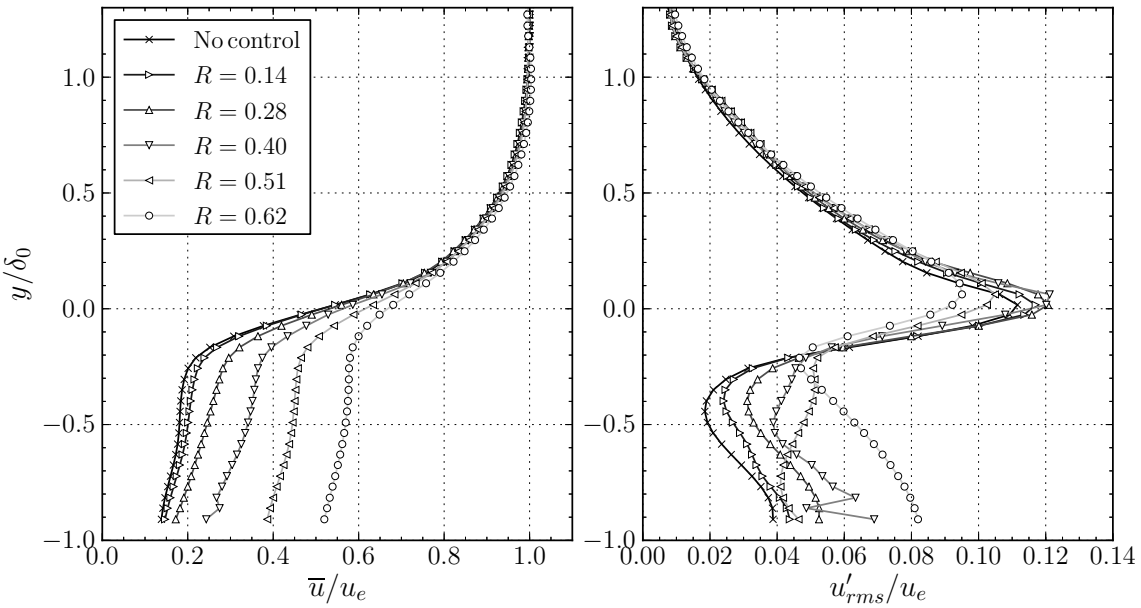

Figure 5.9. Profiles of the mean velocity, (a), and of the root-mean-square value of the velocity fluctuations (b), at $x/L = 0.58$, for different forcing amplitudes, at $f_j = 75$ Hz.

increase of the jet velocity ratio R is clear, since a distinct increase in the mean velocity inside the cavity region is observed, all along the tested range of R. The shear layer mean velocity profile is less steep under the action of the control, as a results of the lower velocity difference between the upper and lower velocities, i.e. between the external and the internal speeds. The lower $\partial\overline{u}/\partial y$, clearly results in a lower turbulent kinetic energy production as confirmed by the lower value of the peak of u'_{rms}/u_e at the larger R, as shown in figure 5.9-(b), at about $y/\delta_0 \approx 0$. On the other hand, the increase of the jet velocity ratio leads to an increase of the velocity fluctuations inside the cavity flow, mostly as a result of the strong unsteadiness introduced by the synthetic jet actuation.

The control of the cell flow, which produces a more intense trapped vortical structure, also modifies the flow downstream of the cell. Figure 5.10 shows the effects of the actuation parameters f_j and R on the normalised mean velocity in a reference control point downstream of the cell, at $x/L = 1.91$ and $y/\delta_0 = 0.09$. Although the velocity measurements were limited at $f_j = 200$ Hz, the effects of the control are evident and confirm the findings of CASE1. There is not a strong

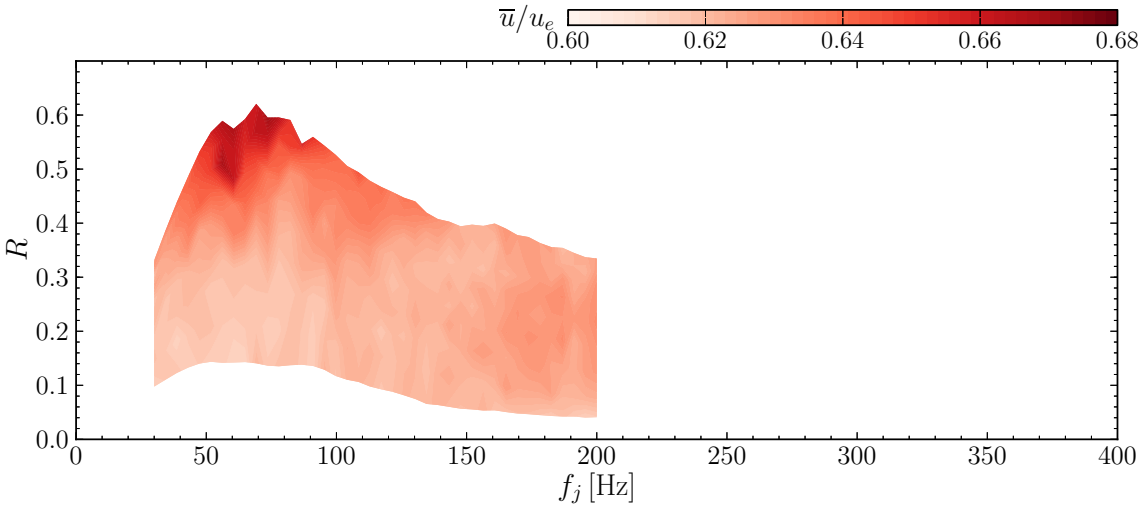

Figure 5.10. Color map of the mean velocity downstream of the cell at $x/L = 1.91$, $y/\delta_0 = 0.09$, as a function of synthetic jet control parameters.

effect of the forcing frequency, if any, but the influence of the jet velocity ratio is much more noticeable. The mean velocity at the reference point increases more consistently at frequencies around 75 Hz, even though the increase is weak and of the order of 13%, much lower than what observed for CASE1, essentially because of the smaller R achievable.

Boundary layer velocity profiles were then measured at the same reference downstream location $x/L = 1.91$, for several jet velocity ratios at a frequency of 75 Hz. These are shown in figure 5.11, which reports the profiles of $\overline{u}/u_e$ and of u'_{rms}/u_e, in parts (a) and (b), respectively. For clarity, only the profile for the largest value of R is reported, together with the no-control condition and the upstream profile at $x/L = -0.14$. This is necessary because the effect of the control is weak and only the case for the maximum R shows a significant deviation from the no control condition. Please also note that the profiles are scaled by outer variables, and not by wall variables. In fact, the velocity profiles downstream of the cavity have virtually no logarithmic region, due to the large velocity defect, rendering impossible to estimate the wall shear stress τ_x, for example with Clauser's method.

Under the action of control, the velocity deficit in the near-wall region, $y/\delta_0 < 0.1$ in the mean velocity profile of the controlled case has been recovered. The profile closely matches that of the upstream boundary layer. This seems likely due to the larger velocities in the cavity region, which prevent the strong loss of momentum of these layers of fluid. In this same region, the velocity fluctuations are $15 \div 20\%$ higher than that of the uncontrolled case, which showed in turn a near wall peak of u'_{rms}/u_e of the same intensity of the upstream profile. This is likely due to the higher velocity fluctuations of the cavity flow, introduced by the actuation.

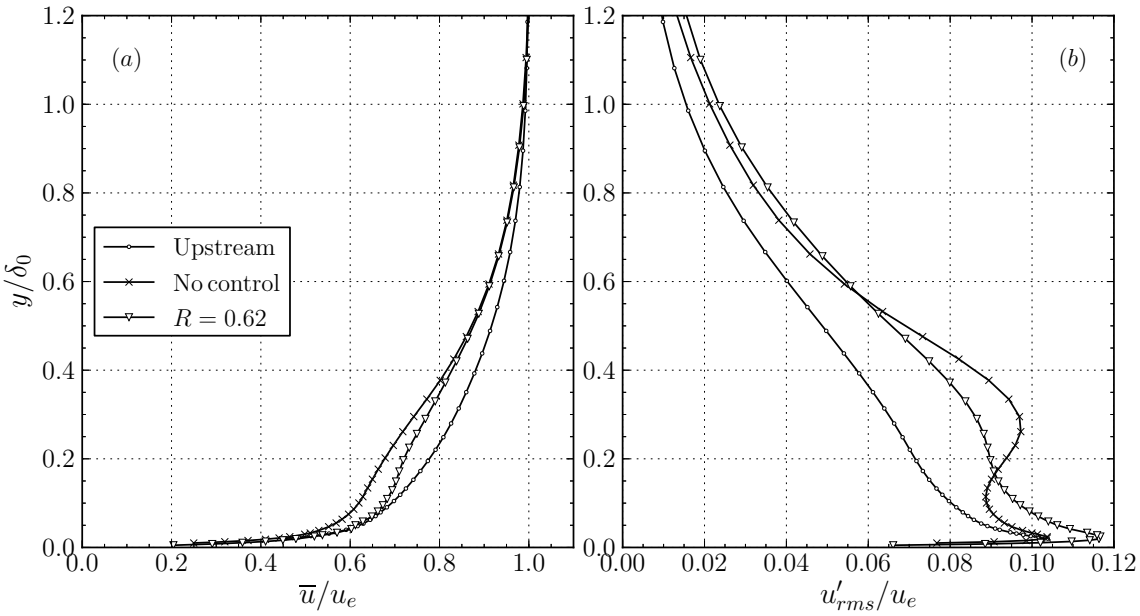

Figure 5.11. Profiles of the mean velocity, (a), and of the root-mean-square value of the velocity fluctuations (b), at $x/L = 1.91$, for different forcing amplitudes at $f_j = 75$ Hz. The upstream profiles are also reported for comparison.

Nonetheless, for larger distances from the wall, i.e. for $y/\delta_0 > 0.1$, the mean velocity deficit is still significant and entirely comparable to that of the uncontrolled case, especially for $y/\delta_0 > 0.4$. However, in this region, and in particular in the region of larger velocity defect, i.e. $y/\delta_0 \approx 0.3$, the structure of the turbulence is modified by the control since the velocity fluctuations are less intense, as observed in the profile of u'_{rms}/u_e at the same distance from the wall, which indicates a reduction of about 10% in the intensity of the turbulent velocity fluctuations. This is entirely due to the different evolution of the shear layer in controlled conditions, which evidences lower velocity fluctuations across the shear layer, as evidenced for example by the reduction in the peak observed in figure 5.9-(b) for the larger value of R. In fact, as it was discussed in section 3.3, the origin of the second peak of u'_{rms}/u_e at $y/\delta_0 \approx 0.3$ is due to the shear layer flow lifting up in the impingement region, and it thus corresponds to the peak of u'_{rms}/u_e in the shear layer.

Spectral analysis

Figure 5.12 shows the result of the spectral analysis of the velocity fluctuation signals measured across the entire boundary layer downstream of the cavity at $x/L = 2.05$. The colour maps shows the base ten logarithm of the power spectral density of $u^* = u'/u_e$ for three different forcing conditions at $f_j = 75$ Hz and in the no-control

case, at the bottom.

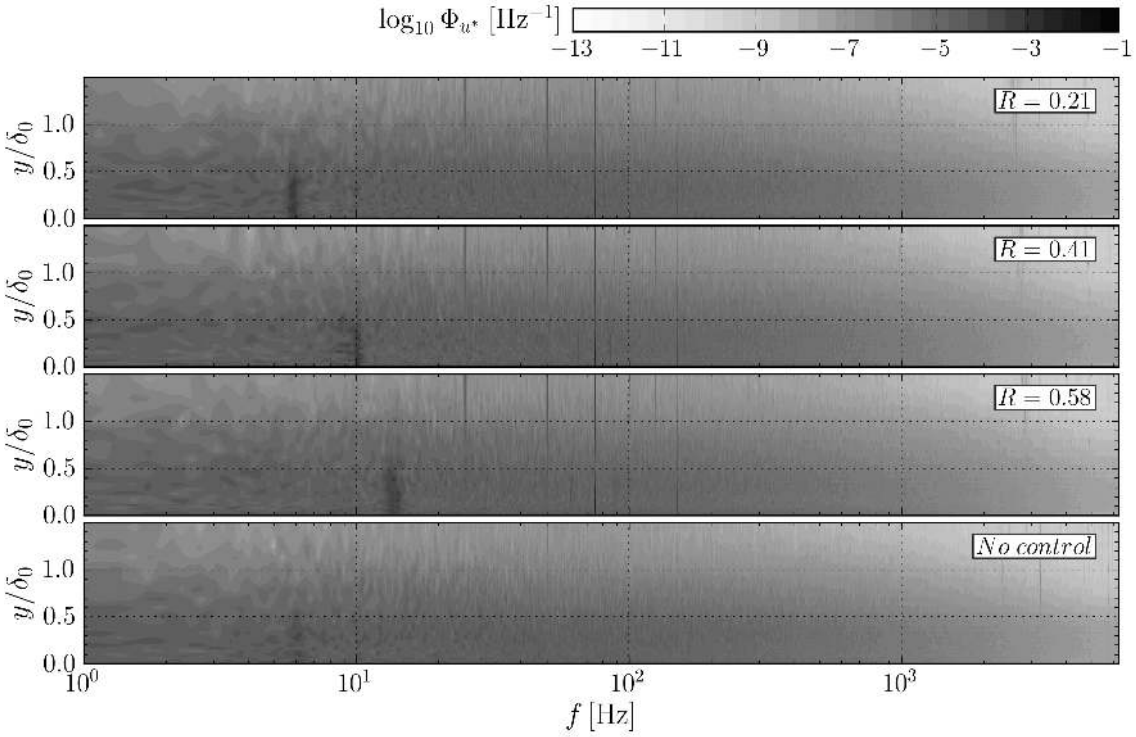

Figure 5.12. The colour maps show the power spectral densities of the velocity fluctuations across the boundary layer downstream of the cell at $x/L = 2.05$, for three forcing conditions at $f_j = 75$ Hz and in no-control conditions.

The spectrograms of the velocity fluctuations in control conditions, top three figures, indicate as expected large spectral energy at the forcing frequency, across the entire boundary layer, with $\log_{10}\Phi_{u^*}$ of the order of -1. Sub-harmonics and higher harmonics of the forcing frequency can be also detected.

However, the interesting feature of the spectral analysis is that quite large spectral energy can be observed at low frequencies, in the first half of the boundary layer, below $y/\delta_0 = 0.5$. This features also characterises the no-control conditions, but the control seems to enhance this phenomenon. The peak frequency increases from a value of about 6 Hz and at $R = 0.21$ and in no-control conditions, to 10 Hz for $R = 0.41$ and to 14 Hz for the largest forcing amplitude.

Such a spectral peak is due to the same low frequency oscillation of the vortex core observed in no-control conditions and when the cavity flow is controlled by suction, and the signature of this motion is present in the near-wall flow downstream of the cell. The oscillation frequency increases with the forcing amplitude because

the latter is strictly connected to the rotational velocity of the vortex. Flow visualisations of the cavity flow when the control is on, not reported here for the sake of brevity, clearly evidence such a mechanism, which is thus a characteristics of the cavity flow in both natural and forced conditions.

The modification of the flow by the synthetic jet is such that the instability of the vortex core is not controlled but it is enhanced, since the vortex core is more coherent. However, the extent by which this instability affects the performances of the TVC as a control device are not clear and should be the object of further research.

5.3.3 A further investigation at lower speed, CASEx

The results presented for the two cases above have clearly highlighted that the effectiveness of the control is proportional to the jet velocity ratio R. In order to better highlight this property, tests were conducted at a slightly lower speed than that for CASE1, i.e. at $u_e = 5$ m/s, corresponding to a Reynolds number based on the cavity length equal to 22700. With this external velocity a maximum velocity ratio equal to 1.45 could be achieved. The essential physics, (lock-in, weakly rotating vortex, erratic injection of high-energy packets into the cavity, ...), are very similar to that of CASE1.

Velocity profiles have been measured at the same frequency $f_j = 75$ Hz, and for several velocity ratios. Figure 5.13 shows profiles of the mean velocity and of u'_{rms}/u_e, in no control and control conditions with $R = R_{max} = 1.45$, at $x/L = 1.91$, as well the usual upstream profile, taken at $x/L = -0.14$. Note that δ_0 is slightly larger than in CASE1 and it is equal to 5.5 mm. For clarity only the profile for the maximum velocity ratio is shown.

The mean velocity profile downstream of the cavity in control condition indicates a much more thinner boundary layer than the upstream profile, about a third. What is more, a velocity overshoot is observed in a quite large region of the flow, between $y/\delta_0 = 0.35$ up to $y/\delta_0 = 2$. This overshoot is clearly due to the momentum transfer from the fast cavity flow to the incoming boundary layer, which accelerates the boundary layer flow itself. This results is a further demonstration that the driving physical mechanism for synthetic jet control is momentum transfer from the highly energised vortical flow to the shear layer.

The thinning of the downstream boundary layer is also associated to a large reduction of the region of large velocity fluctuations with respect to the unforced case, clearly evidenced in figure 5.13-(b). The profile of u'_{rms}/u_e shows a very intense peak of velocity fluctuations in the near wall region, at around $y/\delta_0 \approx 0.18$. These are probably associated to both the larger near-wall velocities and the strong velocity fluctuations of the cavity flow introduced by the actuation.

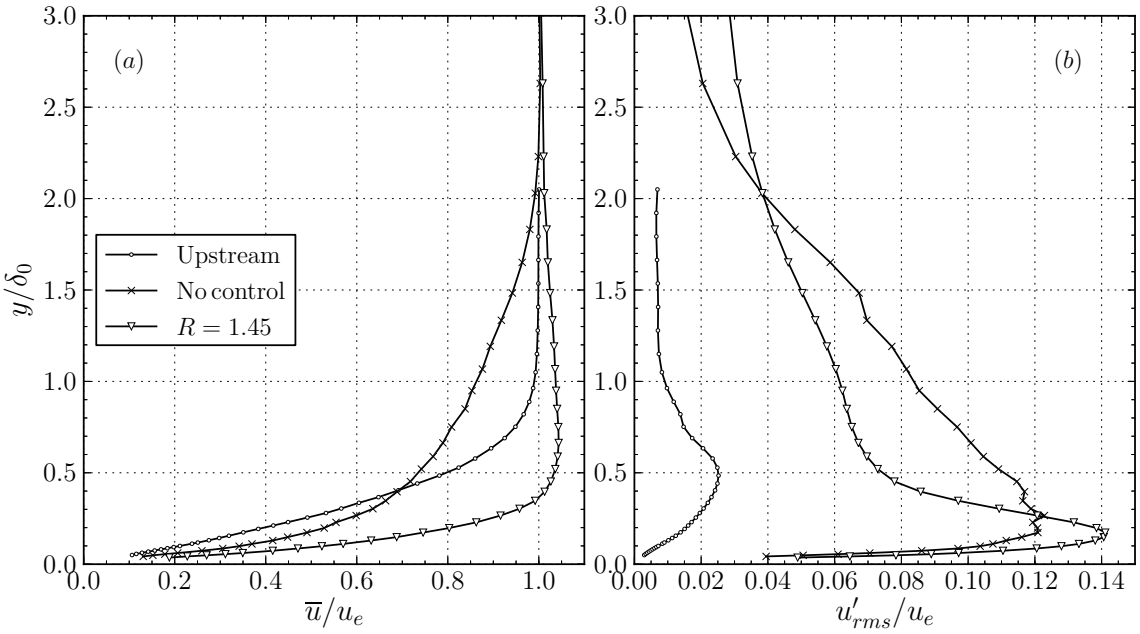

Figure 5.13. Profiles of the mean velocity, (a), and of the root-mean-square value of the velocity fluctuations (b), at $x/L = 1.91$, for different forcing conditions at $u_e = 5$ m/s. The upstream profiles are also reported for comparison. $f_j = 75$ Hz.

5.4 Effects of the control on the downstream boundary layer momentum thickness

To summarise the results reported in the previous pages, figure 5.14 shows a summary plot of the ratio θ/θ_0 as a function of the jet velocity ratio R, at $f_j = 75$ Hz. These results refers to the three cases tested, CASE1, CASE2 and CASEx, at the lower velocity.

The effect of the jet velocity ratio on θ/θ_0 is very clear from this figure. For an upstream laminar boundary layer, CASE1 and CASEx, the downstream boundary layer is essentially unaffected by the forcing up to $R^* \approx 0.8$, such that below this range there is no useful variation of θ. The ratio fluctuates around a value of 2.0 which is indicative of the forced transition of the boundary layer from laminar to turbulent and to the high dissipation along the shear layer. However, as the velocity ratio is further increased past the threshold value $R^* \approx 0.8$, the momentum thickness of the downstream boundary layer eventually starts to decrease, as an almost linear function of the velocity ratio. For very large values of the velocity ratio the momentum thickness of the downstream boundary layer is negative, a nonphysical result entirely due to the origin of an overshoot in the mean velocity profile. Interestingly, the threshold velocity ratio and the slope of θ/θ_0 as a function

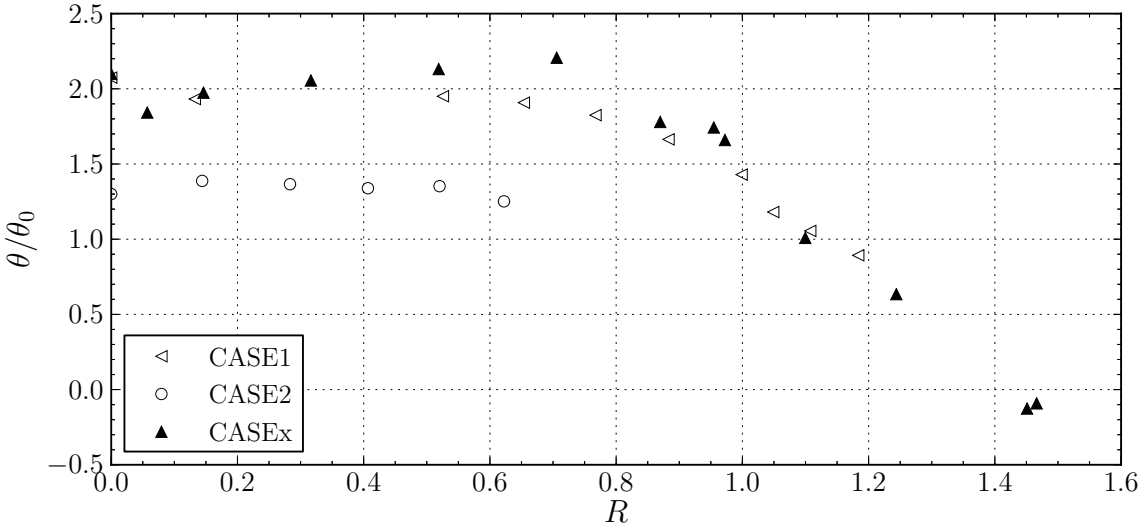

Figure 5.14. Upstream/downstream boundary layer momentum thickness ratio as a function of the jet velocity ratio, for all the investigated cases.

of R for $R > R^*$, seem virtually unaffected by the change in freestream velocity, indicating that R is the relevant parameter to estimate the effectiveness of the control.

For CASE2, the initial plateau value is set around 1.3, because the incoming boundary layer is already turbulent, and the slight increase in θ, by about 30%, is due to losses in the evolution of the turbulent shear layer along its evolution. Here again it is pointed out that if the cavity was not present, the momentum thickness would have increased by about 15% over the same length considered here, due to skin friction. For CASE2, the maximum value of R was about 0.65, due to limitations of the synthetic jet performance. Thus, it was not possible to verify that θ decreases for values of R of about 0.8. Nonetheless, since the mechanism by which the boundary layer is energised has been understood, it is likely that the control would be more effective for larger velocity ratios, even in CASE2.

The presence of the plateau and the start of the decrease of θ for $R > R^* \approx 0.8$ is not completely understood. One explanation, particularly suited for CASE1 and CASEx could be that it is necessary a relatively high rotational velocity in the cell to break up the mechanism by which momentum is lost along the shear layer, i.e. the break up of the coherent structures developing in this region. If the parameter R is low this mechanism is still active and not much influenced by it. However, as R increases the mean velocity in the cavity increases as well and modifies the structure of the shear layer so that the detrimental effects of the shear layer instability are reduced. Then for $R > R^*$ a beneficial transfer of momentum to the outer layers can take place so that θ can decrease.

However, this explanation does not hold for CASE2 since there is no instability to control here, and the above description is likely not realistic.

5.5 Dynamic response of the flow for CASE1

The results presented above in this chapter, regarding essentially the mean flow, did not show fully an important aspect that emerged during the investigations. This phenomenon is that concerning the complexity of the dynamic response of the flow to the periodic forcing, and in particular of the shear layer. Such considerations apply strongly for CASE1, where the shear layer is strongly receptive to amplify external perturbations.

The shear layer flow is known to have a very complex response to external excitation, see e.g. Olsman and Colonius [2011] and Sipp [2012]. A first example of such a complexity is that it can show a "lock-in" phenomenon, whereby the oscillation of the shear layer at its natural frequencies can be "captured" by the external forcing, such that the shear layer is actually "driven" by the forcing. In fact, CASE1 is a paradigmatic example of such a behaviour, because the shear layer oscillations are forced by the acoustic resonance of the wind tunnel. Therefore, in the present experiments the synthetic jet actuation is a second source of periodic disturbances.

As shown in section 3.2, the shear layer instability is responsible in a large part of the transition to turbulence of the flow downstream of the cavity. This phenomenon is clearly detrimental since it causes a significant increase of the momentum thickness of the downstream boundary layer, which make the use of a TVC counter-productive. Thus and understanding of how the control interacts with this phenomenon is required to proceed to effective control.

In this regard the present synthetic jet control affects the flow by two separate mechanisms. On the one hand, the injection of momentum from the synthetic jet controls the intensity of the recirculating flow inside the cavity. On the other hand, due to strongly periodic nature of the forcing, a significant effect of the shear layer dynamics also present. Regarding the latter issue, a fundamental question is the effect of the control parameters. Therefore, specific experiments were conducted to investigate on this problem. The hot wire probe was positioned in the shear layer region, at $x/L = 0.58$ and $y/\delta_0 = 0.0$, a significant point at the end of the region of exponential growth of the velocity fluctuations in the shear layer. Then, the forcing frequency f_j was set to a constant value and a velocity time history was sampled for several increasing values of A_j to assess the dynamics response of the shear layer. The power spectral density of the measured velocity fluctuations was then evaluated. Results of this analysis are reported in figure 5.15, where each subfigure is related to a given forcing frequency f_j, indicated in the top-right labels. Each subfigure reports a colour map of the power spectral density of $u^* = u/u_e$, as a function of

the forcing amplitude A_j and of the frequency f.

On the left of each subfigure, a red symbol indicates the frequency of the wind tunnel resonance at $f = f_{wt} = 150Hz$, while the white symbol on the right indicates the forcing frequency. Note that the horizontal scale of the figure is the driving signal amplitude A_j and not the jet velocity ratio. Furthermore, the scale is logarithmic and a very large range of voltage amplitudes has been tested, from some mV to about 1 V. The experiments were conducted at frequencies from 20 to 400 Hz, in steps of 20 Hz, but the figure only reports the most representative results.

Please note that at the velocity of CASE1 the natural instability modes would occur at multiples of about 45 Hz, if the forcing of the wind tunnel acoustic resonance were not present. These frequencies can be deduced from the spectrograms of figures 3.1 and 3.2, and well match Rossiter formula of equation 1.1.

At $f_j = 20$ Hz, the forcing frequency is quite low with respect to the natural oscillation frequency of the shear layer and most importantly to the wind tunnel resonance frequency. For this reason, low levels of forcing are not able to drive away the shear layer from the wind-tunnel resonance frequency, which dominates the oscillation. In fact, the spectrogram shows a dominant peak at $f = f_{wt}$ and its first harmonic at 300 Hz, as well a sub-harmonic at 50 Hz, for a very large range of forcing amplitudes, up to about $\log_{10} A_j = -1.4$. A significant change in the spectral content of the velocity signal is observed at $\log_{10} A_j \approx -1.4$ where the signature of the forcing starts to appear in the spectrum. However, the peaks at f_{wt} and at its harmonics are still observed. Time-frequency spectral analyses of the velocity signals, not reported here, indicate a superposition of the two frequency rather then an erratic switching of the main oscillation. As the amplitude increases between $log_{10}A_j = -0.7$ and -0.3, the entire harmonic family multiple of 10 Hz is excited and the spectrum displays dozens of peaks. Finally, for large forcing amplitudes, the shear layer is locked onto the forcing and only the harmonic family of the forcing frequency $f_j = 20$ Hz remains. The response of the shear layer look qualitatively similar to that of the Van der Pol model, a non linear oscillator, see Sipp [2012] and Rowley and Williams [2006].

At $f_j = 60$ Hz, the signature of the forcing and of its harmonic family can be identified at much lower forcing amplitudes, of the order of some milliVolts. The forcing also excites oscillations at 30 and 90 Hz, for amplitudes ranging from $10^{-2.3}$ to $10^{-0.7}$ V. The latter frequency is very close to the second natural instability mode of the shear layer but it could be a non-integer higher harmonic of f_j. A complete lock-in of the shear layer to the forcing eventually occurs at around $10^{-0.6}$, where the flow is solely driven by the forcing.

This generic behaviour holds up to $f_j = 140$ Hz, very close to the wind tunnel resonance frequency. At this forcing frequency, a very small forcing amplitude, of the order of $A_j = 10^{-2}$ V is required to drive the shear layer away from f_{wt} onto f_j. In fact, from this forcing amplitude on, the shear layer remains locked onto the

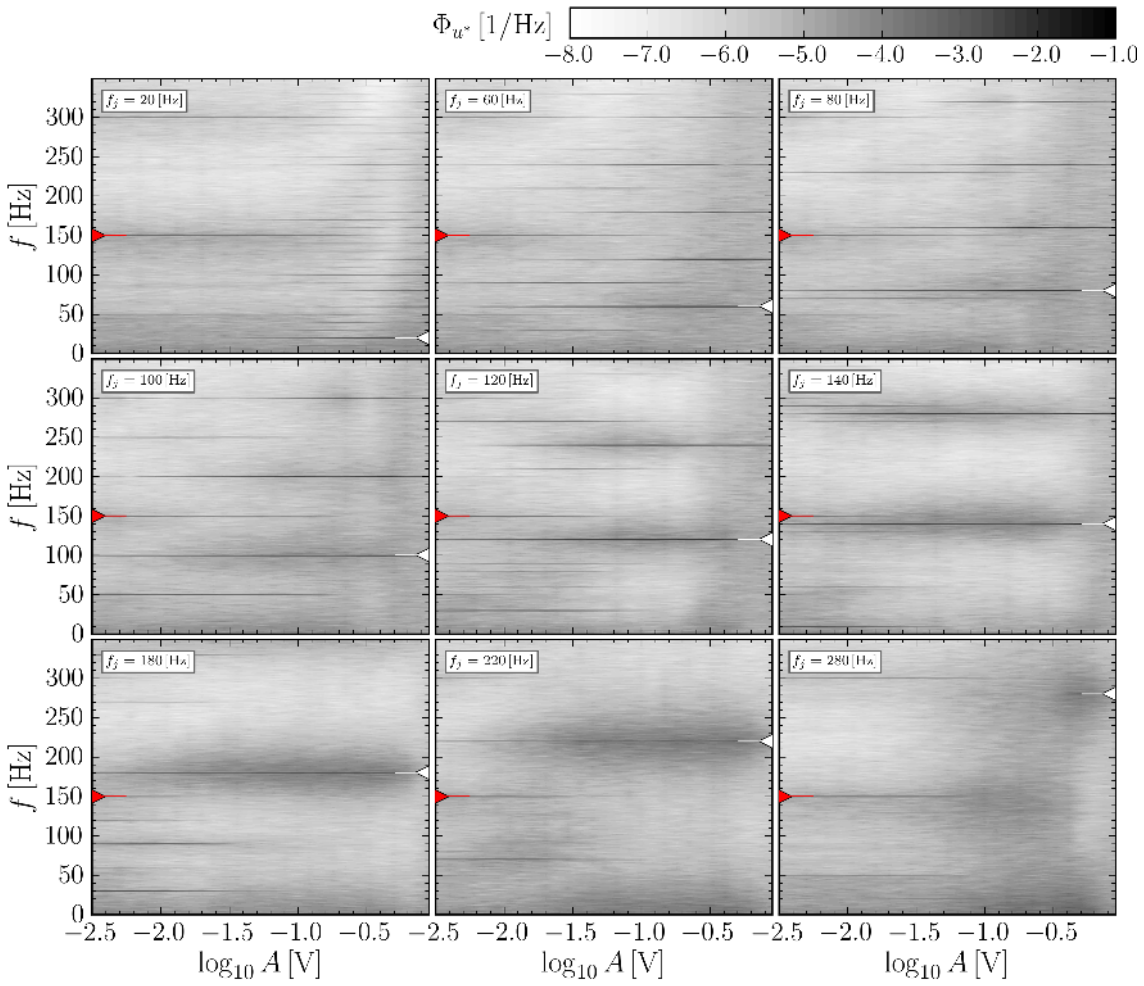

Figure 5.15. Forcing amplitude-frequency spectrograms of the normalised velocity fluctuations in $x/L = 0.58$, $y/\delta_0 = 0$, for several values of the forcing frequency.

forcing frequency. At this frequency, and for very low amplitudes also is noteworthy the presence of the harmonic family associated to $f_{wt} - f_j$, with peaks at $f = 10$ and 20 Hz.

As the forcing frequency increases to 180, 220, and 280 Hz, an ever increasing forcing amplitude is required to capture the shear layer from its locked state onto f_{wt}. For example, at $f_j = 180$, an amplitude of $10^{-1.8}$ V is required to suppress oscillations at f_{wt}, but this amplitude is as large as $10^{-1.0}$ V at $f_j = 280$.

The complex behaviour shown by the shear layer in response to the periodic forcing of the synthetic jet, and briefly documented in this last section of this chapter, without the objective of being exhaustive, seems, however, not so influential to

the effectiveness of the TVC controlled by the synthetic jet actuation. In fact, for instance, figure 5.2, does not present the strong effect of the frequency, which instead is a very relevant parameter to explain the behaviour of the shear layer flow. One partial explanation is that, despite its locked state onto f_{wt} or f_j, the shear layer always results in large velocity fluctuations, which cause the transition to turbulence in the flow downstream of the cavity. Therefore, in terms of control, the increase of the rotational velocity in the cavity seems a more important aspect.

5.6 Remarks and conclusions

In this chapter, results of open-loop control of the TVC flow using a synthetic jet device have been presented and discussed. It has been demonstrated that this form of control is superior with respect to control by suction, since a larger reduction of θ can be achieved. Furthermore, it is estimated that the power requirement of the synthetic jet system is about one order of magnitude lower than that of control by suction for the same end effect, and it is, therefore, more efficient. Nevertheless, a positive net energy balance has certainly not been achieved. The control mechanisms in this case is that injection of momentum into the cavity by the synthetic jet produces a stronger vortical flow inside the cell which is able, for velocity ratios large enough, to drive and energize the shear layer at the point of producing a velocity overshoot in the boundary layer profile downstream of the cavity.

An important issue at hand is the response of the shear layer subject to periodic forcing, which has displayed an high complexity of behaviour for CASE1. Therefore, for the case of large cavities, i.e. cavities large enough with respect to the incoming boundary layer to develop self-sustained oscillations, it must be recognised that deep understanding of the dynamics of the shear layer, its response to forcing and its effective control are key elements for the success of the TVC control technique. Nevertheless, the effect of the frequency, which strongly affects the response of the shear layer, seems not very influential for the effectiveness of this control strategy, as the mean velocity profile of the boundary layer downstream of the cavity is not greatly influenced.

Chapter 6

Optimisation of open-loop control signal using Evolutionary Strategies.

This chapter discusses the use of evolutionary computation techniques to search in the space of signals for that which can optimally control the cavity flow, such as to obtain a velocity in the downstream boundary layer larger than what is possible using sinusoidal forcing.

In the past years, open-loop flow control has traditionally thought in the form of a sinusoidal input of a given frequency and amplitude. This is a simple waveform to generate and usually optimisation of frequency and amplitude, often in non-dimensional form, was carried out. Other types waveforms have been considered, Vukasinovic et al. [2004], Zhang and Wang [2007], Feng and Wang [2012], but these were based on the intuition of the researcher rather than on an extensive and in-depth optimisation of the control signal.

The procedure that is described in this chapter tries to cast the flow control problem at hand, i.e. decreasing as much as possible the ratio θ/θ_0, into an optimisation problem which is solved with an evolutionary strategy.

Evolution strategies are search heuristics inspired by biological evolution of species by natural selection, Beyer and Schwefel [2002]. The fundamental idea of evolutionary algorithms is straightforward: a population of competing solutions undergoes random variation and selection with respect to a given evaluation function for some number of generations. Such algorithms have powerful search characteristics and are particularly suited for non-convex, high-dimensional, time-varying, non-smooth, not-differentiable optimisation problems. A detailed presentation of evolutionary computation methods is beyond the scope of this work, but excellent books on the subject are those of Michalewicz and Fogel [2004] and Beyer [2001].

From another point of view, it can be argued that the proposed technique

searches for the appropriate spectral content which best matches or couples to the dynamics of the flow, in a much more automatic way and robust way than using a trial and error procedure. For example, in a flow where more than one temporal and spatial scale is involved, the optimal control signal may target them all, by having large spectral density at the corresponding frequencies, possibly largely separated. An instance of such behaviour is the case of a separating flow over an airfoil, Mittal et al. [2005], where the control may target booth the wake dynamics/vortex shedding and the the high frequency dynamics of the separating boundary layer.

6.1 Signal parameterisation

A suitable representation of solutions to the optimisation problem is crucial for the performance of the evolution strategy Michalewicz and Fogel [2004]. In the present case, a first choice would be to select an sufficiently long vector $\mathbf{x}$, such that $e[i] = e(i\Delta t) = x_i \quad i = 0, \ldots, N$, i.e. where the vector $\mathbf{x}$ completely defines the discrete-time control input signal $e[i]$ in Volts, along the whole acquisition period $T_{acq} = N\Delta t$, where Δt is the signal sampling period. This approach is however impractical for obvious reasons, since N would tend to be very large thus making the search problem very difficult to solve, if not impossible.

However, it seems reasonable to introduce the assumption that the control signal should periodic, with a period $T_p << T_{acq}$. In this setting, the discrete-time control signal can be defined by repeating in time a pattern $e_p[k]$ defined by a vector of N^* real numbers such that $e_p[k] = e_p(k\Delta t) = x_k$. This substantially reduces the search problem complexity. However, it is possible to further simplify the signal representation by choosing the vector $\mathbf{x}$ to represent $n << N^*$ equally spaced control points along the pattern period T_p and then by re-sampling appropriately these points at the frequency of generation of the signal. Figure 6.1-(a) illustrates this idea and shows the control points, as well as the reconstruction using a re-sampling technique. Figure 6.1-(b) shows instead the vector representation of the same signal in figure (a). Note, that a further improvement is to allow the spacing between the control points δt to vary during the search process, leaving space for a finer tuning of the frequency content of the control signal. This is achieved by setting the first element of the object vector x_0 to represent this spacing.

The number of control points n and their spacing in time δt also determines the upper and lower bounds of the frequency components of the input signal. Then, in order to obtain the actual control signal from the object vector $\mathbf{x}$, the control points are using the Whittaker-Shannon interpolation formula, and the pattern is repeated in time as much as needed.

In practical terms, a large value of n would be desirable, as more complex signals can be found, resulting in better adaptivity and thus in higher control performance.

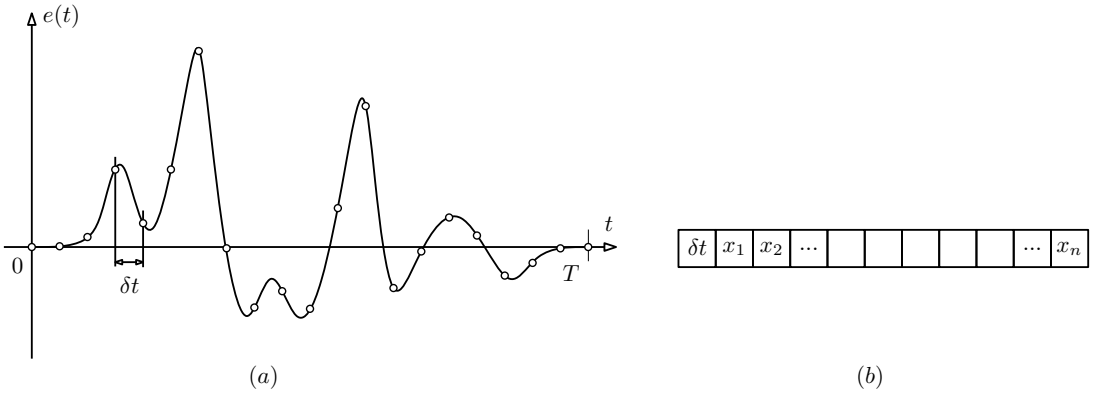

Figure 6.1. Discrimination and re-sampling of the control signal, (a), and vector representation of a candidate solution, (b).

However, searching in a large space is a demanding task and requires larger resources. For this reason a compromise value of $n = 20$ was chosen. This value provides sufficient flexibility for the waveform, and the optimisation problem can still be solved easily.

In practice, the continuous time signal is sampled at a high rate and fed as input to the loudspeaker amplifier by the D/A converter, using a zero-order hold. In the experiments this generation frequency was set to 50 kHz, in order to achieve a satisfactory resolution of the control signal.

The search of the optimal object vector $\mathbf{x}$ is unconstrained over all the parameters, i.e. the control points can assume any value from minus to plus infinity and the signal pattern period can be any positive number. However, for practical hardware limitation reasons, the signal is eventually clipped between -1 and 1 Volt, before being fed to the loudspeaker amplifier. This clipping was preferred to setting hard constraint on the object vector since it does not introduce the delicate problem of dealing with constraints in the search space, using penalty functions or repeated sampling, Michalewicz and Fogel [2004].

6.2 The Evolution Strategy (ES) algorithm

The search algorithm chosen for the optimisation of the control signal is the Covariance Matrix Adaptation Evolution Strategy, a state-of-the-art evolutionary computation algorithm. A detailed explanation of the algorithm is far beyond the scope of this document and the reader is referred to Hansen and Ostermeier [2001] for a thorough description.

In the present work it would be natural to select as optimisation problem the

minimisation of the momentum thickness of the boundary layer at some distance past the cavity θ, i.e. we should find the optimal object vector, encoding the input control signal as defined previously, such that.

$$\mathbf{x}^o = \arg\min_{\mathbf{x}\in\mathbb{F}\subset\mathbb{R}^n} \theta(\mathbf{x}) \tag{6.1}$$

This is a rather tedious problem since it implies that for each candidate solution, i.e. for each control signal under test, the boundary layer mean velocity profile must be measured, resulting in large total optimisation times. In order to make the problem tractable, $\overline{u}_P(\mathbf{x})$, the mean velocity in a control point P in the boundary layer developing downstream of the cavity, is chosen as the objective function to be minimised, as often shown in previous chapters. The optimisation problem is thus:

$$\mathbf{x}^o = \arg\max_{\mathbf{x}\in\mathbb{F}\subset\mathbb{R}^n} \overline{u}_P(\mathbf{x}) \tag{6.2}$$

where the control point P is located at $x/L = 2.05$ and $y/\delta_0 = 0.45$. The choice of the acquisition time to estimate the mean velocity is a compromise between having faster search processes and an accurate evaluation of the objective function. However, in general, genetic algorithm are far more robust to function evaluation noise than other conventional optimisation techniques, Michalewicz and Fogel [2004], since they are population-based heuristics. For this reason, the acquisition time is set to 10 seconds. With these settings the relative uncertainty in the estimate of the objective function was equal to 0.3%. This value was obtained a posteriori by computing the standard deviation of a hundred repeated function evaluations of the final optimal signal.

In the following discussion the objective function to be maximised is normalised:

$$J(\mathbf{x}) = \overline{u}_P/\overline{u}_{Pnat} \tag{6.3}$$

where $\overline{u}_{Pnat}$ is the mean velocity at the control point in no-control conditions.

6.2.1 Algorithm control

A dedicated control computer runs the CMA Evolution Strategy algorithm implemented in a main Python program. This main program is also responsible of data-acquisition/signal-generation by direct call to the National Instrument NIDAQmx driver for communication with the acquisition boards. For each candidate solution to be evaluated at each generation, the control signal is obtained and it is fed to the loudspeaker. After a small time delay of about 2 seconds to allow the cavity flow to reach a steady condition, the acquisition of the hot wire probe is started.

6.3 Results and discussion

6.3.1 Sinusoidal open-loop forcing

A first set of experiments was targeted at finding accurately optimal values for the amplitude and frequency of a pure sine signal, to control the flow in CASE1. It was initially observed that the mean velocity at point P increases monotonically with the forcing amplitude. For this reason, tests varying the frequency were conducted at a fixed value of the amplitude set to $A = 1$ Volt, i.e. the same maximum allowed amplitude for a candidate signal. Note that the resulting signal has a peak-to-peak amplitude of 2 Volts.

In figure 6.2 the objective function J is plotted as a function of the forcing frequency f. Since the most effective region of sinusoidal control is when f_j is around 80 Hz, this range of frequencies was investigated in very small steps of frequency.

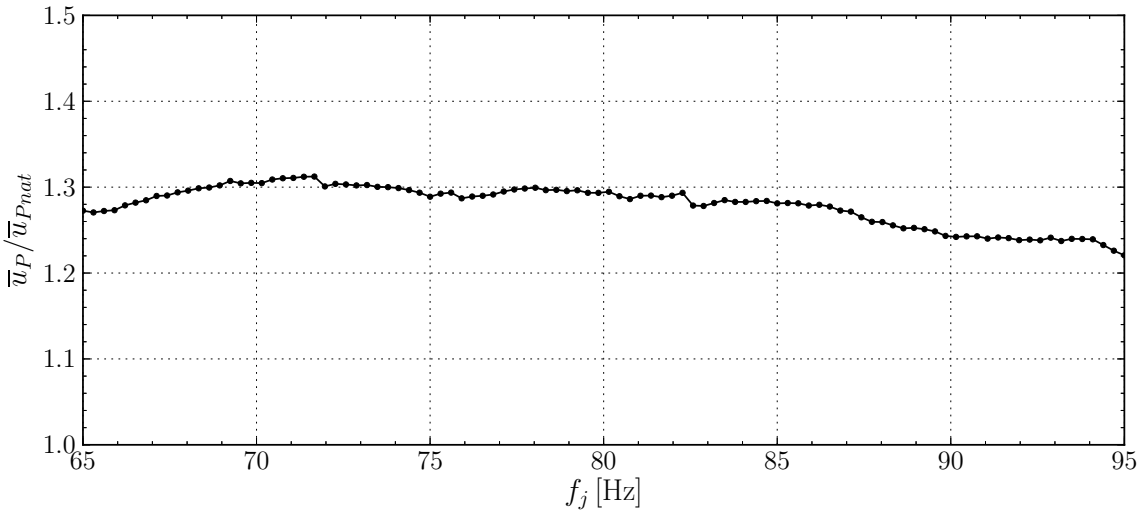

Figure 6.2. Mean velocity percent increment at point P as a function of the forcing frequency of a pure sinusoidal control signal. The sine amplitude is 1 Volt.

The curve shows a peak at a frequency of 72 Hz, at which the sinusoidal open-loop control is able to increase the mean velocity at point P by approximately 32%. As pointed out repeatedly in the previous chapter, the peak at this frequency is due to the resonance of the synthetic jet system which produces a larger output at such a frequency.

6.3.2 Optimal open-loop forcing

The optimisation procedure detailed previously is applied to search for the optimal open-loop control signal. To reduce the complexity of the search and to reduce total

optimisation times, the initial guess is chosen as to represent a 1 Volt amplitude pure sine wave of frequency equal to 72 Hz, i.e. the best sinusoidal signal. In spite of the bias introduced into the search by this choice this condition is a reasonably good first guess candidate solution.

The CMA-ES is run for about 130 generations, which are sufficient to reach a stable solution. Result of the optimisation process are reported in figure 6.3, which shows the evolution of the objective function. The open circles represent all the individuals tested. Two horizontal lines are also shown in the graph, indicating the limit reached by the final optimal signal, solid line, and the limit of the best sinusoidal signal, dashed line. The CMA-ES algorithm quickly finds improvements

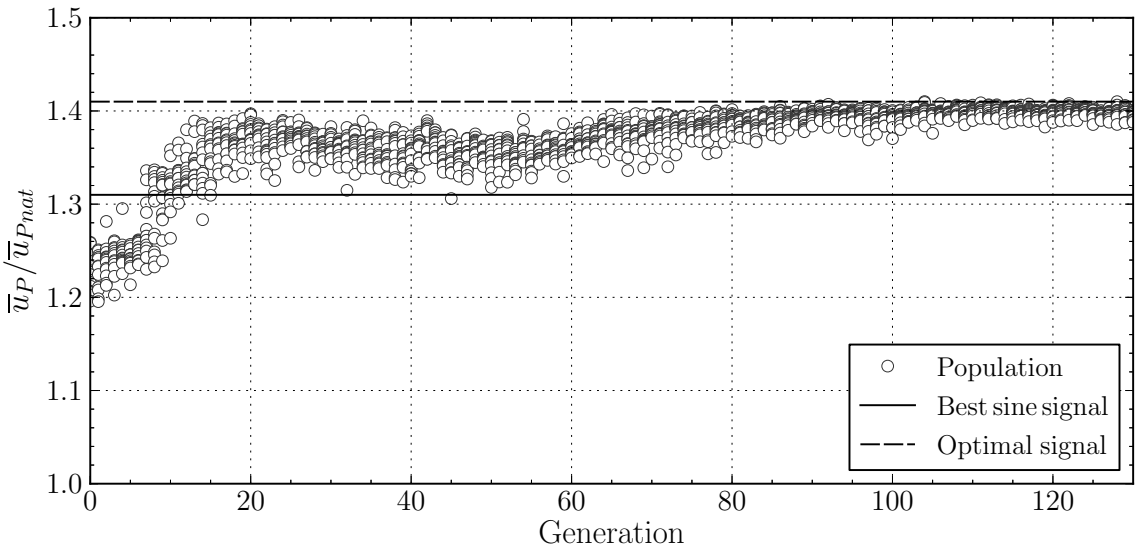

Figure 6.3. Objective function evolution history.

of the solution in the first 20 generations and gradually reaches an asymptotic state after about 80 more generations, after which no better solutions are found. The optimisation procedure is therefore stopped at this stage.

It is important to observe that the optimal control signal found by the evolution process is superior to the best pure sine signal, resulting in a mean velocity which is about 12% higher than that obtained with a pure sine wave signal, reaching a 41% increment of the mean velocity, with respect to the uncontrolled flow case.

It must be said that the optimisation algorithm never reaches a truly stable optimal solution but the population fluctuates randomly in a small region of the parameter space around the optimum. This fact is due essentially to the inherently noisy and time varying properties of the evaluation of the fitness function. In fact, the evaluation of the mean velocity in the control point for a given candidate signal is intrinsically affected by measurement inaccuracy, by limited convergence to the

actual mean value due to limited acquisition time and to long-term drifts and time-varying properties of the cavity flow. Such drawbacks would have been impossible to cope with if classical optimisation techniques were used. Instead, the population-based stochastic evolutionary strategy algorithm used for the optimisation has by far larger performances in these conditions.

The final optimal signal pattern is shown in figure 6.4. In the figure, the control points and the actual control signal are reported. It is clear that the signal evolution

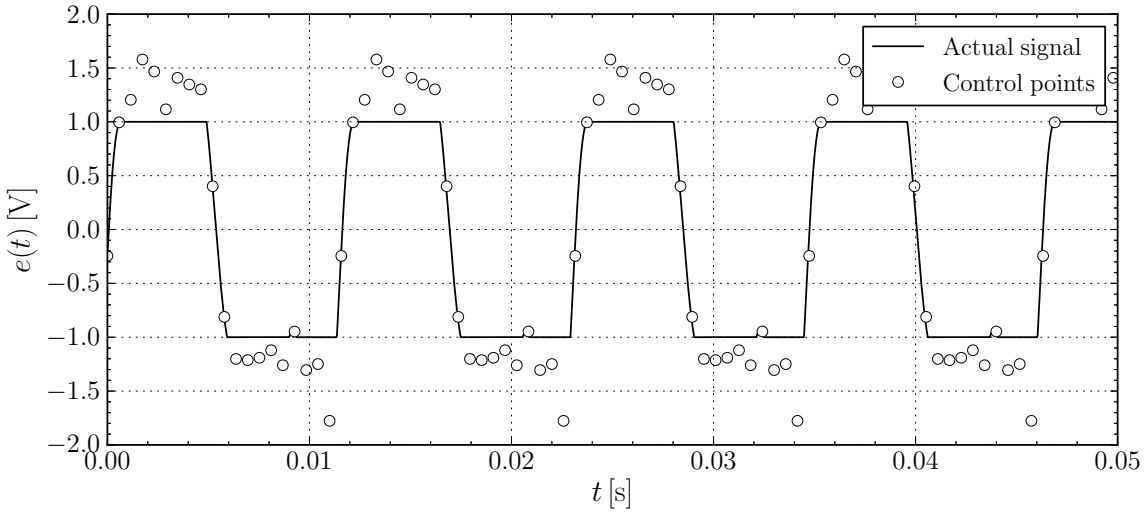

Figure 6.4. Optimized control signal.

path has been directed towards a sort of square wave. The frequency of the waveform is equal to 86 Hz and has a duty cycle, the ratio between the time during which $e(t)$ is positive and the waveform period, approximately equal to 0.42. Interestingly, only *some* of the points define the signal since many of the point are clipped and do not contribute to the shape of the actual waveform.

Of more interest, is the time history of the velocity signal measured at the synthetic jet slot resulting from the application of the optimal control signal, which is shown in figure 6.5-(a). Part (b) of the same figure shows the corresponding time history for the sinusoidal control signal measured at the same exact location. Note that the velocity measured by the hot wire is always positive, and it is not possible to distinguish between the suction and the blowing phases, since the hot wire probe does not distinguish the direction of the velocity vector but only its modulus. Please also note that the two signals in the figure are not aligned in time with each other. This comparison shows that under the action of the optimized signal, the synthetic jet does not produce a much larger peak velocity, which remains of the order of 23 m/s. Instead, the velocity signal in the optimized case rises and falls much more quickly, in reason of the steeper motion of the loudspeaker membrane induced by

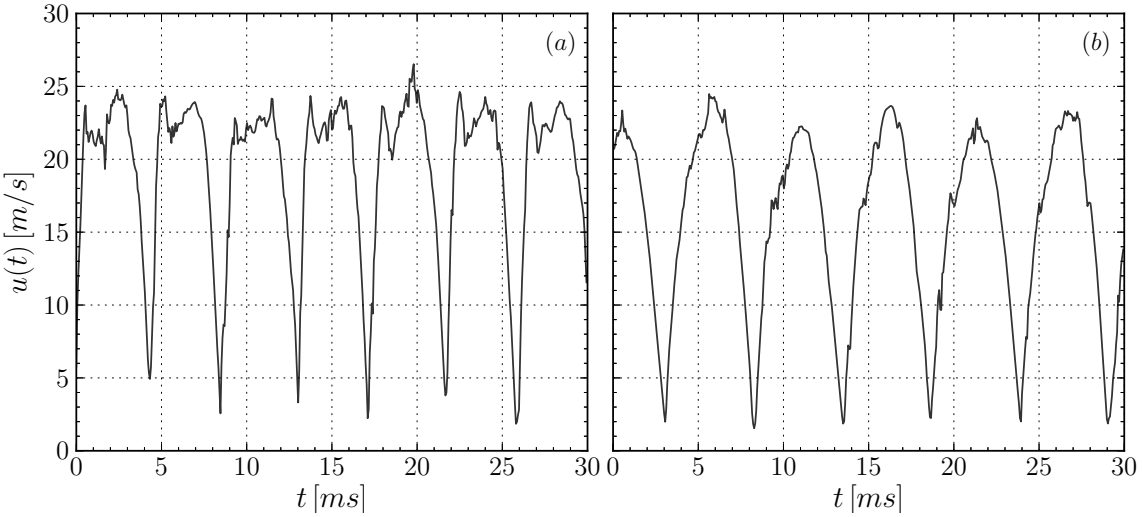

Figure 6.5. Velocity time history measured at the slot exit for the optimized signal, (a), and for the sinusoidal signal at $f_j = 72$ Hz, (b).

the square-like waveform of the control signal. As a result, the mean jet velocity, and the associated momentum injected in the cell, is larger for the optimized case by about 17%, since the it increase from about 8 m/s to 9.41 m/s. The jet velocity ratio is thus larger by the same percentage, which justifies the increase in velocity at the downstream point. Actually, this is a conservative value since due to the larger blowing phase of the jet, visible in the figure, the mean jet velocity during the blowing phases is slightly larger.

This result seems to indicate that the evolutionary strategy has optimized the objective function by finding a control signal which extracts the maximum performance from the actuator. This is obtained by creating a signal which produces rapid motions of the membrane, at the right frequency and with the correct duty cycle.

Figure 6.6 shows a comparison of the profiles of the normalised mean velocity, (a), and of the normalised root-mean-square value of the velocity fluctuations, (b), for the non controlled and controlled conditions, measured at the reference location $x/L = 2.05$. The optimal control case and the sinusoidal forcing case are reported. As discussed in chapter 5, it is evident that the sinusoidal open-loop forcing is able to increase the mean velocity of the downstream boundary layer flow, due to the enhanced rotation of the vortex flow in the cavity, which transfer momentum to the shear layer flow. The figure also indicates that the optimized signal is able to increase even further the velocity in the entire boundary layer, at the point of producing a small velocity overshoot of about 5% of u_e over a very large region, from $y/\delta_0 = 0.4$ up to $y/\delta_0 = 3$. In this condition the boundary layer thickness is about 40% of that of the upstream boundary layer.

The strong velocity increase across the boundary layer with respect to the no-control case results in a drastic reduction of the momentum thickness. In fact, this is reduced from 1.56 mm of the no-control case, to 0.45 of the sinusoidal case, to about 0 for the optimized signal case. However, the decrease of momentum thickness is not as large as one would expect for extrapolation of the results of figure 5.14, by setting a value of R equal to $9.41/6 = 1.57$.

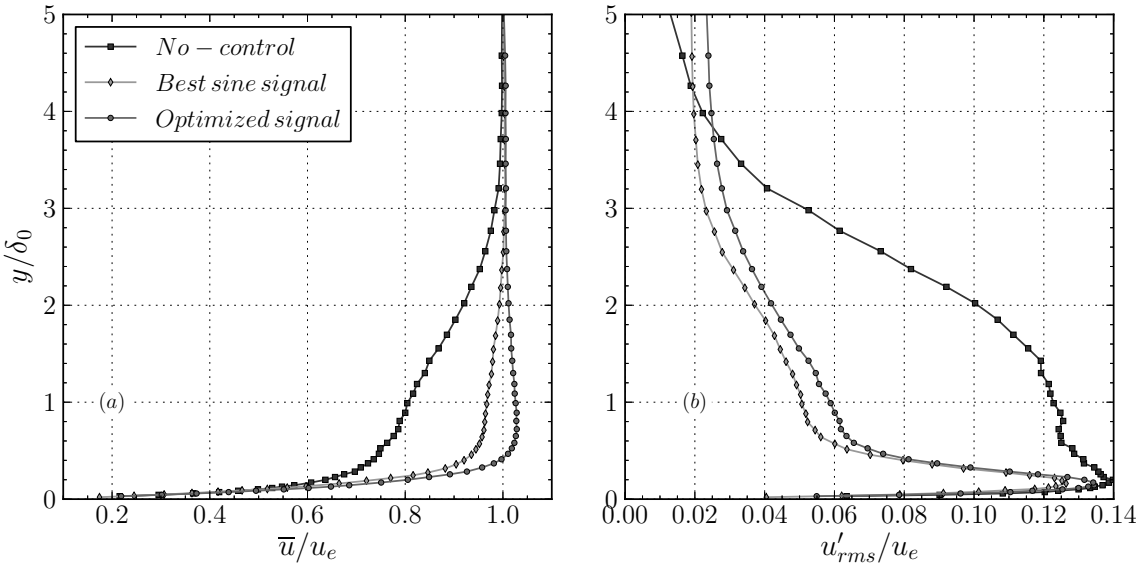

Figure 6.6. Profile of the mean streamwise velocity $\overline{u}/u_e$, (a), and of the root-mean-square value of the velocity fluctuations u'_{rms}/u_e, (b), at location $x/L = 2.05$, downstream of the cavity.

Regarding the profile of u'_{rms}/u_e, it is evident that a significant reduction of the turbulent fluctuations occurs when the control is switched on in the region $0.3 < y/\delta_0 < 4$, both for the sinusoidal forcing case and with optimized signal. As discussed previously in chapter 5, the reason for such a large decrease is related to the different evolution of the cavity shear layer in control conditions. For the natural case the shear layer is locked-in with the wind tunnel resonance and develops coherent fluctuations of large amplitude. This leads to a relatively large growth of the shear layer thickness which results in a region of large turbulent fluctuations about three times the upstream boundary layer thickness. For the controlled cases, the flow velocity in the cavity region just below $y/\delta = 0$, is of the same order, if not higher, of the external velocity and there is not a true shear layer. Thus the flow is not truly subject to the Kelvin-Helmoltz instability, although the signature of the forcing is energetically strong. This prevents the growth of the high-amplitude oscillations region observed for the no-control case, resulting in a smaller area of large fluctuations, located in the near wall region. Nevertheless, the peak value of

the turbulent fluctuations seems not particularly affected by the control.

As a last comment to these results, the controlled cases show larger fluctuations than the natural case for large distance from the wall, $y/\delta_0 > 4$, in the external flow region. This increment is exclusively due to the coherent velocity fluctuations induced by the acoustic field of the loudspeaker. Also note, that the control with the optimized signal produces slightly larger fluctuation in this region than with sinusoidal forcing. This is connected to the square-like waveform which results in an acoustic field of larger intensity.

6.4 Remarks and conclusions

In this chapter a technique to find optimal input signals for open-loop control of fluid flows has been presented. The technique is based on an evolutionary strategy which searches in the space of signals, defined by an appropriate encoding, for that which is able to optimise a given objective function.

In the present case, the objective function is the mean velocity in a control point in the boundary layer downstream of the cavity. The proposed technique solves the optimisation problem successfully and find an optimal signal which is similar to a square waveform with duty cycle equal to 0.42. When the synthetic jet actuator is driven with this signal the mean velocity at the control point increase by 41 % with respect of the no-control case, while with sinusoidal forcing of the same amplitude the increase is only of 31 %. The resulting mean velocity profile at the same location is significantly fuller, than with sinusoidal forcing and it shows a significant velocity overshoot, of about $0.05u_e$. The momentum thickness of this boundary layer is also substantially reduced. This effects are mainly due to the increased mean jet velocity, as velocity measurements at the slot orifice indicate a increase of 17% of this quantity.

It must be observed that the optimized control signal has a much higher power consumption with respect to the sinusoidal signal, of the order of 30% larger. This larger power requirement is due to the square-like waveform, which puts the loudspeaker under rapid variations of voltage, with the associated larger current absorption. Of course, this larger energy is translated into an higher momentum introduced by the synthetic jet actuation, as discussed previously. Furthermore, the optimized signal puts the loudspeaker under larger stresses, posing the significant problem of reduced life expectancy of the actuator.

From this observations it follows that the gains obtained with the optimized signal in terms of increased mean velocity downstream of the cavity are probably not worth the additional energy consumption. Thus the solution found is optimal only with respect to the chosen objective function. As a result, this suggests that since power requirements for the actuation are not negligible in any form of active

control, they should be included in further researches in the objective function.

Chapter 7

Evolutionary design of closed-loop control systems

The last objective of the research, discussed in this chapter of the thesis, was to explore the possibility of designing closed-loop controllers for fluid flows using evolutionary techniques. In this specific application, the objective of control is to suppress the self-sustained shear layer oscillations, a model problem which has been thoroughly investigated in recent years as a canonical benchmark problem for testing advanced control strategies. Examples of such studies are copious in the literature, such as the numerical works of Rowley et al. [2006] and Illingworth et al. [2012], and the experimental studies of Kegerise and Cabell [2004], Efe et al. [2005] and Samimy et al. [2007].

It must be noted that the closed-loop control strategy discussed in this chapter is not applied to achieve an enhancement of the mean velocities in the near wall flow downstream of the cell, as it was discussed extensively in the previous chapters. It is argued that achieving such an objective requires to inject a significant amount of energy into the flow, which is in contrast with the design principles of most closed-loop control studies, i.e. to enter into and modify the spatio-temporal dynamics of a flow in order to suppress a specific instability, e.g. cavity shear layers, (the above cited works); unsteady wakes, (Pastoor et al. [2008]), turbulent channel flows, (Kim and Bewley [2007]).

The typical approach of closed-loop control of fluid flows, used in the previously cited works, requires the derivation of an accurate mathematical description of all the elements of the control loop, such as actuators, flow, sensors, control hardware, noise, etc. Such models may be obtained, for example, by input/output system identification procedures, (Efe et al. [2005]), may be based on a reduced-order description of the dominant structures in the flow, (Noack et al. [2004]), or may take into account the full Navier-Stokes equations, (Bewley et al. [2001]). Then, in most of the cases the controller may be derived analytically, by using well established

design techniques. In this regard, it is not untypical to use linear models, because of the very large body of techniques to design controllers for linear systems.

The performances of the derived controller are thus strongly affected by how faithful and accurate are the mathematical models of the elements of the control loop. This is a challenging task to accomplish since, for complex flows, problems such as the large range of temporal and spatial scales, the strongly non-linear and chaotic behaviour may be difficult to capture correctly. Therefore, in cases of complex, three-dimensional flows, with intense noise components, this model-based approach may have limited effects, especially in experimental setups, were uncertainties may play an important role.

In contrast to all of the cited works, in this chapter we use a "model-free" approach based on concepts from evolutionary computation theory to design closed-loop controllers. The fundamental idea discussed in this chapter is to evolve a population of controllers by random variation and by selection for reproduction of those controllers that best satisfy a performance criterion. An example of synthesising closed-loop controllers, for other applications, with evolutionary methods is given by Tan and Li [2000] and Li et al. [2004], which proved that design of controllers by genetic algorithms can be effective, and more robust than other traditional methods. The problem of designing closed-loop controllers with genetic algorithms was tackled by Suzuki et al. [2001], which investigated experimentally feedback control of wall turbulence using MEMS technology. However, the controller structure used by these authors, a simple linear feedback with no delays or filtering, was probably too simple for their specific problem. In this work, we propose to use a more complex controller structure, fully described in the following, which may prove flexible enough. Although not discussed in this preliminary work, the type, position and characteristics of sensors and actuators may be the result of the optimisation procedure instead of being based on *a priori* knowledge of the uncontrolled flow.

The proposed method may provide a systematic method to obtain effective control techniques and problem-specific knowledge. In this evolutionary framework, the problem of controlling complex flows is seen as a black-box optimisation problem, whereby one searches for suitable inputs able to bring the flow into a desired state. The flow is treated as a blind input/output system, and only the performance index is used to assess the goodness of the controller. This is certainly a major point when little is known about the problem. Furthermore, it is important to stress that a "block-box" optimisation of the control does not require modelling of the flow. Instead, the entire flow and all the elements of the control loop are considered simultaneously in the performance index to design an optimal controller. This leads to a complete avoidance of modelling inaccuracies. As a consequence, control of non-linear systems can also be tackled easily, since only a way to simulate or test the system under control is required.

Evolutionary approaches can lead to the emergence of unexpected/innovative

control solutions. Since evolutionary algorithms can effectively explore large search spaces, the resulting control technique may yield new solutions, not directly obtainable from the available knowledge of the problem. Furthermore, the optimal control solutions found can be used to gain specific knowledge of the flow, possibly leading to a second and refined generation of controllers, incorporating the gained knowledge.

Application of evolutionary algorithms are not new in fluid mechanics. Milano and Koumoutsakos [2002] designed an open-loop control system driving the actuators controlling the flow past a circular cylinder. Shape optimisation of aerodynamic body is also a problem which can be solved by evolutionary algorithm, e.g. Yamamoto and Inoue [1995], Foster and Dulikravich [1997], Chernyshenko et al. [2008].

In what follows, we highlight the relevant points of this research, we present some fundamental results, and we highlight weaknesses and interesting features of this technique.

7.1 Physical system and block diagram

The block diagram of figure 7.1 shows the conceptual structure of the closed-loop system aiming at controlling the shear layer oscillations.

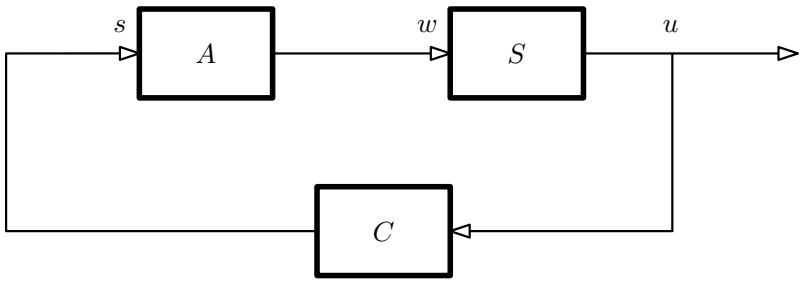

Figure 7.1. Schematic of the closed-loop control system.

All the blocks are treated as Single Input/Single Output (SISO) dynamical systems whose dynamical behaviour may be known or less. The block denoted by "A" represents the actuator device, driven by the voltage signal "s" and which introduces a generic perturbation in the flow, symbolically represented as "w". The dynamical response of the actuator "A" may be determined experimentally, and a suitable mathematical model can be in principle identified, but correctly defining the perturbation "w" may be overly complex. Nevertheless, this perturbation produced by the actuator enters into the flow, represented in the block diagram as "S", forcing it and modifying its dynamics. The cavity flow responds to the forcing and affects the

value of the signal "u", i.e. the velocity fluctuation measured in a suitable position in shear layer. The velocity fluctuation signal "u" is fed back to the controller, i.e. block "C", which has the function of producing a suitable control signal "s". The loop is thus closed but the task at hand is to design an appropriate controller "C".

Since the goal is to dampen the velocity fluctuations in the shear layer, we could set the control problem as to find "C" such that the performance index:

$$J(C) = \frac{1}{N} \sum_{k=0}^{N-1} u[k]^2 dt \tag{7.1}$$

is minimised. The performance index, the variance of the velocity fluctuations, is positive and identically zero when the shear layer fluctuations are completely suppressed.

It has to be noted that, in the preliminary experiments reported in this chapter, the hot wire probe is used both as a sensor and as a measure of the effectiveness of the control. By contrast, in practical applications, other approaches must be taken, such as using wall-pressure sensors, due to the impracticality of measuring the velocity field.

If the systems "A" and "S" were linear this approach would be that of a Linear Quadratic Regulator, whereby one tries to regulate the system to a zero state. In this case the controller can be designed by an exact analytical process, by solving an algebraic Riccati equation, once a suitable mathematical form for both "A" and "S" is available. However, it may be the case that obtaining an accurate model of the actuator and of how the flow responds to the actuation is difficult, due to the inherent complexity of the flow, such as time varying characteristics and three-dimensional effects. Furthermore, constraints on the input signal may render the performance of the LQR controller sub-optimal. Here the controller is designed iteratively using a genetic algorithm, which being a derivative free optimisation technique, needs only an estimate of the performance index J for a given controller C.

In the present work, in order to further simplify the process, the hot wire voltage fluctuation $e(t)$ is used instead of the velocity fluctuation "u" in the block diagram of figure 7.1. Thus, the controller works on a voltage signal and not on a velocity signal. This choice can be justified, other than for its simplicity of implementation, by the fact that the effects of the non-linearity of the hot-wire calibration curve are small if the measured fluctuations have a small amplitude, such that a linear approximation of the hot wire calibration curve can be taken as reasonably valid. This can be ensured by adequately setting gain and offset of the hot wire signal conditioning unit.

Furthermore, a modified performance index is used, defined as:

$$J^*(C) = \frac{1}{N} \sum_{k=0}^{N-1} e[k]^2 dt \tag{7.2}$$

i.e. we use the fluctuation of the hot wire signal also to estimate the amplitude of the shear layer oscillations. Note that for small voltage fluctuation $J^*(C)$ and $J(C)$ differ only by a multiplication factor, proportional to the derivative of the hot wire calibration curve at the set point.

7.2 Controller structure

The first note to make is that the control problem must be cast in a discrete-time setting since the control hardware, a digital computer, operates at a given sampling frequency. Extensive discussion of the design, implementation and characteristic of discrete-time digital control systems can be found in Gopal [2008].

As a first step we focus the attention only on linear controllers. This choice is justified by their simplicity of implementation, since, in a discrete-time setting, they are basically linear filters. Furthermore, a non-linear controller structure, for example derived from a feed-forward artificial neural network, Narendra and Parthasarathy [1990], is much more difficult to be optimized, due to the increased complexity. If a linear controller is successful, it would be possible to restart the optimisation from a non-linear controller structure, e.g. a neural network, that has been previously trained to mimic the successful linear controller.

In the time domain, a generic linear controller can be specified by the linear constant coefficients difference equation:

$$a_0 s[n] = b_0 e[n] + b_1 e[n-1] + \ldots + b_{n_b} e[n-n_b] + a_1 s[n-1] + \ldots + a_{n_a} s[n-n_a] \quad (7.3)$$

where s is the voltage signal generated by the controller and e is the hot wire voltage signal measured by the hot-wire probe located in the flow. This equation corresponds to a Infinite Impulse Response digital filter with input e and output s. The notation $e[n-i]$ denotes the value of the hot wire fluctuation voltage signal measured at $t = t_0 + (n-i)\Delta t$, where $\Delta t = 1/f_s$ is the sampling period.

The loop frequency might not be set a priori but an optimal value of this parameter may be obtained automatically as a result of the optimisation process. Such an approach allows to use at its maximum capabilities the control hardware, since the genetic algorithm is supposed to find by itself both the details of the controller and the sampling frequency which minimise the performance index J. Thus an *a priori* fixed choice of f_s is not guaranteed to be optimal. However, for the sake of simplicity, in this application we used a fixed loop frequency of 1 kHz.

Since the controller structure is chosen, the search problem is to find the values of the coefficients a_i and b_i, such that the performance index is minimised. However, a much more useful and robust representation of the controller structure is to determine the zeros and poles of its transfer function. Therefore, a more suitable form can be obtained by z-transforming the time domain equation 7.3, (Hayes [1996],

Gopal [2008]). The controller is now defined by the transfer function $C(z)$, which reads as:

$$C(z) = \frac{b_0 + b_1 z^{-1} + b_2 z^{-2} + \ldots + b_{n_b} z^{-n_b}}{a_0 + a_1 z^{-1} + a_2 z^{-2} + \ldots + a_{n_a} z^{-n_a}} \tag{7.4}$$

where z is a complex variable. This form can be factorised and written in the gain, zeros, poles form:

$$C(z) = g \frac{\prod_{k=0}^{n_b-1} (1 - z_k z^{-1})}{\prod_{k=0}^{n_a-1} (1 - p_k z^{-1})} \tag{7.5}$$

where z_k and p_k are the zeros and poles of $C(z)$ and g is the gain of the controller.

Figure 7.2 shows an example of position of poles and zeros on the imaginary plane, for a controller with two complex-conjugate zeros and three complex-conjugate poles. In the figure, only the upper imaginary half-plane is represented since $C(z) = C(z^*)$, with * denoting conjugation.

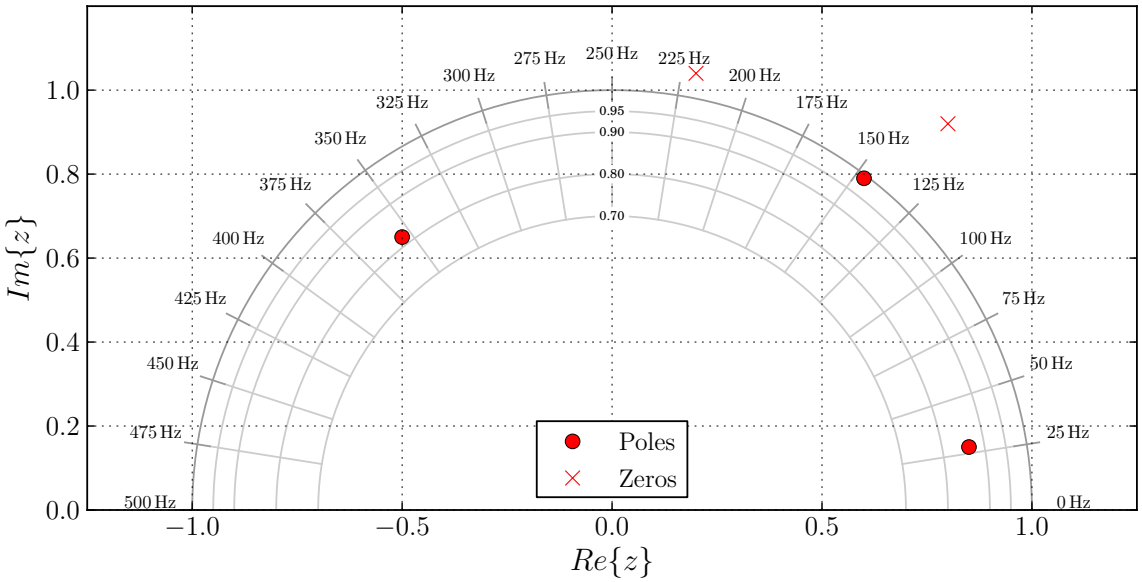

Figure 7.2. Example of controller's poles and zeros on the complex z plane. Only the positive imaginary half-plane is shown, since it is specular to the negative half-plane, as the controller coefficients must be real.

For a given set of zeros, poles and gain, the controller can be characterised by its *frequency response*, which is obtained by evaluating the transfer function on the

unit circle of the imaginary plane z. Thus:

$$C(e^{i2\pi f}) = g\frac{\prod_{k=0}^{n_b-1}(1 - z_k e^{-i2\pi f})}{\prod_{k=0}^{n_a-1}(1 - p_k e^{-i2\pi f})} \tag{7.6}$$

The frequency response can be conveniently divided into the amplitude response $|C(e^{i2\pi f})|$ and the phase response $\angle C(e^{i2\pi f})$, such that

$$C(e^{i2\pi f}) = |C(e^{i2\pi f})|e^{i\angle C(e^{i2\pi f})} \tag{7.7}$$

The frequency response of the example controller of figure 7.2 is shown in figure 7.3. The amplitude response determines the amplification/attenuation factor for each

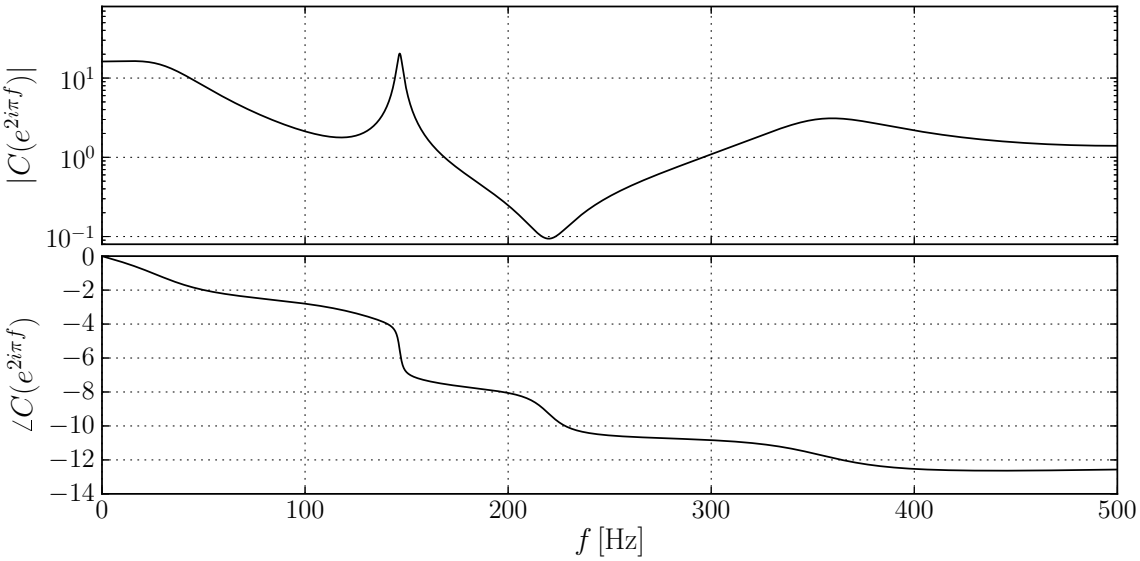

Figure 7.3. Amplitude response, upper, and phase response, lower, of the controller of figure 7.2

frequency component in the e signal, while the phase response determines the phase shift of the actuator signal s with respect to the signal e.

The unknown parameters to be identified are now the locations of the zeros and poles on the imaginary plane, as well as the gain g, which have a more meaningful interpretation that the coefficients a_i and b_i.

However, due to a critical bug in the LABView FPGA code described below, it was not possible to use exactly the controller structures defined here, i.e in a zeros, poles, gain form, which has general validity and should be used preferably. In fact,

it was possible to test only controllers without poles, such that in the time domain the actual control logic is represented by the simpler equation:

$$s[n] = b_0 e[n] + b_1 e[n-1] + \ldots + b_{n_b} e[n-n_b] \tag{7.8}$$

Such a structure has a fundamental limitation, since only simpler behaviours can be modelled with respect to the complete structure, for a given order of the filter. This partially limits the adaptivity of the controller, which is probably an important reason of the poor performances observed, as described in the following.

7.3 Controller design by evolutionary computing

Since the structure of the controller is given, the problem is to find optimal values of the parameters fully defining its performance. The controller is characterised by a set of zeros $Z_C = \{z_k; k = 0, n_z\}$ and the gain g, since the sampling period $1/f_s$ of the control loop is fixed to 1000 μs. Furthermore the number of poles is fixed to 10, so that $n_b = 11$.

The sampling period and the number of zeros n_z, should be let free to vary during the optimisation, even though they may be constrained between upper and lower bounds. This approach may be used since one of the objective should be to extract the most from the control hardware. In fact, it is reasonable to assume that a large value of f_s and a great number of zeros could be able to control better the flow, at the expense of a larger computational cost, and certainly of a higher complexity of the optimisation problem. However, if the control logic is too time consuming, the control hardware cannot satisfy the desired sampling frequency and some cycles can be lost, resulting in a reduced performance.

7.3.1 Algorithm design

In this application, the genetic algorithm is not the CMA-ES, i.e. the state-of-the-art stochastic optimisation technique for continuous problems used in the previous chapter. Instead, a conventional $(\mu + \lambda)$ evolution strategy is used, (Bäck et al. [1991]). The algorithm is characterised by the following parameters. The population size $\mu + \lambda$ is set to 5 individuals, and at each generation the best $\mu = 1$ individual is chosen to produce 4 new controllers. This choice imposes a strong selection pressure on the algorithm at the expenses of a better global search behaviour. The initial population is selected by random sampling of the controller space.

Genetic operators The genome of one individual controller is formed as depicted in figure 7.4.

Figure 7.4. Sketch of the genome of a single individual controller. The controller is defined by its zeros and by the gain.

The genome contains first the n_z complex zeros, then the gain. For the zeros only one of the two complex-conjugates pair is stored and free to variate in the evolutionary process since the other is obtained by taking its conjugate, and cannot vary by itself, which would cause the b_i coefficients to become complex.

Gaussian mutation is used for all the parameters, with an initial standard deviation equal to 0.1 for the zeros, 0.01 for the gain. The mutation strength σ is let free to vary, i.e. a self-adaptive mutation strategy is chosen, (Michalewicz and Fogel [2004]). Note that since the zeros are complex numbers, the mutation is also a complex number. For simplicity, no crossover between individuals is performed, but this additional feature could be useful to implement, since two parents may donate good zeros to the offspring.

7.4 Practical implementation of the controller

Target system A National Instrument Compact-RIO 9074 chassis is used as control platform. This hardware has a 400 Mhz processor running a real-time operating system and the control logic is compiled and run onto an embedded 2 MGates FPGA device. With the chosen control structure this allows sampling frequencies up to about 50 KHz, even tough much lower rates have been used, of the order of 1 kHz.

The CRIO chassis is equipped with a NI9215 analog input acquisition module which has four 16 bits acquisition channels. One of them is connected to the output of the hot wire anemometer, whose signal is adequately pre-conditioned by setting gain and offset. On the same chassis, one of the channels of a NI9263 analog output module drives a power amplifier which drives in turns the three loudspeakers of the synthetic jet system.

The Target systems run a VI in the form of a finite state machine, which, in general, is in a wait state, polling for XML input files. Once a input file is found, sent by the main Python program running the ES as described in the next section, it is parsed and the appropriate parameters are sent to the FPGA device, where the actual control loop is run.

The critical part of this LABView FPGA code is reported in figure 7.5. The code is composed by the for loop I, which is executed $NCycles$ times, where $NCycles$ is typically set large enough to guarantee good convergence of the performance index. This for loop is timed by the "wait until" block G, which has the role of ensuring that

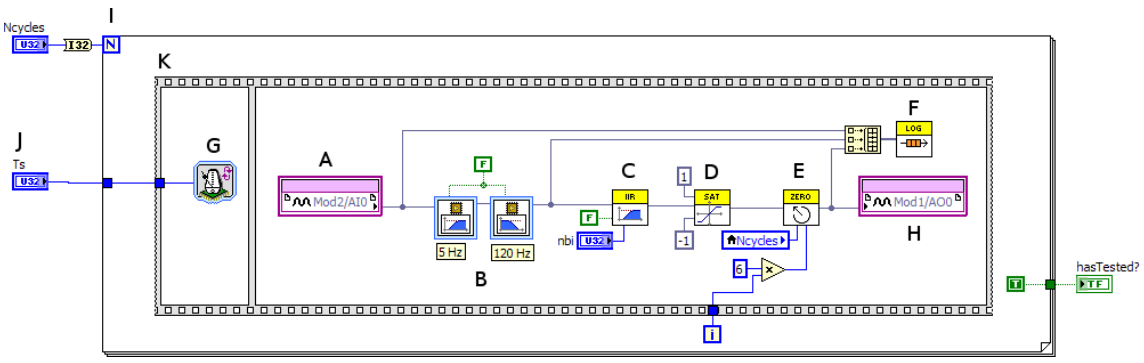

Figure 7.5. Labview FPGA code implementing the closed-loop control logic

the control loop is executed at the correct desired frequency, i.e. $1/Ts$, where Ts measured in microseconds is given by block J. The actual control logic is executed in the second frame of the stacked sequence K, after the timing element G. First, the hot wire signal voltage signal is sampled by block A. This signal is then pass-band filtered by two fourth order Butterworth filters denoted by B. Such a filtering ensures that only the relevant dynamics of the flow enter into the loop, removing high frequency noise and low frequency oscillations associated with the cavity flow. A further advantage of the low pass filter is that the mean value is also removed and only the fluctuation in the pass-band is considered.

The actual control strategy is implemented in block C, where the hot wire voltage signal is filtered by the controller structure described in the previous sections, in the time domain form. Block D is a saturation element which clips the output signal between -1 and 1, in order to prevent damages to the actuator, if the controller signal is too high. It is worth noting at this point that this saturation element would be automatically considered in the evolutionary design of the controller C since only the performance index is used to this aim.

Block E has not an important role but only sets to zero the output signal for the first sixth of the total acquisition period, to show more clearly the effect of the control. Finally, block H puts the control signal on the output module. During the loop the hot wire signal, the filtered hot wire signal and the control signal are sent to block F which implements a Direct Memory Access FIFO Queue to stream data on a file as they are available.

Note that there is a short time delay between execution of blocks A and H, i.e. between the input and the output. For the controllers used in the present experiment this time delay is of the order of 9 μs, which is negligible with respect to the loop period, i.e. 1000 μs.

Host system The evolutionary algorithm described previously is handled by a Python program running on a separate host Linux computer. For each candidate controller to be tested, the program encodes the controller structure and all the required parameters into a single XML file, which is sent to the target computer via FTP protocol. The Python program then goes into a wait state, and polls for the output file generated by the target system when the control-loop has been run for a sufficient amount of time. The Python program then reads the output file and assigns a value of the performance index to that candidate controller using equation 7.2. This process is run for several generations until a suitable solution is found.

7.5 Results

For the sake of simplicity, and due to the initial problems encountered in the experiments, the control experiments have been performed with a fixed size of the controller, with 10 complex-conjugate zeros, i.e. using a filter with 11 coefficients.

Furthermore, the experiments were run at a freestream velocity of 3 m/s, a speed were the lock-in phenomenon of the shear layer with the wind tunnel acoustic forcing is absent, and the flow oscillates at its natural frequency, (see figure 3.1 for reference.) Furthermore, this condition at a lower Reynolds number partially eliminates the problem of dealing with small freestream disturbances present in the upstream laminar boundary layer of CASE1, (see figure 3.3), which may represent a significant issue for the controller design problem.

The control experiments were performed with the hot wire probe located at $x/L = 0.58$ and $y/\delta_0 = 0.9$, with δ_0 equal to 6.1 mm. This choice is motivated by the observation that the location of the control point is probably not very important since the entire flow is dominated by the oscillations of the shear layer. However, it is argued that locations in the second half of the shear layer, $x/L > 0.5$, should likely perform better since the signal is stronger with respect to locations in the initial region of the shear layer. Furthermore, the control point is for $y/\delta_0 > 0$, to eliminate from the loop low-frequency disturbances, due to the cavity flow. The pass-band filters, described in figure 7.5 as blocks B, were set to retain only the dynamics in the range 5-120 Hertz, which contained most of the energy of the velocity fluctuations.

The controller design technique which has been proposed in the previous section has not been successful, since it has not been possible to reduce the amplitude of the velocity fluctuations in the control point *below* the value of the unactuated flow. We report in the following some typical results obtained in closed-loop control conditions, along the evolutionary process. In fact, even though the control is not effective, there is a number of typical behaviour which may be helpful to indicate future directions.

A first typical example of the behaviour observed is given in figure 7.6. This is a characteristic behaviour of controllers at the first generations. The figure shows a portion of the time history of the hot wire voltage signal filtered by the the pass-band elements, in part (a), and the time history of the control signal, in part (b). Closed-loop control is switched on at $t = 1$ s. The behaviour of this initial

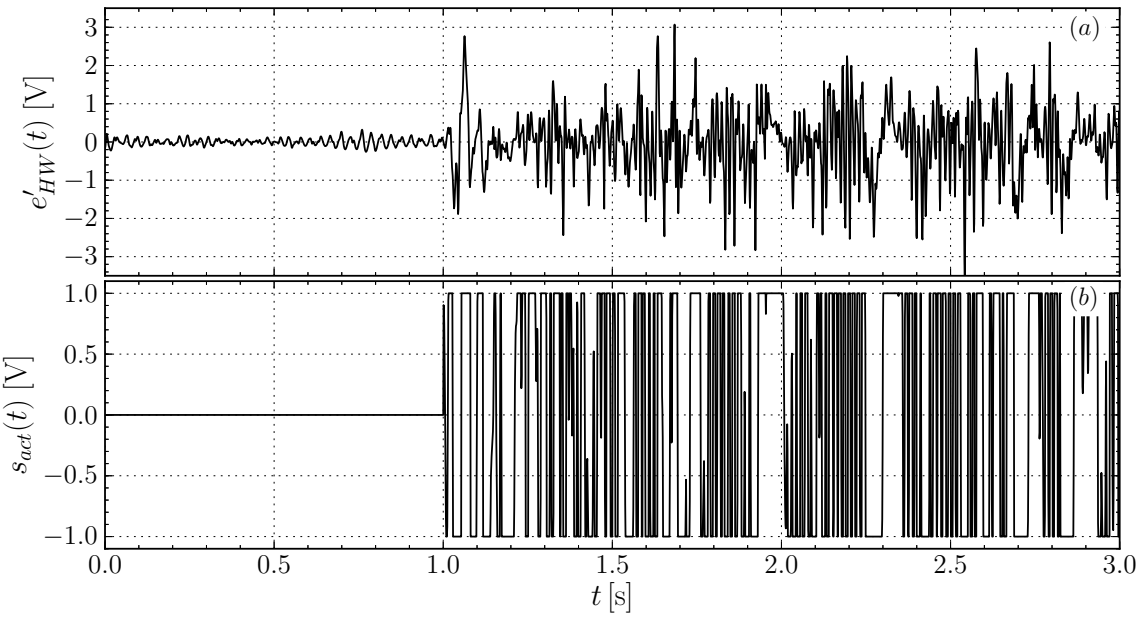

Figure 7.6. Behaviour of an example controller in the initial generations. Time history of the hot wire filtered voltage signal, (a), and time history of the control signal, (b). Closed-loop control is switched on at $t = 1$ s.

controller is dominated by its high gain, which gives rise to large actuation inputs, clipped between -1 and 1 Volts, figure 7.6-(b). Furthermore, due to the saturation limit, it appears that the input signal is essentially random. In reason of the large actuation inputs, the response of the flow is very strong, since very intense and random fluctuations of the shear layer can be observed in when control is switched on. Therefore, the performance index of this type of controller is very high.

It has to be observed that, due to the high-pass component of the pre-filters, the variations of the mean value, occurring in reason of a modification of the mean structure of the flow, are not evidenced by the time history in figure 7.6-(a). In fact, the action of such a type of controller, producing very large inputs, is strongly non-linear. This is essentially due to the intense flow perturbations introduced by the synthetic jet *into* the cavity, which are large scale structures convected along the cavity wall.

As the controller optimisation proceeds, the evolution strategy produces controllers which result in lower actuation inputs. In these cases, there is a interesting

characteristic behaviour emerging. An example of the results of such a type of controller is given in figure 7.7, which reports the same quantities as in figure 7.6. Note that the vertical scale of $e'_{HW}(t)$ covers a much shorter range, since the velocity fluctuations have a smaller amplitude in this case. It can be observed that in no-control

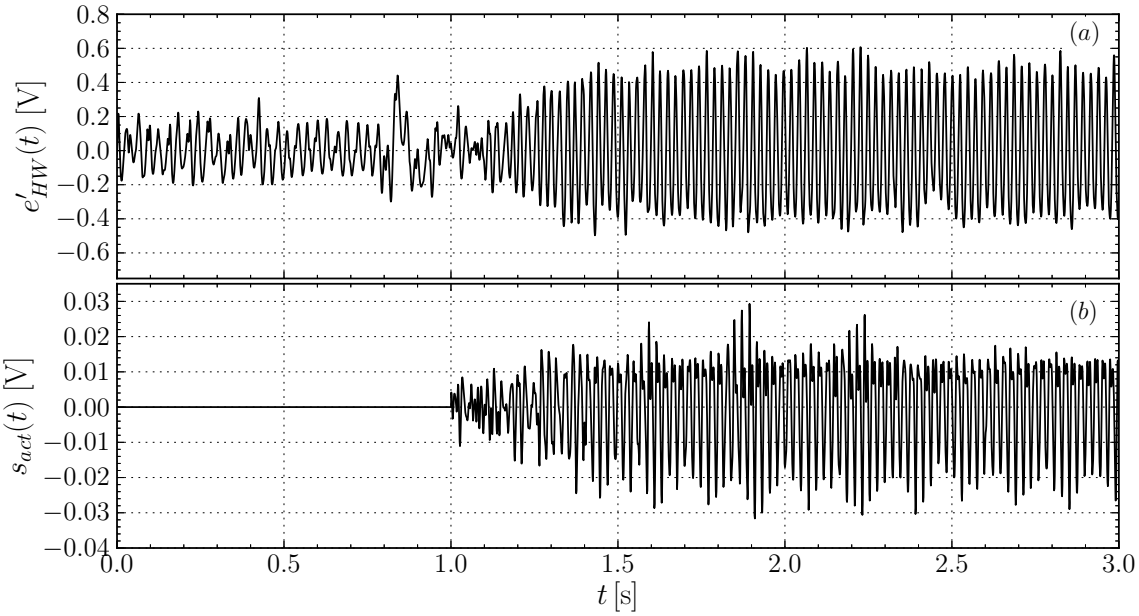

Figure 7.7. Behaviour of an example controller in "lock-in" conditions. Time history of the hot wire filtered voltage signal, (a), and time history of the control signal, (b). Closed-loop control is switched on at $t = 1$ s.

conditions, the hot wire signal fluctuates with a peak-to-peak amplitude of about 0.2 Volts. However, when control is switched on at $t = 1$ s, we observe, after an initial short transient, that the velocity signal is locked onto the actuator signal.

Nevertheless, after the initial transient, the peak-to-peak amplitude of the voltage fluctuations is more than doubled with respect to the unactuated flow, so this specific controller is not effective, even if its performance is superior to that of figure 7.6.

It is observed that the input signal amplitude is very small, with a peak-to-peak amplitude of the order of 40 milliVolts. In terms of jet velocity, such an amplitude corresponds to a mean value of the order of 0.3 m/s. However, in chapter 5 it has been shown that a lock-in condition can manifest even for very low forcing amplitude, due to the high sensitivity of the shear layer flow.

One possible idea would be to reduce the amplitude of the input signal, by simply reducing the gain g of the controller, in order to reduce the amplitude of the shear layer response. In fact, this is the result of the evolutionary optimisation procedure which has been implemented. We observed that, as the generations of the evolution

strategy passed by, the amplitude of the control signal diminished progressively, such as to perturb less and less the flow field. This was achieved by the algorithm mainly as a reduction of the controller's gain, rather than a redistribution of the transfer function zeros. Eventually, the result of the optimisation process is a controller with no effect at all on the flow.

An example result obtained with one of such controllers, is given in figure 7.8. This specific controller is that which resulted in the minimum root-mean-square value of the velocity fluctuations, at the end of the optimisation process. As before, part (a) shows a portion of the time history of the filtered hot-wire signal, while part (b) reports the input control signal. Note that the amplitude of the vertical scale is the same as in the previous figure, for both parts. As discussed above, it

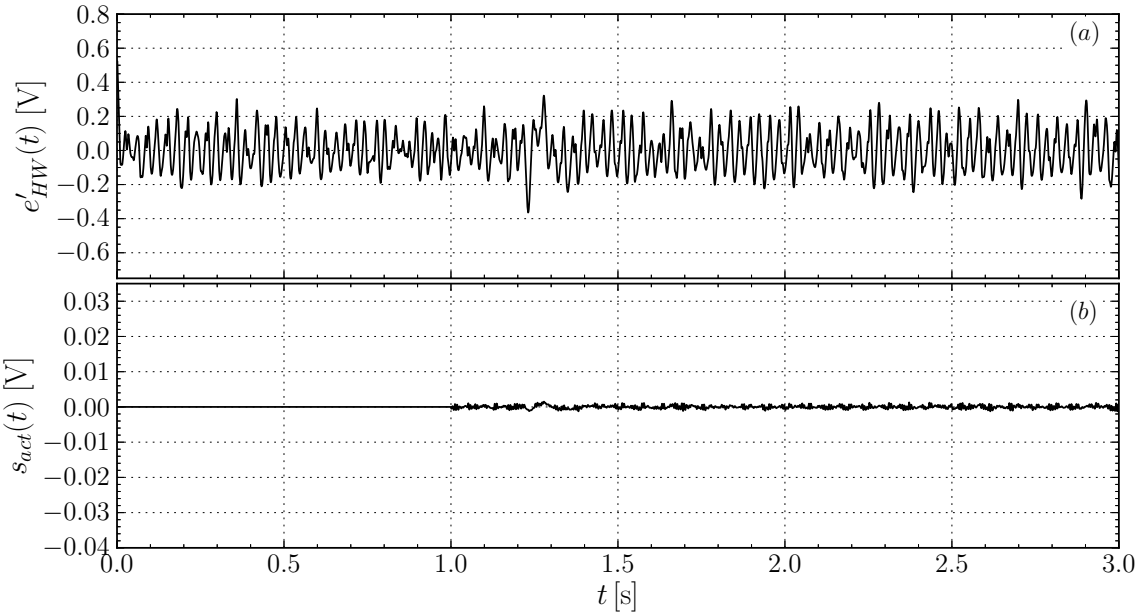

Figure 7.8. Behaviour of an example controller after the optimisation process has come to the end. Time history of the hot wire filtered voltage signal, (a), and time history of the control signal, (b). Closed-loop control is switched on at $t = 1$ s.

is observed that the result of the optimisation process is a controller which has the minimum impact on the shear layer flow. This is, of course, a demonstration that the design procedure has not been successful and possible explanations are given in the following section.

7.6 Remarks

The evolutionary optimisation approach described above was not successful, for a number of reasons. A first motivation is the unfavourable position of the actuator,

which was initially located on the downstream edge of the cavity in order to control the cavity flow in an open-loop manner, by enhancing the intensity of the vortical structure. In many, if not all, studies of closed loop control of cavity flows the actuator is located at the upstream cavity edge, where the shear layer detaches. The physical motivation for such a location is that the shear layer is maximally receptive to disturbances generated in this region, see e.g. Cattafesta et al. [2008]. Here, the control authority of the actuator would be maximised.

Moreover, the location chosen for this application appears not effective because of the physical distance with the region of maximum receptivity; any control action travels upstream across the entire shear layer generating a perturbation which influences a large region of the flow field. It is argued that application of this same procedure applied in an ad-hoc designed experiment may prove more successful.

A further explanation is that it is likely that the type of controller used in these experiments was no sufficiently flexible to be effective. In fact, a controller with poles would have been able to selectively amplify specific frequencies, matching the narrow band dynamics of the shear layer oscillations. Instead, in a zero-only controller such a behaviour is more difficult to achieve, since a very large number of zeros would be required.

Conclusions

The main objective of this research project has been to provide additional insight into the physics and the control of the flow in a Trapped Vortex Cell (TVC), in order to gain a significant understanding of the base flow and of its relevant driving phenomena. Such understanding is required since such a configuration has recently gained interest as a control device to enhance the performances of an airfoil hosting the cell.

To achieve this goal, a simplified configuration has been investigated, where a TVC embedded on a flat plate manipulates the zero-pressure-gradient boundary layer flowing past it. It is important to notice that, in this setting, a measure of the effectiveness of control is the reduction of the boundary layer momentum thickness across the cavity opening. In fact, on a complete airfoil equipped with a TVC, such a reduction implies that separation of the flow downstream of the cell can be prevented or delayed, since a faster wall flow is less subject to separate.

The cell flow has been first investigated in two representative conditions without the action of control, i.e. we use a TVC as a passive control device. In the first condition, at a moderate Reynolds number, the upstream boundary layer is laminar and thin with respect to the cavity opening length. In such a condition the TVC displays strong aero-acoustic oscillations, which are the result of a lock-in condition with an acoustic forcing due to a wind tunnel resonance. A weakly rotating vortex is observed in the cavity, but results indicate clearly that likely the most important element of the TVC as a control device is the shear layer. In fact, the strong amplification of the velocity fluctuations in the shear layer and the break up into turbulence of the coherent structures originated in this region, produce a turbulent boundary layer downstream. This boundary layer is significantly thicker than that upstream and it has the strong signature of the dissipation encountered along the shear layer evolution, visible as a marked velocity defect. Therefore, the presence of the cavity as a passive device in this condition is detrimental, essentially because of the instability of the shear layer.

The second condition is representative of an high Reynolds number flow and it is characterized by a thick turbulent incoming boundary layer. In this condition, due to the large thickness of the boundary layer with respect to the cavity opening,

the shear layer does not develop strong self-sustained oscillations. Nevertheless, a comparison of the mean velocity profiles in the boundary layer between two reference locations upstream and downstream of the cavity clearly indicates a marked velocity defect in the boundary layer downstream, a symptom of a loss of momentum of the fluid flowing past the cell. This velocity defect has been associated to the momentum transfer operated by the turbulent stresses which sustain the rotation of the vortex flow, faster than in the first condition. In addition, this velocity defect is connected to a region of large velocity fluctuations in the downstream boundary layer which develops in the shear layer, and which lifts up from the wall after the impingement.

A further observation for this condition is the presence of a low frequency oscillation of the entire cell flow, consisting in a motion of the centre of the vortex core. The amplitude of this oscillation is modulated in the spanwise direction, evidence as a periodic modulation of the root-mean-square value of the velocity fluctuations along the cavity span. It is likely that such oscillation is similar in nature to that observed by other investigators, e.g. Tutty et al. [2012], Hokpunna and Manhart [2007], which they attributed to a natural inviscid instability of the vortex core. In any case, despite the relevance of this oscillation for the dynamics of the cavity flow, no clear evidence of its effects on the downstream boundary layer, positive or negative, is found.

Therefore, the investigations on the uncontrolled flow suggest that, in both conditions, the key element determining the poor performances of the cell is the shear layer and its evolution, to which the characteristics of the downstream boundary layer are strongly tied to. As a result, it is of no surprise that the effectiveness of the two flow control techniques tested on the TVC flow is strongly coupled to how the control action interacts with the shear layer flow. This behaviour has been observed in both the control techniques which have been investigated.

The first technique is the control of the cell flow by suction, similarly to what has been done by other investigators. In this work, suction has been applied separately in two different regions, inside the cell on the upstream part, and on the downstream cavity edge. In the former case, the effect of the suction is twofold. The first effect is that, by mass conservation principles, the slower layers of the incoming boundary layer flow, and thus of the shear layer, are ingested into the cavity. The entire shear layer is displaced downwards, and the layers with higher momentum impinge on the downstream edge of the cavity. This results in a more energetic boundary layer developing downstream, with a lower momentum thickness. What is more, if the suction is intense enough to capture the entire thickness of the incoming boundary layer, the external flow impinges on the cavity shoulder, giving rise to a fresh, laminar boundary layer, thinner even than the upstream one. The second effect of the control by suction is that ingestion of high-momentum external fluid into the cavity leads to an enhancement of the intensity of the vortex flow. This modification of the mean flow results in an alteration of evolution of the shear layer, yielding a

lower growth rate of the perturbations in the shear layer, which will thus display a lower level of fluctuations. Nevertheless, it is argued that such an enhancement is not causally connected to the observed increase of the velocity in the wall-flow downstream of the cell.

Furthermore, it has been demonstrated that the relevant parameter that characterise the effectiveness of this control strategy is when the suction rate Q is rescaled to the thickness y_q, that is the thickness of the upstream boundary layer through which flows the flow rate Q. It is observed that the effectiveness of the cell, in terms of reduction of the momentum thickness, is strongly dependent on this parameter. Initially, an increase of suction implies a reduction of the momentum thickness of the wall flow downstream of the cell. However, when the suction rate is such that y_q is equal to δ_0, the entire boundary layer/shear layer is ingested into the cavity and only external flow impinges on the cavity shoulder and there are no further gains.

For what concerns application of suction over the second region, on the downstream edge of the cell, a large difference in the structure of the cell's flow is observed, with respect to suction inside the cell. In fact, the intensity of the vortical structure forming in the cavity as a result of the ingestion mechanism is reduced, since the mass removed from the cavity region is lower, due to the limited area of the porous wall extending inside the cell. Nevertheless, the structure of the wall flow at some distance downstream of the cell itself, appears very similar to that observed for the first suction case. Likely, this happens because of the fact that suction modifies favourably the near wall flow just downstream of the impingement, by removing the layers of turbulent fluid nearest the wall. This important result suggests that the location of suction may not be so crucial for the performances of a vortex cell.

The main drawback of control of the TVC flow by suction is that it is energetically very expensive and it is thus strongly non-efficient. For this reason, a second alternative technique has been investigated. This technique is based on a much more efficient actuation system, i.e. a synthetic jet device. The synthetic jet slot is located just below the downstream edge of the cavity and it is oriented such as to inject momentum tangentially into the cell. It is observed that such an arrangement enhances the rotational velocity of the vortex and regularises the erratic injection of high-energy packets shed into the cavity from the downstream edge, a feature of both the conditions investigated in no-control. The cell flow is significantly affected by the actuation through two separate mechanisms. The first is that the enhanced rotation of the vortex flow causes a net momentum transfer from the topmost layers of the cavity flow to the shear layer. This results in a reduction of the momentum thickness of the downstream boundary layer, and even in a velocity overshoot in the mean velocity profile, for large actuations. However, this mechanism only occurs if the actuation intensity is larger than a threshold value, below which no strong effects are observed on the downstream boundary layer. The second effect of the actuation is that related to a complex coupling between the unsteady forcing and the shear

layer instability, which always results in an increase of the velocity fluctuation in this region. This mechanism is more relevant in the first condition investigated, when the thin shear layer is affected by self-sustained oscillations. However, no significant influence of this strong coupling is found in the properties of the downstream boundary layer, which is instead much more affected by the first mechanism, strictly connected to the amplitude of the forcing.

Appendix A

Theoretical foundations of the Multi-Time-Delay Linear Stochastic Estimation technique.

A.1 Multi-time-delay Linear Stochastic Estimation approach

The Linear Stochastic Estimation (LSE) technique was introduced by Adrian [1977] as a means to approximate the conditional average of the fluctuating velocity vector field given the occurrence of an event vector $\mathbf{E}$. This conditional average is defined as:

$$\hat{\mathbf{u}}(\mathbf{x}, t) = \langle \mathbf{u}(\mathbf{x}, t) | \mathbf{E} \rangle \tag{A.1}$$

and can be expanded in a Taylor series of the event. In general, $\mathbf{u}$ indicates the velocity fluctuation, since the mean flow is known and does not need to be estimated, Brereton [1992].

As demonstrated by several authors, e.g. Picard and Delville [2000], Naguib et al. [2001], Ukeiley and Murray [2005], the event can be also obtained from wall-mounted pressure sensors. For the single sensor case, the event reads as :

$$\mathbf{E} = \{p_e < p(t) < p_e + \mathrm{d}p\} \tag{A.2}$$

and confines the wall-pressure into a small window between p_e and $p_e + \mathrm{dp}$. The linearly truncated Taylor expansion of the conditional average then reads as:

$$\hat{\mathbf{u}}(\mathbf{x}, t) = \mathbf{a}(\mathbf{x}) p(t) \tag{A.3}$$

and the coefficients $\mathbf{a}(\mathbf{x})$ are obtained from unconditional statistics, i.e. two point correlations, which result from a minimum square error procedure, fully described

in Guezennec [1989]. This is a *single-time-delay* approach (STD), in that the event vector $\mathbf{E}$ specifies a condition on the wall-pressure only at a single time instant. This time instant can be the present time t or can refer to a past time $t - \tau$, as shown for example by Naguib et al. [2001]. The technique can then be used to reconstruct the time-resolved dynamics of the conditional flow field, based on wall-pressure measurements.

The basic idea of the *multi-time-delay* approach (MTD) is that in order to obtain a more accurate time resolved reconstruction of the flow field $\hat{\mathbf{u}}(\mathbf{x}, t)$ at time t, multiple past wall-pressure samples should be taken into account. Only past samples are considered here, since this would be the natural approach to take in a real-time flow control scheme. For the single sensor case, this corresponds to defining an event vector $\mathbf{E}$ of the form:

$$\mathbf{E} = \{ \quad p_{e_0} < p(t) < p_{e_0}+\mathrm{d}p,\ p_{e_1} < p(t-\Delta t) < p_{e_1}+\mathrm{d}p,\ \ldots\ p_{e_n} < p(t-n\Delta t) < p_{e_n}+\mathrm{d}p\}, \tag{A.4}$$

which is made up of $n+1$ simoultaneous conditions on the past values of the wall-pressure time history. This event vector can also be naturally extended to contain past samples from multiple sensors, defining a *multi-point*, multi-time-delay Stochastic Estimation technique. The motivation for specifying such an event vector derives from the observation that this expanded event imposes a *dynamic* condition on the average of the flow field, which may provide a more detailed description of the temporal evolution of the flow. On the other hand, specifying only a single-time-delay condition, whether from single or multiple sensors, is an incomplete description of the dynamic state of the flow and corresponds to an average over all the possible dynamic flow states.

Given these considerations, the linearly truncated expansion of the conditional average A.1, using the event of equation A.4 and including multiple sensors, can be written as:

$$\hat{\mathbf{u}}(\mathbf{x}, t) = \sum_{j=1}^{M} \sum_{k=0}^{n} \mathbf{b}_{kj}(\mathbf{x}) p_j(t - k\Delta t). \tag{A.5}$$

The first summation is done over the M available wall-pressure sensors, while the second is done over the $n+1$ samples of the wall-pressure time history. We call n the model order. It is immediately apparent that the case $n = 0$ and $M = 1$ corresponds exactly to the definition of the single-point, single-time-delay Linear Stochastic Estimation of equation A.3. In this paper only the linearly truncated expansion is considered and treated, but extensions to higher order terms may also be developed.

The problem of finding the coefficients $\mathbf{b}_{kj}(\mathbf{x})$ is solved in the same way as for single-time-delay estimates, as described by Guezennec [1989], by choosing the values of $\mathbf{b}_{kj}(\mathbf{x})$ which provide a minimum mean-square estimation error. However, for a multi-time-delay approach there are some fundamental differences, briefly reviewed

here in the following. For a more thorough description of the Least Sqaure method the reader is referred to Ljung [1998].

A.1.1 Single-point, multi-time-delay linear Stochastic Estimation

We first consider the problem of single-point estimates, $M = 1$, leaving the different details specific to the multi-point approach, $(M > 1)$, to section A.1.2. Furthermore, the problem of estimating only one of the velocity components at a given point $\mathbf{x}_0$ is treated. This is, in fact, the "base" problem, independently repeated over all the spatial locations and for all the available velocity components.

From simultaneous measurements of the velocity fluctuation $u(t)$ at point $\mathbf{x}_0$ and of the wall-pressure $p(t)$, statistically significant collections of N samples are extracted: $\{u(i)\}$, $\{p(i)\}$ $i = 1, \ldots, N$, where $p(i) = p(i\Delta t)$, with Δt being the sampling interval. Introducing a matrix notation, equation A.5 may be rewritten as:

$$\hat{u}(i) = \boldsymbol{\varphi}(i)^T \boldsymbol{\theta}, \tag{A.6}$$

where $\boldsymbol{\varphi}(i) = [p(i)\, p(i-1) \ldots p(i-n))]^T$ is called the regressors vector at time instant i and $\boldsymbol{\theta} = [b_0\, b_1 \ldots b_n]^T$ is the vector of the unknown coefficients. These two vectors have size $(n+1) \times 1$. Furthermore, since data is not available for $i < 0$, the first full regressors vector can be obtained at $i = n - 1$.

The unknown coefficients vector is found as the minimizing argument of the mean-square estimation error (MSEE), defined as:

$$E(\theta) = \frac{1}{N-n} \sum_{i=n-1}^{N} \Big[u(i) - \hat{u}(i) \Big]^2 = \frac{1}{N-n} \sum_{i=n-1}^{N} \left[u(i) - \sum_{k=0}^{n} b_k p(i-k) \right]^2 \tag{A.7}$$

and it is obtained by deriving equation A.7 with respect to θ and setting to zero, which yields a set of linear equations called the *normal equations*:

$$\left[\frac{1}{N-n} \sum_{i=n}^{N} \boldsymbol{\varphi}(i) \boldsymbol{\varphi}^T(i) \right] \boldsymbol{\theta} = \frac{1}{N-n} \sum_{i=n}^{N} \boldsymbol{\varphi}(i) u(i), \tag{A.8}$$

compactly written as:

$$\mathbf{R}\boldsymbol{\theta} = \mathbf{f}. \tag{A.9}$$

The matrix $\mathbf{R}$ has a particular structure which allows the computation of its elements in a fast and convenient way. It is straightforward to see that:

$$\mathbf{R} = \frac{1}{N-n} \sum_{i=n}^{N} \begin{bmatrix} p_i p_i & p_{i-1} p_i & \cdots & p_{i-n} p_i \\ p_{i-1} p_i & p_{i-2} p_i & \cdots & p_{i-n} p_{i-1} \\ \vdots & \vdots & \ddots & \vdots \\ p_{i-n} p_i & p_{i-n} p_{i-1} & \cdots & p_{i-n} p_{i-n} \end{bmatrix}, \tag{A.10}$$

where $p_i = p(i)$. This means that:

$$\mathbf{R}_{ij} = r_{pp}(\kappa), \qquad \kappa = j - i, \tag{A.11}$$

where $r_{pp}(\kappa)$ is the auto-correlation function of the pressure signal, defined as:

$$r_{pp}(\kappa) = \overline{p(i)p(i+\kappa)}. \tag{A.12}$$

The matrix $\mathbf{R}$ is thus a Toeplitz matrix with size $(n+1) \times (n+1)$, which can be formed from the auto-correlation function of the pressure signal, and reads as:

$$\mathbf{R} = \begin{bmatrix} r_{pp}(0) & r_{pp}(1) & \dots & r_{pp}(n) \\ r_{pp}(1) & r_{pp}(0) & \dots & r_{pp}(n-1) \\ \vdots & \vdots & \ddots & \vdots \\ r_{pp}(n) & r_{pp}(n-1) & \dots & r_{pp}(0) \end{bmatrix}. \tag{A.13}$$

The column vector $\mathbf{f}$, of size $(n+1) \times 1$, can be obtained in a similar way, by considering that:

$$\mathbf{f} = \frac{1}{N-n} \sum_{i=n}^{N} \begin{bmatrix} p_i \\ p_{i-1} \\ \vdots \\ p_{i-n)} \end{bmatrix} u(i) = \begin{bmatrix} r_{pu}(0) \\ r_{pu}(1) \\ \vdots \\ r_{pu}(n) \end{bmatrix}, \tag{A.14}$$

where we have introduced the cross-correlation function between the pressure and the velocity $r_{pu}(\kappa) = \overline{p(i)u(i+\kappa)}$.

The matrices $\mathbf{R}$ and $\mathbf{f}$ can thus be constructed from the auto- and cross-correlation functions of the wall-pressure and velocity measurements. The computational time required for obtaining these matrices can be significantly reduced by exploiting the Correlation Theorem and using Fast Fourier Transform techniques to obtain the correlation function. Then the unknown coefficients vector can be obtained by solving the linear system $\mathbf{R}\boldsymbol{\theta} = \mathbf{f}$.

A.1.2 Multi-point multi-time-delay Stochastic Estimation

For a multi-point estimate with $M > 1$ sensors, the procedure described above is still valid, but there are some small differences, detailed here. The regressors vector in equation A.6 becomes a column vector of $M(n+1) \times 1$ elements which reads as:

$$\boldsymbol{\varphi}(i) = [p_1(i),\, p_1(i-1),\, \dots,\, p_1(i-n),\, \dots\, p_M(i),\, p_M(i-1),\, \dots,\, p_M(i-n)]^T, \tag{A.15}$$

and contains past values of the M wall-pressure time histories. Similarly, the unknown coefficients vector $\boldsymbol{\theta}$ reads as:

$$\boldsymbol{\theta} = [b_{10},\, \dots,\, b_{1n}, b_{20},\, \dots,\, b_{2n}, \dots, b_{M0},\, b_{M1},\, \dots,\, b_{Mn}]^T \tag{A.16}$$

The matrix $\mathbf{R}$ in the normal equations A.9 is derived in the same way as before, but it is now a symmetric block matrix, composed of $M \times M$ blocks of size $(n+1)\times(n+1)$. Each block is a Toeplitz matrix made up of auto- or cross-correlation values between the wall-pressure sensors. The matrix has the form:

$$\mathbf{R} = \begin{bmatrix} \mathcal{R}_{p_1p_1} & \mathcal{R}_{p_1p_2} & \dots & \mathcal{R}_{p_1p_M} \\ \mathcal{R}_{p_2p_1} & \mathcal{R}_{p_2p_2} & \dots & \mathcal{R}_{p_2p_M} \\ \vdots & \vdots & \ddots & \vdots \\ \mathcal{R}_{p_Mp_1} & \mathcal{R}_{p_Mp_2} & \dots & \mathcal{R}_{p_Mp_M} \end{bmatrix}, \tag{A.17}$$

where the i-th,j-th block $\mathcal{R}_{p_ip_j}$, is such that:

$$\mathcal{R}_{p_ip_j} = \begin{bmatrix} r_{p_ip_j}(0) & r_{p_ip_j}(1) & \dots & r_{p_ip_j}(n) \\ r_{p_ip_j}(1) & r_{p_ip_j}(0) & \dots & r_{p_ip_j}(n-1) \\ \vdots & \vdots & \ddots & \vdots \\ r_{p_ip_j}(n) & r_{p_ip_j}(n-1) & \dots & r_{p_ip_j}(0) \end{bmatrix}, \tag{A.18}$$

with $r_{p_ip_j}(\kappa)$ being the cross-correlation function between the i-th and j-th sensors signals.

In a similar way the column vector $\mathbf{f}$ in the normal equations, equation A.9, becomes:

$$\mathbf{f} = \begin{bmatrix} \mathcal{R}_{p_1u} \\ \mathcal{R}_{p_2u} \\ \vdots \\ \mathcal{R}_{p_Mu} \end{bmatrix}, \tag{A.19}$$

where each of the M blocks $\mathcal{R}_{p_iu}$ is a $(n+1)\times 1$ column vector composed of the values of the cross-correlation function $r_{p_iu}(\kappa)$ between pressure and velocity for $k = 0, \dots n$. The linear system $\mathbf{R}\boldsymbol{\theta} = \mathbf{f}$ can then be solved for each spatial location and for each velocity component, yielding the full set of coefficients $\mathbf{b}_{kj}(\mathbf{x})$. With these and from new wall-pressure measurements the spatio-temporal evolution of the flow can be estimated, using equation A.5.

Bibliography

R. C. Adkins. A short diffuser with low pressure loss. *Journal of Fluids Engineering*, 97:297–302, 1975.

R. J. Adrian. On the role of conditional averages in turbulence theory. In *Turbulence in Liquids*, pages 323–332, 1977.

AGARD-AR-336. *Wind tunnel wall corrections*. NATO Research and Technology Organisation, 1998.

R. A. Antonia, Y. Zhu, and M. Sokolov. Effect of concentrated wall suction on a turbulent boundary layer. *Physics of Fluids*, 7(10):2465–2474, 1995.

T. Bäck, F. Hoffmeister, and H.P. Schwefel. A survey of evolution strategies. In *Proceedings of the Fourth International Conference on Genetic Algorithms*, pages 2–9. Morgan Kaufmann, 1991.

J. Basley, L. R. Pastur, F. Lusseyran, T. M. Faure, and N. Delprat. Experimental investigation of global structures in an incompressible cavity flow using time-resolved PIV. *Experiments in Fluids*, 50(4):905–918, 2010.

J. S. Bendat and A. G. Piersol. *Random data: analysis and measurement procedures*. Wiley & Sons, 1986.

T. R. Bewley, P. Moin, and R. Temam. DNS-based predictive control of turbulence: an optimal benchmark for feedback algorithms. *Journal of Fluid Mechanics*, 447: 179–225, 2001.

H. G. Beyer. *The Theory of Evolution Strategies*. Natural Computing Series. Springer, 2001.

H. G. Beyer and H. P. Schwefel. Evolution strategies. A comprehensive introduction. *Natural computing*, 1:3–52, 2002.

G. J. Brereton. Stochastic estimation as a statistical tool for approximating turbulent conditional averages. *Physics of Fluids A*, 4(9):2046–2054, 1992.

G. Brès and T. Colonius. Three-dimensional instabilities in compressible flow over open cavities. *Journal of Fluid Mechanics*, 599:309–339, 03 2008.

J.C. Bruggeman, A. Hirschberg, M.E.H. van Dongen, A.P.J. Wijnands, and J. Gorter. Self-sustained aero-acoustic pulsations in gas transport systems: Experimental study of the influence of closed side branches. *Journal of Sound and Vibration*, 150(3):371 – 393, 1991.

A. V. Bunyakin, S. I. Chernyshenko, and G. Y. Stepanov. High-reynolds-number batchelor-model asymptotics of a flow past an aerofoil with a vortex trapped in a cavity. *Journal of Fluid Mechanics*, 358(-1):283–297, 1998.

L. N. Cattafesta, Q. Song, D. Williams, C. W. Rowley, and F. Alvi. Active control of flow-induced cavity oscillations. *Progress in Aerospace Sciences*, 44(7-8):479–502, 2008.

L. Chatellier, J. Laumonier, and Y. Gervais. Theoretical and experimental investigations of low mach number turbulent cavity flows. *Experiments in fluids*, 36(5): 728–740, 2004.

S. I. Chernyshenko. Fundamentals of actively controlled flows with trapped vortices. *EU Executive summary report for contract no. AST4-CT-2005-012139*, 2009.

S. I. Chernyshenko, B. Galletti, A. Iollo, and L. Zannetti. Trapped vortices and a favorable pressure gradient. *Journal of Fluid Mechanics*, pages 235–255, 2003.

S. I. Chernyshenko, I. P. Castro, T. Hetsch, A. Iollo, E. Minisci, and R. Savelsberg. Vortex cell shape optimization for separation control. In *5th. European Congress on Computational Methods in Applied Sciences and Engineering (ECCOMAS 2008)*, Venice, Italy, 2008.

F. De Gregorio and G. Fraioli. Flow control on a high thickness airfoil by a trapped vortex cavity. In *14th International Symposium on Applications of Laser Techniques to Fluid Mechanics*, Lisbon, Portugal, 2008.

R. Donelli, S. I. Chernyshenko, P. Iannelli, A. Iollo, and L. Zannetti. Flow models for a vortex cell. *AIAA Paper*, 2(47):451–467, 2009.

M. Ö. Efe, M. Debiasi, P. Yan, H. Özbay, and M. Samimy. Control of subsonic cavity flows by neural networks-analytical models and experimental validation. *AIAA Paper*, 294:2005, 2005.

T. M. Faure, P. Adrianos, F. Lusseyran, and L. Pastur. Visualizations of the flow inside an open cavity at medium range Reynolds numbers. *Experiments in Fluids*, 42(2):169–184, 2006.

T. M. Faure, L. Pastur, F. Lusseyran, Y. Fraigneau, and D. Bisch. Three-dimensional centrifugal instabilities development inside a parallelepipedic open cavity of various shape. *Experiments in Fluids*, 47(3):395–410, 2009.

L. H. Feng and J. J. Wang. Synthetic jet control of separation in the flow over a circular cylinder. *Experiments in Fluids*, 53:467–480, 2012.

N. F. Foster and G. S. Dulikravich. Three-dimensional aerodynamic shape optimization using genetic and gradient search algorithms. *Journal of Spacecraft and Rockets*, (1):36–42, 1997.

A. Garcia-Sagrado and T. Hynes. Stochastic estimation of flow near the trailing edge of a NACA0012 airfoil. *Experiments in Fluids*, 51:1057–1071, 2011.

M. Gharib and A. Roshko. The effect of flow oscillations on cavity drag. *Journal of Fluid Mechanics*, 177(1):501–530, 1987.

A. Glezer and M. Amitay. Synthetic Jets. *Annual Review of Fluid Dynamics*, 2002.

M. Gopal. *Digital Control & Stat Var Methd 3E.* McGraw-Hill Education (India) Pvt Limited, 2008.

Y. G. Guezennec. Stochastic estimation of coherent structures in turbulent boundary layers. *Physics of Fluids A*, 1:1054–1060, 1989.

N. Hansen and A. Ostermeier. Completely derandomized self-adaptation in evolution strategies. *Evolutionary computation*, 9(2):159–95, 2001.

M. H. Hayes. *Statistical Digital Signal Processing and Modeling.* John Wiley & Sons, Inc., New York, NY, USA, 1st edition, 1996.

A. Hokpunna and M. Manhart. A large-eddy simulation of vortex cell flow with incoming turbulent boundary layer. *Int J Mech Syst Sci Eng*, 1:123–128, 2007.

S. J. Illingworth, A. S. Morgans, and C. W. Rowley. Feedback control of cavity flow oscillations using simple linear models. *Journal of Fluid Mechanics*, 709:223–248, 2012.

W.A. Kasper. Aircraft wing with vortex generation, 1974. U.S Patent No.3831885.

M.A. Kegerise and R.H. Cabell. Real-time adaptive control of flow-induced cavity tones(invited). 42^{nd} *AIAA Aerospace Sciences*, pages 1–13, 2004.

J. Kim and T. R. Bewley. A Linear Systems Approach to Flow Control. *Annual Review of Fluid Mechanics*, 39(1):383–417, 2007.

C. H. Kuo and S. H. Huang. Influence of flow path modification on oscillation of cavity shear layer. *Experiments in Fluids*, 31(2):162–178, 2001.

L. Larchevêque, P. Sagaut, and O. Labbé. Large-eddy simulation of a subsonic cavity flow including asymmetric three-dimensional effects. *Journal of Fluid Mechanics*, 577:105–126, 2007.

D. Lasagna, R. Donelli, F. De Gregorio, and G. Iuso. Effects of a trapped vortex cell on a thick wing airfoil. *Experiments in Fluids*, 51:1369–1384, 2011.

D. Lasagna, M. Orazi, and G. Iuso. Multi-time-delay, multi-point linear stochastic estimation of a cavity shear layer velocity from wall-pressure measurements. *Physics of Fluids*, 25(1):017101, 2013.

Y. Li, K. H. Ang, G. C. Y. Chong, W. Feng, K. C. Tan, and H. Kashiwagi. Cautocsd-evolutionary search and optimisation enabled computer automated control system design. *International Journal of Automation and Computing*, 1(1):76–88, 2004.

J. C. Lin and D. Rockwell. Organized oscillations of initially turbulent flow past a cavity. *AIAA Journal*, (36):1139–1151, 2001.

L. Ljung. *System Identification: Theory for the User*. Pearson Education, 1998.

D. J. Maull and L. F. East. Three-dimensional flow in cavities. *Journal of Fluid Mechanics*, 16:620–632, 1963.

Z. Michalewicz and D. B. Fogel. *How to Solve It: Modern Heuristics*. Springer, 2004.

C. Migeon. Details on the start-up development of the Taylor-Gortler-like vortices inside a square-section lid-driven cavity for 1,000 <Re< 3,200. *Experiments in Fluids*, 33:594–602, 2002.

M. Milano and P. Koumoutsakos. A clustering genetic algorithm for cylinder drag optimization. *Journal of Computational Physics*, 175(1):79 – 107, 2002.

R. Mittal, R. B. Kotapati, and L. N. Cattafesta. Numerical study of resonant interactions and flow control in a canonical separated flow. *AIAA Paper*, 1261: 1–12, 2005.

L. Mongeau, H. Kook, D. V. Brown, and S. I. Zorea. Analysis of the interior pressure oscillations induced by flow over vehicle openings. *Noise Control Engineering Journal*, 45, 1997.

A. M. Naguib, C .E. Wark, and O. Juckenhofel. Stochastic estimation and flow sources associated with surface pressure events in a turbulent boundary layer. *Physics of Fluids*, 13(9):2611, 2001.

K. S. Narendra and K. Parthasarathy. Identification and control of dynamical systems using neural networks. *Neural Networks, IEEE Transactions on*, 1(1):4–27, 1990.

B. Noack, G. Tadmor, and M. Morzynski. Low-Dimensional Models for Feedback Flow Control. Part I: Empirical Galerkin Models. *AIAA Flow Control Conference*, pages 1–11, 2004.

W. F. J. Olsman and T. Colonius. Numerical simulation of flow over an airfoil with a cavity. *AIAA Journal*, 49:143–149, 2011.

M. Pastoor, L. Henning, B.N. King R. Noack, and G. Tadmor. Feedback shear layer control for bluff body drag reduction. *Journal of Fluid Mechanics*, 608:161–196, 2008.

C. Picard and J. Delville. Pressure velocity coupling in a subsonic round jet. *International Journal of Heat and Fluid Flow*, 21(3):359 – 364, 2000.

F. O. Ringleb. Separation control by trapped vortices. In *Boundary Layer and flow control, Pergamon Press, Ed. Lachmann G.V.*, 1961.

D. Rockwell and C. Knisely. Observations of the three-dimensional nature of unstable flow past a cavity. *Physics Fluids*, 23:425–431, 1980.

D. Rockwell and E. Naudascher. Review - self-sustaining oscillations of flow past cavities. *Journal of Fluids Engineering*, 100(2):152–165, 1978.

J.E. Rossiter. Wind-tunnel experiments on the flow over rectangular cavities at subsonic and transonic speeds. *Aeronautical Research Council*, (No. 3438), 1964.

C. W. Rowley and D. R. Williams. Dynamics and control of high-reynolds number flow over open cavities. *Annual Review of Fluid Mechanics*, 38(1):251–276, 2006.

C .W. Rowley, T. Colonius, and A. J. Basu. On self-sustained oscillations in two dimensional compressible flow over rectangular cavities. *Journal of Fluid Mechanics*, 455:315–345, 2001.

C. W. Rowley, D. R. Williams, T. Colonius, R. M. Murray, and D. G. Macmynowski. Linear models for control of cavity flow oscillations. *Journal of Fluid Mechanics*, 547:317–330, 2006.

M. Samimy, M. Debiasi, E. Caraballo, A. Serrani, X. Yuan, J. Little, and J. H. Myatt. Reduced-Order Model-Based Feedback Control of Subsonic Cavity Flows—An Experimental Approach. *Active Flow Control*, pages 211–229, 2007.

V. Sarohia. *Experimental and analytical investigation of oscillations in flows over cavities*. PhD thesis, 1975.

V. Sarohia and P. F. Massier. Control of cavity noise. *Journal of Aircrafts*, 9(14): 833–837, 1977.

R. Savelsberg and I. Castro. Vortex flows in open cylindrical-section cavities. *Exp Fluids*, 46(3):485–497, 2008.

A. I Savitsky, L. N. Schukin, and V. G. Kareljn. Method for control of the boundary layer on the aerodynamic surface of an aircraft, and the aircraft provided with boundary layer control system, May 1995. U.S Patent No. 5417391.

A. Seifert, T. Bachar, D. Koss, M. Shepshelovich, and I. Wygnanski. Oscillatory blowing : a tool to delay boundary-layer separation. *AIAA J.*, 31:2052–2060, 1993.

D. Sipp. Open-loop control of cavity oscillations with harmonic forcings. *Journal of Fluid Mechanics*, 708:439–468, 2012.

V. Suponistsky, E. Avital, and M Gaster. On three dimensionality and control of incompressible cavity flow. *Physics of Fluids*, 17(104103), 2005.

Y. Suzuki, K. I. Morimoto, K. Iwamoto, and N. Kasagi. Feedback control of wall turbulence based on the streamwise wall shear stress. In *APS Division of Fluid Dynamics Meeting Abstracts*, 2001.

K. C. Tan and Y. Li. Identification and model reduction for robust control. *Proceedings of the Institution of Mechanical Engineers Part I: Journal of Systems and Control Engineering*, 214(3):231–238, 2000.

O. Tutty, R. Savelsberg, and I. Castro. Three-dimensional flow in circular cavities of large spanwise aspect ratio. *Journal of Fluid Mechanics*, 707:551–574, 2012.

L. Ukeiley and N. Murray. Velocity and surface pressure measurements in an open cavity. *Experiments in Fluids*, 38:656–671, 2005.

B. Vukasinovic, D. G. Lucas, and A. Glezer. Direct manipulation of small-scale motions in a plane shear layer. *AIAA Paper*, 2617:1–13, 2004.

K. Yamamoto and O. Inoue. Applications of genetic algorithm to aerodynamic shape optimization. In *AIAA Computational Fluid Dynamics Conference, 12 th, San Diego, CA*, pages 43–51, 1995.

L. Zannetti. Vortex equilibrium in flows past bluff bodies. *Journal of Fluid Mechanics*, pages 151–171, 2006.

K. Zhang and A. M. Naguib. Effect of finite cavity width on flow oscillation in a low-Mach-number cavity flow. *Experiments in Fluids*, 51(5):1209–1229, 2011.

P. F. Zhang and J. J. Wang. Novel signal wave pattern for efficient synthetic jet generation. *AIAA Journal*, 45(5):1058–1065, 2007.